BOSTON UNIVERSITY

GRADUATE SCHOOL OF ARTS AND SCIENCES

Dissertation

SEARCHES FOR PROTON DECAY WITH THE SUPER–KAMIOKANDE DETECTOR

by

SCOTT T. CLARK

B.S., University of Kansas, 2001

Submitted in partial fulfillment of the

requirements for the degree of

Doctor of Philosophy

2007

Approved by

First Reader

Edward T. Kearns, Ph.D.
Associate Professor of Physics

Second Reader

John Butler, Ph.D.
Professor of Physics

Acknowledgments

I would like to thank all of the people whose support, advice, and encouragement have been so helpful during my graduate education. Particular thanks go to my advisor Ed Kearns for his guidance and advice, as well as to Chris Walter for guiding my entry into the Super–Kamiokande collaboration. I would also like to thank my thesis committee members, Claudio Rebbi, James Stone, John Butler, and Karl Ludwig, for their insightful questions and comments.

The other researchers in the BU Super-K group have been a consistent source of ideas, discussions, and friendship. Many thanks to Jen Raaf, Mike Litos, Fanny Dufour, Wei Wang, Shantanu Desai, Dan Gastler, Aaron Herfurth, and Johnny Penwell.

The Super–Kamiokande collaboration is very well served by the leadership of its spokesmen, Yoichiro Suzuki, James Stone, and Henry Sobel. The atmospheric neutrino/proton decay analysis group is equally well served by the guidance of Takaaki Kajita and Ed Kearns. Special thanks go to Masato Shiozawa, Kazuyoshi Kobayashi, Kenji Kaneyuki, Masaki Ishitsuka, and Kimihiro Okumura whose work and advice have been so useful in this research.

I also wish to thank my family, who have given me unending support and encouragement throughout my entire graduate career. My parents Jim and Carol deserve great credit for inspiring me to pursue graduate education, as do my parents-in-law Tony and Carmella, whose warm welcome to Boston and their family has been a great comfort. My sister Laura has been a consistent inspiration to me. And lastly, but most importantly, I would like to thank my wife. Gina, your love, support, and encouragement have been unending, even through my frequent trips to Japan. I'd never want to try something like this without you.

SEARCHES FOR PROTON DECAY WITH THE SUPER–KAMIOKANDE DETECTOR

(Order No.)

SCOTT T. CLARK

Boston University Graduate School of Arts and Sciences, 2007

Major Professor: Edward T. Kearns, Associate Professor of Physics

ABSTRACT

This dissertation presents searches for proton decay via four modes, using a 141.3 kiloton-year exposure of the Super–Kamiokande water Cherenkov detector. The running period called SK-I contributes 91.8 kiloton-years, with 11,146 photomultiplier tubes (PMTs) providing a 40% photocathode coverage. The SK-II period contributes 49.5 kiloton-years, and, due to an accident, used 5,183 PMTs providing 20% photocathode coverage. This difference provides an opportunity to compare the effectiveness of a detector with a factor of two reduction in the number of PMTs, with implications for the cost of a future megaton-scale detector.

The modes studied are $p \to e^+\pi^0$, which is favored by non-supersymmetric grand unified theories, the closely related mode $p \to \mu^+\pi^0$, the supersymmetry-favored mode $p \to \bar{\nu}K^+$, and the related mode $p \to \bar{\nu}K^*(892)^+$. The method used is based on the comparison of Monte Carlo simulated datasets representing proton decay events versus the background from atmospheric neutrinos. This comparison is used to develop criteria to distinguish proton decay events from the background. These criteria are applied to the real data to seek proton decay candidates.

No evidence for proton decay via any of these modes is found, so lower limits on the partial lifetimes into these modes are set at the 90% confidence level. These limits are:

$$\begin{aligned} p \to e^+\pi^0 \qquad & 8.0 \times 10^{33}\text{years} \\ p \to \mu^+\pi^0 \qquad & 6.3 \times 10^{33}\text{years} \\ p \to \bar{\nu}K^+ \qquad & 1.5 \times 10^{33}\text{years} \\ p \to \bar{\nu}K^*(892)^+ \qquad & 0.13 \times 10^{33}\text{years} \end{aligned}$$

The performance of SK-II versus SK-I is shown to be substantially worse for $p \to \bar{\nu}K^+$, though similar for $p \to e^+\pi^0$ and the other modes studied. These results tighten previous constraints on Grand Unified Theories based on the symmetry group $SO(10)$, particularly with respect to how $SO(10)$ may be broken to the Standard Model.

An additional independent method is used to set another limit on $p \to \bar{\nu}K^+$. This method considers the momentum spectrum of muon events. The predicted background spectrum plus proton decay signal (both coming from Monte Carlo simulations) is fit to the observed spectrum, using a χ^2 analysis, to determine the maximum allowable size of the proton decay signal. This method similarly yields no evidence of proton decay, and a second independent 90% confidence limit on the proton lifetime into $p \to \bar{\nu}K^+$ of 0.59 $\times 10^{33}$ years is set.

Contents

List of Tables

List of Figures

List of Abbreviations

ADC ..... Analog to Digital Converter

ATM ..... Analog Timing Module

BG ..... Background

CC ..... Charged Current

CCD ..... Charge-Coupled Device

CL ..... Confidence Level

DAQ ..... Data Acquisition

DIS ..... Deep Inelastic Scattering

EM ..... Electromagnetism

FRP ..... Fiber-Reinforced Plastic

GONG ..... GO-NoGo

GUT ..... Grand Unified Theory

HPW ..... Harvard-Purdue-Wisconsin

ID ..... Inner Detector

IMB ..... Irvine Michigan Brookhaven

KAMLAND ..... Kamioka Liquid Scintillator Anti-Neutrino Detector

KGF ..... Kolar Gold Field

LEP ..... Large Electron-Positron Collider

LHC ..... Large Hadron Collider

LINAC ..... Linear Accelerator

MC ..... Monte Carlo

MS-fit ..... Muon-Shower Fitter

NC ..... Neutral Current

NUSEX ..... Nucleon Stability Experiment

OD ..... Outer Detector

PDF ..... Probability Density Function

PE ..... Photoelectrons

PID ..... Particle identification

PMT ..... Photomultiplier tube

QE ..... Quasi-Elastic

QTC ..... Charge-to-Time Converter

SCH ..... Super-Controller Header

SK ..... Super-Kamiokande

SK-I ..... Super-Kamiokande I

SK-II ..... Super-Kamiokande II

SM ..... Standard Model

SMP ..... Super Memory Partner

SNO ..... Sudbury Neutrino Observatory

Super-K ..... Super-Kamiokande

SUSY ..... Supersymmetry

TDC ..... Time-to-Digital Converter

TKO ..... Tristan KEK Online

TS ..... Time Signature

VME ..... Versa Module Europa

Chapter 1

Introduction

Physics is, at root, a science of models. The fundamental goal of physics is to devise a model of nature that can successfully explain all observed aspects of the physical world, as well as predict the results of all future observations. This search for an ideal model proceeds through a succession of imperfect models, each a little bit better than the last. In this way, physicists come ever closer to a true understanding of the fundamental workings of the universe.

The basic process of physics, and indeed all science, is based on the construction of a model that explains some aspect of nature – in particular, a model that can account for a specific set of empirical observations. That model will then predict the results of other observations. In general, not all of these predictions will turn out to be accurate. By considering exactly how the model fails to reflect the real universe, an improved model will be constructed. This improved model will turn out to be inaccurate in other ways, which will lead to a still better model, and so on.

In particle physics, the most current model has proved to be so successful, and is so universally accepted, that it has earned the name of the "Standard Model." This Standard Model is one of the great success stories of science, in both breadth and

accuracy. It provides an understanding of all known matter, and the interactions between matter, to a truly astounding degree of accuracy. But that very success is, in a way, extremely frustrating.

The problem is that the Standard Model is not yet a complete description of the universe. This is most obvious with respect to gravity. Gravity is one of the most obvious and important forces in everyday life. The gravitational interaction has been quantitatively understood for more than three centuries, ever since Sir Isaac Newton devised his law of universal gravitation. Undergraduates and even high school students learn about it in their very first physics course. And yet, the Standard Model provides no explanation whatsoever for gravity. It is, in fact, completely absent from the theory.

The natural next step is then to proceed to that broader and more accurate theory that will replace the Standard Model in our understanding of the world around us. But there we encounter the frustrating aspect. The Standard Model is, in some sense, too good. We know it is not the ultimate theory of the universe. But constructing a superior theory must be guided by the failures of the Standard Model. Unfortunately, no experiment has yet shown any of its predictions to be fundamentally incorrect.

So, to inspire the successor to the Standard Model, particle physicists search for those failures that will serve as signatures of new physics. Major approaches to such a search include performing experiments at higher energy scales, making extremely precise measurements of physical parameters, and looking for rare processes. Each approach has its own unique advantages and drawbacks.

The extension of experiments to high energies has been highly successful in the past. It was this approach that demonstrated, for example, that protons and neutrons were not fundamental particles, but rather were composed of smaller particles now called quarks. Looking toward the future, this paradigm is expected to pro-

duce major new discoveries in a few years when the Large Hadron Collider, or LHC, begins taking data.

Experiments devoted to precision measurements of Standard Model predictions are ongoing, and reaching very impressive accuracy [1]. One particularly notable achievement along these lines is the measurement of the muon's magnetic moment, which is now known to within 0.00005% – and is not definitively different from the Standard Model prediction [2], differing by less than 3 σ.

Another way to look for deviations from the Standard Model involves searching for direct contradictions. Observation of a process that is deemed impossible in the Standard Model would be one example of a contradiction implying physics beyond the Standard Model. One instance of this is the decay of protons, which are predicted to have an unobservably long lifetime in the Standard Model. It is this approach which is pursued in this dissertation.

Proton decay experiments generally share a common pattern. One starts with as large a sample of matter as practical. That sample is then observed for as long a time as practical, using some form of detector capable of detecting the products from a single proton decay. The practical aspects, however, are significantly more complex. For example, muons produced by cosmic rays produce a troublesome background. For this reason, proton decay experiments are generally located deep underground to shield them from such muons.

For this dissertation, the Super–Kamiokande detector is used. This is a large water Cherenkov detector located in the Mozumi mine operated by the Kamioka Mining and Smelting Company, in Japan's Gifu prefecture. The 50,000 tons of water contained in the detector provide a very large sample of protons; decay products are identified via the production of Cherenkov light and subsequent detection by the photomultiplier tubes lining the detector.

This dissertation presents the results of searches for several different modes of proton decay. These modes include the dominant predictions by various proposed theories. Also included are modes that are less theoretically favored, but for that reason would be even more interesting if they were observed.

Chapter 2

Theoretical Background

2.1 The Standard Model

Within the Standard Model, the basic constituents of matter are particles with spin $\frac{1}{2}$, called fermions. The Standard Model fermions are separated into two groups, called quarks and leptons. Each fermion also has an anti-particle, which has the same mass, but opposite quantum numbers, such as electric charge. The most familiar example of a lepton is the electron. Quarks, unlike leptons, are never found in isolation. They always form groupings with other quarks. The two major forms of these groupings are mesons such as the pion, which consist of a quark and an antiquark, and baryons such as the proton which consist of three quarks.

In nature, four fundamental forces, or interactions, are observed: strong, weak, electromagnetic, and gravitational. The strong force is responsible for such processes as nuclear fission and fusion. Picking up a paper clip using a magnet is an electromagnetic interaction. The weak force is responsible for radioactive decays such as beta decay: $n \rightarrow pe^{-}\bar{\nu}_e$. Gravity is responsible for such things as holding a rock to the ground.

The Standard Model accounts for the first three of these, but provides no explanation for gravity. Within this framework, all interactions are mediated by so-called "gauge bosons" which are exchanged between particles to produce an interaction. Each force has its own set of bosons. Gluons carry the strong force and photons the electromagnetic, while the W and Z bosons carry the weak interaction. In each case, only particles carrying a certain type of charge participate in the interaction. For example, only particles carrying "color," (*i.e.* quarks) interact strongly, while only particles carrying electric charge interact electromagnetically. All left-handed fermions interact via the weak interaction.

2.1.1 Conservation and Symmetries

Physical quantities that do not change in any interaction are said to be "conserved." Examples familiar from basic physics include energy and momentum, as well as electric charge. Less familiar examples are color, lepton number, and baryon number. While these conservation laws are superficially similar, they actually arise from very different considerations.

Conservation laws in particle physics are understood to arise from symmetries. A "symmetry" is some operation that does not change the underlying physics of the universe (or, more formally, leaves the Lagrangian invariant). According to Noether's Theorem, for any symmetry, there is an associated conservation law. For example, translation in space, translation in time, and rotation are all symmetries. These symmetries, which are all special cases of the more general symmetry under Lorentz transformations, result in the conservation of momentum, energy, and angular momentum respectively.

In physics, symmetries and conservation laws are often described using group

theory. For example, spin-$\frac{1}{2}$ systems are described by the $SU(2)$ group of traceless unitary matrices. Any such matrix $\mathcal{R}$ can be written as

$$\mathcal{R} = e^{i\vec{\alpha}\cdot\vec{L}} \tag{2.1}$$

for some vector $\vec{\alpha}$ if one defines $L_i = \frac{1}{2}\sigma_i$, where the σ_i are the Pauli spin matrices. The L_i are called "generators" of $SU(2)$. The group can be completely defined by the commutation relations of its generators L_i:

$$[L_i, L_j] = i\epsilon_{ijk}L_k, \tag{2.2}$$

where ϵ_{ijk} is the completely antisymmetric tensor of rank three.

These generators can be used to describe spin-$\frac{1}{2}$ systems by noting that such systems have two orthogonal eigenstates, $|+\rangle$ and $|-\rangle$ – such a pairing of states is often called a "doublet" – and writing

$$L_\pm = L_1 \mp iL_2, \tag{2.3}$$

which implies that $L_\pm |\mp\rangle = |\pm\rangle$. The entire system can then be described in terms of its generator matrix L and its doublet ϕ:

$$L = \frac{1}{2}\begin{bmatrix} l_3 & l_+ \\ l_- & -l_3 \end{bmatrix} \tag{2.4}$$

$$\phi \rightarrow \begin{pmatrix} \text{up} \\ \text{down} \end{pmatrix}. \tag{2.5}$$

The diagonal elements of L represent projections of the state ϕ, while the off-diagonal

elements are transformations between up and down.

This is related to gauge theories in particle physics. The $L_\pm$ and L_3 matrices are related to bosons, such as the $W^\pm$ and the Z. The doublet of up and down is analogous to a doublet of fermions, such as the electron and its neutrino.

2.1.2 $SU(3)_C \times SU(2)_L \times U(1)_Y$

The Standard Model is based on the direct product gauge group $SU(3)_C \times SU(2)_L \times U(1)_Y$ [3, 4, 5]. The group $SU(3)_C$ describes the strong force, and has a corresponding conserved quantity called color. The different colors form a triplet, and are labeled as red, blue, and green. The group $SU(3)$ has eight independent generators, which become the gluons. In analogy to Eqs. 2.4 and 2.5, this system can be written

$$G_{gluons} = \begin{bmatrix} g_{r\bar{r}} & g_{r\bar{g}} & g_{r\bar{b}} \\ g_{g\bar{r}} & g_{g\bar{g}} & g_{g\bar{b}} \\ g_{b\bar{r}} & g_{b\bar{g}} & g_{b\bar{b}} \end{bmatrix} \tag{2.6}$$

$$\phi_C \rightarrow \begin{pmatrix} \text{red} \\ \text{green} \\ \text{blue} \end{pmatrix}, \tag{2.7}$$

where $g_{b\bar{b}} = -g_{r\bar{r}} - g_{g\bar{g}}$ (and is therefore not a ninth independent generator). Under this group, each quark is a triplet, while the leptons are all singlets.

The electromagnetic and weak interactions are in turn governed by the $SU(2)_L \times U(1)_Y$ electroweak group. The subscript L denotes the fact that only left-handed particles interact via this group. This statement is equivalent to the fact that all right-handed particles are singlets under this group. Y indicates the quantity "weak

hypercharge:"

$$Y = 2(Q - T_3), \tag{2.8}$$

where Q is the electromagnetic charge and T_3 is the eigenvalue for the third component of "weak isospin," the conserved quantity from $SU(2)_L$. This equation, and in particular the fact that it includes both electromagnetic and weak charge, illustrates that the electromagnetic and weak forces are very closely related.

This relationship is expressed in terms of spontaneous symmetry breaking. An unbroken $SU(2)_L \times U(1)_Y$ would result in the four gauge bosons related to this group – the $W^{\pm}$, Z, and photon – all being perfectly massless, just like the gluons. Of these four, however, only the photon is observed to be massless in nature.

This symmetry breaking is described via the "Higgs mechanism" [6]. In this formulation, there are many possible ground states of the universe. These degenerate ground states are related by transformations under $SU(2)_L \times U(1)_Y$. However, only one of these exists in nature. Because of this the underlying symmetry is broken – these states are no longer truly symmetric, because one of them is realized and the others are not. However, some part of the symmetry is still realized because the existing state still respects it. This remaining symmetry is $U(1)_{EM}$ (as distinct from $U(1)_Y$), and is identified with electromagnetism at low energies.

This process produces a new boson, called the Higgs boson, and gives the W and Z bosons masses while mixing the gauge bosons together:

$$Z_\mu = -a^\mu \sin\theta_W + W_3^\mu \cos\theta_W \tag{2.9}$$

$$A^\mu = a^\mu \cos\theta_W + W_3^\mu \sin\theta_W, \tag{2.10}$$

where μ is the space-time dimension index, A_μ is the photon gauge field, and θ_W is the "weak mixing angle" which parameterizes the relationship between the weak and electromagnetic forces. The coupling constants for the $SU(2)_L$ and $U(1)_Y$ gauge groups are then expressed in terms of θ_W and the fine structure constant of electromagnetism α_{em}.

Under $SU(2)_L$, each right-handed quark or charged lepton is a singlet, while right-handed neutrinos do not exist in the Standard Model. This implies that neutrinos are exactly massless. The left-handed quarks and leptons form doublets:

$$\begin{pmatrix} \nu_e \\ e \end{pmatrix} \begin{pmatrix} u \\ d' \end{pmatrix}, \tag{2.11}$$

and similarly for the other two generations. Here the d', s', and b' are mixtures of the d, s, b mass eigenstates. This mixing is described by the Cabibbo-Kobayashi-Maskawa, or CKM, matrix. The specification of the Standard Model gauge groups is then completed by noting that the left-handed leptons have $Y = -1$ and the left-handed quarks have $Y = 1/3$.

It is worth noting that the proton's lifetime in the Standard Model, while long, is not infinite. The proton is perfectly stable against perturbative interactions, but non-perturbative effects do lead to proton decay. However, the proton lifetime in the Standard Model is roughly 10^{150} years [7]. Since no proton decay experiment has yet reached lifetimes of even 10^{34} years, this is far beyond the reach of any presently conceivable experiment. Any experimental observation of proton decay must therefore be a signature of physics beyond the Standard Model.

2.1.3 Problems

While the Standard Model is certainly a successful theory, it has certain unattractive features. Most notably, it is hardly simple. With a gauge group formed by a direct product of three different gauge groups, and the many representations the various fermions populate under those groups, it begs the question of why such a complex structure should exist. Various attempts have been made to address this question, most notably in the context of Grand Unified Theories (GUTs).

Other problems include the overly large number of free parameters – 18, even when massless neutrinos are assumed. The addition of neutrino masses and mixings increases the number of free parameters to 25. Also, as mentioned earlier, gravity is not described by the Standard Model. Either or both of these can be addressed in the context of a GUT, as well.

2.2 Grand Unified Theories

Since the underlying $SU(2)_L \times U(1)_Y$ gauge group being broken to the $U(1)_{EM}$ of electromagnetism is a normal feature of the Standard Model, it is perhaps natural to wonder whether a similar effect might be responsible for the $SU(3)_C \times SU(2)_L \times U(1)_Y$ gauge group. And just as the $SU(2)_L \times U(1)_Y$ structure is recovered from $U(1)_{EM}$ at sufficiently high energies (*i.e.* comparable to the W and Z masses), this hypothetical larger group would become evident at still higher energies. This line of thought leads to development of Grand Unified Theories.

2.2.1 Running Coupling Constants

The strongest experimental suggestion of unification is a consequence of the running of the SM coupling constants, which are not truly constant, but vary with energy. The evolution of these coupling constants is fairly closely (though not exactly) described by:

$$\frac{1}{\alpha_i(E)} = \frac{1}{\alpha_{GUT}} + \frac{b_i}{6\pi} \log \frac{M_{GUT}}{E}, \tag{2.12}$$

where α_i are the three coupling constants, E is the energy scale at which measurements are being made, and b_i are coefficients for each coupling constant, which depend what model of physics beyond the Standard Model is assumed, particularly on what particles beyond those in the Standard Model are assumed to exist. It can therefore be seen that, at energy $E = M_{GUT}$, all three interactions will have strength α_{GUT}. This is exactly what would be expected if some single gauge group were spontaneously broken to the Standard Model at a characteristic energy scale M_{GUT}.

This is illustrated in Fig. 2.1. While the coupling constants do not precisely meet, they come close enough to be suggestive. Historically, when the first GUTs were proposed, the uncertainties on the coupling constants were large enough to be compatible with perfect unification. Improved measurements, however, have now demonstrated that perfect unification does not occur without the addition of new particles.

2.2.2 Minimal $SU(5)$

The simplest possible GUT (*i.e.* the smallest simple gauge group which can contain $SU(3) \times SU(2) \times U(1)$) is called "minimal $SU(5)$" because its gauge symmetry is the

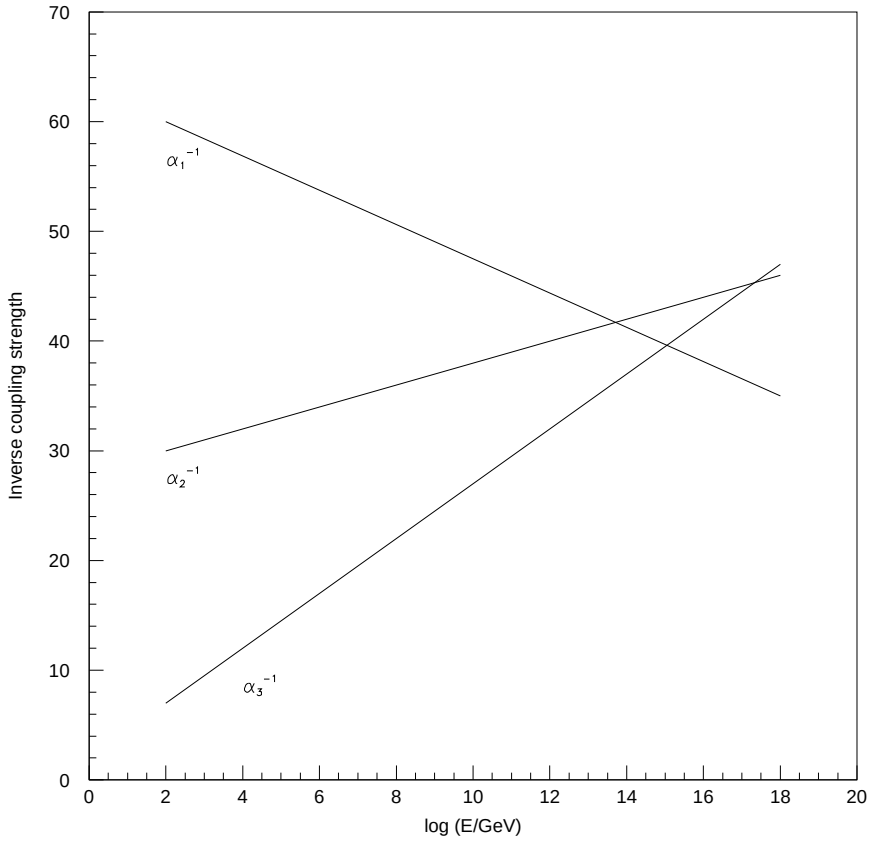

Figure 2.1: Running coupling constants with Standard Model particles only.

$SU(5)$ group. The "minimal" aspect refers to the fact that it assumes the smallest possible Higgs sector for the gauge group. This theory was first proposed by Georgi and Glashow in 1974 [8]. In this theory, the generator matrix can be written as:

$$V_{SU(5)} = \left[\begin{array}{ccc|cc} g_{r\bar{r}} - \frac{2}{\sqrt{30}}a & g_{r\bar{g}} & g_{r\bar{b}} & X_1 & Y_1 \\ g_{g\bar{r}} & g_{g\bar{g}} - \frac{2}{\sqrt{30}}a & g_{g\bar{b}} & X_2 & Y_2 \\ g_{b\bar{r}} & g_{b\bar{g}} & g_{b\bar{b}} - \frac{2}{\sqrt{30}}a & X_3 & Y_3 \\ \hline \bar{X}_1 & \bar{X}_2 & \bar{X}_3 & \frac{1}{\sqrt{2}}W^3 + \frac{3}{\sqrt{30}}a & W^+ \\ \bar{Y}_1 & \bar{Y}_2 & \bar{Y}_3 & W^- & -\frac{1}{\sqrt{2}}W^3 + \frac{3}{\sqrt{30}}a \end{array}\right]. \tag{2.13}$$

The structure of the Standard Model is evident within $V_{SU(5)}$. The top left 3×3 contains the gluons, the bottom right 2×2 contains the W bosons of $SU(2)_L$, and the a of $U(1)_Y$ is along the diagonal. The bottom left and top right sections contain new X and Y bosons.

In minimal $SU(5)$, the fermions are contained in $\bar{\mathbf{5}}$ and $\mathbf{10}$ representations, instead of the SM's numerous singlets, doublets, and triplets:

$$\bar{\mathbf{5}} = \begin{pmatrix} \bar{d}_r \\ \bar{d}_g \\ \bar{d}_b \\ e^- \\ -\nu_e \end{pmatrix}_L \tag{2.14}$$

$$\mathbf{10} = \left(\begin{array}{ccc|cc} 0 & \bar{u}_b & -\bar{u}_g & -u_r & -d_r \\ -\bar{u}_b & 0 & \bar{u}_r & -u_g & -d_g \\ \bar{u}_g & -\bar{u}_r & 0 & -u_b & -d_b \\ \hline u_r & u_g & u_b & 0 & e^+ \\ d_r & d_g & d_b & -e^+ & 0 \end{array}\right)_L, \tag{2.15}$$

An interesting feature of minimal $SU(5)$ is that it naturally results in charge

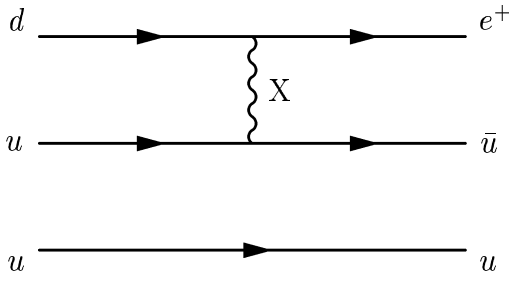

Figure 2.2: An example of proton decay in SU(5).

quantization. The photon, which is the generator of electric charge, is a generator of $SU(5)$. This means it must be traceless when applied to a representation of $SU(5)$, and applying this condition to the $\bar{\mathbf{5}}$ results in the statement that the charge on the $\bar{d}$ is $-1/3$ the charge on the e^-. This nicely explains the somewhat peculiar values of Y in the Standard Model.

In the Standard Model, interactions can change fermions within their multiplets. The strong interaction changes the color of quarks, and the weak interaction can change leptons within the weak doublets, so that a ν_e will be turned into an e^-, for example. This principle applies equally well in GUTs, so since quarks and leptons are combined in the multiplets in representations of $SU(5)$, baryon number violation, and hence proton decay, is permitted. Such decays are mediated by the new X and Y bosons, and are predicted to be dominated by $p \to e^+\pi^0$. One example of how this could happen is shown in Fig. 2.2.

The proton lifetime in this theory goes as:

$$\tau_p \sim \frac{1}{\alpha_{GUT}^2}\frac{M_{GUT}^4}{m_p^5}, \tag{2.16}$$

where M_{GUT} is approximately the mass of the X and Y bosons. By applying Eq. 2.12, with b_i calculated in minimal $SU(5)$, it results that $M_{GUT} \sim 10^{15}$ GeV/c^2. This leads to a prediction of $\tau_p \sim 10^{30\pm1.5}$ years [9]. The uncertainty here is dominated by the

masses of the X and Y bosons, as they are not exactly M_{GUT}.

While minimal $SU(5)$ is the simplest possible GUT, it is unfortunately not in agreement with experiment. Its predicted proton lifetime of $10^{30\pm1.5}$ years was excluded when IMB set a limit on $p \to e^+\pi^0$ of 5.5×10^{32} years [10]. More recent measurements by Super-K have extended this limit, further ruling out minimal $SU(5)$ [11]. Additionally, minimal $SU(5)$ predicts that $\sin^2\theta_W = 0.214 \pm 0.003$ [12], while the measured value is $\sin^2\theta_W = 0.23120 \pm 0.00015$ [13].

2.2.3 $SO(10)$

Other GUTs, however, are still viable. One currently popular example is based on the gauge symmetry $SO(10)$, which includes the same kind of X and Y bosons as $SU(5)$. A very interesting aspect of $SO(10)$ is that it places all fermions of a specific generation in a single **16** representation. This is possible despite the fact that the Standard Model and minimal $SU(5)$ each include only 15 particles per generation, because $SO(10)$ naturally and necessarily includes a right-handed neutrino. It is, in fact, the simplest possible left-right symmetric GUT.

Because of this, $SO(10)$ predicts massive neutrinos, which is particularly notable due to the recent strong evidence of mass-induced neutrino oscillations [14]. While right-handed neutrinos (and hence neutrino mass) can be readily added to minimal $SU(5)$ or the Standard Model by introducing them as a new singlet representation, they are an inevitable result of $SO(10)$.

It has been shown that most models of the breaking of $SO(10)$ to the Standard Model gauge group predict proton decay lifetimes via $p \to e^+\pi^0$ that are at most as long as in minimal $SU(5)$ [15]. Such models are therefore ruled out as well. In fact, minimal $SO(10)$ is only viable if the symmetry breaking goes through one of a

limited number of groups [16]. One prominent possibility is the group $SU(4)_{EC} \times SU(2)_L \times SU(2)_R$. This is called the Pati-Salam group [17], and is also referred to as $G(224)$. The $G(224)$ group contains the same $SU(2)_L$ as the Standard Model, as well as a right-handed counterpart. The $SU(4)_{EC}$ group is an extension of the $SU(3)_C$ group, with lepton number treated as a fourth color. Another option is the similar group $SU(3)_C \times SU(2)_L \times SU(2)_R \times U(1)_{B-L}$, also called $G(2213)$. In either case, parity may or may not be a symmetry as well. So there are four patterns of symmetry breaking for minimal $SO(10)$.

Depending on which pattern is chosen, the prediction for the proton lifetime into $p \to e^+\pi^0$ varies from $2 \times 10^{32\pm2}$ years for $G(224)$ with parity to $7 \times 10^{37\pm2}$ years for $G(2213)$ without parity [16]. While this high end is well beyond the reach of current experiments, the region predicted by $G(224)$ with parity is accessible to Super-K. In fact, most of it is ruled out, and the rest is within reach. Continued efforts should therefore be able to constrain the pattern of symmetry breaking in $SO(10)$.

2.3 Supersymmetry

Another possible type of new physics has been named supersymmetry, or SUSY [18]. SUSY proposes that each of the Standard Model particles has a so-called "superpartner," with almost the same quantum numbers. The major difference is that the superpartner of a boson would be a fermion, and the superpartner of a fermion is a boson. So, the u and d quarks would be joined by the $\tilde{u}$ and $\tilde{d}$ squark bosons, the gluons g would be mirrored by the $\tilde{g}$ gluino fermions, and so on. It is also known that, if SUSY exists, the superpartners must all be very heavy, since none of them have yet been observed in colliders (though the LHC will likely be able to find at least some of them, assuming they exist). While SUSY can technically exist

on its own, it is most often considered in the context of a GUT. This combination is referred to as a SUSY GUT. The most prominent candidates for the GUT are, again, $SU(5)$ and $SO(10)$.

The reason for this combination is that SUSY improves unification significantly. This is because Eq. 2.12 is not quite correct for non-SUSY GUTs in general, and the coupling constants do not unify exactly, though they come close. However, the introduction of SUSY improves this agreement significantly, to the extent that current measurements are compatible with perfect unification [19]. Specifically, the existence of superpartners modifies the b_i's in Eq. 2.12. The addition of the superpartners changes the running of the coupling constants just enough for them to unify exactly, within the current experimental uncertainties. This is illustrated in Fig. 2.3.

This results in M_{GUT} increasing by a factor of 10, which in minimal SUSY $SU(5)$, by Eq. 2.16, increases the proton lifetime into $p \to e^+\pi^0$ by 10^4. This is enough to be compatible with current limits. Additionally, the prediction of $\sin^2\theta_W$ becomes 0.233 ± 0.003 [12], which is much closer to the experimental value, 0.23120 ± 0.00015 [13].

SUSY GUTs also solve the "hierarchy problem." In non-SUSY GUTs, calculations of the mass of the electroweak Higgs boson include terms on the order of $M_{X,Y}$, which is much greater than the electroweak scale where the Higgs most naturally lies. To produce a reasonable Higgs mass, these contributions must cancel out somehow. SUSY provides a mechanism for this cancellation, since the contributions from superpartners will be of equal magnitude, but opposite sign, to the contributions from the Standard Model particles [7].

However, SUSY leads to proton decay via other modes, in addition to $p \to e^+\pi^0$. Most prominent is the new dimension-5 interaction involving exchange of a Higgsino (the superpartner of the Higgs boson), as shown in Fig. 2.4. This interaction has

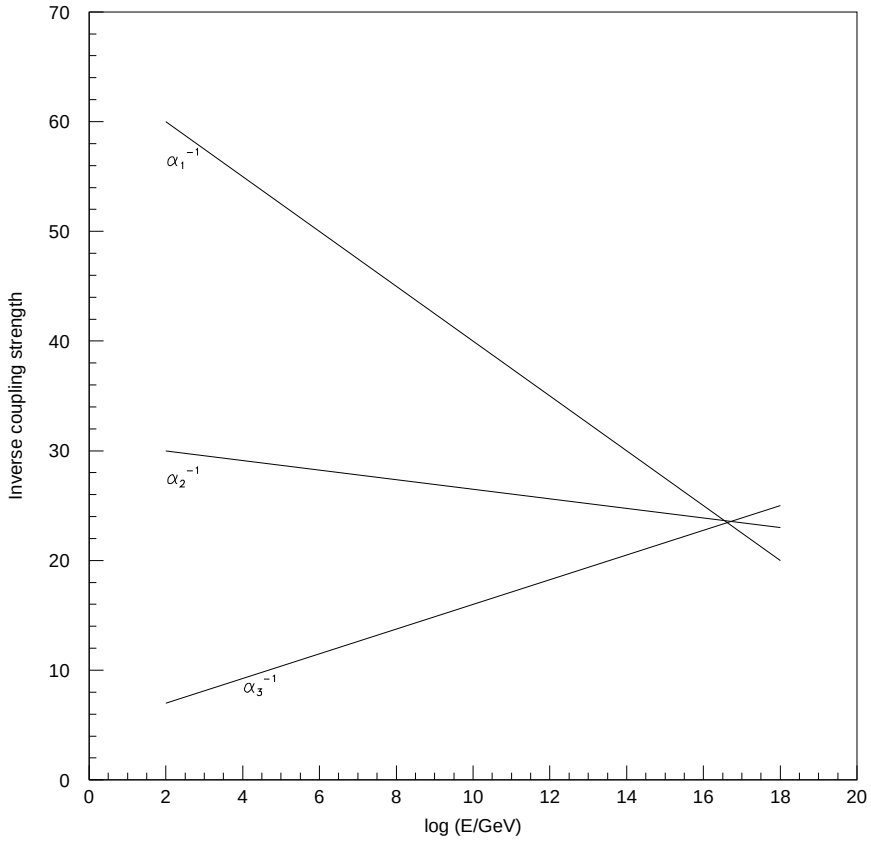

Figure 2.3: Running coupling constants in SUSY.

the interesting property that the particles before and after cannot be of the same generation, or the matrix element for the interaction vanishes [7]. Since the particles making up the proton are all first-generation, the decay products must be second- or third-generation particles. The only such quark that is kinematically allowed is the strange quark, so a K meson is produced. Specifically, the dominant mode is $p \to \bar{\nu} K^+$.

The predictions for SUSY proton decay depend on the GUT selected. For the simplest SUSY GUT, minimal SUSY $SU(5)$, some calculations indicate that the

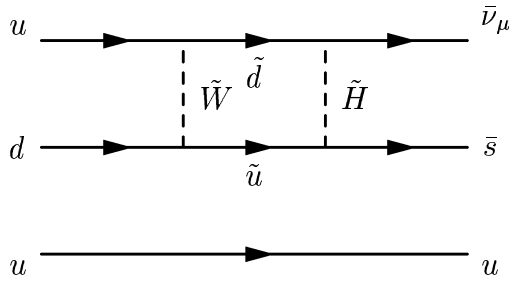

Figure 2.4: An example of supersymmetric proton decay.

proton lifetime into $p \to \bar{\nu}K^+$ is no longer than 2.9×10^{30} years [20]. This is decisively ruled out by recent SK-I results [21]. Other calculations, however, indicate that proton decay can be sufficiently suppressed by fine-tuning of the parameters [22]. So the conclusion must be that "natural" minimal SUSY $SU(5)$ is ruled out, and other alternatives should be investigated.

An interesting variant on SUSY is generated by turning supersymmetry from a global symmetry into a gauge symmetry [23]. This results in the existence of a massless spin-2 boson, identified as the graviton, its spin-3/2 superpartner the gravitino, and the gravitational interaction. For this reason, such theories are called supergravity (SUGRA) models. SUGRA $SU(5)$ results in proton decay via $p \to \bar{\nu}K^+$ with a lifetime of up to 10^{32} to 10^{34} years [24, 25]. Current limits already constrain this range significantly, and improved limits will tighten the constraints.

As in the non-SUSY case, $SO(10)$ is another popular choice for a SUSY GUT. Proton decay rates via $p \to \bar{\nu}K^+$ for this model have been calculated, and range from 1.4×10^{32} years to 2.2×10^{34} years [26]. The upper end of this range is well beyond the current reach of Super-K, so this model, as SUGRA $SU(5)$, is in no immediate danger of being ruled out by proton decay limits. Improved limits will, however, tighten the constraints on the parameters of the model.

More exotic possibilities also exist, such as SUSY $SU(5)$ in five dimensions with an additional $U(1)$ "anomalous flavor" symmetry, which predicts $p \to \bar{\nu}K^+$ with a

Theory	Mode	Predicted lifetime (years)
Minimal $SU(5)$	$p \to e^+\pi^0$	$10^{28.5}$ to $10^{31.5}$ [9]
Minimal $SO(10)$	$p \to e^+\pi^0$	10^{30} to 10^{40} [16]
Minimal SUSY $SU(5)$	$p \to \bar{\nu}K^+$	$\leq 10^{30}$ [20]
SUGRA $SU(5)$	$p \to \bar{\nu}K^+$	10^{32} to 10^{34} [24, 25]
SUSY $SO(10)$	$p \to \bar{\nu}K^+$	10^{32} to 10^{34} [26]

Table 2.1: Summary of proton decay predictions for selected theories.

lifetime between 10^{33} and 10^{36} years [27]. Another exotic model is the "flipped" SUSY $SU(5)$ model, predicting $p \to e^+\pi^0$ with a lifetime of 10^{31} to 10^{35} years or more [28].

A summary of predictions for several models is given in Tbl. 2.1.

Chapter 3

Historical Overview of Proton Decay Searches

Searches for nucleon decay as a test of baryon number conservation have a history spanning more than 50 years. A wide range of experiments have been conducted over that time, using such methods as radiochemical and geochemical studies, liquid scintillator detectors, tracking iron calorimeters, and water Cherenkov detectors. All such experiments share certain characteristics which are required due to the fact that the nucleon lifetime is, at a minimum, extremely long.

Any nucleon decay search must involve a large sample of nucleons to improve the probability that a nucleon decay would actually occur within the experiment's time frame. Running the experiment for a long time is also important for the same reason. High efficiency for detection of such decays is also very important, since only a few decays might be expected in any given experiment, even under the most optimistic assumptions.

Unfortunately, running time and efficiency can only be increased to a limited extent. It is impractical, at the very least, for an experiment to take data for, say, a

millennium. Efficiency improvements similarly can only grant limited benefits once reasonable efficiency of a few tens of percent is reached. After that point, even an increase to 100% efficiency will only increase limits by a factor of a few, when orders of magnitude are desired. Because of these limitations, the biggest improvements in the sensitivity of nucleon decay experiments have come from increasing their size.

3.1 Indirect Detection

The earliest searches for nucleon decay used radiochemical and geochemical methods. These methods are based on searching for nuclei of rare isotopes produced by nucleon decay. Since they are sensitive to the absence of a nucleon, rather than detecting the decay products, these are called indirect detection methods. The great advantage of these methods is that they are sensitive to any conceivable decay channel. However, the difficulty of assembling a sufficiently large and pure sample of material to carry out such an experiment limits them to relatively short lifetimes. A good review of such experiments may be found in [29].

One of the earliest indirect detection experiments utilized the spontaneous fission of ^{232}Th [30]. Should any of the nucleons in ^{232}Th decay, the resulting nucleus will be left in an excited state. Furthermore, the excitation energy will be sufficient to produce spontaneous fission. Since the half-life of ^{232}Th under spontaneous fission was greater than 10^{21} years, it followed that the nucleon lifetime must be greater than about 2×10^{23} years.

Another approach was to examine geological samples and search for isotopes that are only rarely generated by other processes. For example, nucleon decay within ^{39}K results in ^{37}Ar. By analyzing an appropriate sample of rock and measuring the relative abundances of ^{39}K and ^{37}Ar, a limit is set on the nucleon lifetime.

Method	Lower Limit (years)
^{232}Th Spontaneous Fission	2×10^{23}
^{130}Te $\rightarrow^{129}$ Xe	1.6×10^{25}
^{39}K $\rightarrow^{37}$ Ar	2.2×10^{26}

Table 3.1: Summary of indirect detection experiments.

The most sensitive indirect detection experiment used this same potassium-to-argon reaction, but was carried out by taking a large sample of very pure potassium acetate into the Homestake gold mine. The sample was later analyzed to determine how much argon was present. This led to a limit of 2.2×10^{26} years [31].

A summary of indirect detection experiments is given in Tbl. 3.1 [29].

3.2 Scintillators

Direct detection experiments are based on attempting to detect the decay products from a nucleon. As such, they are generally not sensitive to every possible decay channel, and in general each possible channel must be analyzed separately. However, they are not limited by the difficulty of assembling a large sample of a single isotope, and then later trying to find a few nuclei of another isotope in it. Direct detection experiments have therefore been able to reach much larger sizes than any practicable indirect experiment.

The first direct detection experiment was carried out in 1953 using a tank filled with 300 liters of liquid scintillator [32]. This experiment was located only 30 m underground, so background from cosmic ray muons was a major limiting factor. This experiment was able to set a bound on the proton lifetime of 10^{22} years.

The liquid scintillator approach was improved over the years, including a 20 ton detector located 3200 m underground near Johannesburg, South Africa [33]. This

experiment was able to set a lower bound of 3×10^{30} years, though it was limited to final states containing a muon.

3.3 Iron Calorimeters

Iron calorimeters are constructed from alternating layers of ferrous plates and detectors. In these experiments, the iron layers provide the source of nucleons, while the detector layers are used to detect and track the decay products. Many different types of detector are used, including flash tubes, proportional chambers, streamer tubes, or Geiger counters. Iron calorimeters tend to have excellent tracking granularity, but their cost per ton is quite high compared to water Cherenkov detectors. The interactions of possible decay products with iron nuclei are also more complex than with oxygen and hydrogen. The properties of various iron calorimeter experiments are summarized in Tbl. 3.2.

The Kolar Gold Field, or KGF, detector was constructed in the Kolar gold mine in India [34]. It was composed of 34 layers of iron plates and proportional counters. Its total mass was 140 tons, and it was deep underground, at a depth of 2300 m. It ran from 1980 to 1992. In 1981, KGF reported three possible nucleon decay events, which would imply a nucleon lifetime on the order of 6×10^{30} years. However, this observation has been refuted by later experiments which strictly rule out lifetimes in this range.

Soudan I was the first detector in the Soudan mine, located in Minnesota, and ran from 1981 to 1990. It was constructed of 432 concrete slabs, loaded with taconite (a kind of rock with high iron content) concentrate, each with 8 proportional tubes. It had a total mass of 31.4 tons, and was located 760m underground [35]. Soudan I was able to set limits on proton decay on the order of 10^{30} years.

Detector	Mass (tons)	Depth (m)	Exposure (ton×years)	Sensitive range (years)
Soudan I	31.4	590	300	10^{30}
KGF	140	2300	126	10^{31}
NUSEX	150	1850	130	10^{31}
Frejus	900	1780	2000	10^{32}
Soudan II	963	710	4400	10^{32}

Table 3.2: Summary of iron calorimeter experiments.

The NUcleon Stability EXperiment, or NUSEX, was located 1850 m under Mont Blanc between Italy and France, and ran from 1982-1998. It was built with 134 layers of alternating iron plates and streamer tubes. It had a total mass of 150 tons [36], and set limits on the order of 10^{31} years.

The Frejus experiment, running from 1984 to 1988, was located in the Frejus highway tunnel between Modane, France and Bardonecchia, Italy, at a depth of 1780m [37]. It was constructed of 912 layers of iron plates and flash tubes, with layers of Geiger tubes for triggering. Its total mass was 900 tons, and it set limits on the order of 10^{32} years.

Soudan 2, running from 1988 until 2001, was a larger version of Soudan I [38]. Its total mass of 963 tons was composed of iron sheets and drift tube layers, without using concrete. Like Soudan I, it was located 760m underground. It was more sensitive than its predecessor, able to set limits on the order of 10^{32} years.

3.4 Water Cherenkov Detectors

Water Cherenkov detectors use Cherenkov radiation, light emitted by relativistic particles traveling through water, to track charged particles (see Ch. 4). Water Cherenkov detectors are instrumented with photomultiplier tubes (PMTs), typi-

cally around the edges of the water tank. Because water is very cheap, and it is not necessary to have instrumentation throughout the entire detector volume, water Cherenkov detectors can be constructed much more cheaply per ton than iron calorimeters. For this reason, it is practical to build much larger detectors, with a corresponding increase in sensitivity. Major historical water Cherenkov detectors include IMB and Kamiokande. The characteristics of some important water Cherenkov detectors are summarized in Tbl. 3.3.

Also interesting is the Harvard-Purdue-Wisconsin (HPW) detector, which was constructed at a depth of 525 m outside of Park City, Utah. It ran during 1983 and 1984 with a total mass of 680 tons [39]. Its construction was rather unusual for a water Cherenkov detector, with PMTs suspended inside the tank rather than along the walls, along with mirrored walls to improve light collection efficiency. This made particle tracking difficult, so HPW was unable to set strong limits on nucleon decay.

The Irvine Michigan Brookhaven (IMB) detector was located 600 m underground, in the Fairport salt mine near Cleveland [40]. It ran between 1982 and 1991, with a total mass of 8 kilotons (3.3 kiloton fiducial mass), in two phases called IMB-1 and the upgraded IMB-3. IMB was able to set limits on proton lifetime on the order of 10^{32} years. Other notable achievements were the observation of neutrinos from supernova 1987A, as well as the first suggestions of the atmospheric muon neutrino deficit, which was later confirmed by Super–Kamiokande to be evidence of neutrino oscillations.

The precursor to Super–Kamiokande, Kamiokande was constructed in the Mozumi mine near Kamioka, Japan [41]. It ran from 1983 to 1988 with a total mass of 3 kilotons (1 kiloton fiducial mass). The Kamiokande experiment ran in two phases, Kamiokande I in 1983-4 and the upgraded Kamiokande II in 1986-8. Significant physics successes of Kamiokande included observations of neutrinos from supernova

Detector	Mass (ktons)	Depth (m)	Exposure (kton×years)	Sensitive Range (years)
HPW I	0.68	525	0.2	10^{30}
Kamiokande	3.0	825	3.8	10^{32}
IMB	8.0	600	7.6	10^{32}
Super–Kamiokande	50	825	Still running	10^{34}

Table 3.3: Summary of water Cherenkov detectors.

1987A, confirmation of the solar neutrino deficit, and hints of the atmospheric neutrino zenith angle distribution distortion that Super-K later confirmed.

3.5 Recent Experiments

The Sudbury Neutrino Observatory, or SNO, has recently set limits on "invisible" nucleon decays such as $n \to 3\nu$ [42]. SNO is located near Sudbury, Ontario. It is 6800m underground, and is a water Cherenkov detector containing one kiloton of heavy water. It is sensitive to few-MeV deexcitation photons emitted when a neutron decays in ^{16}O, leaving a nucleus in an excited state, permitting it to measure these invisible decays. That limit is 2×10^{29} years.

The Kamioka Liquid scintillator Anti-Neutrino Detector, or KamLAND, uses a kiloton of liquid scintillator, and is located at the former location of the Kamiokande detector. Similarly to SNO, it is sensitive to the decay of excited nuclei left behind by the decay of a neutron via an invisible mode. KamLAND was able to set a limit on such invisible decays of 1.4×10^{30} years [43]. Earlier, the BOREXINO detector in the Gran Sasso Underground Laboratory in Italy was able to set a limit on similar decays on the order of 10^{25} years [44].

Chapter 4

The Super–Kamiokande Detector

4.1 General

4.1.1 Overview

The Super–Kamiokande detector (shown in Fig. 4.1) is located in the Mozumi mine operated by the Kamioka Mining and Smelting Company, in Gifu prefecture, Japan. It is below the peak of Mt. Ikenoyama, under 1000 m of rock granting shielding from cosmic rays equivalent to 2700 m of water. This reduces the flux of cosmic ray muons to 6×10^{-8} cm^{-2}s^{-1}sr^{-1}, resulting in a muon rate at the detector of about 2 Hz. It contains a total of 50 kilotons of ultra-pure water, making it the largest water Cherenkov detector yet built. The details of the detector have previously been published in [45].

Super-K began running in April 1996, and continued until July 2001, when it was shut down for upgrading and maintenance. This data-taking period is referred to as Super–Kamiokande I (SK-I). Unfortunately, while the tank was being refilled in November 2001 to resume operation, a chain reaction of imploding PMTs destroyed most of them, making extensive repairs necessary. After reconstruction, Super-K

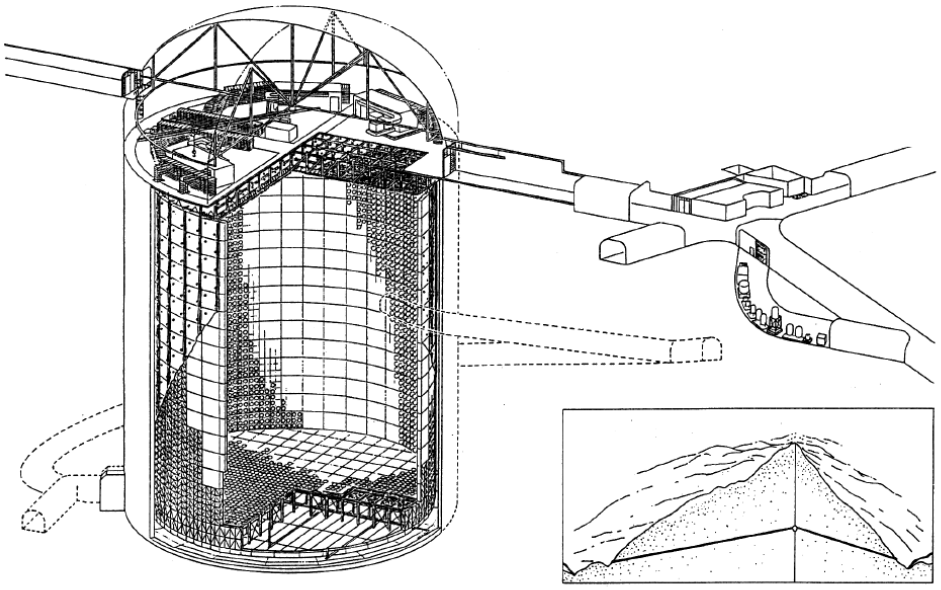

Figure 4.1: A rough schematic of Super–Kamiokande.

began running again in January 2003 and continued doing so until October 2005, when it was again shut down for upgrading and maintenance. This data-taking period is called Super–Kamiokande II (SK-II).

Accident Details

The accident in November 2001 occurred when a single PMT imploded. In itself, this would have been a minor problem. However, the original implosion created a pressure wave in the water, which caused the adjacent PMTs to also implode. These produced additional pressure waves, propagating a chain reaction that destroyed almost all of the PMTs under water at the time. A total of 6779 PMTs in the inner detector (ID), 885 PMTs in the outer detector (OD), and about 700 OD wavelength shifter plates were destroyed.

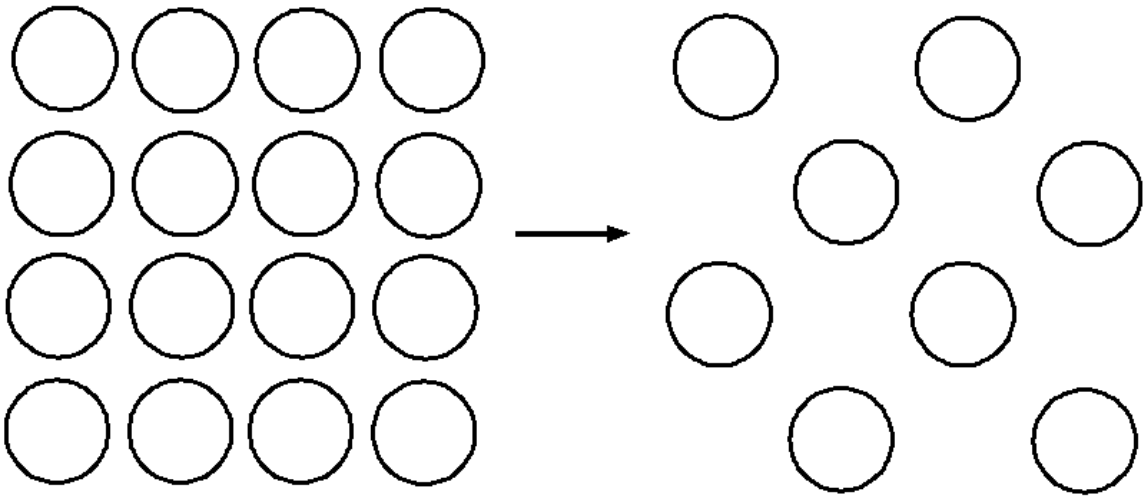

Figure 4.2: Pattern of the PMT placement in SK-I (left) and SK-II (right).

It was possible to produce sufficient replacement OD PMTs in a practical length of time, but not ID tubes. For this reason, SK-II ran with a reduced ID PMT complement. While the PMTs in SK-I were arranged in a tightly spaced grid pattern, this could not be replicated with SK-II's reduced complement. Instead, alternating PMT positions were filled and left empty, resulting in a checkerboard pattern illustrated in Fig. 4.2. Additionally, certain modifications to the PMT assemblies were made to prevent such occurrences in the future, which are discussed later.

4.1.2 Principle of Operation

Super-K detects relativistic charged particles via the emission of Cherenkov light within the water. Cherenkov light is produced when a charged particle travels faster than the speed of light in the medium, which results in a coherent shock front as illustrated in Fig. 4.3. This front gives rise to a cone of light emitted at an angle θ, referred to as the Cherenkov angle:

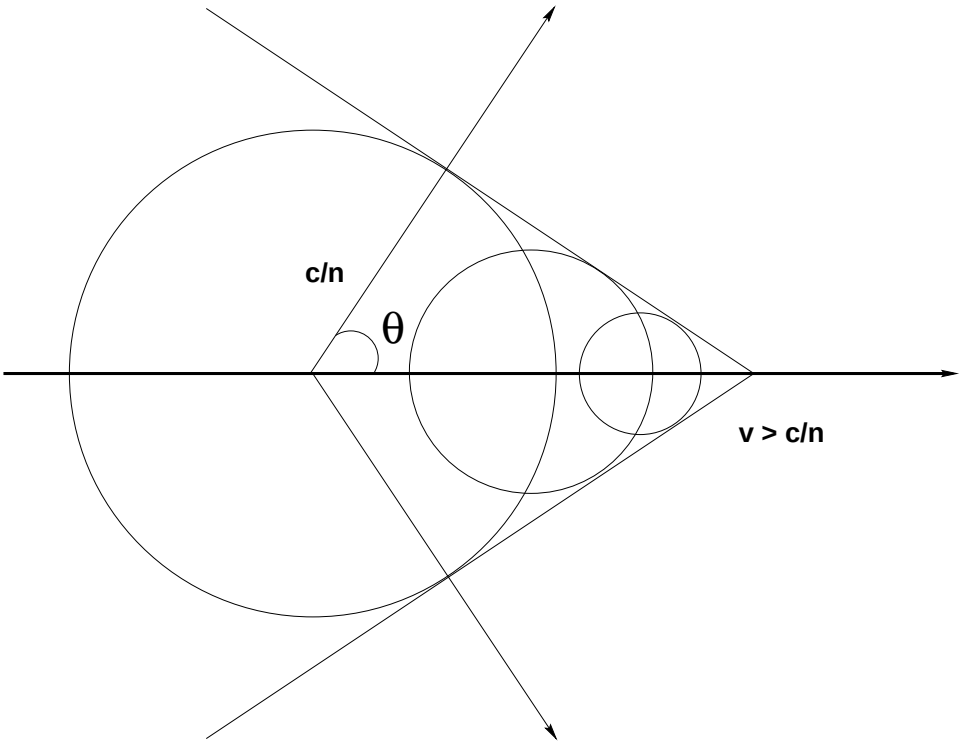

Figure 4.3: An illustration of Cherenkov radiation.

$$\cos\theta = \frac{1}{n\beta}, \tag{4.1}$$

where n is the index of refraction for the medium and β is the speed of the particle divided by c.

It is frequently useful to consider the threshold for emission of Cherenkov light in terms of the particle's momentum p rather than β:

$$p_{thresh} = \frac{m}{\sqrt{n^2 - 1}}. \tag{4.2}$$

Water has an index of refraction of about $n = 1.34$, varying slightly with wavelength. Inserting this into these equations results in a threshold of $p_{thresh} = 1.14m/c$ and a Cherenkov angle of $\theta = 42^\circ$ for $\beta = 1$.

The number of Cherenkov photons N emitted per unit path length dx per unit wavelength $d\lambda$ by a particle of charge ze is given by

$$\frac{d^2N}{dxd\lambda} = \frac{2\pi\alpha z^2}{\lambda^2}\left(1 - \frac{1}{n^2\beta^2}\right), \tag{4.3}$$

which results in about 3400 photons/cm between $\lambda = 300 - 550$nm, where the Super-K PMTs are most sensitive, for a particle with $\beta = 1$. With a detection efficiency around 10%, this leads to the detection of approximately 340 photons/cm.

The cone-shaped emission pattern of Cherenkov light is very useful in analysis. When projected onto the detector wall (and the PMTs mounted there), it appears as a ring. This makes it possible to separate the light emitted by different particles and to determine their momentum, direction of motion, and so on.

4.1.3 Structure

Super–Kamiokande is a cylindrical tank made of stainless steel, 39 m in diameter and 42 m tall, giving it a total capacity of 50 kilotons of water. Within this tank is another cylindrical structure, 34 m in diameter and 36 m tall, which separates the detector into two regions, called the inner detector (ID) and outer detector (OD). This inner structure is lined with black plastic to optically isolate the two detector regions, and also serves as the PMT support structure.

A large dome-shaped cavern is located on top of the detector. This dome contains five electronics huts and calibration equipment including a LINAC. This cavern also provides access to the interior of the tank, which is pressure-sealed during operation for optical isolation and to reduce background radioactivity.

The primary purpose of the OD is to veto cosmic ray muons, which must pass through it to reach the ID. As these muons would otherwise present a large back-

ground to proton decay, the OD's veto capability is extremely useful in searches for proton decay. It is viewed by 1885 outward-facing 8-inch PMTs. The detection efficiency of these PMTs is increased by equipping them with wavelength shifter plates and by lining the OD walls with a reflective material called Tyvek.

The OD is assisted in rejecting cosmic ray muons by four scintillator caps, which are placed over the points where bundles of cables to the PMTs enter the OD. These caps are used to detect cosmic ray muons that travel along the cable bundles to reach the ID. As muons traveling such a path will emit no Cherenkov light in the OD, this capability is quite valuable.

The ID is the primary physics detector. It contains 32 kilotons of water. During SK-I, it was viewed by 11,146 20-inch PMTs, which covered 40% of the total ID surface with their photocathodes. For SK-II, losses in the accident required running with only 5,183 PMTs, providing 20% photocathode coverage.

The earth's magnetic field is 450 mG at Super-K, which is strong enough to negatively affect the response of the PMTs. Therefore, a system of 26 Helmholtz coils surrounds the tank, reducing the field inside to about 50 mG.

4.1.4 Water Purification System

The water in Super-K is continuously recirculated through a sophisticated purification system (Fig. 4.4 [46]). The major purposes of this system are to reduce the light attenuation within the tank and to remove radioactive impurities, especially radon. Such radioactive impurities are a major background to low-energy physics analysis but are largely irrelevant to proton decay searches. Reduction of the light attenuation produces a general increase in the light collected by the detector, which improves accuracy for all physics, including proton decay.

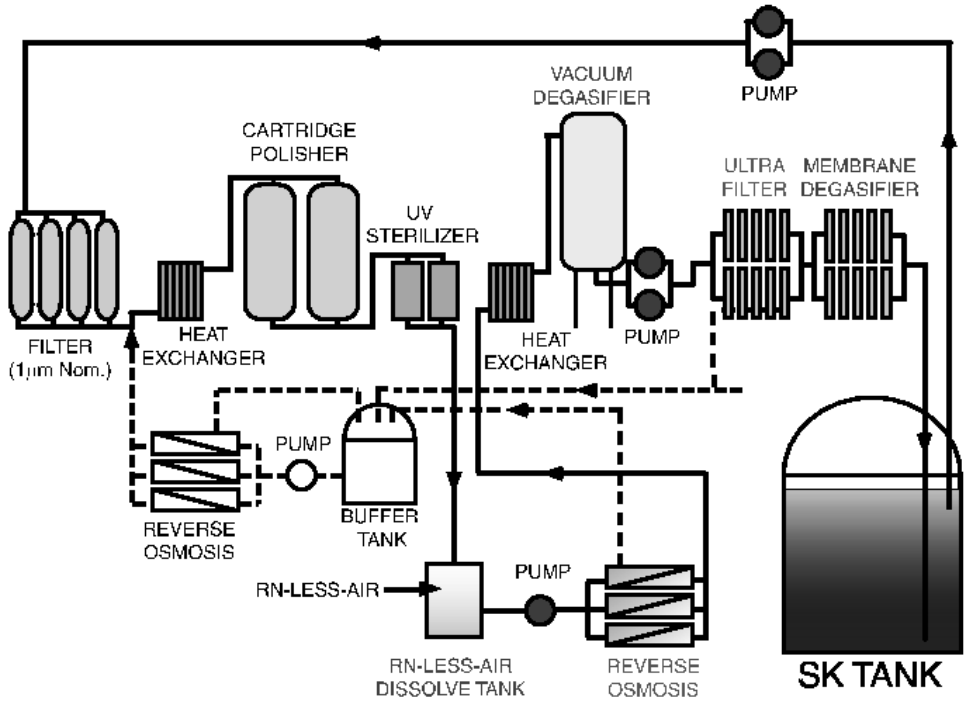

Figure 4.4: The water purification system.

The first step in the purification system is a filter which removes dust larger than 1 μm. The water is then chilled to 13° C and passed through a cartridge polisher to remove heavy ions, an ultraviolet sterilizer to kill bacteria, and a reverse osmosis and vacuum degasifier system to remove radon and other dissolved gases. Finally, it goes through a second filtering stage to remove particles down to sizes of 10 nm and a membrane degasifier to further reduce radon levels. It is then returned to the tank.

This system has a capacity of 30 tons per hour during normal operation, which allows it to recirculate the entire tank in 70 days. The resulting radon levels are around 0.4 mBqm^{-3}, and the attenuation length is roughly 100 m for 420 nm light.

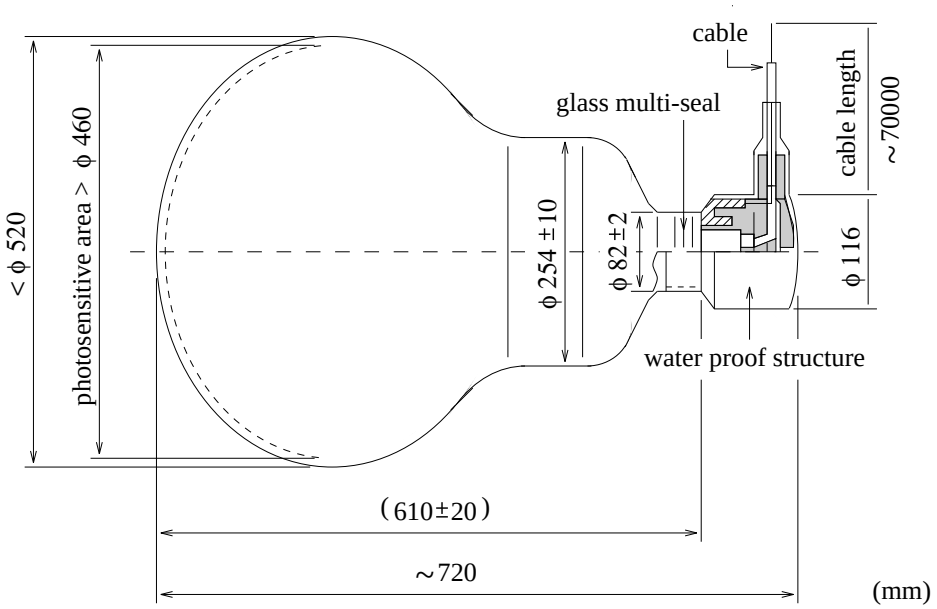

Figure 4.5: The 20-inch phototubes used in Super-K.

4.2 Inner Detector Electronics

4.2.1 Photomultiplier Tubes

The 20-inch photomultiplier tubes used in the inner detector were designed and built by the Hamamatsu corporation, and are detailed in [46]. A schematic view of one of these PMTs is shown in Fig. 4.5. Their quantum efficiency, or probability that a single photon will release a photoelectron, peaks at 21% at a wavelength of 400 nm (Fig. 4.6). Important features of these PMTs are summarized in Tbl. 4.1.

Modifications for SK-II

In order to prevent any future accidents along the lines of November 2001, SK-II encloses the PMTs in protective cases. These consist of an acrylic hemisphere over the photocathode and a Fiber-Reinforced Plastic (FRP) shell, with small holes in

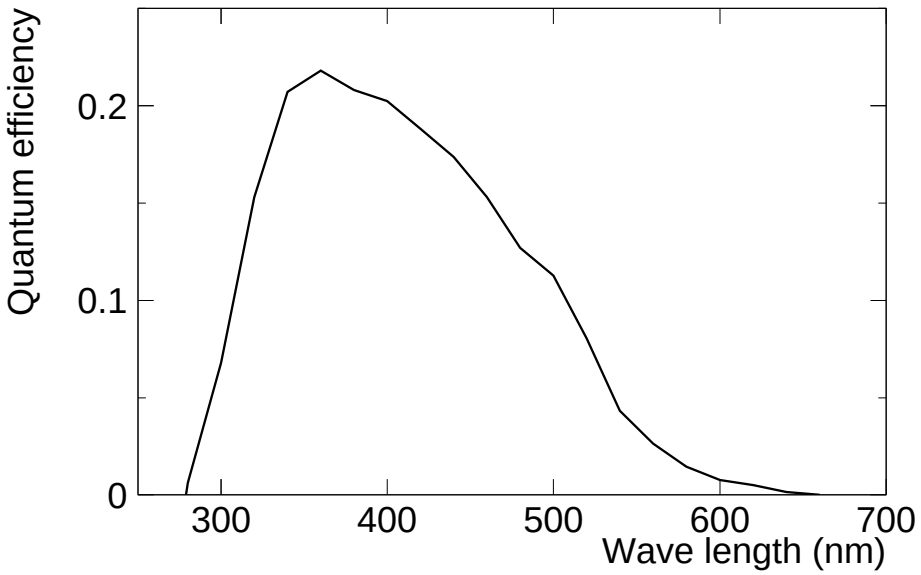

Figure 4.6: 20-inch PMT quantum efficiency as a function of wavelength.

Photocathode diameter	20 inches (50 cm)
Photocathode material	Bialkali (Sb-K-Cs)
Dynodes	11 stage Venetian blind
Peak quantum efficiency	21% at 400 nm
Gain	10^7 at 2 kV
Transit time	100 ns
Transit time spread	2.2 ns
Dark rate at 0.25 PE threshold	3 kHz

Table 4.1: Characteristics of the 20-inch PMTs.

it, around the rest of the PMT (Fig. 4.7) [47]. While this casing will not prevent a PMT from imploding, it will confine any resulting pressure wave, preventing a chain reaction from occurring.

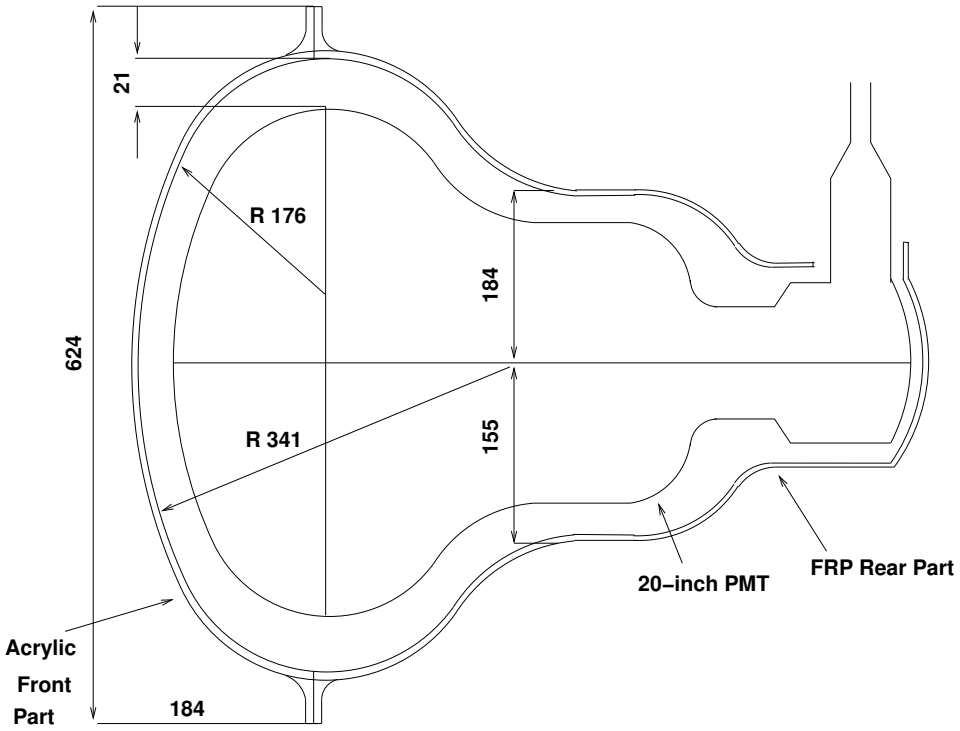

Figure 4.7: Diagram of acrylic and FRP casing for SK-II PMTs.

4.2.2 Electronics and Data Acquisition

The signals from the ID PMTs are fed into 48 Tristan KEK Online (TKO) crates, located in four electronics huts on top of the tank. Each crate contains 20 Analog Timing Modules (ATMs) which process the signal, outputting the arrival time and the total charge of the signal. Each ATM channel contains two Analog-to-Digital Coverters, enabling them to handle two closely-spaced events without losing information. This capability is important for such things as detecting muon decay electrons or handling the high event rates expected from a supernova.

In addition to the ATMs, each crate contains a GO-NoGo (GONG) module, which is responsible for triggering (discussed in Sec. 4.4), and a Super-Controller Header (SCH) module. When a trigger signal is received, the SCH is responsible

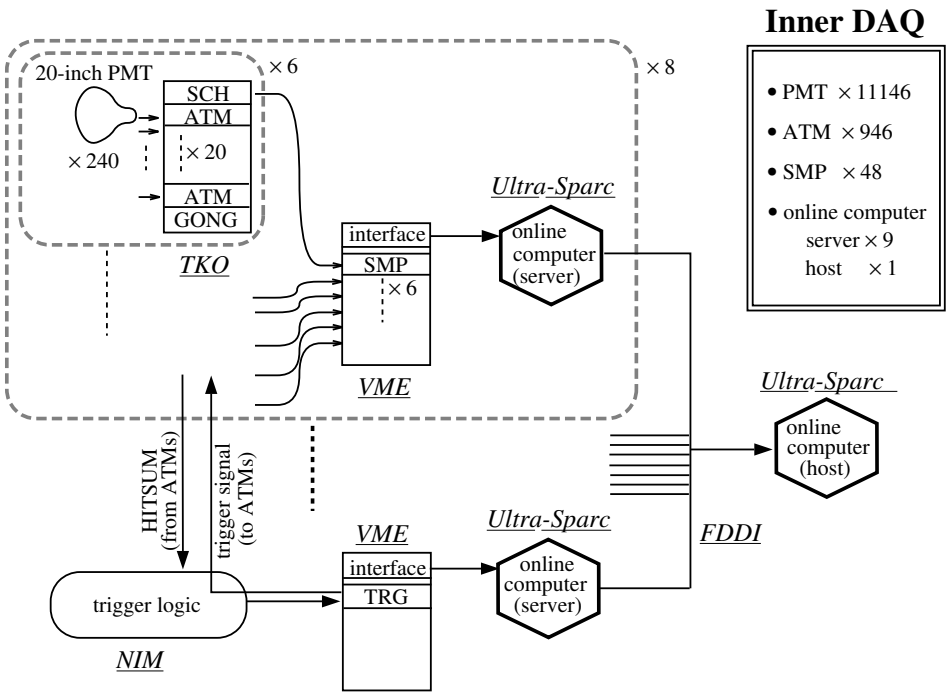

Figure 4.8: The inner detector data acquisition system.

for transferring the ATM information to a Super Memory Partner (SMP) module located in a VME crate within the hut.

The information from the SMP modules then is read out by two workstations per hut. A ninth workstation, located in the central electronics hut, then assembles all of the information into events. The events are then sent it to an offline computer for storage and analysis. A schematic of the ID data acquisition system is shown in Fig. 4.8 [46].

4.3 Outer Detector Electronics

4.3.1 Photomultiplier Tubes

The outer detector uses 8-inch PMTs, also manufactured by the Hamamatsu corporation. During SK-I, most of the PMTs used were recycled from the IMB experiment, though some were newly manufactured. However, the accident required that most of the PMTs be replaced with ones newly manufactured for SK-II.

These PMTs are optically coupled to 60 cm x 60 cm x 1.3 cm wavelength shifter plates, which are acrylic doped with bis-MSB. The bis-MSB absorbs Cherenkov photons in the near ultraviolet and re-emits them in the blue-green, where the PMTs are more sensitive. This process degrades the timing resolution of the OD PMTs from 13 ns to 15 ns. However, it also improves the light collection efficiency by 50%. Since precise timing resolution is of relatively little importance in the functioning of the OD as a veto counter, this is a very worthwhile trade-off.

4.3.2 Electronics and Data Acquisition

The signals from the OD PMTs are fed into the same four huts as the ID signals. Within each hut, 2 crates each contain 5 custom-built Charge-to-Time Converter (QTC) modules. Each QTC handles 48 PMTs, from which it receives signals through 4 "paddle cards." The QTCs serve to measure the charge and timing information from the PMTs, converting it into a form easily read by the Time-to-Digital Converters (TDCs) to which they send their output. When a trigger is received, the signals from the TDCs are output to a Sun workstation in the central hut, which assembles all the OD information and adds it to the overall event.

4.4 Triggering

The primary triggering is based on HITSUM signals. HITSUM signals are produced for both the ID and the OD, and record the number of PMTs hit within a 200 ns time window. If, within that window, the ID HITSUM exceeds 29 hits or the OD HITSUM exceeds 19 hits, a trigger signal is issued to the detector electronics and data are read out to be processed. There is also an "Intelligent Trigger" system used for very low energy events, but such events are not used in this thesis and will not be discussed here.

4.5 Calibration

4.5.1 Water Transparency

Laser Measurement

The water transparency in Super–Kamiokande is measured directly using the setup shown in Fig. 4.9 [46]. An Nd:YAG laser is used to pump a titanium-sapphire laser, the intensity of which is measured using an external PMT. The laser light is delivered via optical fiber to a diffuser ball which is suspended inside the tank. This ball is then viewed, through the water, using a CCD camera mounted above the tank. By comparing the PMT measurement of the laser intensity with the light intensity recorded by the CCD camera as a function of the diffuser ball's position in the tank, the water transparency is calculated. This is done over a range of wavelengths by tuning the laser's output, and over time to account for the variation in water transparency as it circulates through the purification system.

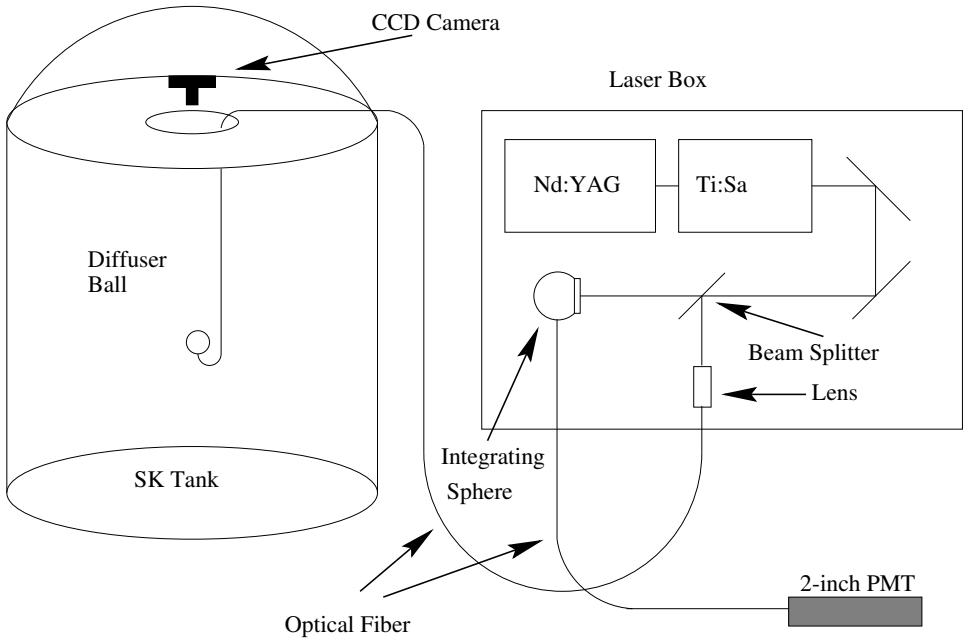

Figure 4.9: Laser system to measure water transparency.

Cosmic Ray Measurement

The water transparency is also measured using cosmic ray muons that pass completely through the detector. These muons are highly energetic, and produce an almost constant number of Cherenkov photons per meter travelled in the detector. Because of this, it is possible to correlate the charge in a PMT with its distance from the muon track on a tube-by-tube basis, providing a measurement of the water transparency. This method has the significant advantage that it can be used during normal operation.

4.5.2 Light Scattering

The water transparency depends on both absorption and scattering effects, and it is useful to separate these. To accomplish this, dye lasers and N_2 lasers of various wavelengths are fired into the tank using optical fibers. Each laser fires every 6

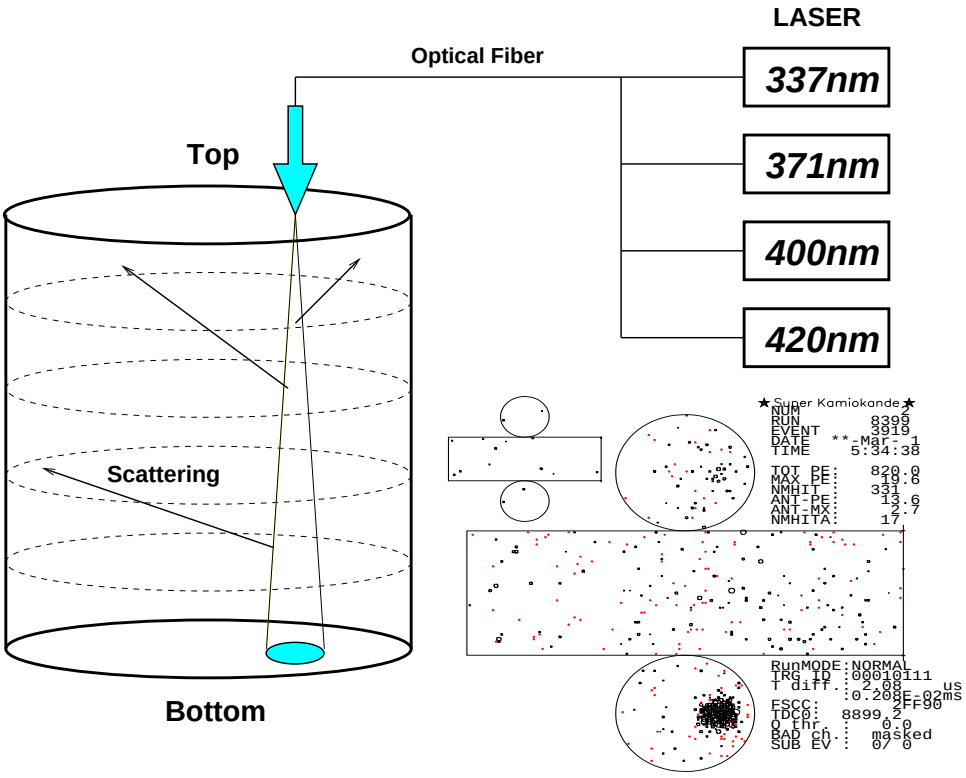

Figure 4.10: System for measuring light scattering.

seconds during normal data taking, with the firing times staggered so two lasers never fire at the same time. The setup of this system, and a typical event using it, are shown in Fig. 4.10 [46].

The event display shows the ID (the main part) and the OD (upper left) in unrolled form. The large rectangle is the barrel of the cylinder, while the circles are the end caps. PMT hits are represented by dots. The large cluster of hits on the bottom of the ID is the direct laser light. The hits on the barrel and top are due to scattering and reflection. The scattering parameters in the Monte Carlo simulation are tuned until they accurately reproduce the number of scattered hits as a function of time.

4.5.3 Relative Timing

It is important to understand the time lag between a photon hitting a PMT and that hit actually being recorded. This lag depends on the length of the signal cable and on the electronics. It is different for each PMT, and is a function of the observed charge as well. The system used to measure the relative timing of the PMTs is shown in Fig. 4.11 [46].

The N_2 laser emits light at 337 nm in a pulse of less than 3 ns. This light is converted to 384 nm by a dye laser module before being passed to a diffuser ball inside the tank via optical fiber. The intensity is controlled by a filter. The diffuser ball consists of a NiO_2 diffuser tip inside a ball of LUDOX silica gel. This produces somewhat diffuse light without significantly increasing the timing spread.

For each PMT, a scatter plot of timing vs. observed charge, called a "TQ map," is constructed using the measurements from this laser system. This TQ map is then applied to the data to determine the true timing of the PMT hits.

4.5.4 Relative Gain

The gain of each PMT is controlled by setting the value of the high voltage supplied to it. In order to set all PMTs to have almost the same gain, the system shown in Fig. 4.12 is used [46].

In this system, light from a Xe lamp is passed through an optical fiber to a scintillator ball inside the tank. The scintillator is an acrylic ball containing BBOT wavelength shifter and MgO powder diffuser. The BBOT emits 440 nm light, and the intensity of the Xe lamp is such that each PMT records a few tens of photoelectrons.

The relative gain of each PMT is then determined by correcting the observed charge for water transparency, geometrical PMT acceptance, and the uniformity of

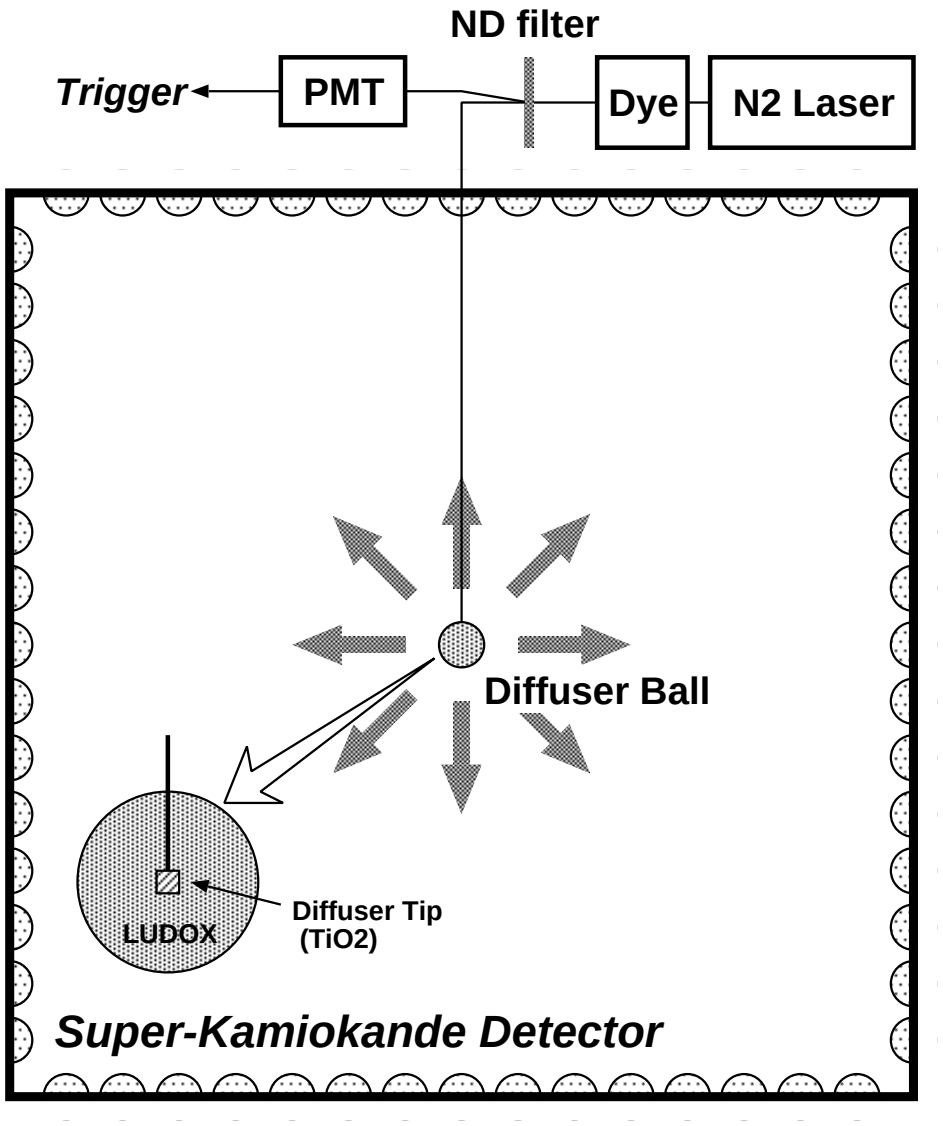

Figure 4.11: System for relative timing calibration.

the scintillator ball. Based on this information, the high voltage to each PMT is adjusted so that they all have about the same relative gain.

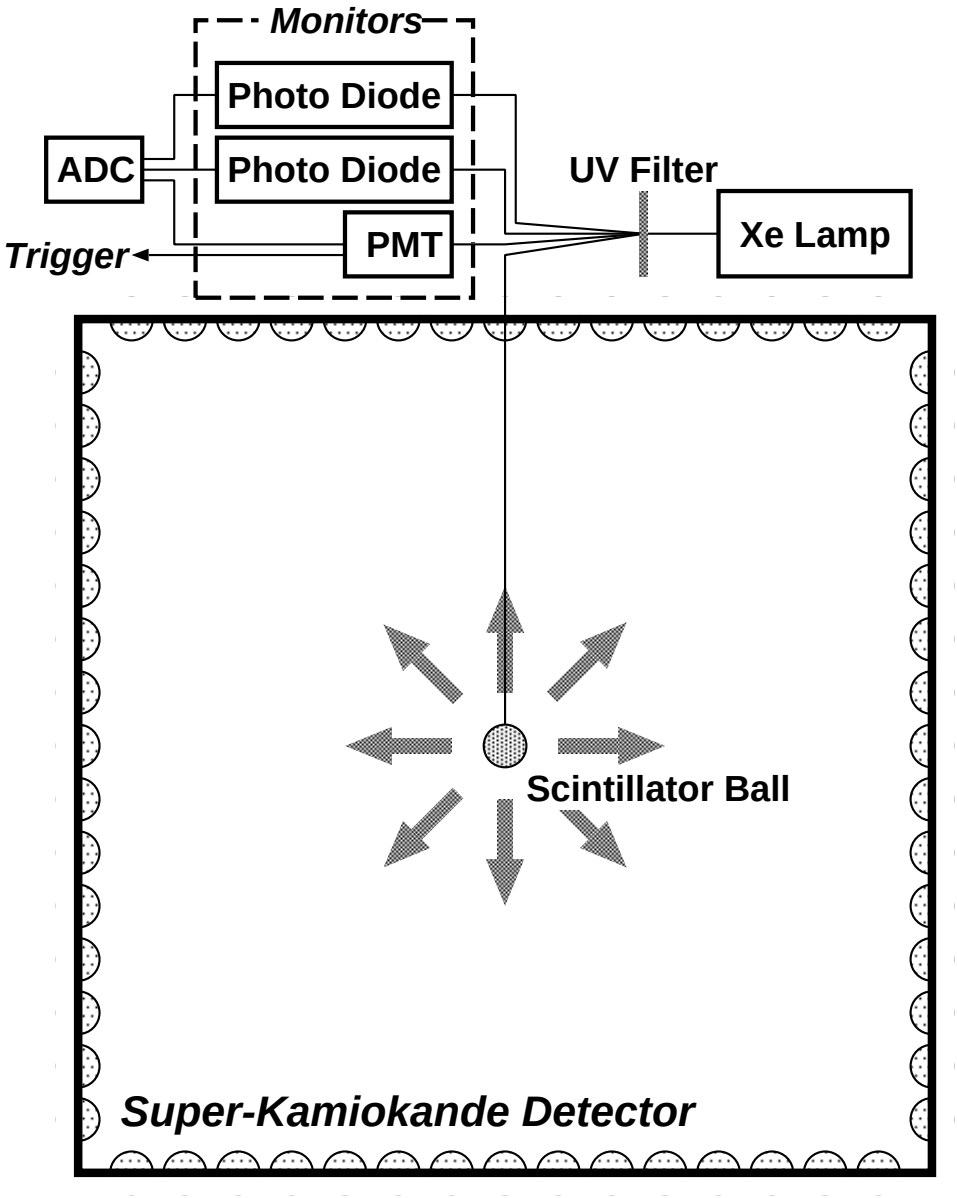

Figure 4.12: Relative gain measurement system.

4.5.5 Absolute Gain

Precise knowledge of the energy scale (that is, the relationship between particle energy and observed PMT charge) in Super-K is critical for many physics studies, including this thesis. For this reason, several different methods are used, which cover a wide range of energies. In each case, particles of known energy are introduced into the detector by some method. The data from such measurements are compared to Monte Carlo simulations to calibrate the energy scale.

LINAC

For low energies (a few MeV), an electron LINAC is used to inject electrons into the detector. The energy of these electrons is controlled by a series of magnets; it ranges from 5 to 16.3 MeV. By comparing LINAC data and tuning the Monte Carlo to agree, the accuracy of the absolute energy scale is found to be better than 1%.

^{16}N Decay

Another energy calibration is performed by introducing a ^{16}N source into the detector. This is accomplished by lowering a deuterium-tritium generator into the detector, firing it to produce ^{16}N, and removing it. When the ^{16}N decays, the decay energy is dominated by an electron with up to 4.3 MeV of energy and a 6.1 MeV photon. This method gives an energy scale which agrees with the LINAC-tuned Monte Carlo to within 0.64%.

Decay Electrons

Muons frequently stop within the detector and decay, providing an abundant source of electrons with a known energy spectrum, having typical energies of a few tens of

MeV. Comparing the data with the Monte Carlo simulation shows that they agree to within 2.0% within this energy range.

Stopping Muons

Muons that stop within the detector are themselves used as an energy calibration, in two different ways, covering two different energy ranges. At low momenta (up to about 400 MeV/c), the Cherenkov angle is a good measure of the muon momentum. Above this range, the Cherenkov angle rapidly approaches 42° and is no longer useful because it no longer strongly depends on the muon energy. The muon momentum obtained this way is then compared with a momentum calculated from the number of photoelectrons, for data and Monte Carlo. This approach indicates that the agreement between data and Monte Carlo energy scale is within 1.5% over the range of 200 to 400 MeV.

The energy of higher-momentum muons can be inferred from the distance they travel within the detector before stopping. This distance is obtained by measuring the distance between the muon's entry point into the detector and the observed decay electron position. One then compares this momentum to a momentum obtained from the number of photoelectrons, and checks data against Monte Carlo. Using this sample shows that the data and Monte Carlo agree to within 2.6% between 700 MeV and 3.5 GeV.

π^0 reconstruction

When atmospheric neutrinos interact via the neutral-current interaction inside Super-K, single π^0s are often produced. These π^0s then decay into two photons, which are detected. From the measured photon momenta, the invariant mass of the original π^0 can be reconstructed and compared between data and Monte Carlo to find the

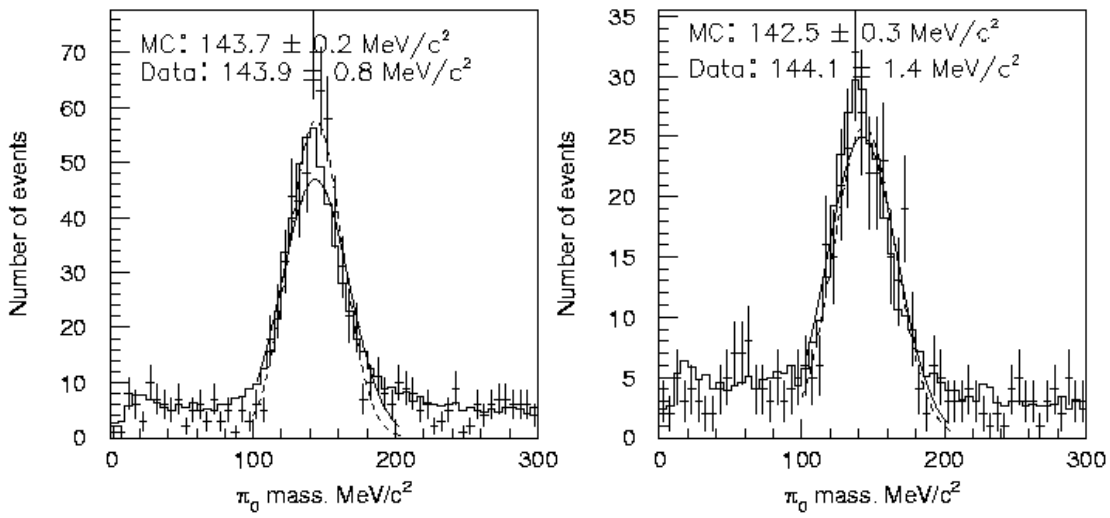

Figure 4.13: π^0 mass distributions in SK-I (left) and SK-II (right). Gaussian fits are shown for the Monte Carlo (solid) and data (dashed). The fitted peak, with fit uncertainty, is shown.

accuracy of the energy scale over the typical energy range of 150 to 600 MeV. This method finds agreement to within 1%.

This is illustrated in Fig. 4.13. To make these distributions, all events with two e-like rings are considered, and their invariant mass calculated. Then a Gaussian is fit to each distribution over the range 100 MeV/c^2 to 200 MeV/c^2. The data and MC agree well for SK-I. They also agree well for SK-II, but SK-I and SK-II differ somewhat, with SK-II masses being about 1% lower than in SK-I.

The energy scale calibrations are summarized in Fig. 4.14. All calibration methods agree to within about 2% for both SK-I and SK-II.

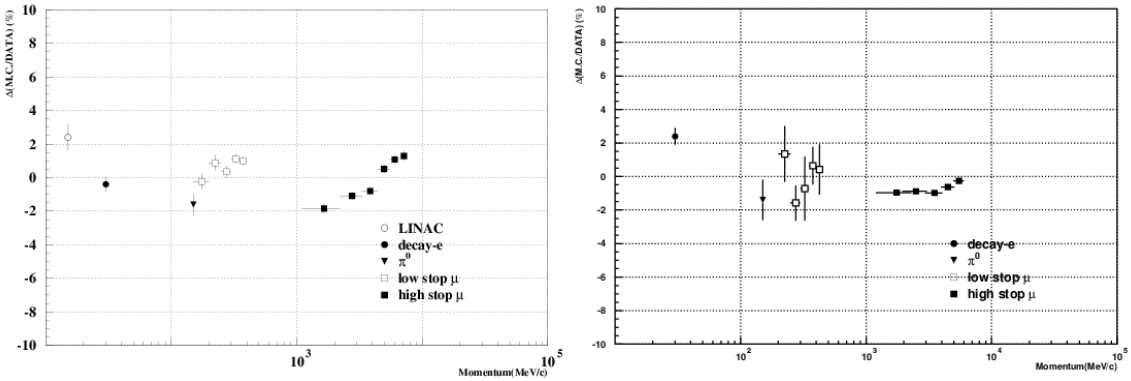

Figure 4.14: Summary of energy scale calibration methods in SK-I (left) and SK-II (right).

Chapter 5

Data Processing

In Super-K, there are several different datasets used for different purposes. These include data on upward-going muons, low-energy events, neutrino interactions that start inside the ID and have one or more particles penetrate the OD, and high-energy (hundreds of MeV to GeV) events that are completely contained within the ID. There are independent data reduction and data analysis processes for each of these, but only the fully-contained events with visible energy less than about 1 GeV are relevant to proton decay. So, only the reduction and reconstruction for this dataset will be described here.

5.1 Data Reduction

Each day, Super-K records about 10 gigabytes of data from more than a million triggers. Most of these events are backgrounds that are uninteresting to atmospheric neutrino or proton decay analysis. Prominent background categories include low-energy events, cosmic ray muons, and so-called "flasher" PMTs, among others. Several reduction steps have been developed to reduce this dataset to a reasonable size by eliminating these backgrounds [14]. Unless otherwise noted, these procedures

are the same for SK-I and SK-II.

5.1.1 First Reduction

The first reduction step is composed of cuts that can be executed very quickly, without requiring significant computer time. This is a necessary requirement due to the extremely large size of the unreduced data set. This 1st reduction makes three cuts to eliminate cosmic ray muons, their decay electrons, and low energy events:

- There must be fewer than 50 hits in the OD within an 800 ns time window. This cut removes cosmic ray muons entering through the OD.
- There must be more than 200 photoelectrons (PE) in SK-I, or 100 in SK-II, recorded in the ID within a 300 ns time window. This corresponds to about 23 MeV of visible energy, and the cut removes events that are below the 30 MeV threshold for analysis.
- The time since the previous event must be more than 100 μs, to eliminate events due to decay electrons from cosmic ray muons that stopped inside the detector.

This reduction reduces the number of events by a factor of about 400, and passes roughly 3000 events per day.

5.1.2 Second Reduction

The second reduction is designed to eliminate noise events and further reduce cosmic ray muons. It applies two cuts to accomplish this:

- No PMT may record charge greater than half of the total charge within a 300 ns window. This eliminates events containing a single large noise hit.

- The number of OD hits within a 500 ns window must be less than 50, or it must be greater than 25 with less than 10^5 PE recorded within the ID (5×10^4 in SK-II). This removes additional cosmic ray muons.

This reduction reduces the number of events by a factor of about 15, leaving approximately 200 events per day.

5.1.3 Third Reduction

After the first two reduction steps, the event sample is small enough to allow the application of more complex cuts requiring more computer time. There are a total of five cuts within the third reduction, which are used to eliminate more cosmic ray muons, low energy events, and "flasher" PMTs.

Through-going muons

A muon that enters the detector, travels completely through it, and exits the other side is called "through-going." An event is considered a possible through-going muon if at least one ID PMT recorded more than 230 PE and there are at least 1000 hit PMTs in SK-I, or 500 in SK-II, in the ID. For such events, a muon fitting algorithm is applied to determine the entry and exit points. The entry point is assumed to be at the earliest-hit PMT that has at least two other hit PMTs adjacent to it. The exit point is taken to be the center of the region of saturated PMTs. If there are then 10 or more OD hits within 8 m of the entry or exit points inside an 800 ns window, the event is considered a through-going muon and discarded.

Stopping muons

A muon that enters the detector but stops inside instead of going through is called "stopping." A possible entry point is determined in the same manner as for through-going muons. Then, a direction is found. This is done by maximizing the total charge within a cone of opening angle 44 degrees, with its apex at the entry point. The axis of that cone is taken as the muon direction. A goodness of fit is then calculated, and the direction extrapolated backward. Events with goodness of fit greater than 0.5 and 10 or more OD hits within 8 m of the back-extrapolated entry point within an 800 ns window are discarded as stopping muons.

Low energy events

To eliminate additional low energy events, a vertex fitter is applied to events with fewer than 500 total hits in the ID in SK-I, or 250 hits in SK-II. If the goodness of fit is less than 0.5, the event is rejected. Otherwise, "residual times" are calculated for each PMT by subtracting the time it would take for a photon to travel to the PMT from the fitted vertex from the recorded time of the PMT hit. If no possible 50 ns window in residual time contains more than 50 hits in SK-I, or 25 in SK-II (corresponding to energy of about 10 MeV), the event is rejected.

Flasher PMTs

Sometimes, a breakdown occurs in a PMT's dynode chain. This causes the PMT to emit a flash of light, and therefore such PMTs are called "flashers." Such events tend to have very wide timing distributions. So, the minimum number of hits within a 100 ns time window, sliding between 200 and 800 ns after the trigger, is calculated. If this minimum is 15 or more (8 or more in SK-II), or 10 or more (5 or more in

SK-II) with fewer than 800 (400 in SK-II) ID hits, the event is labeled a flasher and rejected.

Cable hole muons

It is possible for a cosmic ray muon to enter the ID without leaving any signal in the OD. This is because of four cable bundles that enter the OD to reach the PMTs. It is possible for a muon to travel along these bundles to reach the ID without ever entering the water in the OD and producing Cherenkov light. To tag such events, scintillation counters are installed above each such bundle. If one of these counters records a signal, the stopping muon fitter is applied. If the reconstructed entry point is within 4 m of the scintillator, the event is rejected.

About 45 events per day pass all of the 3rd reduction cuts.

5.1.4 Fourth Reduction

The fourth reduction step consists of a program called "flashscan." This is a more sophisticated approach to tagging and removing flasher PMTs. Essentially, flashscan uses the fact that flashers tend to produce multiple events with similar light patterns. It removes events with light patterns that are very similar to other events. The details of this program are found in [48]. Flashscan removes about 27 events per day, leaving about 18 per day.

5.1.5 Fifth Reduction

Two final cuts are made in the fifth reduction step. First, an analysis similar to the third reduction cosmic ray muon analysis is conducted, but using a more precise fitter. Also, decay electrons from invisible cosmic ray muons that are below Cherenkov

Reduction step	Events/day
Pre-reduction	1,200,000
1st reduction	3,000
2nd reduction	200
3rd reduction	45
4th reduction	18
Fifth reduction	16
Fiducial volume	8.2

Table 5.1: Event rates at each reduction step.

threshold in the inner detector are removed by calculating the maximum number of OD hits in a 200 ns time window, for any window from 100 to 8900 ns before the trigger. If this number of hits is more than a certain limit, the event is rejected. This limit is 10 in SK-I, but 16 in SK-II. About 16 events per day pass these cuts.

5.1.6 Final Sample

After all reduction steps, 16 events per day remain. Of these, 8.2 events per day are subsequently reconstructed with a vertex within the fiducial volume (more than two meters from the ID wall). The estimated loss of atmospheric neutrino or proton decay events from all reduction steps is less than 0.1%. Event rates after each reduction step are summarized in Tbl. 5.1.

The final event sample for SK-I contains 23887 events, of which 13313 are subsequently reconstructed within the fiducial volume with a total event energy less than 1.33 GeV, which is called the "sub-GeV" region. As the mass of a proton is just under 1 GeV/c^2, this is the region of interest for proton decay. For SK-II, there are 12379 events, 7139 of them sub-GeV and within the fiducial volume.

5.2 Event Reconstruction

After reduction, events are reconstructed to determine the interesting characteristics of the event, such as the event vertex, the identities and momenta of the particles involved, and so on. This takes place over several steps.

5.2.1 Vertex and Single Ring Fitting

The first step in the reconstruction finds the event vertex. For atmospheric neutrinos, this is the location of the neutrino interaction. For proton decay, it is the location of the decaying proton. This process is carried out by a program called "afit", which also locates the first Cherenkov ring.

The vertex is determined using the hit times for each PMT, assuming that all the light originated at a single point at a single time. The position that best fits this assumption is taken to be the vertex. This is implemented by finding the point which maximizes the goodness of fit:

$$G_{vertex} = \frac{1}{N_{hit}} \sum_i \exp\left[\frac{(t_i - \bar{t})^2}{2a^2\sigma_t^2}\right], \tag{5.1}$$

where N_{hit} is the total number of hit PMTs considered, $a = 1.5$ is a factor to account for light scattering, σ_t is the typical timing resolution of 2.5 ns, and $\bar{t}$ is the average of the residual times t_i:

$$t_i = t_i^0 - \frac{d_i}{v(d_i, q_i)}, \tag{5.2}$$

where t_i^0 is the recorded hit time for the PMT, d_i is the distance from the trial vertex to the PMT, and v is the velocity of light in water as a function of d_i and the recorded charge q_i to account for wavelength and acceptance effects.

After the vertex fitting is complete, the direction and opening angle θ_C of the first Cherenkov ring (generally the brightest) is found. This is based on consideration of $Q(\theta)$, which is the charge distribution as a function of θ (the angle between the track direction and the direction to the PMT) for different directions.

Different methods are used for this fitting in SK-I and SK-II. This is necessary because the SK-I method did not give satisfactory performance in SK-II, due to the reduced PMT coverage. Therefore, the fitter was modified for better performance to compensate.

In SK-I, the quantity

$$G_{dir} = \frac{\int_0^{\theta_C} Q(\theta) d\theta}{\sin\theta_C} \exp\left[-\frac{(\theta_C - \theta_0)^2}{\sigma_a^2}\right] \tag{5.3}$$

is used. Here, θ_0 is the Cherenkov angle in water for $\beta = 1$ and σ_a is the estimated rms spread of PMT hits around θ_C. By varying the test direction and opening angle θ_C to maximize G_{dir}, a direction and opening angle is found.

SK-II uses a method similar to the particle identification algorithm, which is discussed in Sec. 5.2.3. Specifically, a likelihood is calculated as in Eq. 5.9, for different directions and values of θ_C, trying both e-like and μ-like charge distribution patterns. The direction and θ_C giving the maximum likelihood are accepted. This provides superior performance, because it considers the charge distribution in more detail. However, it is more computationally intensive.

These vertex and direction fits are rough, however, because they assume all light is emitted from the vertex. They do not take into consideration the finite track length of the particle making the ring. Also, the differences in timing resolution between PMTs are not considered. A refined vertex and direction are found (using the same method for both SK-I and SK-II) by defining the quantities

$$G_I = \sum_i \frac{1}{\sigma_i^2} \exp\left(-\frac{(t_i - \bar{t})^2}{2a^2\bar{\sigma}^2}\right) \tag{5.4}$$

$$G_O = \sum_i \frac{1}{\sigma_i^2} \max\left[\exp\left(-\frac{(t_i - \bar{t})^2}{2a^2\bar{\sigma}^2}\right), 0.8\exp(-\frac{t_i - \bar{t}}{20\text{ns}})\right] \tag{5.5}$$

$$G_{total} = \frac{G_I + G_O}{\sum_i \sigma_i}, \tag{5.6}$$

where 20 ns is the average time difference between direct and scattered light, G_I accounts for direct light and considers those PMTs with $\theta < \theta_C$ or $t_i < \bar{t}$, G_O accounts for scattered light and considers tubes with $\theta > \theta_C$ and $t_i > \bar{t}$, and G_{total} is then the final goodness-of-fit.

G_{total} is used to find a final vertex and direction by first estimating the particle track length, based on the number of PE within 70° of the track direction. Then, the residual times t_i are recalculated under the assumption that the light came from a particle traveling along the track. Using these new t_i's, G_{total} is maximized as a function of vertex and direction. This procedure iterates until a final, stable fit is reached.

The vertex fitter resolution, determined by the distance between true and reconstructed vertices for Monte Carlo events, is shown in Fig. 5.1 for different subsamples, comparing SK-I and SK-II. Resolutions range from 50 cm up to 90 cm, and are overall about the same for SK-I and the improved SK-II fitters.

5.2.2 Ring Counting

After the vertex and first ring are found, a ring counting algorithm is used to determine the number and location of any additional rings. This algorithm is discussed in detail in Appendix A. Essentially, it uses a Hough transform method to locate

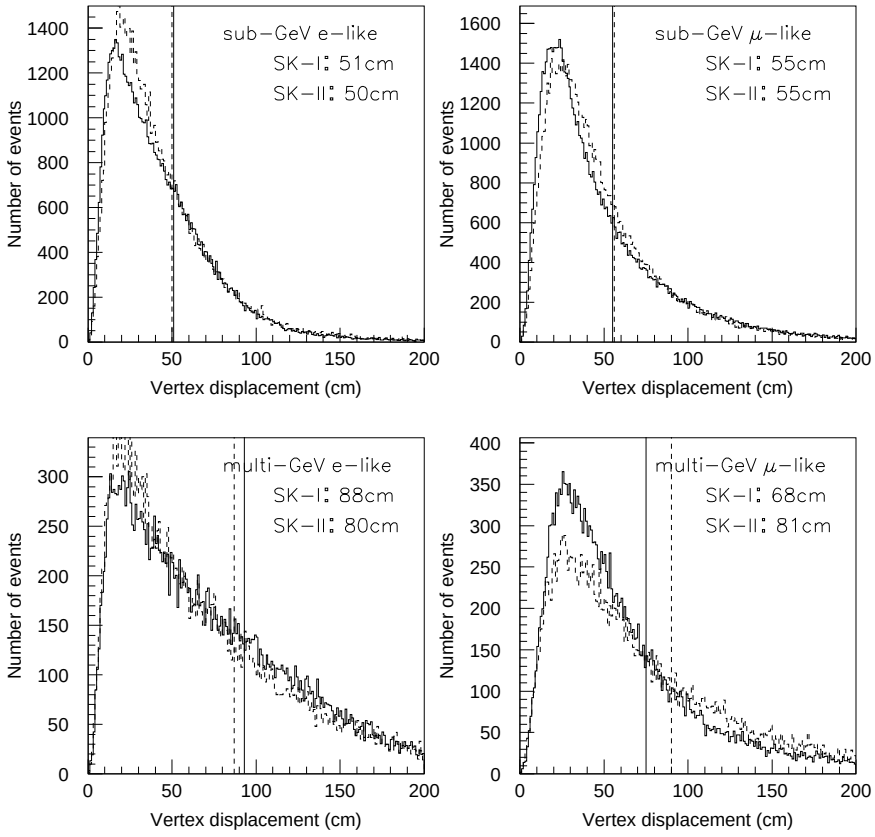

Figure 5.1: Distance between the true vertex and afit reconstructed vertex for sub-samples, SK-I (solid) and SK-II (dashed). 68% of vertices are fit within the distance indicated by the numbers and vertical lines.

candidate rings, which are then accepted or rejected by calculating a likelihood. The process iterates until no additional rings are found.

5.2.3 Particle Identification

In Super-K, rings are categorized as being caused either by electromagnetic showers or by single particles. Electromagnetic showers are produced by low-mass particles such as electrons or photons, and are therefore called "e-like." Heavier particles

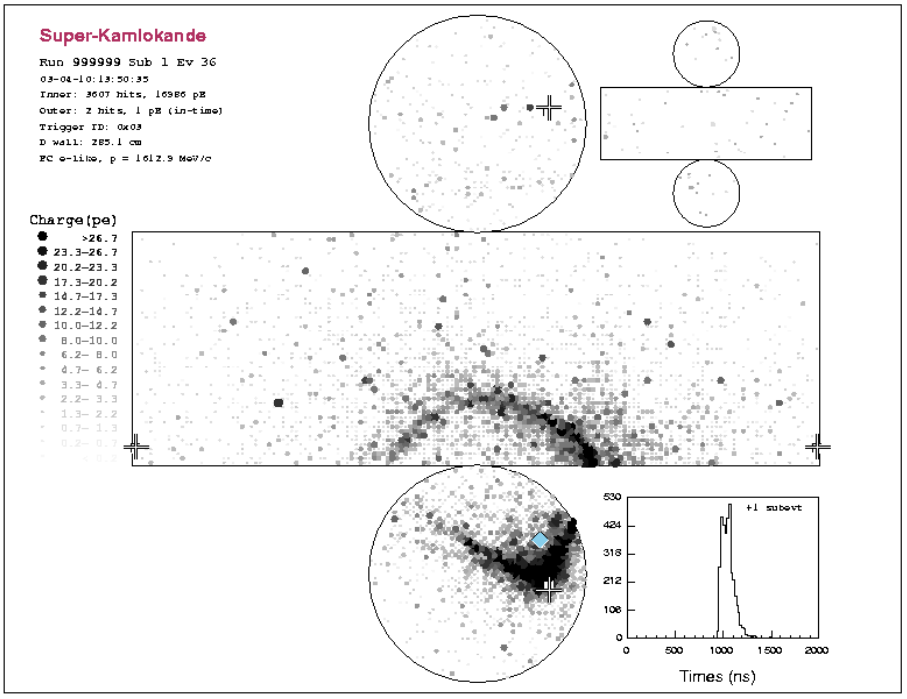

Figure 5.2: An e-like ring.

do not produce showers, so all Cherenkov light is from the original particle. Since the most common non-showering particle in Super-K is the muon, such particles are called "μ-like." These are distinguished by the charge distribution: e-like rings tend to be much less sharp than μ-like rings, as shown in Figs. 5.2 and 5.3.

In Super-K, particle ID is determined by comparing the likelihood that a given light distribution would arise from an e-like track versus a μ-like track. This requires knowledge of the expected PE distribution for the two types of rings.

For e-like rings, this distribution is given by $Q_{MC}(\theta, p_e)$, which is the expected PMT charge incident on a sphere of radius 16.9 m at polar angle θ for an electron of momentum p_e. $Q_{MC}(\theta, p_e)$ is determined by Monte Carlo simulations of electromagnetic showers in perfectly clear water initiated by electrons of momentum 100,

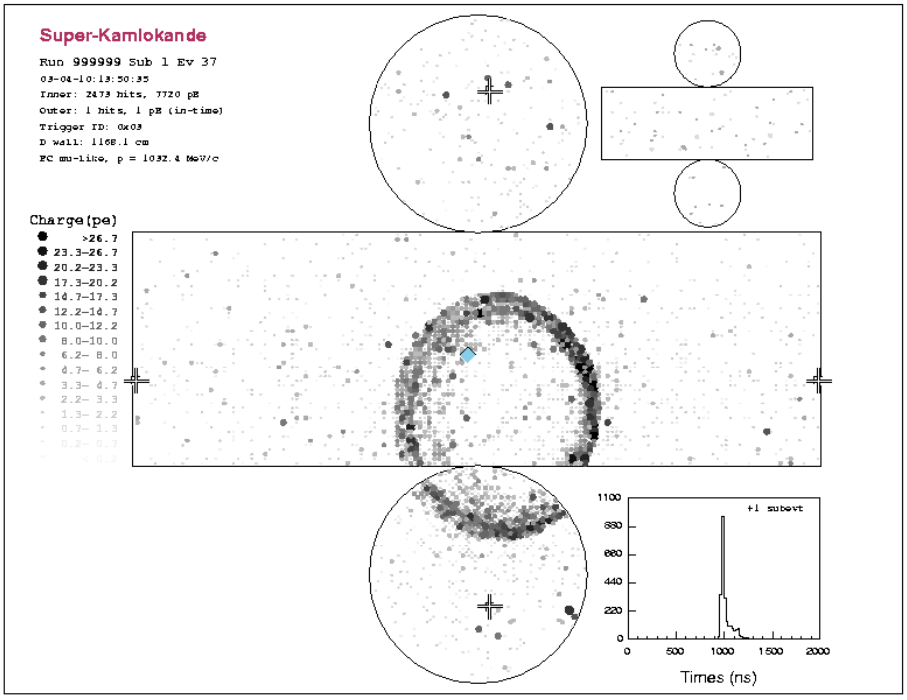

Figure 5.3: A μ-like ring.

300, and 1000 MeV/c. Values for other momenta are determined by interpolation. Making use of this template charge distribution, the expected charge in the ith PMT for e-like rings is calculated as

$$Q^{e}_{exp}(i) = Q_{MC}(\theta_i, p_e) \left(\frac{16.9\text{m}}{l_i}\right)^{1.5} \exp\left(\frac{l_i}{L}\right) f(\Theta), \tag{5.7}$$

where θ_i and l_i are the polar angle and distance from the vertex to the PMT, L is the light attenuation length in the Super-K water, and $f(\Theta)$ is the angular acceptance of the PMT. The factor $(16.9\text{m}/l_i)^{1.5}$ accounts for differences in diffusion between the simulated path length of 16.9 m and the actual path length l_i, while the exponential accounts for light attenuation in the water.

For μ-like rings, the expected charge is given by

$$Q^{\mu}_{exp}(i) = \left[\frac{\alpha_{\mu}\sin\theta_i{}^2}{l_i\left(\sin\theta_i + l_i\frac{d\theta_C}{dr}\right)} + Q^{\delta}_i\right]\exp\left(\frac{l_i}{L}\right)f(\Theta), \tag{5.8}$$

where α_{μ} is a normalization factor, Q^{δ}_i is the expected charge from δ-ray production, and $l_i\left(\sin\theta_i + l_i\frac{d\theta_C}{dr}\right)$ accounts for the fact that, as the muon loses energy and slows down, the Cherenkov angle becomes smaller. The other parameters are the same as the e-like case.

Two likelihoods are then calculated using these expected distributions, compared to the observed distribution and taking scattered light into account. This calculation uses only those PMTs with polar angle less than $1.5\theta_C$ from the fitted direction. The likelihoods are:

$$\mathcal{L}^{e,\mu} = \prod_i P[t_i, Q_{obs}(i), Q^{e,\mu}_{exp}(i)], \tag{5.9}$$

where P is the probability of observing charge Q_{obs} at residual time t given an expected charge Q_{exp}.

Light scattering is accounted for by assuming that all charge outside of the $1.5\theta_C$ cone is scattered light. A residual time histogram of this charge is made, and the peak time t_{peak} and width σ_{peak} of this distribution are found. Light arriving near t_{peak} is assumed to be direct light, while other light is assumed to be scattered.

Using this information, P is calculated:

$$\begin{aligned} P^{e,\mu} &= p[Q^{e,\mu}_{exp,direct}(i), Q_{obs}(i)], -30\text{ns} < t_i - t_{peak} < 2\sigma_{peak} + 5\text{ns} \\ &= p[Q^{e,\mu}_{exp,direct}(i), 0]p[Q^{e,\mu}_{exp,scat}(i), Q_{obs}(i)], \text{otherwise}, \end{aligned} \tag{5.10}$$

for the direct and scattered cases. Here $p(Q_{exp}, Q_{obs})$ is the probability of observing Q_{obs} charge with an expectation of Q_{exp}. For smaller charges ($Q_{obs} < 20$PE) this is determined from the measured single-PE distribution. For larger charges, it is a Gaussian:

$$p(Q_{exp}, Qobs) = \frac{1}{\sqrt{2\pi}\sigma} \exp\left[-\frac{(Q_{exp} - Q_{obs})^2}{2\sigma^2}\right], \tag{5.11}$$

where $\sigma^2 = 1.2^2 Q_{exp} + (0.1 Q_{exp})^2$ accounts for the uncertainty in PMT gain and resolution.

For single ring events, the opening angle of the Cherenkov ring is also considered. This is useful since heavy (μ-like) particles may have β significantly less than 1, while light (e-like) particles will have $\beta \approx 1$. To accomplish this, an expected Cherenkov angle $\theta^{e,\mu}_{exp}$ is calculated based on the estimated momentum of the particle. Then the probability is computed:

$$P^{e,\mu}_{\theta} = A \exp\left[-\frac{(\theta^{e,\mu}_{exp} - \theta_C)^2}{\sigma^2_{\theta}}\right], \tag{5.12}$$

where A is a normalization constant and σ_θ is the uncertainty in the fitted Cherenkov angle.

Using these probabilities, a total probability is computed:

$$\begin{aligned} P^{e,\mu}_{tot} &= (P^{e,\mu}_{\theta})^{\alpha(E)} P^{e,\mu}, \qquad \text{single} - \text{ring} \\ &= P^{e,\mu}, \qquad \text{multi} - \text{ring}, \end{aligned} \tag{5.13}$$

where α is a weighting parameter to control the relative contribution of the angle and charge probabilities, as a function of energy. This parameter was introduced for

SK-II to improve the PID. For SK-I, $\alpha = 1$ always. Finally, a particle identification parameter PID is calculated:

$$PID = \sqrt{-\log P^{e}_{tot}} - \sqrt{-\log P^{\mu}_{tot}}, \tag{5.14}$$

and an ID is assigned. For $PID < 0$, the ring is classed as e-like, while for $PID > 0$ it is called μ-like.

The distribution of the PID parameter is shown in Fig. 5.4 for quasi-elastic interactions fitted with exactly one ring. The most notable feature of these plots is that the SK-II distributions are closer to zero. This is understood by observing the form of Eq. 5.9, a product over PMTs. The product becomes a sum over PMTs after taking the logarithm. So, since SK-II has about half the number of PMTs, PID is expected to be a factor of about $\sqrt{2}$ smaller. It should also be observed that the mis-ID probability is generally reduced in SK-II. This is due to the introduction of the weighting function α.

5.2.4 Muon/Shower Fit

Since the original vertex and direction fit is based mainly on timing information, it has a bias between electron and muon events. This happens because the light from a muon with long track length comes from many points along the track. By assuming that the light is all emitted from a single point, the vertex is biased to fit somewhere in the middle of the track, rather than at the beginning. To correct for this effect, a "muon-shower" fitter called "MS-fit" is used to refine the vertex for single-ring events using PID and Cherenkov angle information.

MS-fit has three basic steps. First, the direction and vertex position are varied to maximize the goodness of fit, just as in the original fit. Second, the vertex position is

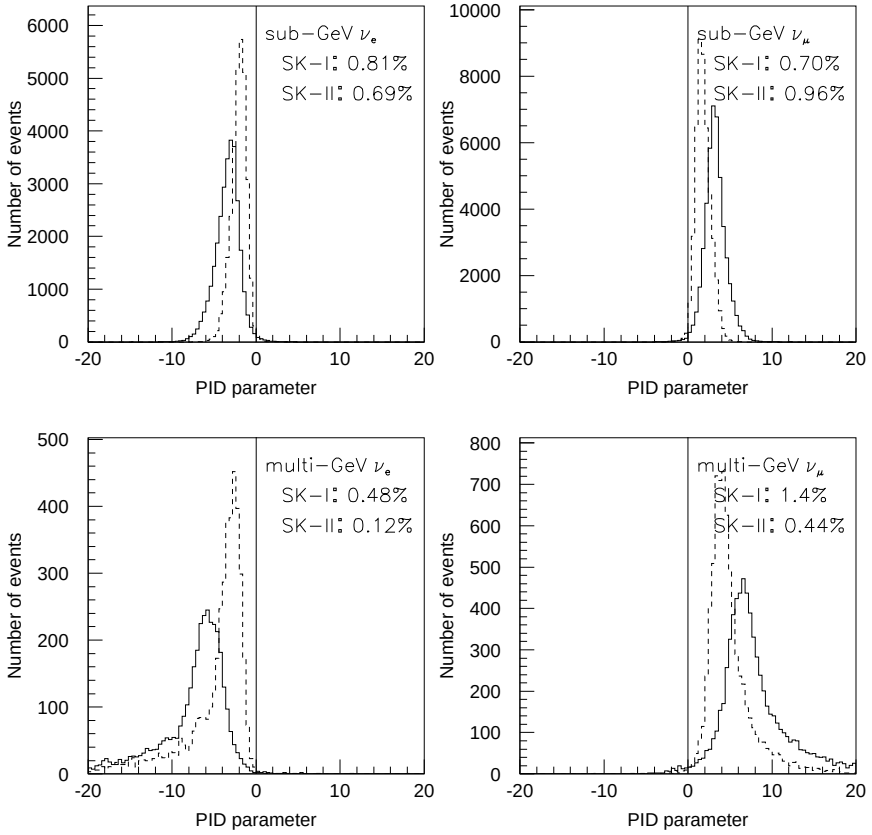

Figure 5.4: PID parameter for single-ring quasi-elastic subsamples, SK-I (solid) vs. SK-II (dashed). Vertical lines separate e-like and μ-like events. Mis-identification probabilities are indicated.

varied along the track direction to maximize P^e_{tot} or P^μ_{tot}, as appropriate. Finally, the direction is again varied to maximize $P^{e,\mu}_{tot}$. This process iterates until it converges on a final direction and vertex.

The vertex resolution of MS-fit is shown in Fig. 5.5. Multi-GeV e-like events are the most difficult, fitting with a resolution of about 50 cm. Other categories have resolutions from 24 to 32 cm. It should be observed that performance is in general not quite as good for SK-II, as expected. Also, note that the difference is most

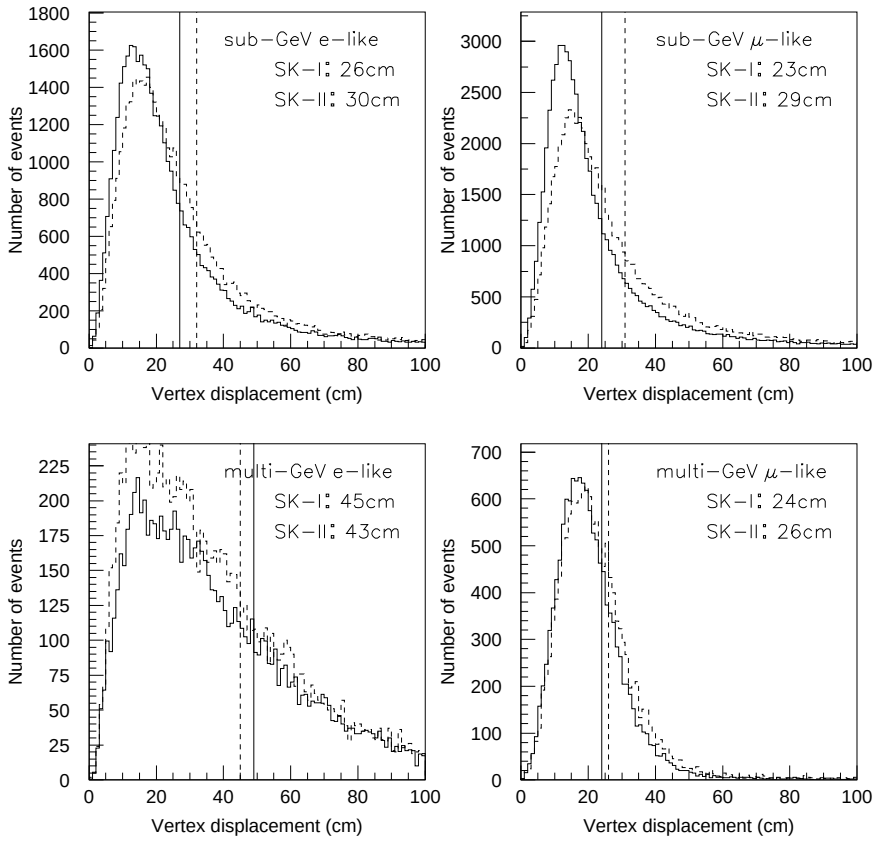

Figure 5.5: MS-fit vertex resolution for subsamples, SK-I (solid) vs. SK-II (dashed). 68% of all vertices are fit within the distance indicated by numbers and line.

pronounced for the sub-GeV samples. This makes sense, as there is enough light in the multi-GeV events that they should be less sensitive to PMT coverage. Also note the substantial improvement in resolution relative to Fig. 5.1.

5.2.5 Decay Electron Counting

Electrons from muon decay may occur within the same event as the main trigger ("in-gate"), or they may occur in a later event ("sub-event"). These two possibilities

are considered separately.

In searching for electrons within the main trigger, the first step is to find the maximum peak in the distribution of residual times t_i. This defines the starting point for the search. After this time, decays are sought by maximizing the number of hits within a 30ns sliding time window. A decay electron is tagged if it satisfies the following criteria:

- 100 ns $< t <$ 800 ns
- $N_{hit}^{30} \geq \begin{cases} 60, & \mathrm{SK-I} \\ 30, & \mathrm{SK-II} \end{cases}$
- $G_{vertex} > 0.5$,

where t is the time of the decay electron candidate, N_{hit}^{30} is the number of hits in the 30ns window (required to be 60 for SK-I, but 30 for SK-II), and G_{vertex} is the same as in the vertex fitter. The first criterion avoids looking too close to the peak or the end of the event. The latter two ensure the hits are from an electron that was reasonably fit.

Electrons within a later trigger are selected in a similar manner, but with slightly different cuts. In this case the criteria are:

- 1.2 μs $< t <$ 20 μs
- $N_{hit}^{30} \geq \begin{cases} 40, & \mathrm{SK-I} \\ 20, & \mathrm{SK-II} \end{cases}$
- $G_{vertex} > 0.5$.

Here, the first cut rejects after-events which occur too late to be from muon decay and ensures that the detection efficiency remains constant over the entire time window.

The others require 40 hits in SK-I and 20 in SK-II and a reasonable vertex fit to, again, ensure the hits are from a reasonably fit electron. Note that decay electrons between 800 ns and 1200 ns will not be found in either sample. This is because, in such a case, it can happen that some of the electron's light will be found in one trigger, and the rest in a later trigger, so that it is partially in-gate and partially sub-event. These cannot be properly reconstructed, and are lost.

Based on Monte Carlo studies, the SK-I efficiencies to detect decay electrons in sub-GeV events is estimated to be 72.0%. Studies with stopping cosmic-ray muons confirm that this is accurate to within 1.5%. The efficiency in SK-II is somewhat lower, at 70.5%.

5.2.6 Momentum Fitting

The momentum of a particle is determined by considering its PID and the total charge due to that particle. First, the charge corresponding to the particle is determined by adding up the charge from all PMTs within 70° of the track direction and with residual time within -50 ns and +250 ns of the average residual time. A conversion to momentum is then applied, based on Monte Carlo studies and the calibration sources discussed in Sec. 4.5.

This algorithm has resolution as shown in Fig. 5.6. SK-II performance is clearly inferior to SK-I by one to two percent. Events are also, on average, fit about 1% higher in SK-II than in SK-I.

5.2.7 Comparison of SK-I and SK-II performance

The performance of the event reconstruction for SK-I and SK-II sub-GeV events (the region of interest for proton decay) is summarized in Tbl. 5.2. The efficiency for

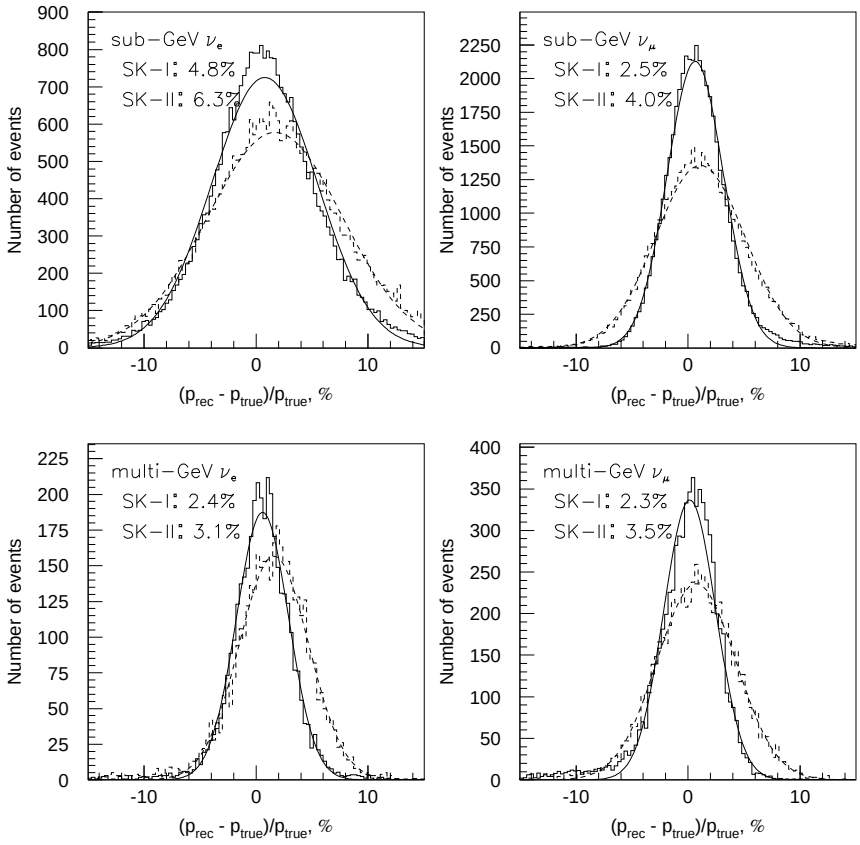

Figure 5.6: Momentum resolution for subsamples, SK-I (solid) and SK-II (dashed). Quasi-elastic interactions fit with one ring and the correct PID are considered. The width of a Gaussian fit is shown.

correctly fitting single-ring events as single-ring is described in Appendix A. Overall, the performance of SK-II is somewhat worse, as expected. The greatest differences are seen in the resolution for MS-fit and momentum fitting.

	SK-I e-like	SK-II e-like	SK-I μ-like	SK-II μ-like
Afit resolution (cm)	51	50	55	55
Single-ring efficiency	93.4%	92.4%	96.0%	95.9%
Mis-PID probability	0.81%	0.69%	0.70%	0.96%
MS-fit resolution (cm)	26	30	23	29
Decay electron efficiency	72.0%	70.5%	N/A	N/A
Momentum resolution	4.8%	6.3%	2.5%	4.0%

Table 5.2: Performance of the reconstruction for SK-I and SK-II sub-GeV events.

Chapter 6

Monte Carlo

6.1 Proton Decay Monte Carlo

When searching for proton decay, it is critical to know the signature which will identify such events. This is determined by Monte Carlo simulations of proton decay. By examining such events, and comparing them to simulations of the background from atmospheric neutrinos, one devises a set of criteria to select proton decay events. Once such criteria are established, the proton decay Monte Carlo is again useful for estimating their efficiency, and the atmospheric neutrino Monte Carlo for estimating the background.

6.1.1 Initial Particle Kinematics

There are three distinct sorts of protons in water. First, there are the effectively free protons (two per water molecule) as hydrogen atoms. An additional eight protons reside within the ^{16}O nucleus, along with eight neutrons. These sets of eight protons include two in an s-wave state and six in a p-wave state. The free protons and the ^{16}O protons have decidedly different kinematics, and the s and p protons also differ.

For this dissertation, it is assumed that s, p, and free protons are all equally likely to decay.

The free protons are the simplest case. They are effectively at rest with respect to the detector, and have energy equal to the proton mass times c^2. The bound protons have more complex initial kinematics. Due to the Pauli exclusion principle, they have a positive momentum called "Fermi momentum." The distribution of this momentum used for the Monte Carlo is based on fits to measurements of electron-^{12}C scattering [49], and is shown in Fig. 6.1. Also, due to the nuclear binding energy, the mass distribution of the ^{16}O protons is not the free proton mass, but instead is distributed as shown in Fig. 6.2. For decays of bound protons, values are randomly drawn from these distributions.

With a proton mass m_{nuc} determined, the kinematics of the decay are calculated in the rest frame of the proton. For two-body decays such as those studied in this dissertation, these are easily determined. The momenta of the two decay products with masses m_1 and m_2 are equal and opposite, with magnitude p_{out} given by:

$$p_{out} = \frac{1}{2m_{nuc}}[m_{nuc}^2 - (m_1^2 + m_2^2)]c. \tag{6.1}$$

The direction of p_{out} and the proton Fermi momentum are determined randomly and isotropically, and the final momenta in the detector rest frame are determined by applying a Lorentz boost by the proton Fermi momentum.

For decays of bound protons, the initial position within the nucleus is important for determining subsequent nuclear interactions. This is drawn randomly from the Woods-Saxon density distribution:

$$\rho(r) = \frac{\rho(0)}{1 + \exp\left(\frac{r-a}{b}\right)}, \tag{6.2}$$

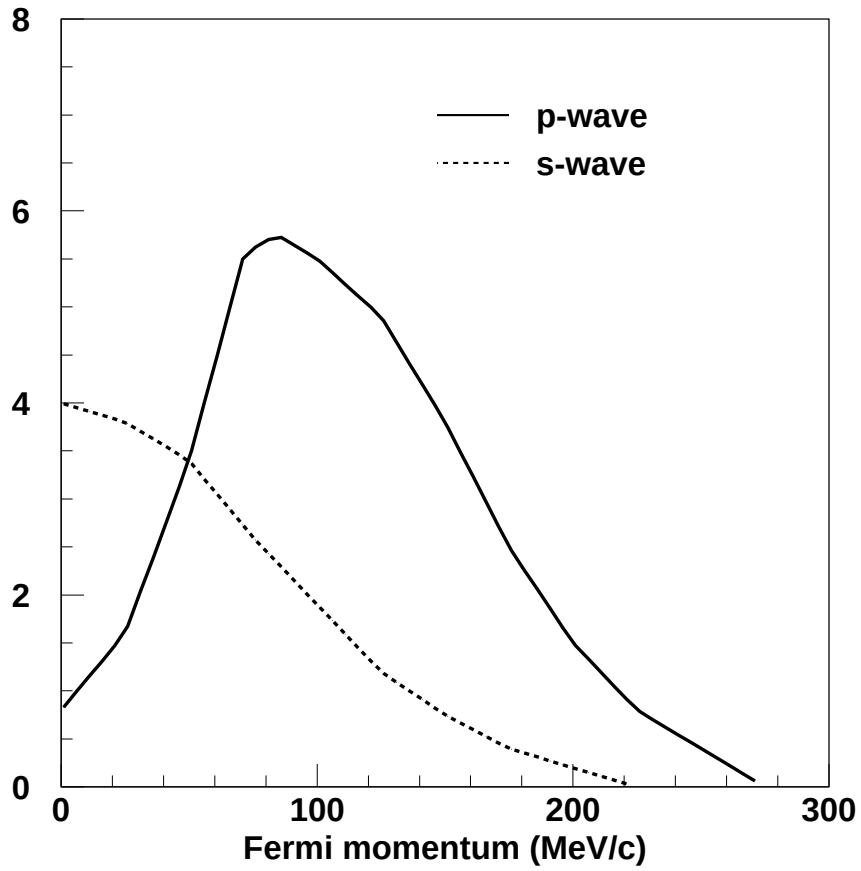

Figure 6.1: Fermi momentum distribution for s and p states in ^{16}O.

where $a = 1.07A^{1/3} = 2.69$ fm for ^{16}O, $2b = 0.82$ fm is the thickness of the nuclear surface, and r is the distance from the center of the nucleus.

Decays of electrons in the $p_{3/2}$ and $s_{1/2}$ shells of ^{16}O leave the resulting ^{15}N nucleus in an excited state. This nucleus then immediately deexcites, sometimes by emitting a photon. The analysis used for this simulation was performed by Ejiri [50], and the modes resulting in a photon are summarized in Tbl. 6.1.

The location of the decaying proton is determined randomly, with a uniform distribution extending to within one meter of the detector wall. After the initial-

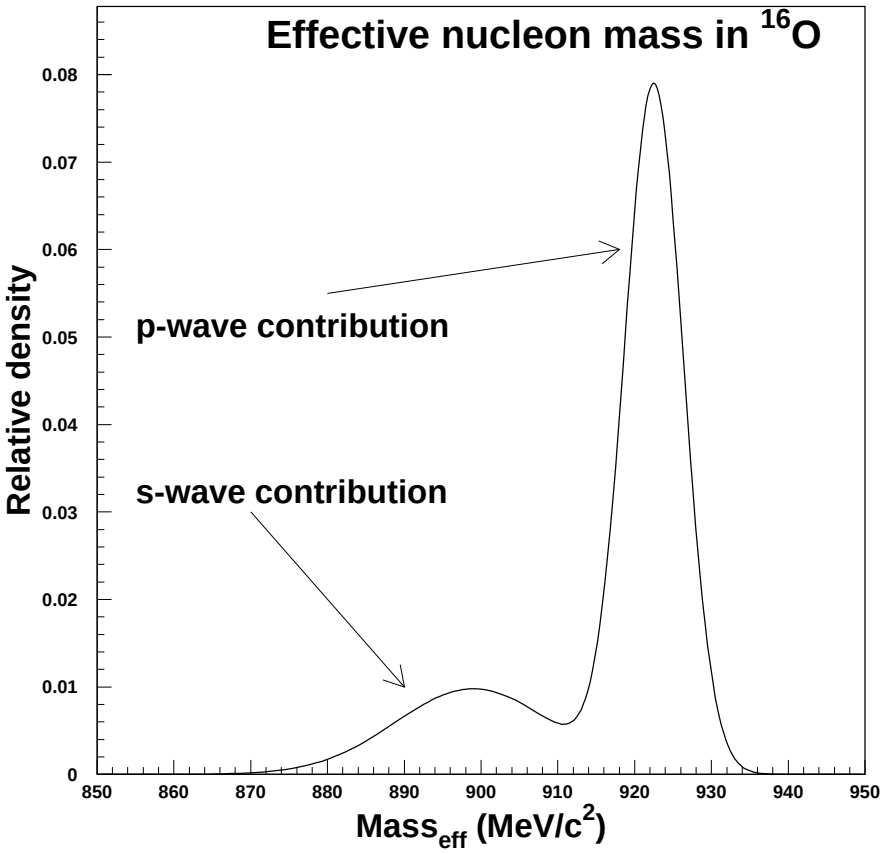

Figure 6.2: Effective proton mass distribution in ^{16}O.

Hole	Deexitation products	E_γ (MeV)	Probability
$p_{3/2}$	^{15}N, γ	6.32	41%
$p_{3/2}$	^{15}N, γ	9.93	3%
$s_{1/2}$	^{14}N, n, γ	7.03	2%
$s_{1/2}$	^{14}C, p, γ	7.01	2%

Table 6.1: Deexcitations of ^{15}N including a photon.

state particles are generated in this manner, the nuclear interactions in ^{16}O and detector simulations proceed as described in Secs. 6.3 and 6.4.

6.2 Atmospheric Neutrino Monte Carlo

The interactions of atmospheric neutrinos within the detector comprise the only significant background to proton decay searches with Super-K, thanks to the veto capability of the outer detector. For this reason, careful simulation of such events is important in understanding the background. This serves to guide the selection of cuts that will eliminate as much of that background as possible. It is also important for estimating the remaining background after applying such cuts.

Atmospheric neutrinos are produced when cosmic rays interact with air molecules in the upper atmosphere. Such interactions produce mesons, most notably pions and kaons. The decay chains of these mesons then produce neutrinos, which pass almost unhindered through the rock surrounding Super–Kamiokande. Some small fraction of these neutrinos will then interact with water molecules within the detector, producing an event with no OD signature which must be distinguished from a proton decay event.

6.2.1 Flux

The flux of atmospheric neutrinos at Super–Kamiokande can be calculated using any of several models. The neutrino oscillation analysis uses the calculation by Honda [51], with the calculations by Barr [52] and Battistoni [53] as cross-checks. The fluxes resulting from these calculations agree to within about 10% up to neutrino energies of 10 GeV, as described in [14]. Therefore, it is sufficient to use the Honda calculation for this analysis.

Honda's calculation starts with primary cosmic rays based on measured fluxes, and includes solar modulation and geomagnetic field effects. Interactions of cosmic ray particles with air nuclei, propagation of secondary particles, and decay of secondary particles are all simulated to produce a neutrino flux specific to the location of Super–Kamiokande. Based on measurements of cosmic ray flux over time [54, 55], the atmospheric neutrino Monte Carlo for SK-I is calculated for 3 years of solar minimum, 1 year of changing activity, and 1 year of solar maximum. SK-II Monte Carlo assumes solar minimum only.

6.2.2 Neutrino Cross-sections

For this dissertation, two different neutrino interaction models are considered. This provides a valuable cross-check to the estimates of atmospheric neutrino-induced background. Here, the NEUT model [56] will be described. This model is used for the primary background estimate. The second model, NUANCE, is described elsewhere [57]. NEUT and NUANCE use generally the same model for quasi-elastic scattering and single meson production, though NUANCE uses different parameters for the latter, and also considers more possible resonances. This results in roughly 10-20% less pion production in NUANCE compared to NEUT. The model of deep inelastic scattering is quite different, but such interactions are of little relevance to proton decay.

In the Super-K NEUT Monte Carlo, five kinds of interactions are modeled:

1. Quasi-elastic scattering

2. Single π production

3. Coherent π production

4. Deep inelastic scattering

5. η, K production.

For each of these interactions, Fermi momentum effects for ^{16}O nucleons are taken into account by giving the target nucleon an initial momentum drawn from Fig. 6.1, as well as by Pauli blocking. Pauli blocking is accounted for by requiring that the recoil nucleon have a momentum greater than the Fermi surface momentum p_F:

$$p_F(r) = \hbar \left(\frac{3\pi^2}{2} \rho(r) \right), \tag{6.3}$$

with $\rho(r)$ as calculated by Eq. 6.2.

Quasi-elastic scattering

Quasi-elastic (QE) interactions, both charged-current and neutral-current, are calculated using standard $V-A$ theory, specifically the calculation by Llewellyn-Smith [58].

These events typically produce exactly one ring in Super-K, from the outgoing charged lepton in the case of charged-current interactions or from the recoil nucleon for neutral-current interactions.

Single meson production

Interactions producing single pions are important for neutrino energies above about 1 GeV. Cross-sections for this reaction are provided by the model by Rein and Sehgal [59]. This model considers the formation of resonances which decay via pion emission. Fourteen different resonances are simulated, with both charged-current and neutral-current scenarios.

Below 1.4 GeV, the $\Delta(1232)$ resonance is dominant. The angular distribution

of pions from this resonance is given by the Rein and Sehgal model. For all other resonances, the angular distribution is assumed to be isotropic.

While much less common than pion production, K mesons produced by neutrino interactions are an important background to proton decay modes containing such a meson, such as $p \to \bar{\nu} K^+$. So, the production of η and K mesons is included based on another model by Rein and Sehgal [59].

Coherent π production

Coherent pion production occurs when, instead of interacting with a single nucleon, a neutrino scatters off an ^{16}O nucleus as a unit. Such interactions are clean, in the sense that the resulting pion begins outside of the nucleus and is therefore not subject to nuclear interaction effects. Coherent interactions can only produce single pions, and are handled by another model by Rein and Sehgal [60, 61].

Deep inelastic scattering

Deep inelastic scattering is handled by two different models for different energy ranges. If the invariant mass W of the resulting hadrons is between 1.3 and 2.0 GeV/c^2, a custom program is used to generate the final hadrons [62]. Above 2.0 GeV/c^2, PYTHIA/JETSET is used [63]. In these calculations, the GRV94 parton distribution function is used [64].

The mean number of pions produced in these interactions, $\bar{n}_\pi$, was studied at Fermilab [65], and is given by:

$$\bar{n}_\pi = 0.09 + 1.83 \ln W^2. \tag{6.4}$$

The BEBC experiment determined the forward-backward asymmetry of the pion

production, which is given by [66]

$$\frac{\bar{n}_\pi^f}{\bar{n}_\pi^b} = \frac{0.35 + 0.41 \ln W^2}{0.50 + 0.09 \ln W^2}. \tag{6.5}$$

The neutral-current cross-sections are calculated from the charged-current cross-sections using the relations outlined in [67, 68].

6.2.3 Normalization

Previously, a simple rescaling of the atmospheric neutrino background was used to account for neutrino oscillations and flux uncertainties. In this rescaling, all neutral-current events, as well as charged-current ν_e events, were given a weight of 1.07. Charged-current ν_μ events were given a weight of 0.67. These values were chosen so as to match the number of single-ring e-like and μ-like events in the Monte Carlo and the data. However, for this work, a more detailed and precise normalization scheme is used.

The normalization of the atmospheric neutrino Monte Carlo used for this analysis is based on the results of the neutrino oscillation analysis [14]. In that analysis, 39 systematic uncertainties such as the absolute neutrino flux normalization and the ν_μ/ν_e ratio are considered.

As part of that analysis, the 39 uncertainties are fitted along with the oscillation parameters. A normalization factor is also calculated for each bin used in the oscillation analysis. This factor reflects how the number of events in that bin is changed by the fitted values of the uncertainties. For example, the best-fit value for the normalization of the neutrino flux is 11.9% higher than the assumption used to generate the Monte Carlo. Thus the normalization factor would be (neglecting the other uncertainties for this example) 1.119 for every bin, accounting for the fact that

the neutrino flux seems to be higher than expected.

For this analysis, these normalization factors are applied on an event-by-event basis. Each event receives a normalization equal to the product of the normalization factors for most of the 39 systematic uncertainties. For ν_μ charged-current interactions, this is multiplied by the oscillation survival probability for that neutrino as calculated according to the best-fit oscillation parameters. In this way, the normalization is set to be that suggested by the oscillation analysis, and takes into account the oscillation parameters and most of the 39 systematic uncertainties.

Some of the uncertainties are either irrelevant to this analysis (numbers 14, 25, 27, 28, 33, and 38 from [14]), cannot be expressed as a normalization factor (11, 37, 39), or are sufficently minor, yet difficult to implement, that their inclusion is not worthwhile (10, 12). These are ignored here.

6.3 Nuclear Interactions

Mesons produced inside an ^{16}O nucleus, whether by proton decay or neutrino interactions, may interact before they escape from the nucleus. The simulation of these interactions is critical to nucleon decay studies, since they may absorb or change the decay products, or even just scatter them (thus altering the kinematics). All of these possibilities have significant effects on the detection efficiency.

The starting point for such a meson is determined by the Woods-Saxon distribution (Eq. 6.2). Inelastic scattering, charge exchange, and absorption are all simulated using a cascade model. First, the mean free path for each interaction is calculated using a model that depends on the meson position and momentum [69, 70, 71]. If inelastic scattering or charge exchange takes place, the resulting pion momentum is determined using the results of a phase shift analysis from $\pi - N$ scattering exper-

iments [72]. In all interactions, Pauli blocking is considered in the same manner as for neutrino interactions.

6.4 Detector Simulation

The simulation of particles within the detector is carried out using the GEANT3 Monte Carlo program developed at CERN [73]. This program handles physics processes, detector geometry and response, and run and event control. For simulation of hadronic interactions, two different programs are used. For interactions above 500 MeV, the CALOR program, also developed at CERN, is used [74]. Below 500 MeV, a custom program originally developed for the Kamiokande experiment is used [62].

The number of Cherenkov photons generated at each wavelength is simulated as a Poisson distribution with mean given by Eq. 4.3. They are emitted at the angle given in Eq. 4.1. Once they are emitted, Rayleigh scattering, Mie scattering, and absorption are simulated with contributions determined as described in Sec. 4.5.1.

Once photons strike the surface of a PMT, the response is modeled using the quantum efficiency curve (Fig. 4.6) and the single photoelectron distribution.

Several modifications to the detector simulation for SK-II were necessary to account for the differences from SK-I. Most notably, the removal of half the PMTs, and the precise positions of the remaining PMTs, was added to the simulation. Also, the acrylic and fiberglass covers, added to prevent a future chain reaction of implosions, were added to the simulation to account for absorption within the covers, as well as reflections at the boundaries with the water. The opaque "black sheet" which optically isolates the ID and OD was also moved slightly. It was also necessary to retune many parameters of the simulation to account for the new PMTs and other changes (new Tyvek, for example) made during the reconstruction of SK-II.

Chapter 7

Searches for Proton Decay

All searches for proton decay presented in this dissertation use the same basic strategy. A sample of decay events for the mode being studied is generated using the methods described in Ch. 6. These events are then compared to the standard Super–Kamiokande atmospheric neutrino Monte Carlo. Based on this comparison, cuts are developed to separate the signal from the atmospheric neutrino-induced background.

These cuts are applied to the proton decay Monte Carlo to estimate the detection efficiency, to the atmospheric neutrino Monte Carlo to estimate the expected background, and finally to the real Super-K data. The number of data events passing the cuts is then compared to the expected background and limits are set using the methods described in Appendix C.

This chapter describes searches for proton decays into four modes using data from the complete SK-I and SK-II running periods, constituting a total exposure of 2293 days (141.3 kiloton-years). Of this total, SK-I contributes 91.8 kiloton-years, and SK-II contributes 49.5 kiloton-years. The atmospheric neutrino Monte Carlo is equivalent to a total exposure of 320 years. There are 200 years (4500 kiloton-years) for SK-I, divided equally between the NEUT and NUANCE models. The remaining

120 years (2700 kiloton-years) are for SK-II, and again are equally divided between NEUT and NUANCE.

The 100 years of SK-I NEUT Monte Carlo contains 511,543 events, of which 306,592 are reconstructed as sub-GeV events within the fiducial volume. The 100 years of SK-II NUANCE Monte Carlo contains 467,300 events, 289,086 of them sub-GeV in the fiducial volume. The 60 years of SK-II NEUT Monte Carlo contains 293,482 events, including 177,579 sub-GeV fiducial volume events. Finally, the 60 years of SK-II NUANCE Monte Carlo contains 270,275 events, 177,630 in the fiducial volume.

The first three searches, for $p \to e^+\pi^0$, $p \to \mu^+\pi^0$, and $p \to \bar{\nu}K^+$, have previously been performed for parts of the SK-I running period [75, 11, 21]. This work represents an update of these searches for the complete SK-I and SK-II periods. The fourth search, for $p \to \bar{\nu}K^*(892)^+$, has not previously been attempted in Super-K.

7.1 $p \to e^+\pi^0$

The decay $p \to e^+\pi^0$ (see Fig. 7.1 for an example event display), has previously been published for SK-I [76, 75, 11]. That analysis used an exposure of 786 days (48.4 kiloton-years), and set a 90% confidence limit on the lifetime of the proton into $p \to e^+\pi^0$ of 2.6×10^{33} years.

In this mode, the final state particles are relatively easy to detect. The e^+ has a momentum of 459.4 MeV/c, and produces a very bright e-like ring in the detector. The π^0 will have the same momentum, and will decay into two photons, at least one of which will be readily detected. The greatest problem for this mode is that, should the decay occur in ^{16}O, the probability that the π^0 will escape the nucleus without interacting is only 43%. As any interaction will destroy the signature of the

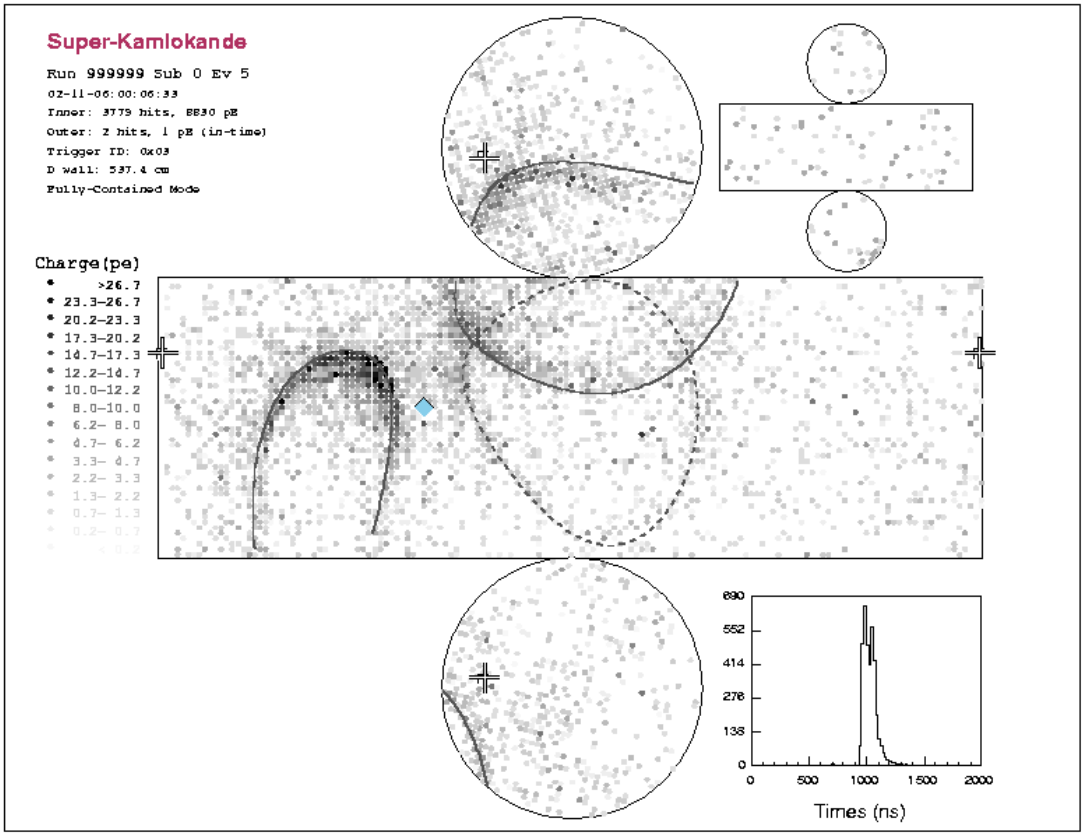

Figure 7.1: An example of a $p \to e^+\pi^0$ event. The e^+ ring is clearly visible, as are the two overlapping rings from the π^0.

event (even elastic scattering will change the kinematics) this imposes an irreducible 46% loss of efficiency after accounting for the fact that decays of free protons are unaffected.

For each of SK-I and SK-II, 2000 proton decay Monte Carlo events are generated. These contain 1675 and 1708 events within the fiducial volume, respectively.

7.1.1 Event Selection

In this search, all cuts have been determined in previous searches [76, 75], and are used without modification. Initial criteria for this search are designed to isolate events containing an e^+ and a π^0, with nothing else. These initial criteria are:

A1. 2 or 3 rings

A2. All rings e-like

A3. 0 decay electrons

A4. 85 MeV/$c^2 < m_\pi <$ 185 MeV/c^2 (3 rings only).

As all searches will use criteria similar to these, additional discussion of how they are set is appropriate. Cuts on the number of decay electrons, as well as the number and type of rings, are determined by what particles are expected to be visible in the event. For most particles this is clear, but there is a small complication for a π^0. While the π^0 decays to two photons 99% of the time, both photons are not always detected. If one photon is emitted in the backwards direction relative to the π^0 momentum, it can be redshifted sufficiently to be missed by the ring counting algorithm. Or, the photons may be closely overlapping and appear as a single ring. Because of this, a π^0 is assumed to contribute either 1 or 2 rings.

For this particular mode, the final-state particles are an e^+, which contributes 1 e-like ring and 0 decay electrons, and a π^0, which contributes 1 or 2 e-like rings and 0 decay electrons. Criteria A1-A3 are set accordingly.

Criterion A4 is the Super–Kamiokande π^0 mass cut. This invariant mass, as all others in this dissertation, is calculated by adding the energies and (3-vector) momenta of the rings involved to find a total energy E_{tot} and a total momentum $\vec{p}_{tot}$ and applying the kinematic relation:

$$m^2 = E_{tot}^2 - |\vec{p}_{tot}|^2. \tag{7.1}$$

In $p \to e^+\pi^0$, the mass cannot be reconstructed if one of the π^0 rings is missed, so A4 is applied only to 3-ring events. As there are three possible pairs of rings that could be from the π^0, all three are checked, and the pair giving a mass closest to 135 MeV/c^2 is selected.

All relevant information about the kinematics of the event are then combined into two final cuts:

A5. $p_{tot} < 250$ MeV/c

A6. 800 MeV/$c^2 < m_{tot} <$ 1050 MeV/c^2,

where p_{tot} and m_{tot} are the momentum and invariant mass obtained by adding all rings. Criterion A5 requires that the overall system have a momentum compatible with the 225 MeV/c Fermi momentum of a proton in ^{16}O, and A6 is centered on the proton mass of 938 MeV/c^2. The distribution of these kinematic variables is shown for SK-I Monte Carlo in Fig. 7.2. The very clear separation between the signal and background distributions is due to the ability to reconstruct all final-state particles completely. Unfortunately, this is not always possible in other proton decay searches.

Passing the $p \to e^+\pi^0$ and NEUT atmospheric neutrino Monte Carlo through criteria A1-A6, 684 events from the $p \to e^+\pi^0$ and 8.9 events (after normalization) from NEUT pass all cuts. Accordingly, the efficiency and background for this mode in SK-I are estimated to be 40.8% and 0.36 events (0.39 events/100 kiloton-years), respectively. The NUANCE atmospheric neutrino Monte Carlo has 4.6 (normalized) events passing the cuts, which predicts a background of 0.19 events (0.21 events/100 kiloton-years). While these differ by almost a factor of 2, the number of events

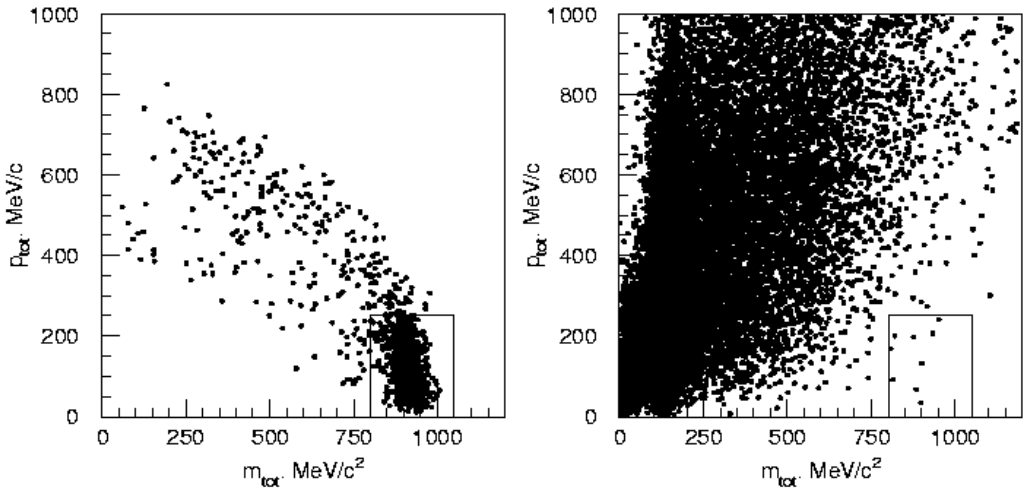

Figure 7.2: p_{tot} vs. m_{tot} for events passing A1-A4 from SK-I $p \to e^+\pi^0$ (left) and atmospheric neutrino (right) Monte Carlo. The boxed region is kept by criteria A5 and A6.

involved is small. The background estimates are therefore consistent within the statistical uncertainties.

The distribution of p_{tot} vs. m_{tot} for the SK-I 1489 days data is shown in Fig. 7.3. No events pass these cuts.

By applying the same criteria to the SK-II Monte Carlo samples (Fig. 7.4), 721 proton decay events and no NEUT atmospheric neutrino events pass the cuts. So, the efficiency and background in SK-II are estimated to be 42.2% and 0 events. The NUANCE atmospheric neutrino sample contains 3.8 (normalized) events passing all cuts, which predicts a background of 0.14 events (0.28 events/100 kiloton-years). This is again consistent with the 0 estimate from NEUT. No candidates are found in the SK-II 804 days data (Fig. 7.5).

The modes contributing to these background estimates are shown in Tbl. 7.1. Overall, charged-current single pion production is dominant. This is due to the fact

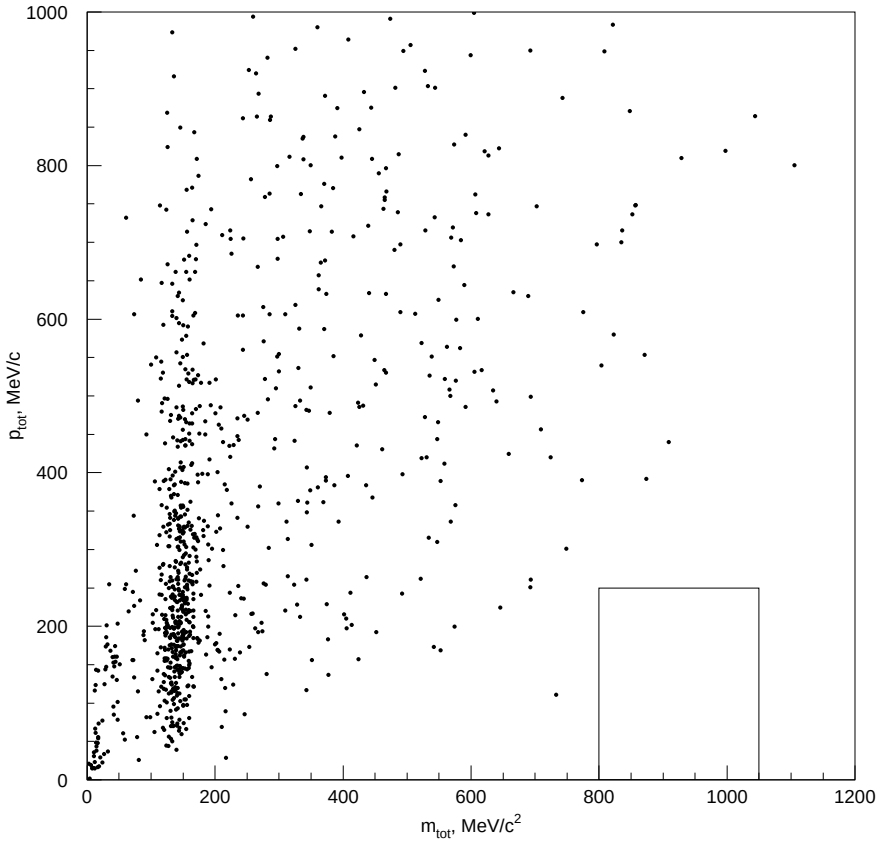

Figure 7.3: p_{tot} vs. m_{tot} for events passing A1-A4 from SK-I 1489 days data. The boxed region is kept by criteria A5 and A6.

that such interactions are the simplest way for a neutrino interaction to produce an e^+ and a π^0.

It is difficult to compare, for example, Figs. 7.2 and 7.3 to determine how well the atmospheric neutrino Monte Carlo reproduces the data, except in a general qualitative way. One way to make a more quantitative comparison is to consider the variable L, which is defined for each event as the distance in the (p_{tot}, m_{tot}) plane from the point (938 MeV/c^2, 200 MeV/c). This is illustrated in Fig. 7.6 [75]. The

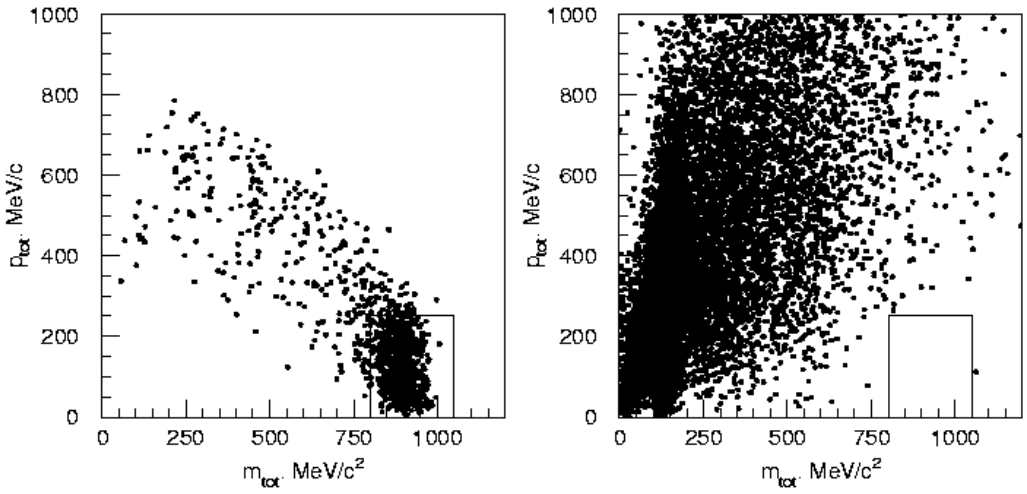

Figure 7.4: p_{tot} vs. m_{tot} for events passing A1-A4 from SK-II $p \to e^+\pi^0$ (left) and atmospheric neutrino (right) Monte Carlo. The boxed region is kept by criteria A5 and A6.

Mode	SK-I NEUT	SK-I NUANCE	SK-II NEUT	SK-II NUANCE
Quasi-elastic	22%	50%	-	0%
CC single π	33%	50%	-	75%
CC multi-π	0%	0%	-	25%
CC coherent π	11%	0%	-	0%
DIS	33%	0%	-	0%
Total BG MC events (unnormalized)	9	4	0	4

Table 7.1: Modes contributing to background for $p \to e^+\pi^0$.

distributions of L for SK-I and SK-II are shown in Figs. 7.7 and 7.8, respectively. The NEUT atomspheric neutrino Monte Carlo reproduces the data reasonably well.

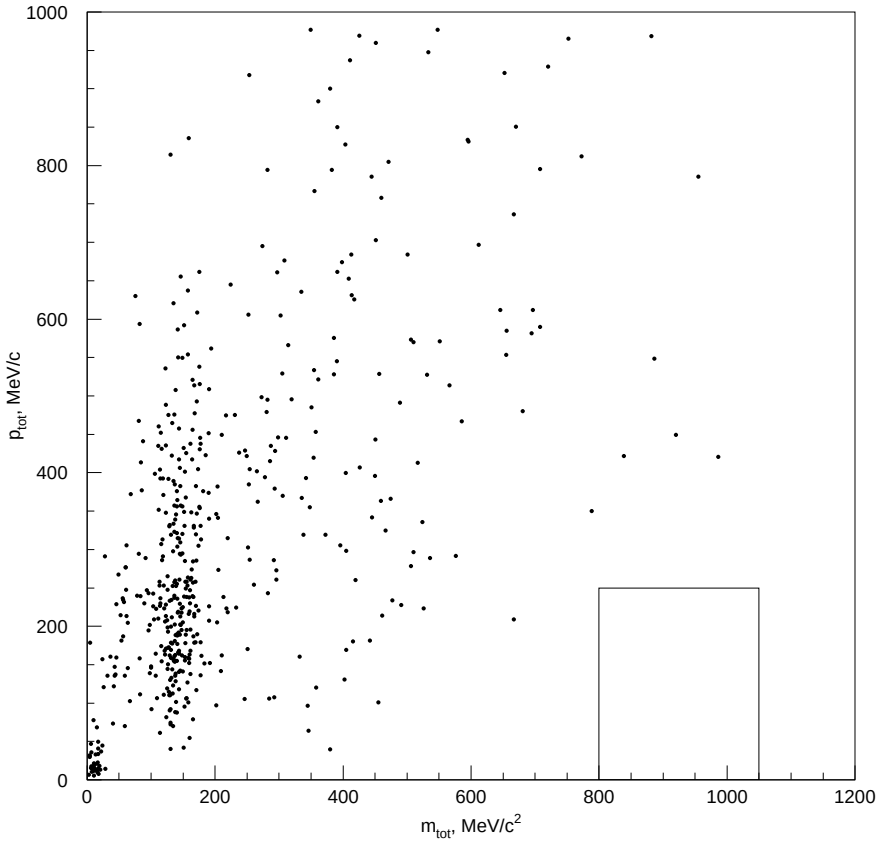

Figure 7.5: p_{tot} vs. m_{tot} for events passing A1-A4 from SK-II 804 days data. The boxed region is kept by criteria A5 and A6.

7.1.2 Systematics

In the calculation of the limit on $p \to e^+\pi^0$, several systematic uncertainties are considered. It has previously been determined [75] that the dominant uncertainty on the efficiency is the probability that the π^0 will escape the nucleus without interacting. The method used for this was to calculate the uncertainty due to several factors – π^0 interactions in the nucleus, energy scale, uniformity of detector gain, particle identification, and various fitting biases – and the π^0 nuclear interactions were shown to

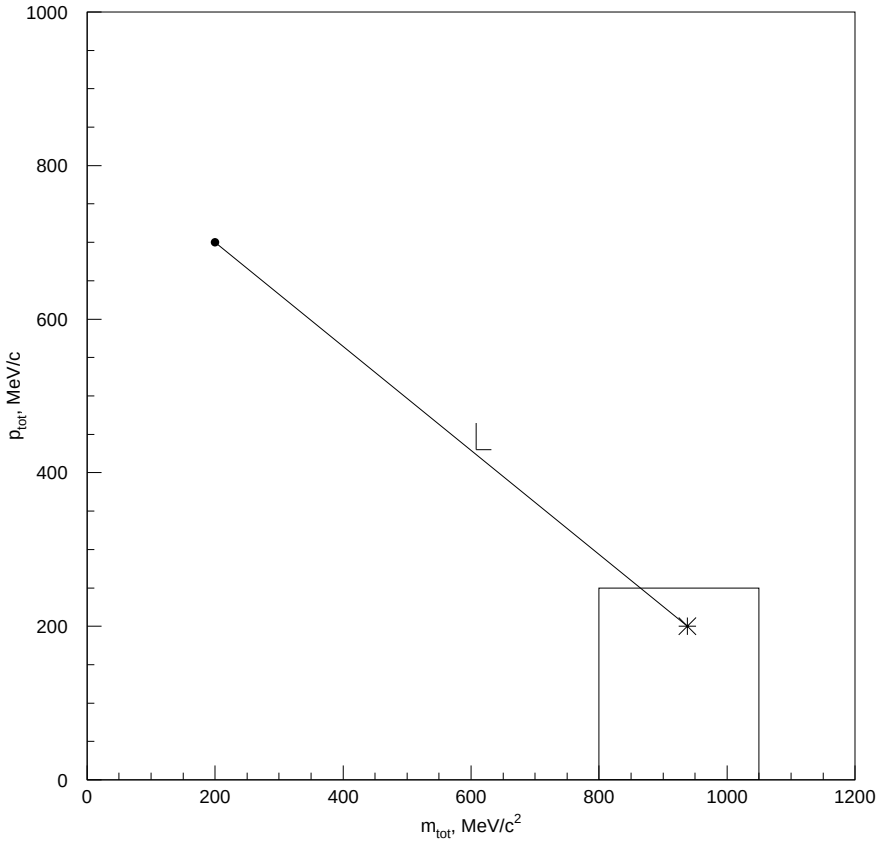

Figure 7.6: Illustration of the variable L.

produce the greatest uncertainty, at 15%. As this is a purely nuclear physics effect, this uncertainty is taken to be the same in SK-I and SK-II.

A second uncertainty is also considered. As can be seen by comparing Figs. 7.2 and 7.4, there is a small shift in the reconstructed proton mass the between SK-I and SK-II proton decay Monte Carlo simulations. This shift is ≈ 20 MeV/c^2, and seems to be due to the performance of the momentum fitting algorithm for events with multiple rings. To account for this, a 2% energy scale uncertainty is assumed, which is similar to the energy scale uncertainty estimated from the calibration studies

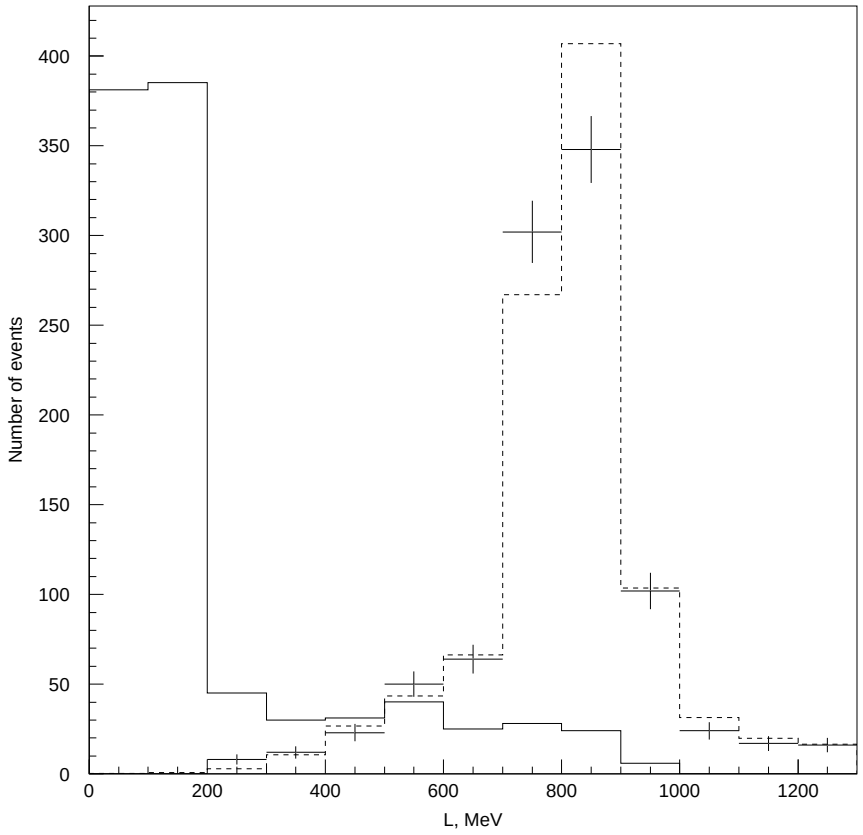

Figure 7.7: L distribution for events passing A1-A4 from SK-I $p \rightarrow e^{+}\pi^{0}$ (solid) and atmospheric neutrino (dashed) Monte Carlo, plus 1489 days data (crosses).

described in Sec. 4.5.5. To estimate the effect of this uncertainty, the efficiency is reestimated with all fitted momenta increased or decreased by 2%. This results in a 1.4% uncertainty in the efficiency for SK-II, and 1.3% in SK-I.

To determine the uncertainty in the background estimate, three different effects are considered. The first effect is the uncertainty in the Monte Carlo statistics, calculated as the square root of the number of background Monte Carlo events passing all cuts. The uncertainties in neutrino interaction cross-sections for various modes

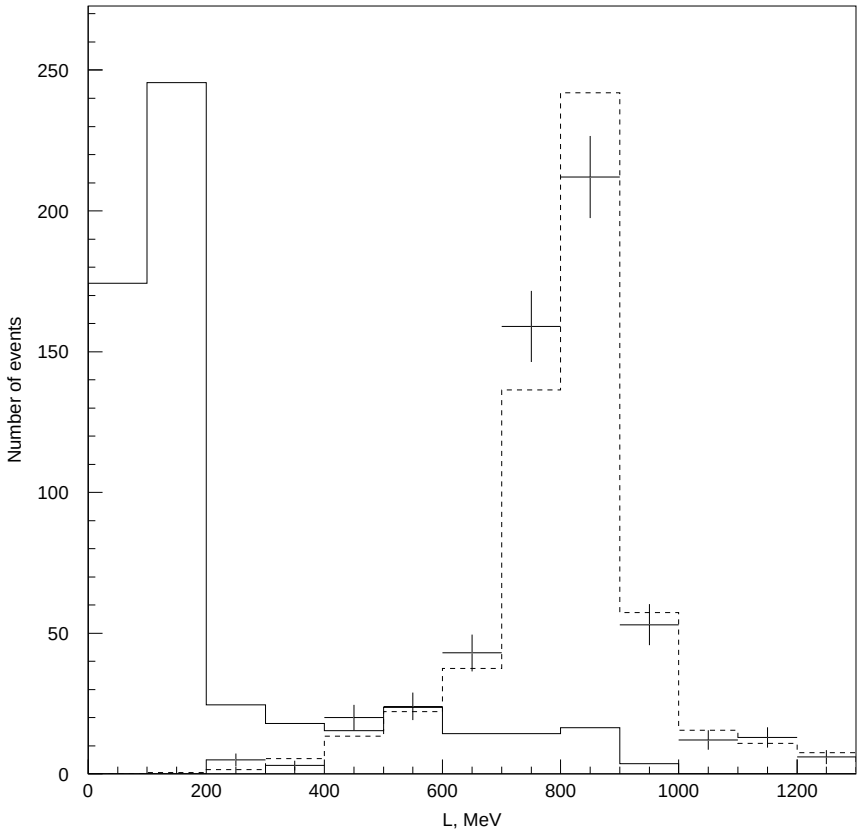

Figure 7.8: L distribution for events passing A1-A4 from SK-II $p \rightarrow e^{+}\pi^{0}$ (solid) and atmospheric neutrino (dashed) Monte Carlo, plus 804 days data (crosses).

are also considered, with values previously estimated [14] as 10% for quasi-elastic and single meson production, 5% for multiple pion production and deep inelastic scattering, and 30% for coherent pion production. Finally, a 10% uncertainty in the total neutrino flux is assumed.

	Efficiency (%)	BG	Data	Limit ($\times 10^{33}$ yrs)
SK-I	40.8 (15%)	0.36 (35%)	0	5.1
SK-II	42.2 (15%)	0	0	2.9
SK-I+II	41.3 (15%)	0.36 (35%)	0	8.0

Table 7.2: Summary of results for $p \to e^+\pi^0$. Systematic uncertainties are in parentheses.

7.1.3 Limits

As no candidates exist in either SK-I or SK-II data, the methods of Appendix C are applied to set 90% CL limits on the partial lifetime into this mode. For SK-I only, this limit is 5.1×10^{33} years, while SK-II only sets a limit of 2.9×10^{33} years. The limits from these two independent searches are combined to give a final limit on the partial lifetime into $p \to e^+\pi^0$ of 8.0×10^{33} years at 90% confidence. These results are summarized in Tbl. 7.2.

It is notable that the performance of SK-II is very similar to that of SK-I for this mode. The efficiency is slightly better, and the background is similar. It appears that the reduced photocathode coverage has little negative impact on this search.

7.2 $p \to \mu^+\pi^0$

The decay $p \to \mu^+\pi^0$ is closely related to $p \to e^+\pi^0$, as the only difference between the two is that a 448.6 MeV/c μ^+ is produced instead of a 459.4 MeV/c e^+, with the π^0 momentum also reduced to 448.6 MeV/c. The cuts for this search are therefore similar to those used for $p \to e^+\pi^0$. See Fig. 7.9 for an example event display for this decay mode. A search for this mode, using a different method, was previously published in [11], using a 786 day (48.4 kiloton-year) exposure of SK-I, with a resulting limit of 2.1×10^{33} years.

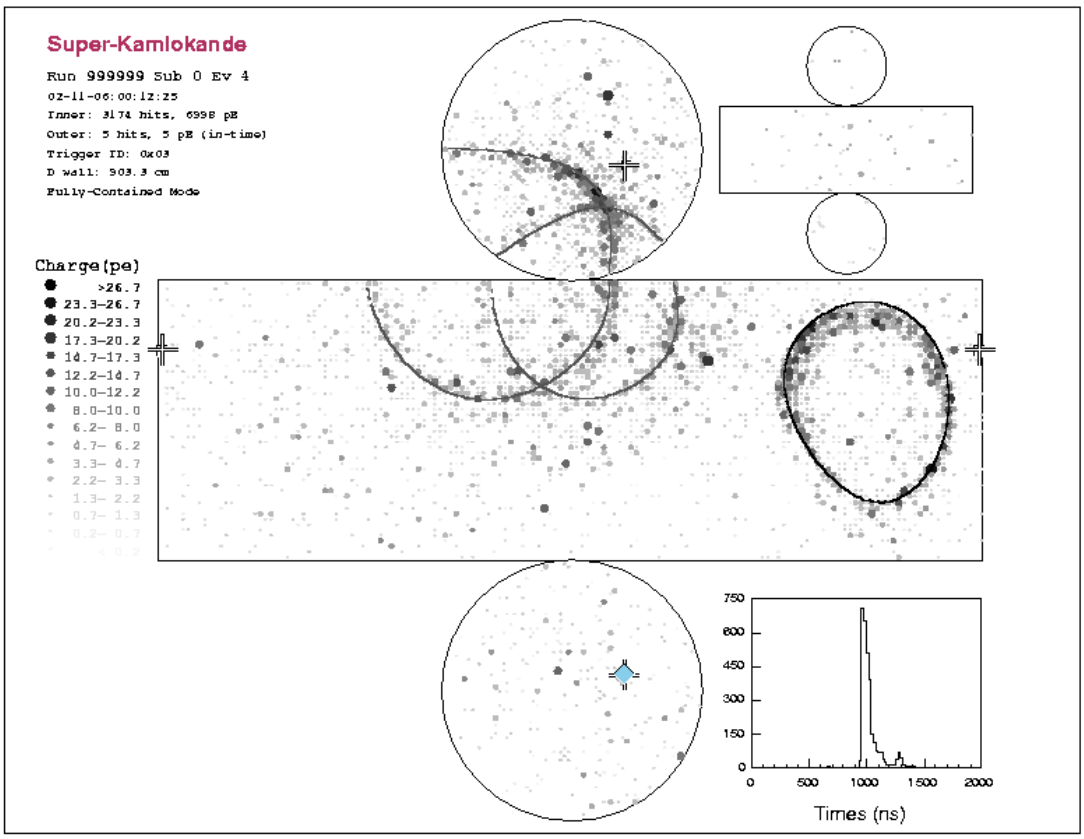

Figure 7.9: An example of a simulated $p \to \mu^+\pi^0$ event. The isolated μ-like ring and two overlapping e-like rings are visible.

For this search, 2000 $p \to \mu^+\pi^0$ Monte Carlo events are generated for each of SK-I and SK-II. Of these, 1646 and 1677 are within the fiducial volume, respectively.

7.2.1 Event Selection

The cuts for this search were originally published in [11], and are used without alteration. Since $p \to \mu^+\pi^0$ is so similar to $p \to e^+\pi^0$, the cuts used for these searches are almost identical. The criteria used for $p \to \mu^+\pi^0$ are:

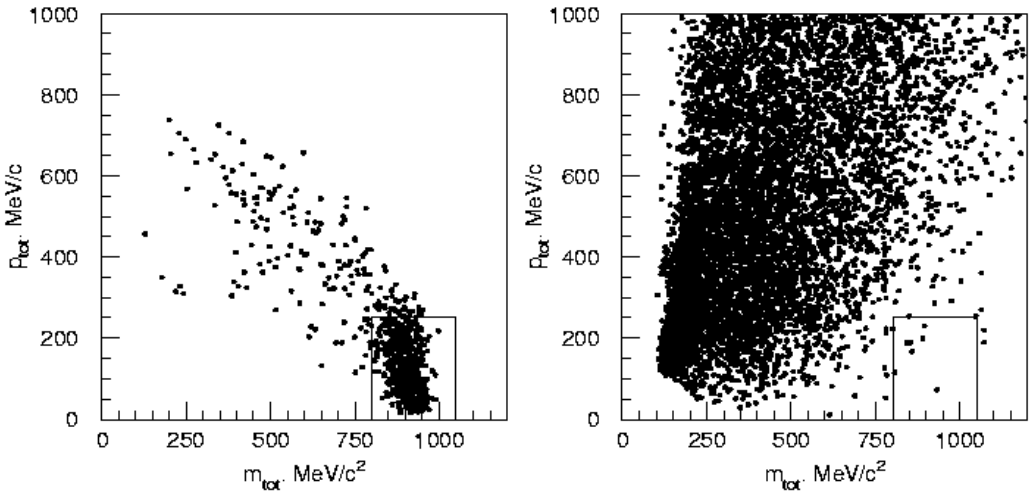

Figure 7.10: p_{tot} vs. m_{tot} for events passing B1-B4 from SK-I $p \to \mu^+\pi^0$ (left) and atmospheric neutrino (right) Monte Carlo. The boxed region is kept by criteria B5 and B6.

B1. 2 or 3 rings

B2. Exactly 1 ring μ-like

B3. 1 decay electron

B4. 85 MeV/$c^2 < m_\pi <$ 185 MeV/c^2 (3 rings only)

B5. $p_{tot} <$ 250 MeV/c

B6. 800 MeV/$c^2 < m_{tot} <$ 1050 MeV/c^2,

where, in this case, m_π is calculated based on the two e-like rings only. The cuts B5-B6 are illustrated in Figs. 7.10 and 7.11 for SK-I.

In SK-I, 532 proton decay events and 5.4 (normalized) NEUT atmospheric neutrino events pass all cuts, so the efficiency and background are estimated to be 32.3%

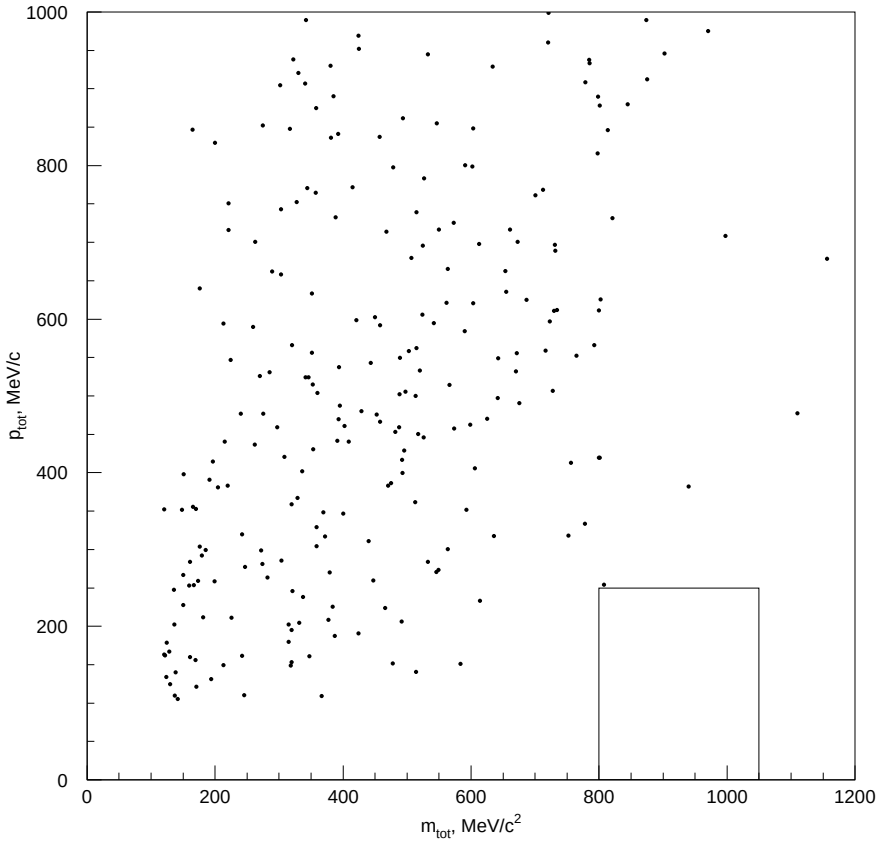

Figure 7.11: p_{tot} vs. m_{tot} for events passing B1-B4 from SK-I 1489 days data. The boxed region is kept by criteria B5 and B6.

and 0.22 events (0.24 events/100 kiloton-years), respectively. The NUANCE atmospheric neutrino sample , from which 4.3 (normalized) events pass all cuts, predicts a similar background of 0.18 events (0.20 events/100 kiloton-years). No events in the 1489 days data pass all cuts. The reduction in efficiency relative to $p \to e^+\pi^0$ is principally due to inefficiency in detection of the decay electron.

Applying the same criteria to SK-II (Figs. 7.12 and 7.13), 538 proton decay events and 5.2 NEUT atmospheric neutrino events pass all cuts. The efficiency and

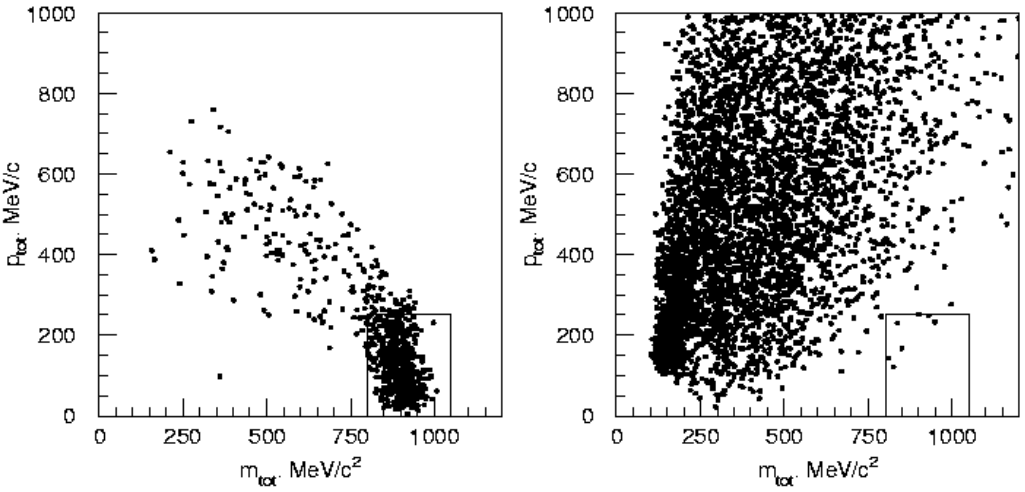

Figure 7.12: p_{tot} vs. m_{tot} for events passing B1-B4 from SK-II $p \to \mu^+\pi^0$ (left) and atmospheric neutrino (right) Monte Carlo. The boxed region is kept by criteria B5 and B6.

background here are estimated to be 32.1% and 0.19 events (0.38 events/100 kiloton-years), while the NUANCE atmospheric neutrino sample predicts a background of 0.093 events (0.19 events/100 kiloton-years), from the 2.5 events passing all cuts. Again, no data events survive the cuts.

The modes contributing to these background estimates are shown in Tbl. 7.3. As in $p \to e^+\pi^0$, charged-current single pion production is dominant, since such interactions are the most straightforward way for a neutrino interaction to produce a μ^+ and a π^0.

Similarly to $p \to e^+\pi^0$, the agreement between data and Monte Carlo is examined using the variable L, shown in Figs. 7.14 and 7.15. Again, we see that the NEUT atmospheric neutrino Monte Carlo reproduces the data well.

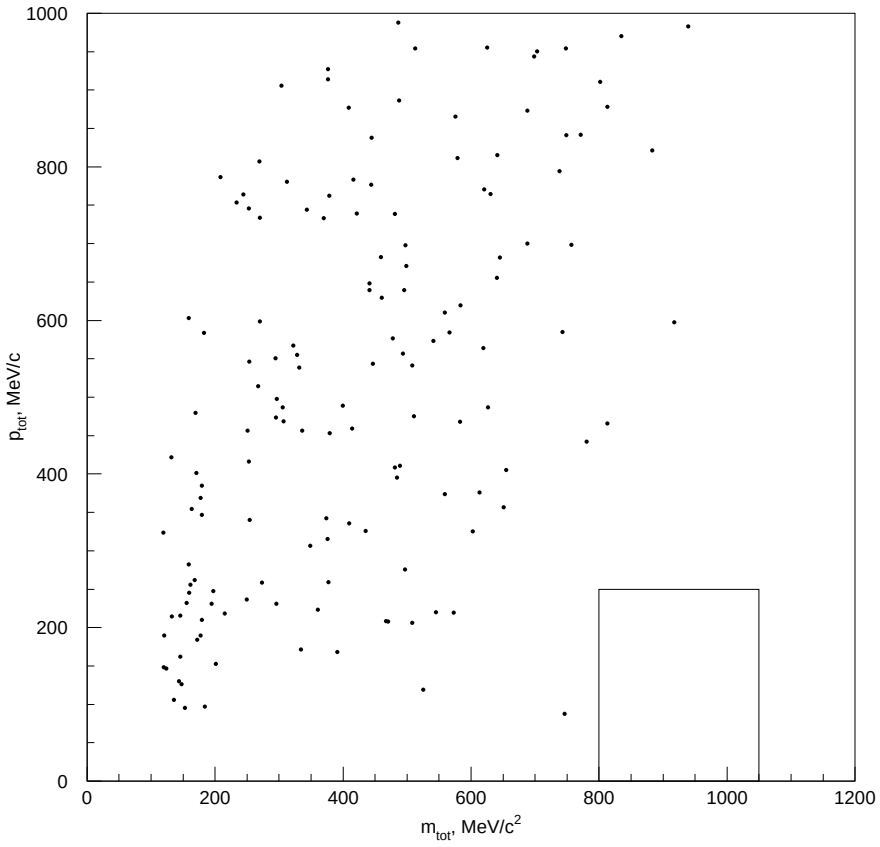

Figure 7.13: p_{tot} vs. m_{tot} for events passing B1-B4 from SK-II 804 days data. The boxed region is kept by criteria B5 and B6.

Mode	SK-I NEUT	SK-I NUANCE	SK-II NEUT	SK-II NUANCE
Quasi-elastic	14%	14%	17%	0%
CC single π	57%	57%	67%	66%
CC multi-π	14%	0%	0%	0%
CC coherent π	0%	0%	0%	33%
NC single π	14%	14%	0%	0%
NC multi-π	0%	14%	0%	0%
DIS	0%	0%	17%	0%
Total BG MC events (unnormalized)	7	7	6	3

Table 7.3: Modes contributing to background for $p \to \mu^+\pi^0$.

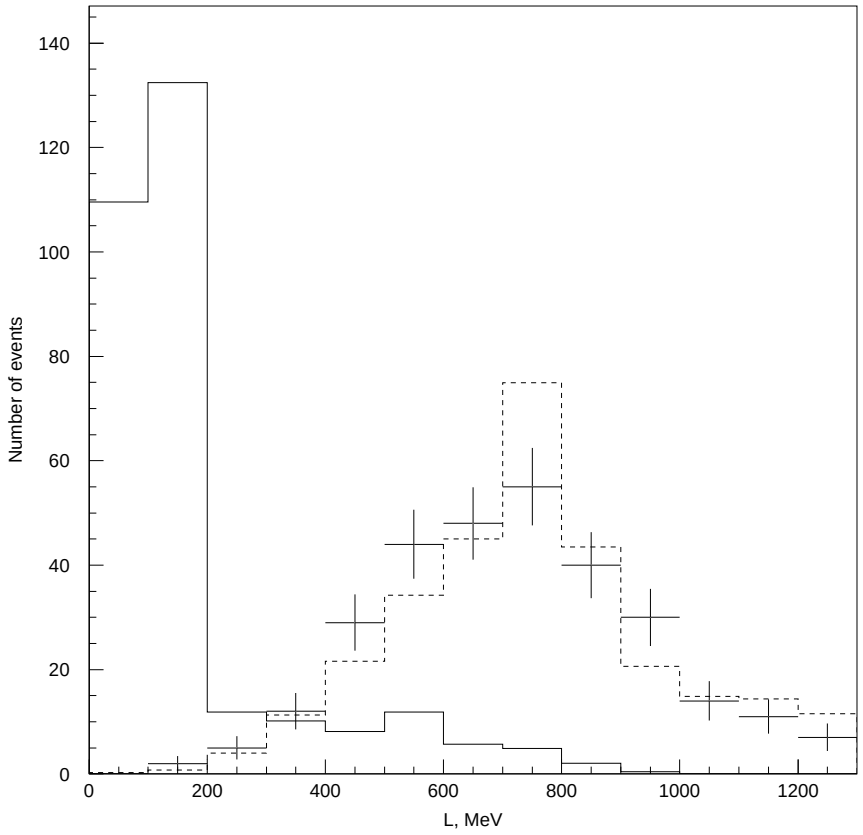

Figure 7.14: L distribution for events passing B1-B4 from SK-I $p \to \mu^+\pi^0$ (solid) and atmospheric neutrino (dashed) Monte Carlo, plus 1489 days data (crosses).

7.2.2 Systematics

The systematic uncertainties for this mode are similar to those in the $p \to e^+\pi^0$ search. The π^0 nuclear interactions impose a 15% uncertainty in the efficiency. There is also a 2% energy scale uncertainty, which results in a 1.9% uncertainty in efficiency for SK-II, and 1.7% in SK-I, in this case.

To determine the uncertainty in the background estimate, three different effects are considered. The first effect is the uncertainty in the Monte Carlo statistics, cal-

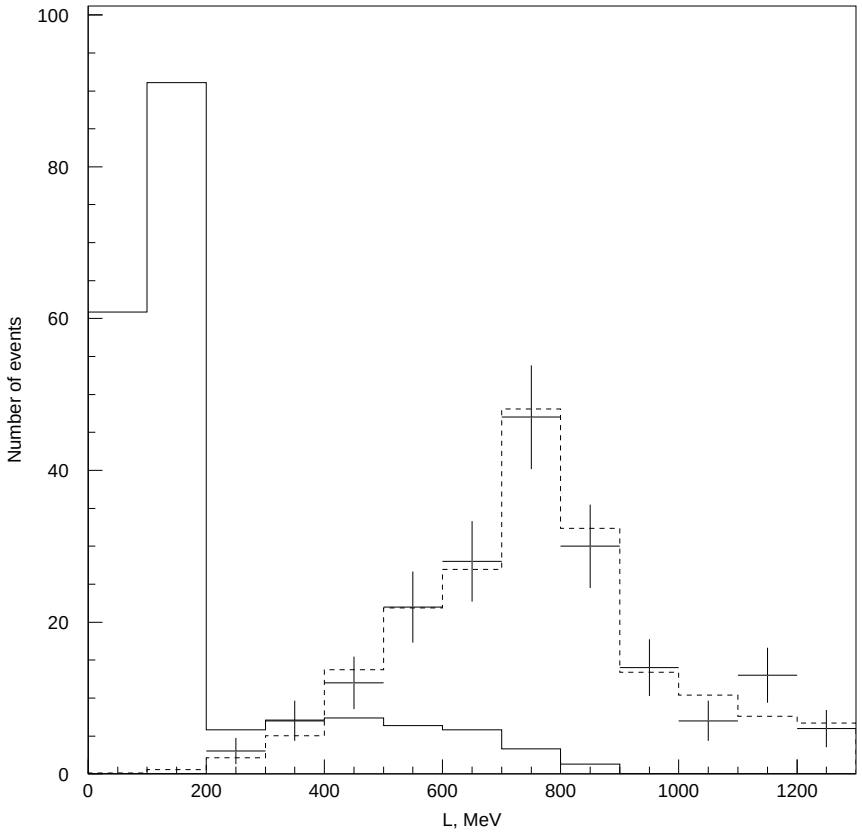

Figure 7.15: L distribution for events passing B1-B4 from SK-II $p \to \mu^+\pi^0$ (solid) and atmospheric neutrino (dashed) Monte Carlo, plus 804 days data (crosses).

culated as the square root of the number of background Monte Carlo events passing all cuts. The uncertainties in neutrino interaction cross-sections for various modes are also considered, with values previously estimated [14] as 10% for quasi-elastic and single meson production, 5% for multiple pion production and deep inelastic scattering, and 30% for coherent pion production. Finally, a 10% uncertainty in the total neutrino flux is assumed.

	Efficiency (%)	BG	Data	Limit ($\times 10^{33}$ yrs)
SK-I	32.3 (15%)	0.22 (45%)	0	4.1
SK-II	32.1 (15%)	0.19 (45%)	0	2.3
SK-I+II	32.2 (15%)	0.41 (32%)	0	6.3

Table 7.4: Summary of results for $p \to \mu^+\pi^0$. Systematic uncertainties are in parentheses.

7.2.3 Limits

As no candidates exist in either SK-I or SK-II data, 90% CL limits are set, again using the methods of Appendix C. SK-I alone provides a limit of 4.1×10^{33} years, while SK-II results in 2.3×10^{33} years. The limits from these two independent searches are combined to give a final limit on the partial lifetime into $p \to \mu^+\pi^0$ of 6.3×10^{33} years at 90% confidence. As in the $p \to e^+\pi^0$ search, the reduced photocathode coverage has little effect for this mode. These results are summarized in Tbl. 7.4.

7.3 $p \to \bar{\nu}K^+$

The decay $p \to \bar{\nu}K^+$ has previously been reported in [21, 77, 78] for SK-I, using the full 91.8 kiloton-year exposure of SK-I and producing a limit of 2.3×10^{33} years. Most of the cuts established in this prior work are used unchanged. In cases where they directly refer to a number of PMT hits or observed charge, the cut values are reoptimized to maximize $S/\sqrt{BG}$. In all other cases, unless otherwise noted, the cuts are duplicated from the previous search without modification.

In this decay, the K^+ is relatively low-momentum, with a β of 0.6. This is below the Cherenkov threshold in water of $\beta = 0.75$, so the K^+ cannot be directly observed. Additionally, the $\bar{\nu}$ will escape the detector without interacting. The primary particles therefore cannot be detected. The cross-section for the K^+ to

interact inelastically is sufficiently small, and its lifetime of 12 ns sufficiently long, that it will come to rest before interacting or decaying more than 90% of the time. Hence, this search is effectively a search for the decay of a K^+ at rest.

The primary decay modes for K^+ are $K^+ \to \mu^+\nu$ and $K^+ \to \pi^+\pi^0$, with branching ratios of 63.5% and 21.2% respectively [13]. These are studied independently, using samples of 50,000 $p \to \bar{\nu}K^+$ Monte Carlo events for each of SK-I and SK-II. In SK-I, 40,274 of these are within the fiducial volume, while there are 39,803 in SK-II.

7.3.1 $K^+ \to \mu^+\nu$ with prompt γ tag

In this mode, the only clearly visible particle in the final state is the μ^+, with a momentum of 236 MeV/c, as illustrated in Fig. 7.16. Due to the large number of neutrino-induced muons in this momentum range, it is highly desirable to seek a method to differentiate muons due to neutrino interactions from those due to proton decay.

A powerful way to distinguish proton decay events is based on the deexcitation "prompt" photons detailed in Tbl. 6.1 [50]. If the proton which decays is in ^{16}O, the residual ^{15}N nucleus is left in an excited state, from which it often decays by emitting a photon, typically of energy 6.3 MeV. This occurs in 41% of all decays of a proton in a p-state, or 25% of all decays. This photon will be emitted before the μ^+, since the deexcitation time is much shorter than the K^+ lifetime of 12 ns. An atmospheric neutrino-induced μ^+, however, will generally be the first light in the event. So, by searching for a small amount of light emitted before the μ^+ time, this type of proton decay event can be distinguished from an atmospheric neutrino event. Recently, a measurement of these prompt photons has been performed [79]. This has the potential to be a significant improvement on Ejiri's theoretical calculation,

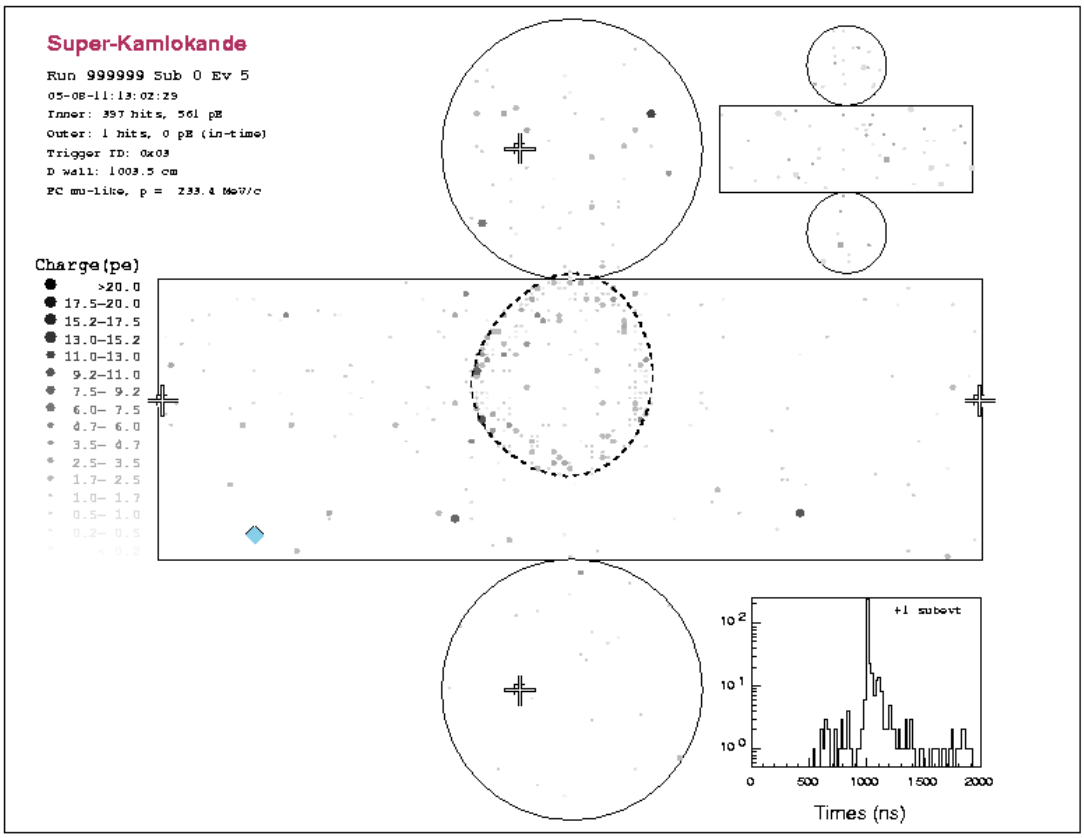

Figure 7.16: An example of a simulated $p \to \bar{\nu} K^+$, $K^+ \to \mu^+ \nu$ event. Early hits from a prompt γ are visible before 1000 ns in the time distribution at the lower right.

particularly with respect to the systematic uncertainty of the emission. However, this work came too late to be used for this dissertation.

To find this prompt photon, a precise vertex fit is very important. In particular, the light from decay electrons can, if included in the vertex fit, result in a poor fit. Due to this, a slightly modified version of the reconstruction algorithms is run on single ring μ-like events which have "in-gate" decay electrons. These are decay

electrons that are part of the primary trigger, rather than a later trigger. Specifically, the "MS-fit" algorithm uses hits within a smaller time window, of 60 ns instead of the standard 280 ns. This modified version of MS-fit is used only for the $p \to \bar{\nu}K^+$ search, and only for events with a single μ-like ring and at least one in-gate decay electron.

The initial criteria for this search select events containing a 236 MeV/c μ^+:

C1. One μ-like ring

C2. One decay electron

C3. 215 MeV/$c < p_\mu <$ 260 MeV/c

C4. Proton rejection.

The criterion C4 is designed to reject events with a poor vertex fit, which can mimic the prompt photon timing signature. The major source of such events is recoil protons from neutral-current neutrino interactions, hence the name "proton rejection." This criterion consists of two cuts:

$$G_{vertex} \geq 0.6 \tag{7.2}$$

$$d_{\mu e} < d_{max}, \tag{7.3}$$

where G_{vertex} is the goodness of the vertex fit described in Sec. 5.2.1, $d_{\mu e}$ is the distance between the reconstructed vertices for the muon and the decay electron (which should be small for a proton decay event), and d_{max} is 200 cm in SK-I and 120 cm in SK-II. This modification to d_{max} is necessary because, otherwise, the efficiency of the proton rejection to cut recoil proton events is substantially lower in SK-II than in SK-I.

This change to d_{max} represents the first cut that was newly determined for this thesis, so it is appropriate to note the procedure used to set the cut values. For any cut, other than those looking for specific particles (*e.g.* C1 and C2, or A1-A4), the value is selected to maximize $S/\sqrt{B}$, where S is the fraction of signal passing the cut, and B is the fraction of background passing.

Having made the preliminary cuts C1-C4, the remaining events are searched for prompt photons. The method used for this is described in detail in [21] and [48], and summarized here.

The first step is to search for t_μ, the time corresponding to detection of the μ^+. This t_μ is defined to be the point in time where $\Delta N_{hit}/\Delta t$ is a maximum, where N_{hit} is the number of PMT hits per unit time. Additionally, t_0 is defined to be the latest time earlier than t_μ where $\Delta N_{hit}/\Delta t = 0$. The search for prompt photon hits is carried out only before this time.

In order to eliminate hits due to the μ^+, all hits within 50 degrees of the μ-like ring are ignored during the remaining steps of the search. The prompt photon is found by sliding a time window, 12 ns wide, backwards in time with its trailing (later time) edge starting at t_0, and finding the maximum number of hits within the sliding window. This maximum is called $N_{hit\gamma}$ (see Figs. 7.17 and 7.18), and the time at which it is achieved is t_γ.

Using these quantities, the next criteria are defined as:

C5. $N_{min} < N_{hit\gamma} < N_{max}$

C6. $t_\mu - t_\gamma < 100$ ns,

where N_{min} is 7 for SK-I and 5 for SK-II, and N_{max} is 60 for SK-I and 30 for SK-II. The value of N_{min} is determined by optimizing the signal-background separation, as measured by $S/\sqrt{BG}$, with S the signal accepted and BG the background accepted.

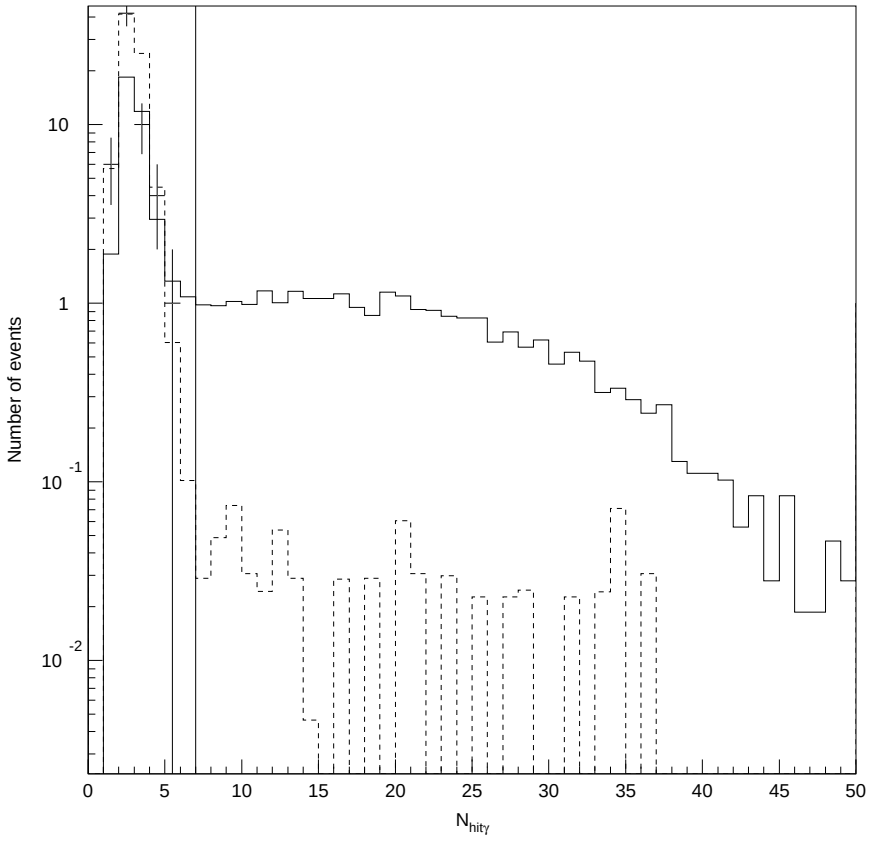

Figure 7.17: The distribution of $N_{hit\gamma}$ for events passing C1-C4 and C6 from SK-I $p \to \bar{\nu}K^+$ (solid) and atmospheric neutrino (dashed) Monte Carlo, plus 1489 days data (crosses). The lower end of cut C5 is shown as a vertical line.

$S/\sqrt{BG}$ as a function of N_{min} is shown in Fig. 7.19. The maximum for $S/\sqrt{BG}$ is definitely at five.

These cuts are the only ones made for SK-I. Passing the SK-I $p \to \bar{\nu}K^+$ and NEUT atmospheric neutrino Monte Carlo through criteria C1-C6, 3412 and 16.3 (normalized) events pass all cuts, respectively. Accordingly, the efficiency and background are estimated to be 8.4% and 0.66 events (0.72 events/100 kiloton-years), respectively. The NUANCE atmospheric neutrino Monte Carlo, with 26.1 (normal-

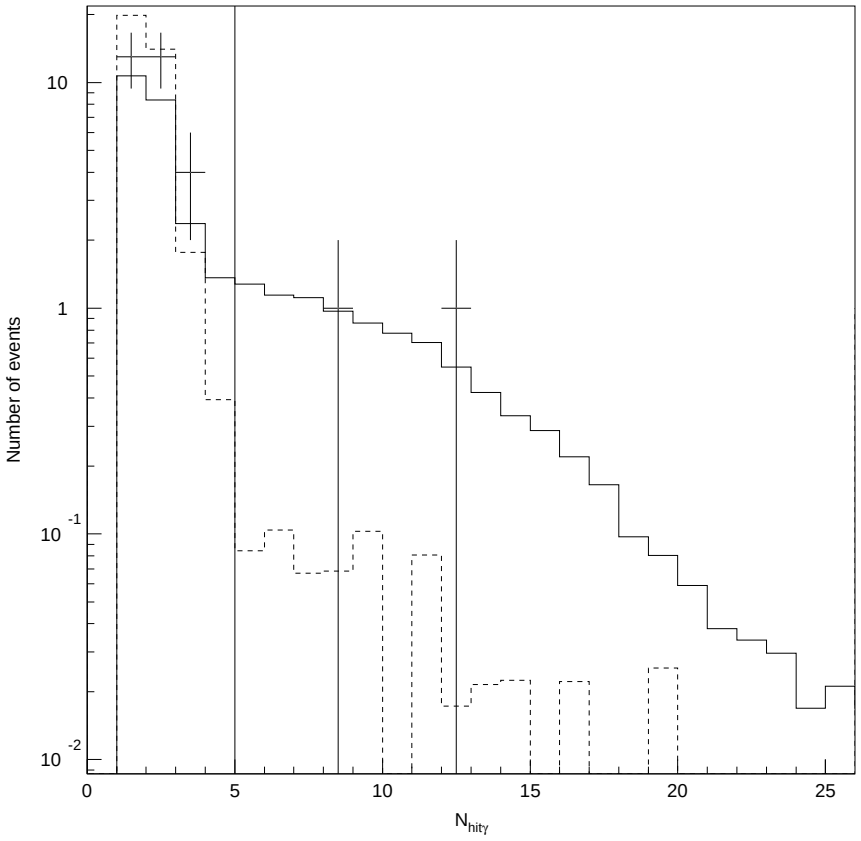

Figure 7.18: The distribution of $N_{hit\gamma}$ for events passing C1-C4 and C6 from SK-II $p \to \bar{\nu} K^+$ (solid) and atmospheric neutrino (dashed) Monte Carlo, plus 804 days data (crosses). The lower end of cut C5 is shown as a vertical line.

ized) events passing, predicts 1.1 events of background (1.2 events/100 kiloton-years). In the SK-I 1489 days data, no events pass all cuts.

When criteria C1-C6 are applied to the SK-II data and Monte Carlo, the efficiency and background are estimated to be 4.7% and 0.67 events (1.4 events/100 kiloton-years). SK-II performance is worse than SK-I, with efficiency reduced by almost half and similar background expected in just over half the live time. Two events in the 804 days data pass these cuts. The probability of a statistical fluctuation from 0.67

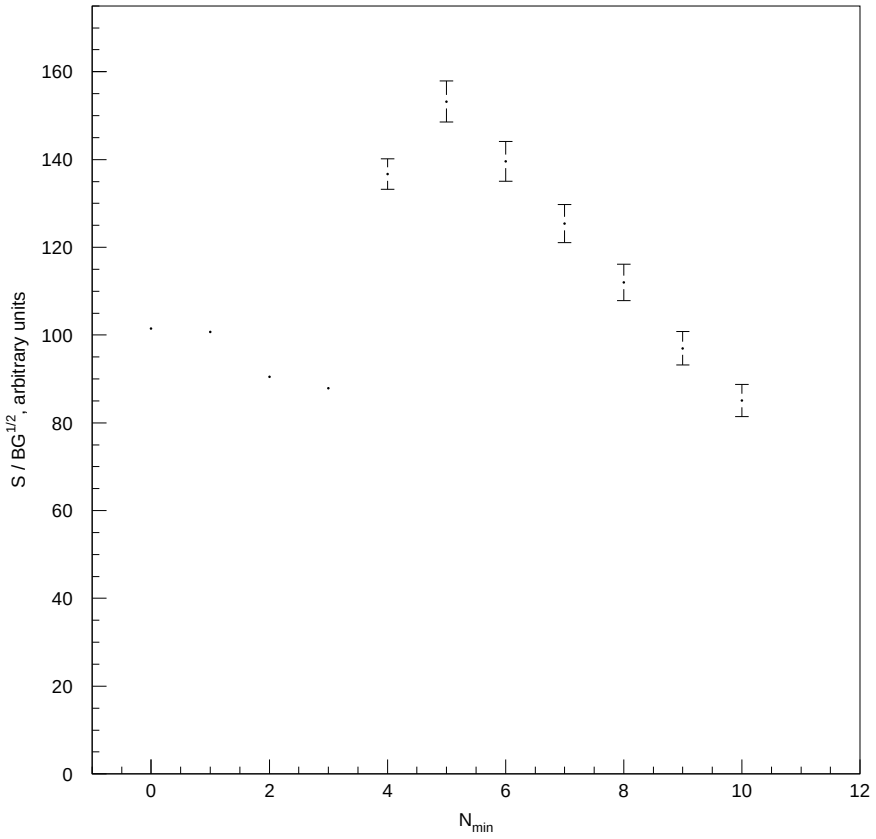

Figure 7.19: $S/\sqrt{BG}$ as a function of N_{min}. The error bars represent the statistical uncertainty.

expected background events to at least two observed events is 15%. This analysis with C1-C6, reoptimizing C5 and $d_{\mu e}$ for $S/\sqrt{BG}$, is the minimally biased set of criteria for SK-II, as they were essentially determined for the previously published result.

The first event passing C1-C6 is shown in Fig. 7.20. There are two clear peaks in the timing distribution. Neither one is identified with a prompt photon. The first is the primary event, and the second is from muon decay. The hits in the first peak

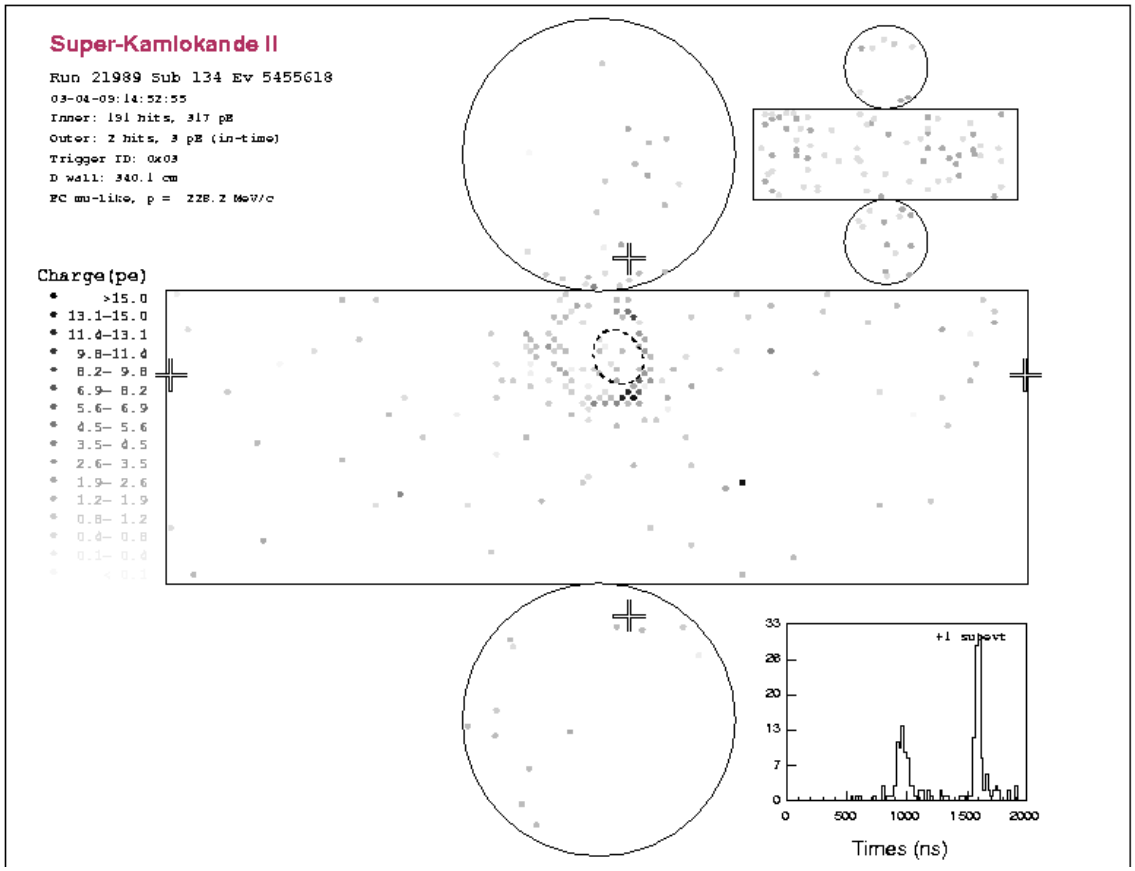

Figure 7.20: The first event passing cuts C1-C6. The dashed line indicates the fitted μ-like ring.

are shown in Fig. 7.21, and those in the second peak are in Fig. 7.22. The hits in the larger ring are in the time peak at 1800 ns, and are likely a decay electron. No clear first ring is visible, and the hits in the first peak are scattered throughout the detector. The interpretation of this event is unclear, but it does not seem to have a convincing 236 MeV/c muon. It is possible that it contains a low-energy muon or charged pion which was below Cherenkov threshold or deposited only a small amount of light in the detector before slowing below Cherenkov threshold. The diffuse hits in Fig. /refmunucandfirst would be from nuclear deexcitation, and the μ-like ring is a failure of the event reconstruction.

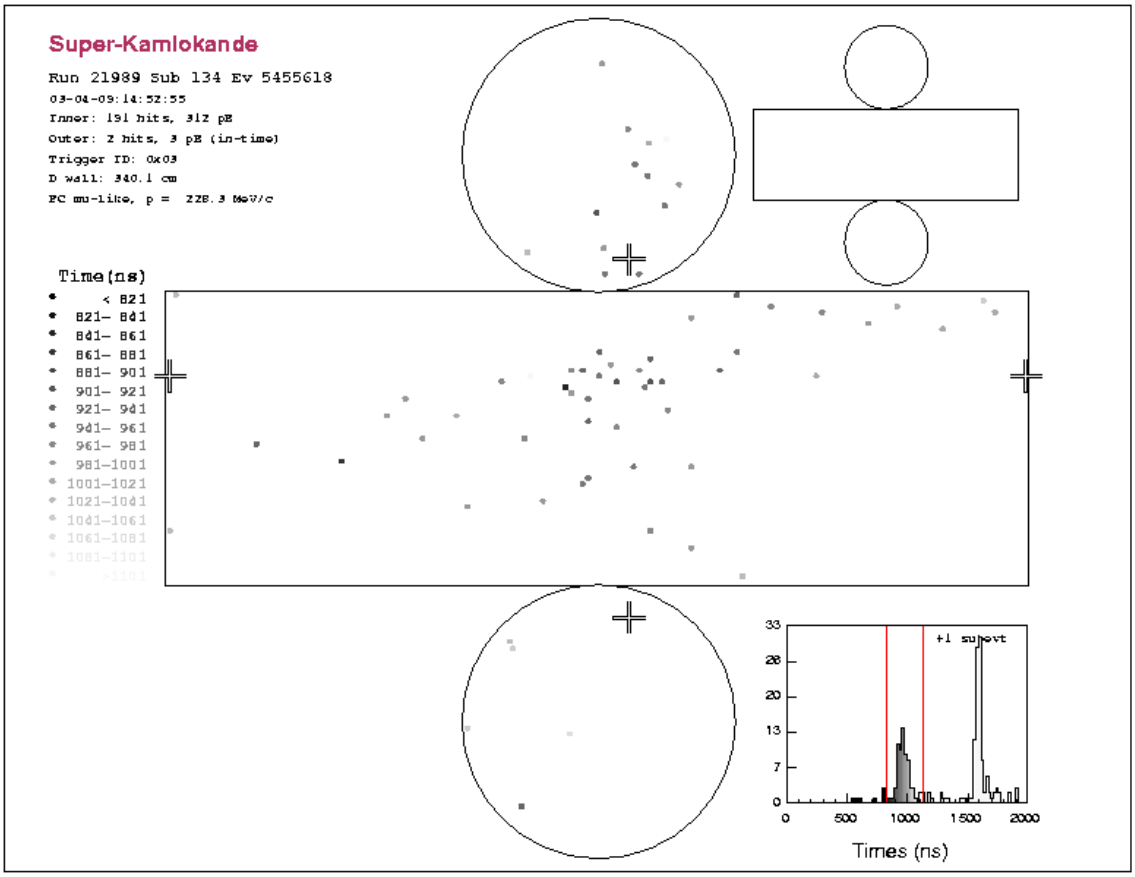

Figure 7.21: The first event passing cuts C1-C6, showing hits only in the first peak. No clear μ-like ring is visible.

The second event passing C1-C6 is shown in Fig. 7.23. There are no obvious defects in this event. A clear μ-like ring is visible and properly fitted (as indicated by the dashed line), while the hits to the left are in the second time peak and are identified as a decay electron.

The analysis using criteria C1-C6 is an unbiased extension of the prior SK-I search to SK-II. However, with the reduced efficiency and higher background, improving the signal-background separation becomes very important to accurately characterize the candidates. So, additional cuts are designed, for SK-II only, to improve the signal-

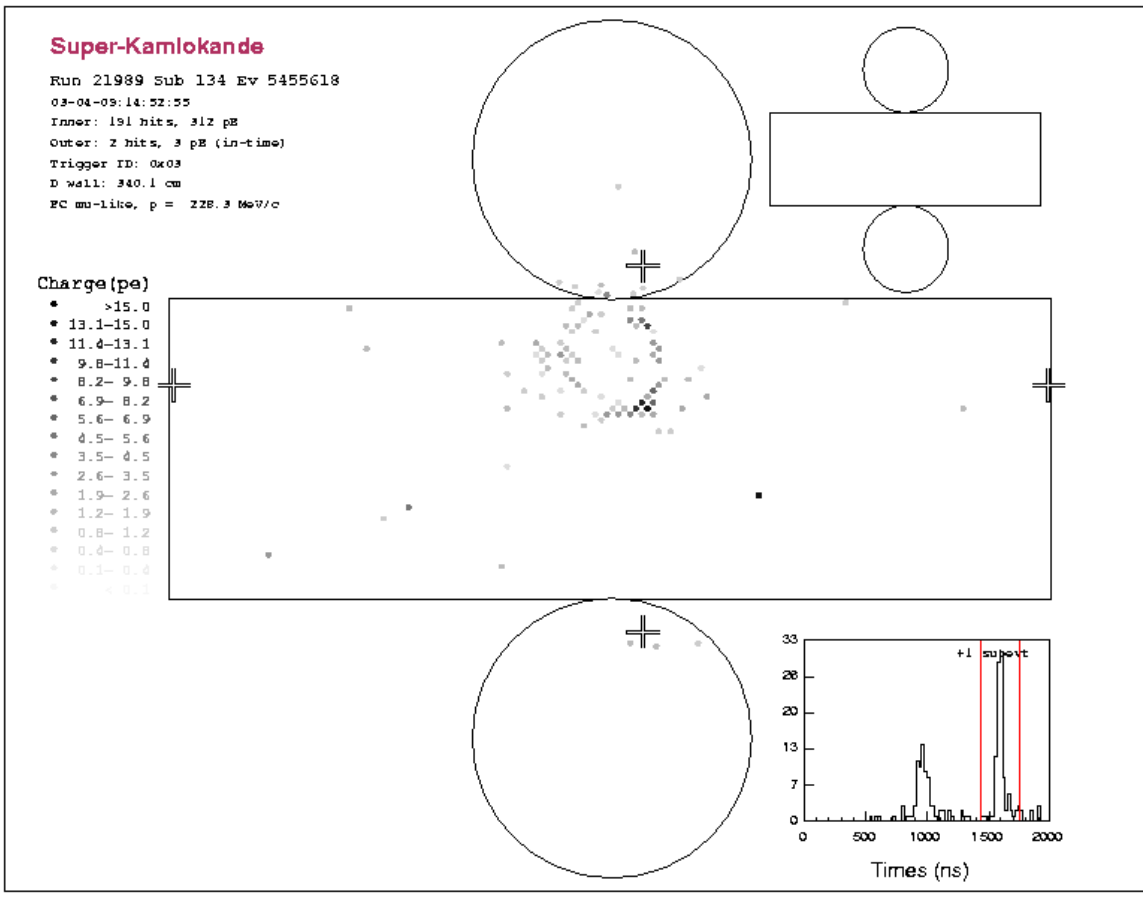

Figure 7.22: The first event passing cuts C1-C6, showing events only in the second peak. A very clear ring, probably a decay electron, is visible.

background separation. These cuts were developed without consideration of any detailed knowledge of the candidate events, though with the knowledge that the candidates existed. The cut values are set strictly based on maximizing $S/\sqrt{BG}$ according to the Monte Carlo samples. Also, this study was performed when only 627 days of the SK-II data had been analyzed. The remaining 177 days were not examined until after the new cuts were finalized.

As an additional way to ensure that the cuts are not biased by the limited BG MC sample, the optimization of the cut values is carried out using momentum sidebars.

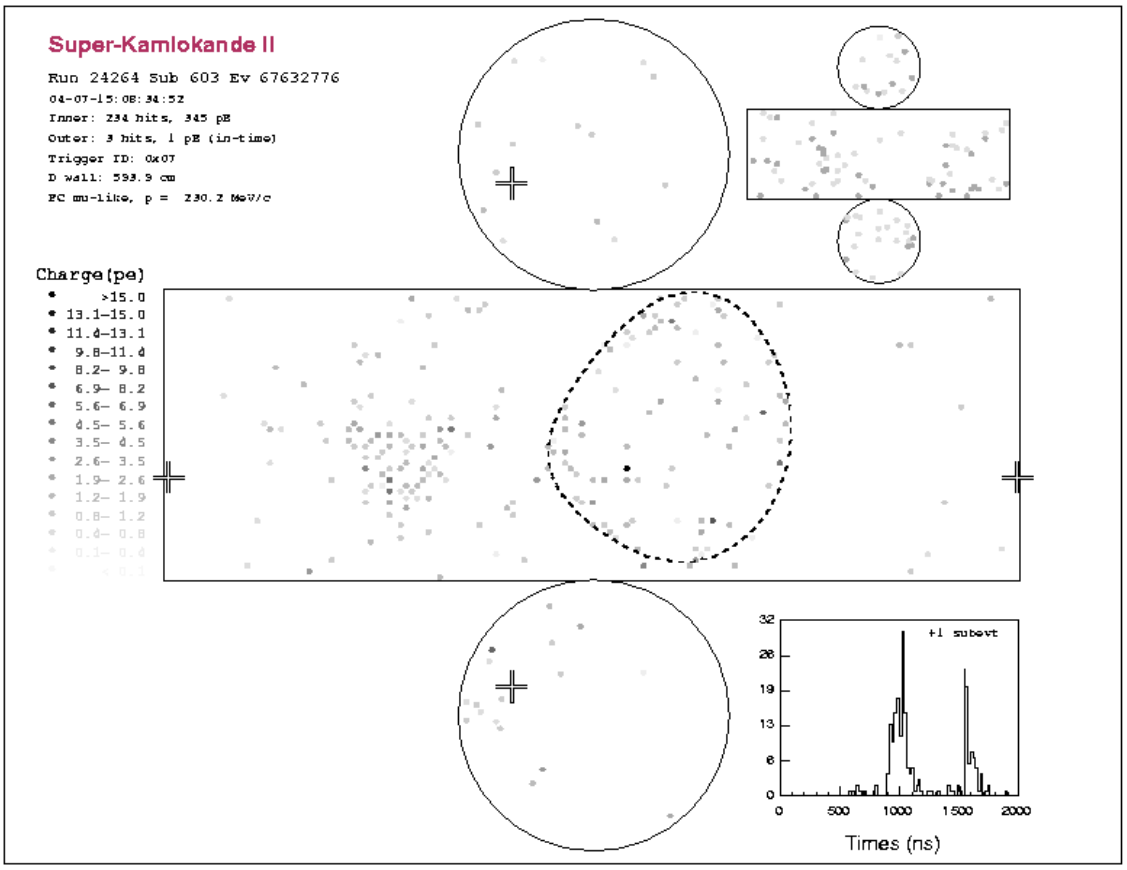

Figure 7.23: The second event passing cuts C1-C6.

The decay search uses only those events passing C3, *i.e.* 215 MeV/c < p_μ < 260 MeV/c. In order to determine cut values, only events with p_μ between 200 and 215 MeV/c, or between 260 and 400 MeV/c, are used.

The first new variable is motivated by the possibility that a random collection of noise hits could combine in a 12 ns window to mimic a prompt photon signal. While the hits from a true prompt photon should be distributed along a Cherenkov ring, a random collection of noise hits should be approximately isotropic. Accordingly, H is defined as a measure of the isotropy of the prompt hits:

$$H = \left| \frac{\sum_{i=1}^{N_{hit\gamma}} \vec{v_i}}{N_{hit\gamma}} \right|, \tag{7.4}$$

where the sum runs over the hits counted in $N_{hit\gamma}$, and $\vec{v_i}$ is a unit vector pointing from the event vertex to each hit PMT. A perfectly isotropic set of hits will result in $H = 0$, while highly directional hits will tend toward $H = 1$. Hits distributed along a Cherenkov ring will result in $H \simeq 0.8$. The distribution of H is shown in Fig. 7.24.

The background sample clearly tends toward low H and the signal toward high H, specifically $H \simeq 0.8$, as expected. This makes H a fairly powerful variable. The cut value which maximizes $S/\sqrt{B}$ for the momentum sidebars is at 0.5. On events passing C1-C6, this cut is 84% efficient, and rejects 31% of background.

Two additional variables designed for this search are called N_{early} and N_{late}. The former, N_{early}, measures the activity before the prompt photon, while N_{late} measures activity between the prompt photon and the muon. These are the number of hits in the 12 ns windows before and after the $N_{hit\gamma}$ window, where N_{late} is restricted to end before t_μ. For a true $p \to \bar{\nu}K^+$ event, these should both be small. However, a bad vertex fit (*e.g.* from a proton event) often results in a broad distribution of hits before the main peak. In such a case, t_γ is fit at the peak of the distribution, but there may be hits before and after which may be picked up, leading to a large N_{early} or N_{late}.

These distributions are shown in Fig. 7.25. N_{early} is not very powerful, but a small fraction (6%) of background events lie at large N_{early} where there is no signal. Therefore, a cut is placed at 8 hits which is essentially 100% efficient and rejects a small amount of background.

N_{late} is far more powerful, since, as shown in Fig. 7.25, background events are

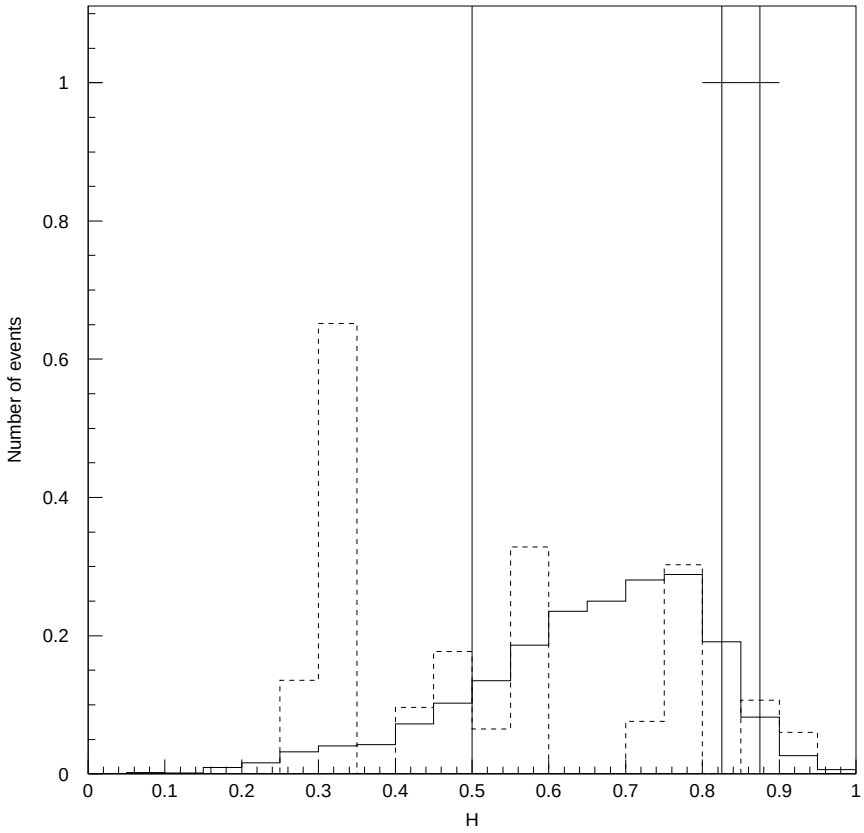

Figure 7.24: The distribution of H for events passing C1-C6 from SK-II $p \to \bar{\nu}K^+$ (solid) and atmospheric neutrino (dashed) Monte Carlo, plus 804 days data (crosses). Cut C7 is shown as a vertical line.

quite prone to have relatively large numbers of late hits. The optimal cut in this case is at 5 hits, which is 82% efficient while rejecting 68% of the background.

This therefore defines the three final criteria, applied only to SK-II:

C7. $H > 0.5$

C8. $N_{early} < 8$

C9. $N_{late} < 5$.

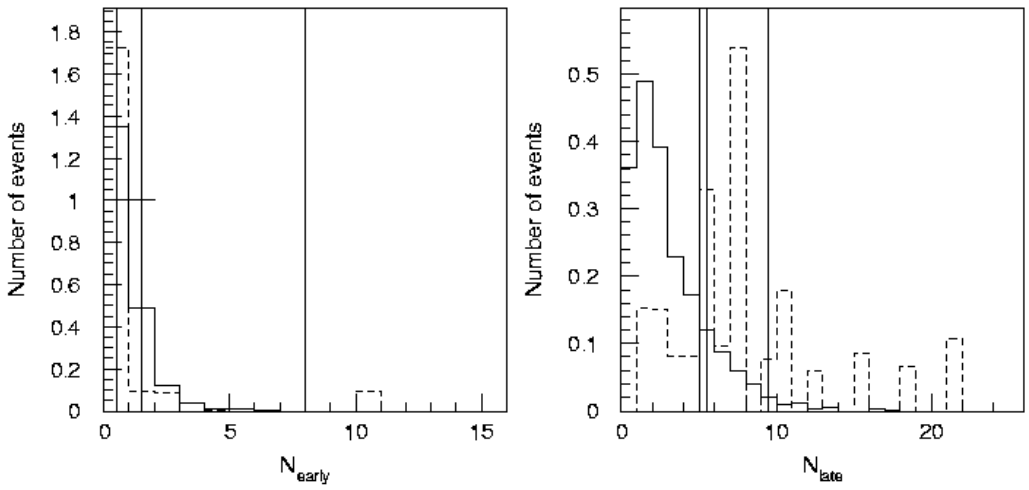

Figure 7.25: The distribution of N_{early} and N_{late} for events passing C1-C6 from SK-II $p \to \bar{\nu} K^+$ (solid) and atmospheric neutrino (dashed) Monte Carlo, plus 804 days data (crosses). Cuts C8 and C9 are shown as vertical lines.

Having applied these cuts, in addition to C1-C6, 1291 proton decay events and 1.1 (normalized) NEUT events pass. So, the final efficiency and background for SK-II in this search are estimated to be 3.2% and 0.04 events (0.08 events/100 kiloton-years), respectively. NUANCE, with 4.3 (normalized) events passing, predicts a background of 0.16 events (0.32 events/100 kiloton-years). No events in the 804 days data pass C1-C9. A summary of the two events passing C1-C6 is given in Tbl. 7.5.

The cut C9 eliminates both events that passed C1-C6, though it should again be stressed that this cut was developed without detailed knowledge of the candidates, and specifically without knowing their values of N_{late}. One candidate has $N_{late} = 5$, barely failing by a single hit. The other has $N_{late} = 8$, and fails by a substantial margin, being well outside the range where there is a significant signal.

The neutrino interaction modes contributing to the background in this mode are

Variable	Acceptance Range	Candidate 1	Candidate 2
Run #		21989	24264
Event #		5455618	67632776
Date		Apr. 9, 2003	July 15, 2004
Time (JST)		2:52 PM	8:34 AM
p_μ (MeV/c)	215 - 260	228	230
G_{vertex}	0.6 - 1.0	0.84	0.73
$N_{hit\gamma}$	5 - 30	8	12
$t_\mu - t_\gamma$ (ns)	0 - 100	12	13
H	0.5 - 1.0	0.88	0.81
N_{early}	0 - 7	1	0
N_{late}	0 - 4	5*	8*

Table 7.5: Summary of events passing C1-C6 for $p \to \bar{\nu}K^+$, prompt γ. Starred cuts are failed. Both candidates have sub-event decay electrons so the $d_{\mu e}$ cut is not applied.

Mode	SK-I NEUT	SK-I NUANCE	SK-II NEUT	SK-II NUANCE
Quasi-elastic charged-current	21%	58%	40%	7%
Elastic neutral current	17%	3%	5%	7%
CC single π	25%	18%	25%	36%
NC single π	29%	11%	25%	0%
NC multi-π	0%	8%	5%	29%
Other	8%	3%	0%	21%
Total BG MC events (unnormalized)	24	38	20	14

Table 7.6: Modes contributing to background for $p \to \bar{\nu}K^+$, $K^+ \to \mu^+\nu$ with prompt γ tag.

shown in Tbl. 7.6. The primary background is from quasi-elastic interactions. Single pion production is also important. These sources are as expected, since muons and charged pions are the primary sources of single μ-like rings.

7.3.2 $K^+ \to \mu^+\nu$ without prompt γ tag

As seen in the previous section, the efficiency of the prompt γ tag is not very high. As noted before, only 25% of decays emit a prompt γ at all, and if the K^+ decays quickly, the μ^+ can come too closely after the γ to distinguish them. Also, the γ may be emitted close to the same direction as the μ^+ and be lost against the μ^+'s Cherenkov ring. Due to this, events passing C1-C2, but failing C5, are used in a spectrum fit to place an additional limit on the proton lifetime.

The procedure for this fit is as follows. The number of events passing C1-C2, but failing C5, are summed in fourteen momentum bins, from 200 MeV/c to 305 MeV/c. A limit is then set by defining:

$$\chi^2 = \sum_i \frac{\left[N_i^{obs} - N_i^{exp}\right]^2}{\sigma_i^2} + \sum_j (\delta_j)^2 \tag{7.5}$$

$$N_i^{exp} = (1 + \sum_j f_j^i \delta_j)(aN_i^{bg} + \Gamma\lambda_i\epsilon_i), \tag{7.6}$$

where the normalization of the atmospheric ν background a and the rate of proton decay Γ are free parameters. Further details are described in Appendix C.

For SK-I, the χ^2 minimum is 26.6 at $a = 1.03$, $\Gamma = -7.3 \times 10^{-34}$ events/proton-year. This is in the unphysical region, with negative decay rate. The minimum in the physical region is 27.1 at $a = 1.0125$, $\Gamma = 0$. Therefore $\chi^2_{min,phys} - \chi^2_{min,unphys} = 0.5$. Using the same prescription as in [14], the 90% CL limit on χ^2 is determined to be $\chi^2_{90} = \chi^2_{min,unphys} + 5.1 = 31.7$. This results in a maximum Γ of 1.9×10^{-33} events/proton-year, and hence a limit on the proton lifetime $1/\Gamma$ of 5.3×10^{32} years.

The same procedure is carried out for SK-II, as shown in Fig. 7.27. Here the χ^2 minimum is 18.2 at $a = 0.8325$, $\Gamma = 8.3 \times 10^{-34}$ events/proton-year. This is in the

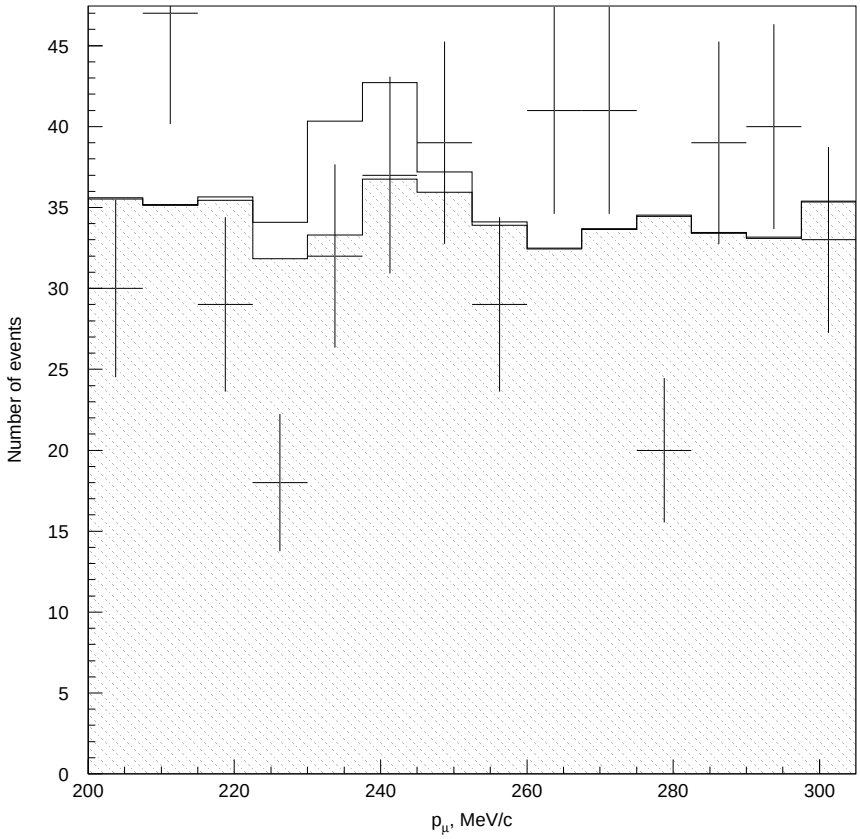

Figure 7.26: The monochromatic μ spectrum for events passing C1-C2, but failing C5, in SK-I. The hatched area is the fitted background from atmospheric neutrinos. The open histogram above it shows the 90% CL upper limit on proton decay events. Crosses display the observed data, in which no excess is seen in the signal region.

physical region, so the 90% CL limit on χ^2 is given by $\chi^2_{90} = \chi^2_{min} + 4.5 = 22.7$. This yields a 90% CL limit on Γ of 4.7×10^{-33} events/proton-year, or a limit on the proton lifetime of 2.1×10^{32} years.

By combining the SK-I and SK-II data together to make a total of 28 bins, a combined fit is performed. In this fit, the minimum χ^2 is 49.5 at $a = 0.97$, $\Gamma = 4.0 \times 10^{-34}$ events/proton-year. This is again in the unphysical region. The

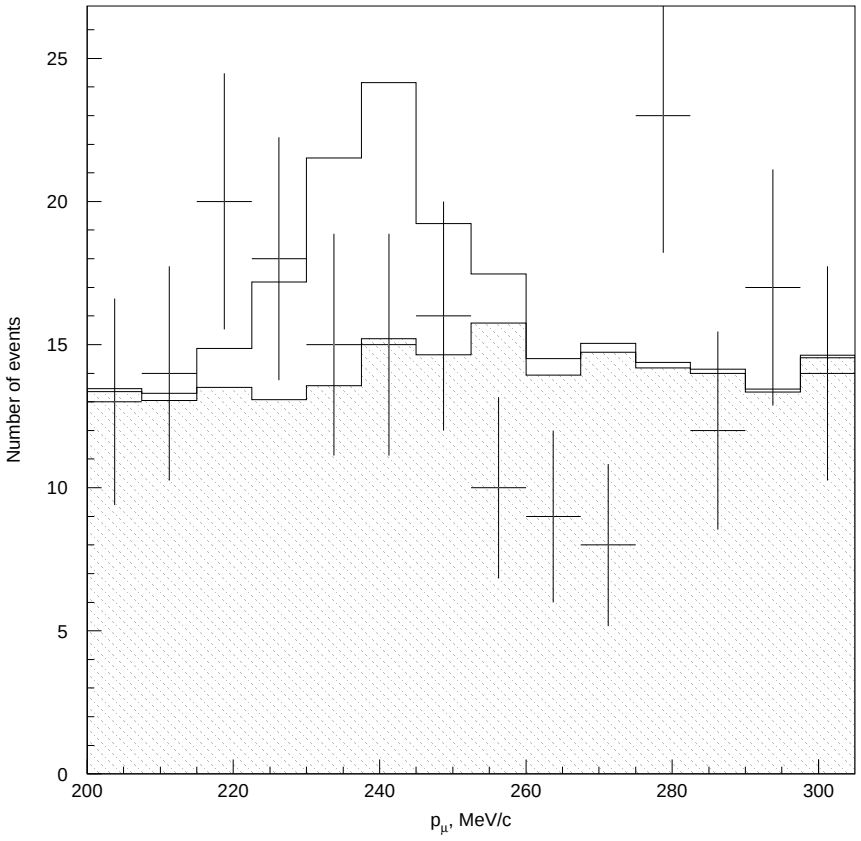

Figure 7.27: The monochromatic μ spectrum for events passing C1-C2, but failing C5, in SK-II. The hatched area is the fitted background from atmospheric neutrinos. The open histogram above it shows the 90% CL upper limit on proton decay events. Crosses display the observed data, in which no significant excess is seen in the signal region.

minimum in the physical region is 49.7 at $a = 0.96$, $\Gamma = 0$. Applying the same prescription as before, $\chi^2_{90} = \chi^2_{min,unphys} + 4.9 = 54.5$, leading to a 90% CL limit on Γ of 1.7×10^{-33} events/proton-year, and hence a limit on the proton lifetime of 5.9×10^{32} years.

7.3.3 $K^+ \to \pi^+\pi^0$

In the decay $p \to \bar{\nu}K^+$, $K^+ \to \pi^+\pi^0$, the resulting π^+ is only barely above Cherenkov threshold, having a momentum of 205 MeV/c. It does not produce enough light to be found by the reconstruction algorithms, but a faint collapsed ring is sometimes visible, as shown in Fig. 7.28. This event view is produced by placing the viewpoint at the event vertex. The detector is then divided into forward and backward hemispheres for display. The π^0 should appear in the forward hemisphere, and the π^+ as a faint collapsed ring in the backward hemisphere. Therefore, this mode is primarily a search for a 205 MeV/c π^0 with some additional light in the opposite direction, plus a decay electron from the π^+.

Initial cuts for this search are defined as

D1. 2 rings

D2. Both rings e-like

D3. One decay electron

D4. 85 MeV/$c^2 < m_\pi <$ 185 MeV/c^2,

where m_π is, as before, the invariant mass of the two rings. In order to eliminate events with faint rings that are not exactly backwards from the π^0, Q_{res} is defined. These are the photoelectrons that cannot be accounted for either by the π^0 or the π^+, and is obtained by adding up all charge more than 90 degrees away from either ring and more than 40 degrees away from the "backwards" direction. That backwards direction is defined as being opposite to the total momentum vector for the two rings. This results in criterion D5:

D5. $Q_{res} < Q_{res,max}$,

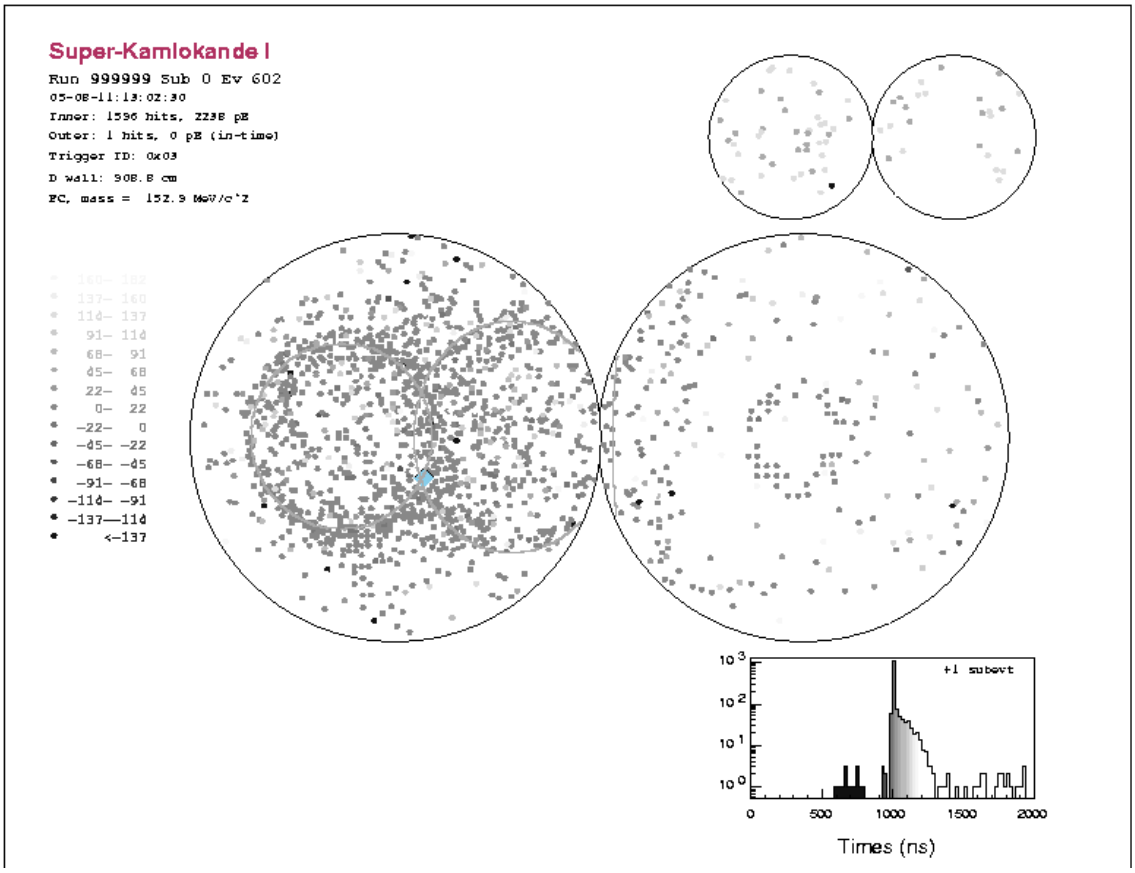

Figure 7.28: An example of a simulated $p \to \bar{\nu} K^+$, $K^+ \to \pi^+ \pi^0$ event. The two e-like rings are on the left, with a faint collapsed ring from the π^+ on the right.

where $Q_{res,max}$ is equal to 70 photoelectrons in SK-I and 35 photoelectrons in SK-II.

A search for a collapsed π^+ ring is applied to events which pass criteria D1-D5. This is accomplished by defining the quantity Q_{back}, which is the total charge in all PMTs within 40 degrees of the backwards direction. With this and the total momentum of the two rings, denoted p_π, two almost-final (an additional D6 will be defined later) criteria are defined:

D7. $175 \text{ MeV}/c < p_\pi < 250 \text{ MeV}/c$

D8. $Q_{back,min} < Q_{back} < Q_{back,max}$,

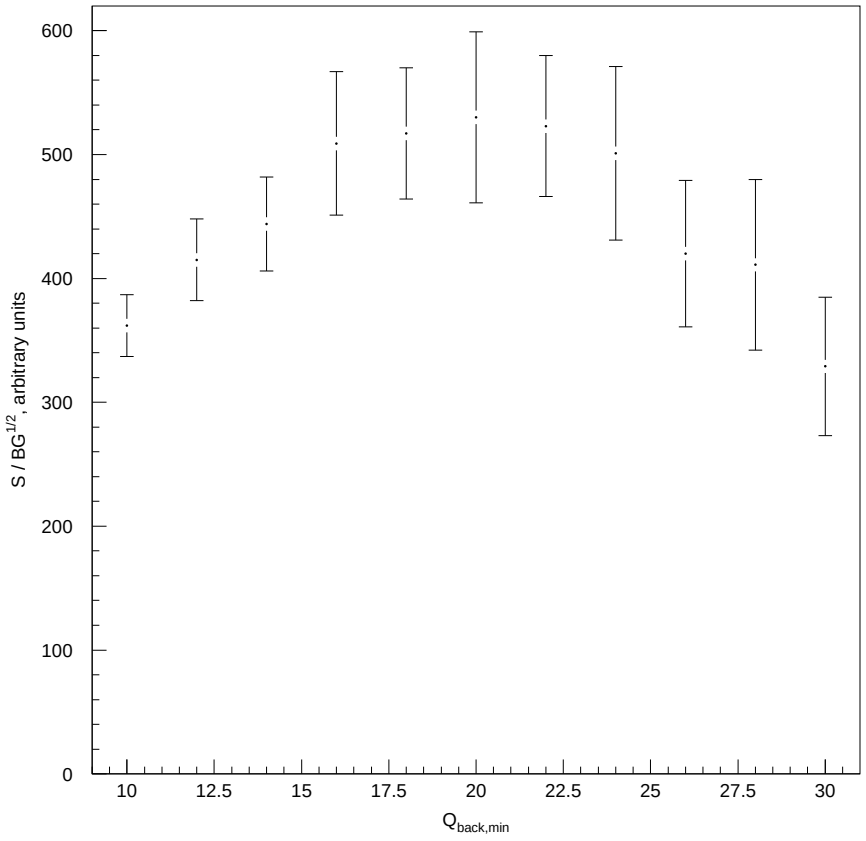

Figure 7.29: $S/\sqrt{BG}$ as a function of $Q_{back,min}$. The error bars represent the statistical uncertainty.

where $Q_{back,min}$ is 40 PE in SK-I and 20 PE in SK-II, and $Q_{back,max}$ is 100 PE in SK-I and 50 PE in SK-II. It is interesting to examine the signal-background ratio as a function of $Q_{back,min}$, as this is a critical cut. This is shown in Fig. 7.29. The optimal cut is indeed at 20, half the SK-I value and in the middle of a broad maximum.

At this point, the efficiency in SK-I is estimated to be 5.7%, with 0.54 background events (0.59 events/100 kiloton-years). Similarly, SK-II is estimated at 5.7% efficiency and 0.51 background events (1.0 events/100 kiloton-years). No events in

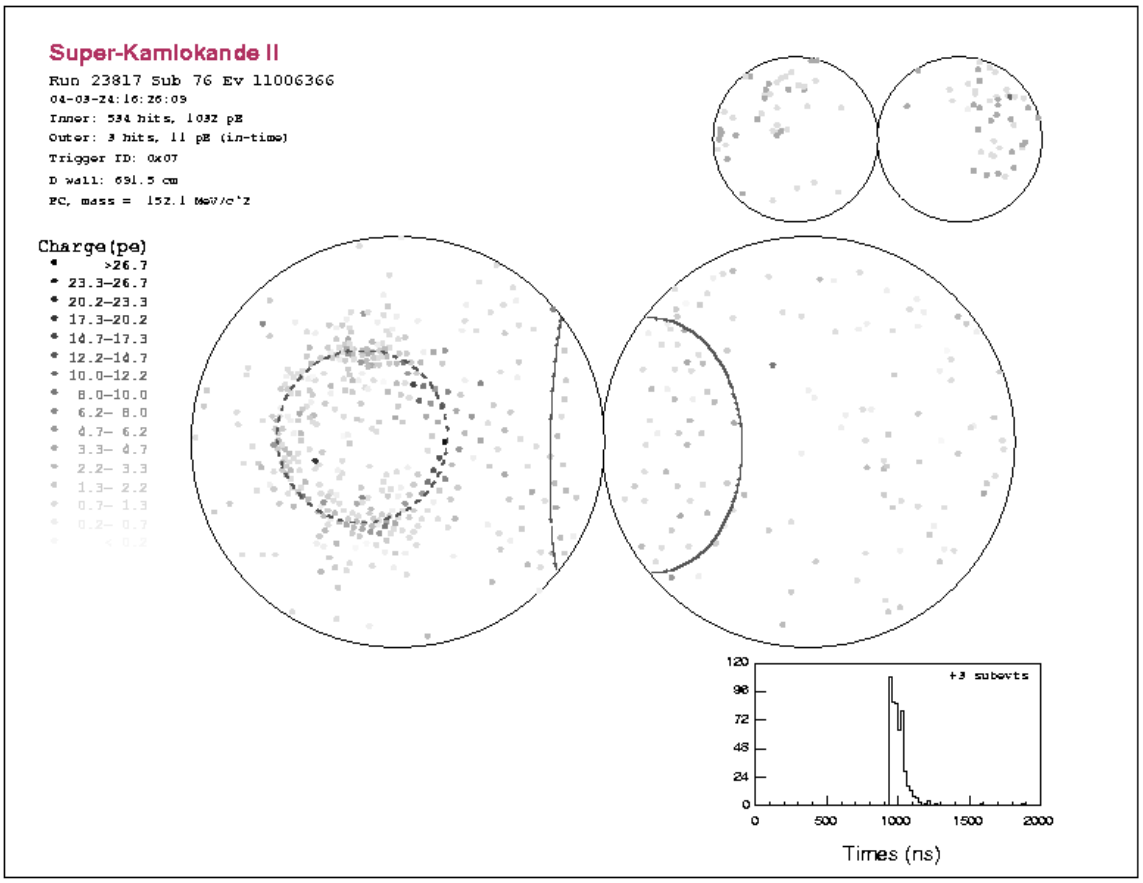

Figure 7.30: An SK-II proton decay candidate passing D1-D5 and D7-D8 with abnormally high portion of Q_{back} in a single PMT.

the SK-I 1489 days dataset pass these cuts.

In previous work, these were the only cuts applied. However, it was observed that a single event in the first 627 days of SK-II data passed criteria D1-D5 and D7-D8. This event, shown in Fig. 7.30, was observed to have an abnormally large proportion of Q_{back}, 7 photoelectrons out of a 22, in a single PMT.

This led to a detailed study of the fraction of Q_{back} contained in a single PMT, which is called F_1. This study started by comparing one-ring sub-GeV atmospheric neutrino events, Monte Carlo versus data, with the backwards direction being op-

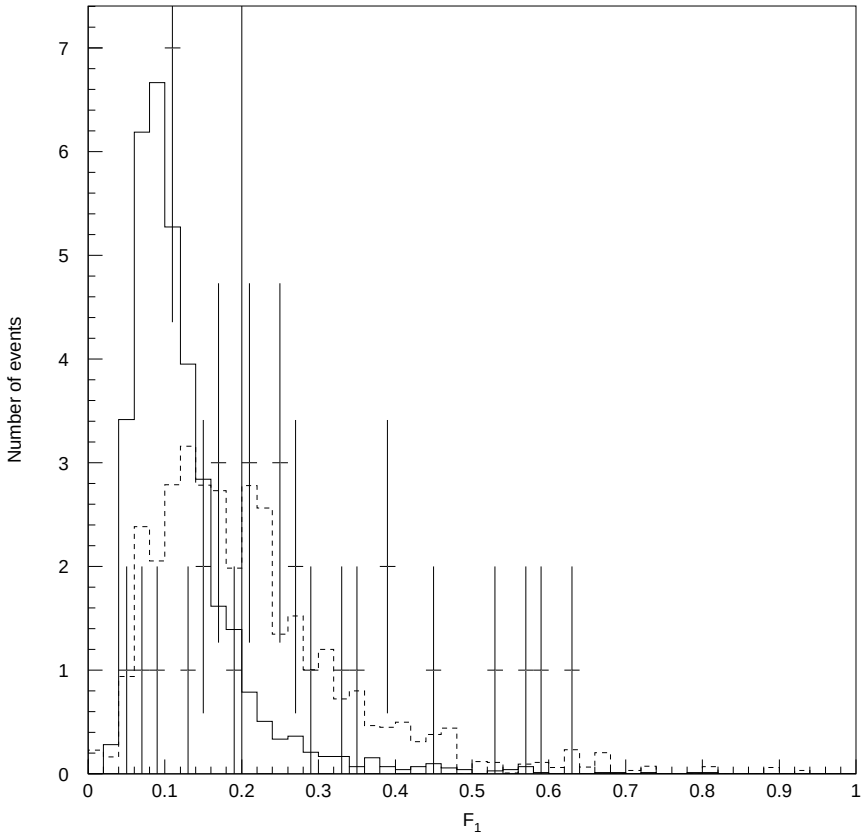

Figure 7.31: F_1 for events passing D1-D5 from SK-I $p \to \bar{\nu}K^+$ (solid) and atmospheric neutrino (dashed) Monte Carlo, plus 1489 days data (crosses). The vertical line indicates cut D6.

posite to the single ring. This is a completely independent data sample to that used in this proton decay search. One-ring sub-GeV events passing D5 and D8 were considered, and compared to the $p \to \bar{\nu}K^+$ Monte Carlo sample. The position of a cut was determined by considering the $p \to \bar{\nu}K^+$ Monte Carlo as the signal S, and the one-ring sub-GeV data events as the background BG, and maximizing $S/\sqrt{BG}$. The distribution of F_1 for events passing D1-D5 is shown in Fig. 7.31.

Two aspects of this plot are particularly notable. First, the background clearly

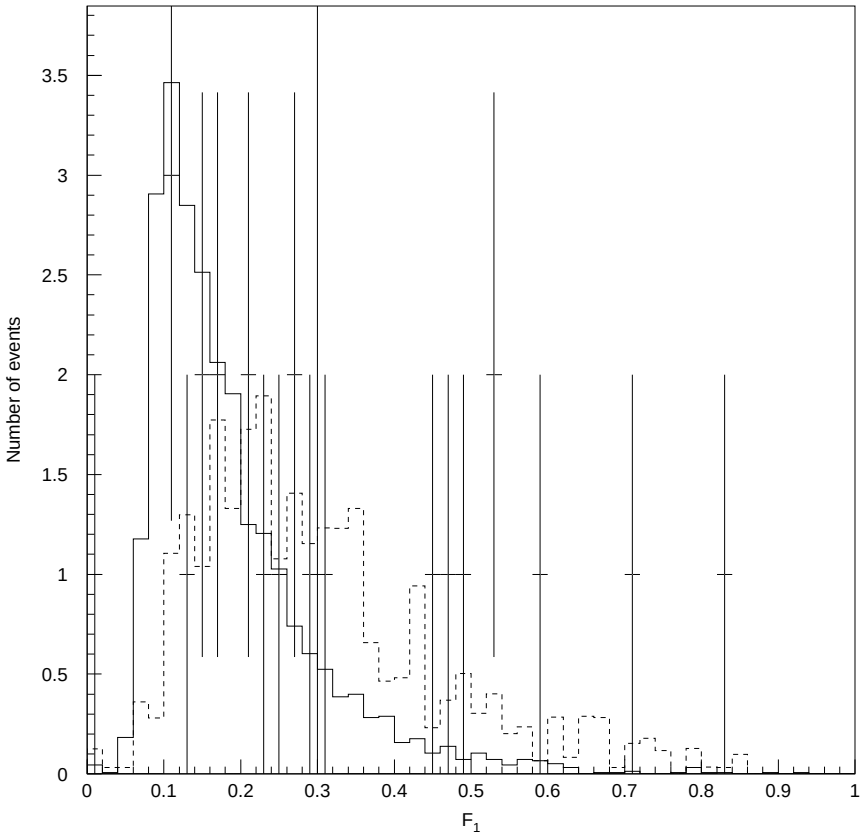

Figure 7.32: F_1 for events passing D1-D5 from SK-II $p \to \bar{\nu}K^+$ (solid) and atmospheric neutrino (dashed) Monte Carlo, plus 804 days data (crosses). The vertical line indicates cut D6.

tends to have higher F_1 than the signal. Therefore, a cut on F_1 will indeed improve the signal/background separation. Also, there is a disagreement between the data and either set of Monte Carlo in the region between 0.3 and 0.6. This discrepancy also seen in SK-II, as shown in Fig. 7.32.

The optimal cuts for signal/background separation in SK-I and SK-II are at 0.2 and 0.3 respectively, using the method described above. These eliminate the region where data and Monte Carlo disagree, so the discrepancy is not a grave concern.

This discrepancy, however, is not well understood. Its source is, as of the time of this work, unknown. Future work will be desirable to isolate the source, and perhaps to improve the Monte Carlo simulation to reflect whatever factor is causing this effect.

While this study was motivated by the candidate, it did not use detailed knowledge of the candidate in determining what cut should be made. Additionally, only 627 days of the SK-II data had been analyzed at the time of the study. The remaining 177 days were not analyzed until the study was complete, and the cuts finalized.

Using F_1, an additional cut D6 is defined:

D6. $F_1 < F_{max}$,

where F_{max} is 0.2 in SK-I and 0.3 in SK-II. Having established the final criteria to be applied in this search, criteria D1-D8 are applied to the SK-I $p \to \bar{\nu}K^+$ and atmospheric neutrino Monte Carlo (see Fig. 7.33). The efficiency and expected background are estimated to be 5.5% and 0.45 events (0.49 events/100 kiloton-years), from 2220 proton decay events and 11 (normalized) NEUT atmospheric neutrino events passing all cuts. So the efficiency is decreased by about 3.5%, but the background is reduced by roughly 25%. This corresponds to an increase of 11% in $S/\sqrt{BG}$. The NUANCE Monte Carlo contains 14 (normalized) events which pass all cuts, which predicts a similar background of 0.58 events (0.63 events/100 kiloton-years). As illustrated in Fig. 7.34, no events in the 1489 days of SK-I data pass criteria D1-D8.

Applying the same criteria to SK-II, as shown in Figs. 7.35 and 7.36, 2137 $p \to \bar{\nu}K^+$ and 13 (normalized) NEUT events pass all cuts. So the efficiency and background for this search are estimated to be 5.4% and 0.46 events (0.93 events/100 kiloton-years), while NUANCE, with 13 (normalized) events passing, predicts 0.47

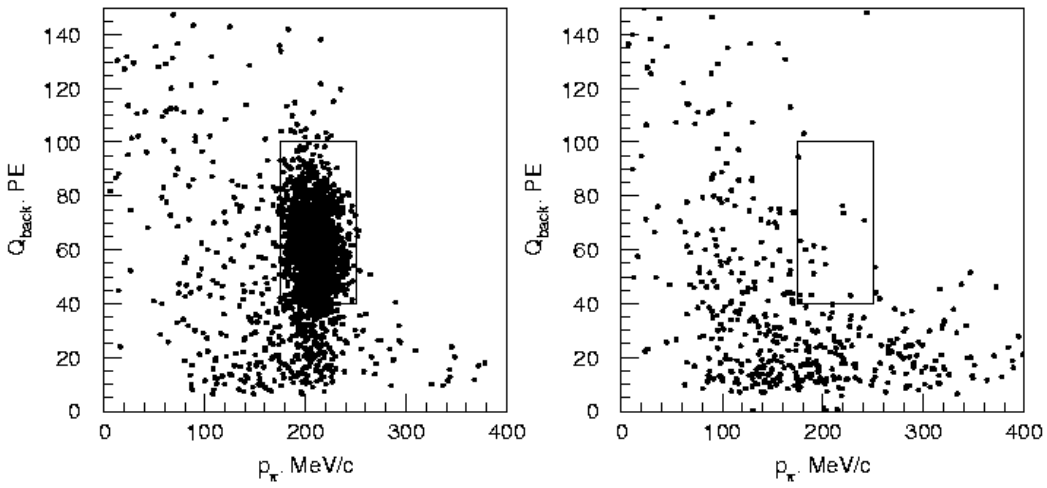

Figure 7.33: Q_{back} vs p_π for events passing D1-D6 from SK-I $p \to \bar{\nu} K^+$ (left) and atmospheric neutrino (right) Monte Carlo. The boxed region is kept by criteria D7-D8.

background events (0.95 events/100 kiloton-years). Two events in the SK-II 804 days dataset pass all cuts.

The first candidate event is shown in Fig. 7.37. This definitely appears to be a π^0 of the correct momentum, as it reconstructs to give $m_\pi = 130$ MeV/c^2 and $p_\pi = 210$ MeV/c, where the expected true values are 135 MeV/$c^2$and 205 MeV/c respectively. However, it has quite low Q_{back}, of only 21 PE, where the threshold is 20. As can be seen in Fig. 7.35, there is a great deal of overlap between signal and background in this region. It passes D1-D8, but is not near the center of the acceptance region.

The second candidate is shown in Fig. 7.38. The reconstructed π^0 mass is 175 MeV/c^2, near the 185 MeV/c^2 upper limit of the acceptance region. This is approximately 1.6 σ away from the central value, as illustrated in Fig. 4.13. However, the backwards hit pattern is not suggestive of a collapsed ring. Based on eye scan of

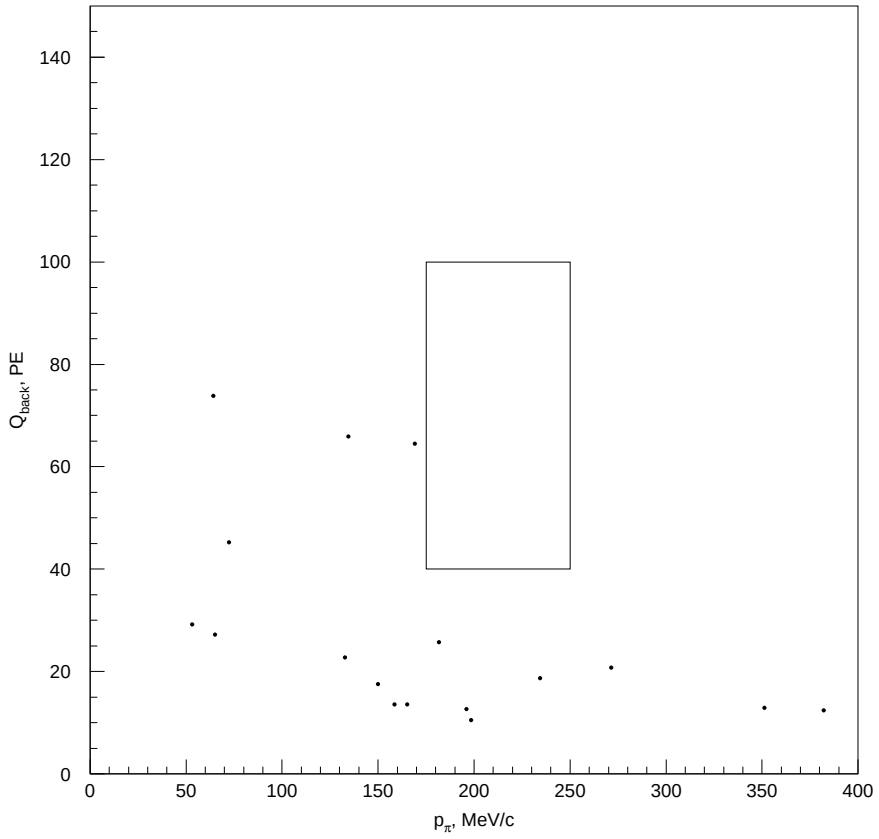

Figure 7.34: Q_{back} vs p_π for events passing D1-D6 from SK-I 1489 days data. The boxed region is kept by criteria D7-D8.

Monte Carlo events, 50% of $K^+ \to \pi^+\pi^0$ proton decay events have a collapsed ring pattern comparable to Fig. 7.28.

There are therefore two candidates in SK-II, against an expected background of only 0.46 events. There is an 8% chance of a statistical fluctuation to two events from that background. Prior to adding cut D6, there are three events against an expected background of 0.51 events. The probability of a fluctuation of this size is 1.5%. A summary of the three events passing D1-D5, D7, and D8 is given in Tbl. 7.7.

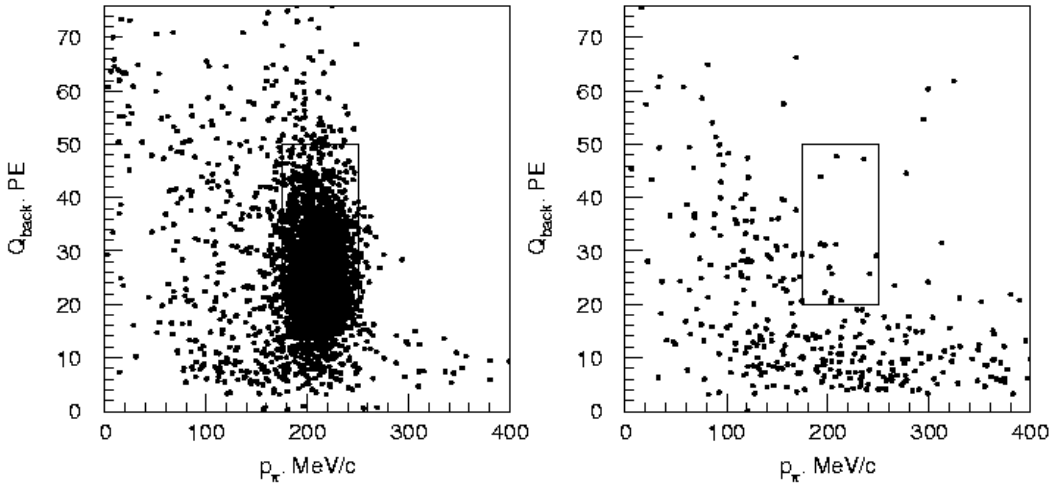

Figure 7.35: Q_{back} vs p_π for events passing D1-D6 from SK-II $p \to \bar{\nu} K^+$ (left) and atmospheric neutrino (right) Monte Carlo. The boxed region is kept by criteria D7-D8.

Variable	Acceptance Range	Candidate 1	Candidate 2	Candidate 3
Run #		23817	25112	25251
Event #		11006366	78066967	19922694
Date		Mar. 24, 2004	May 13, 2005	June 17, 2005
Time (JST)		4:26 PM	1:20 AM	6:51 PM
m_π (MeV/c^2)	85 - 185	152	130	175
p_π (MeV/c)	175 - 250	201	210	195
Q_{back} (PE)	20 - 50	22	21	27
Q_{res} (PE)	0 - 35	14	27	26
F_1	0 - 0.3	0.31*	0.16	0.18

Table 7.7: Summary of events passing D1-D5, D7-D8 for $p \to \bar{\nu} K^+$, $K^+ \to \pi^+ \pi^0$. Starred cuts are failed.

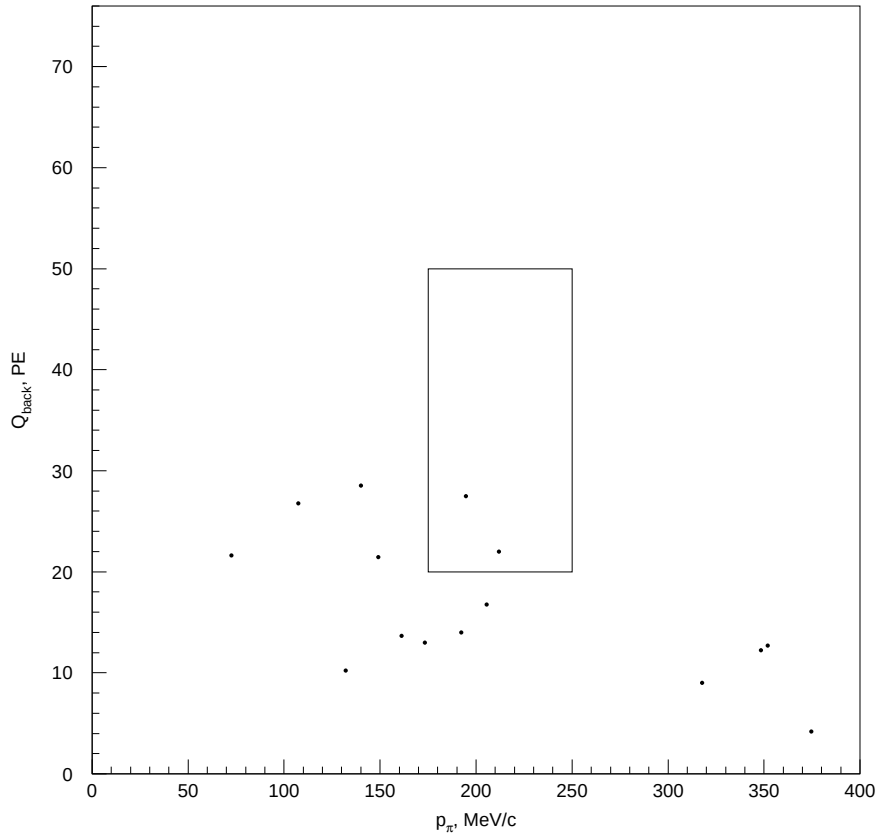

Figure 7.36: Q_{back} vs p_π for events passing D1-D6 from SK-II 804 days data. The boxed region is kept by criteria D7-D8.

The neutrino interaction modes contributing to the background in this mode are shown in Tbl. 7.8. As might be expected when looking for a single π^0 plus a decay electron, single pion production is the dominant background, with almost all of the rest being from multiple pion production.

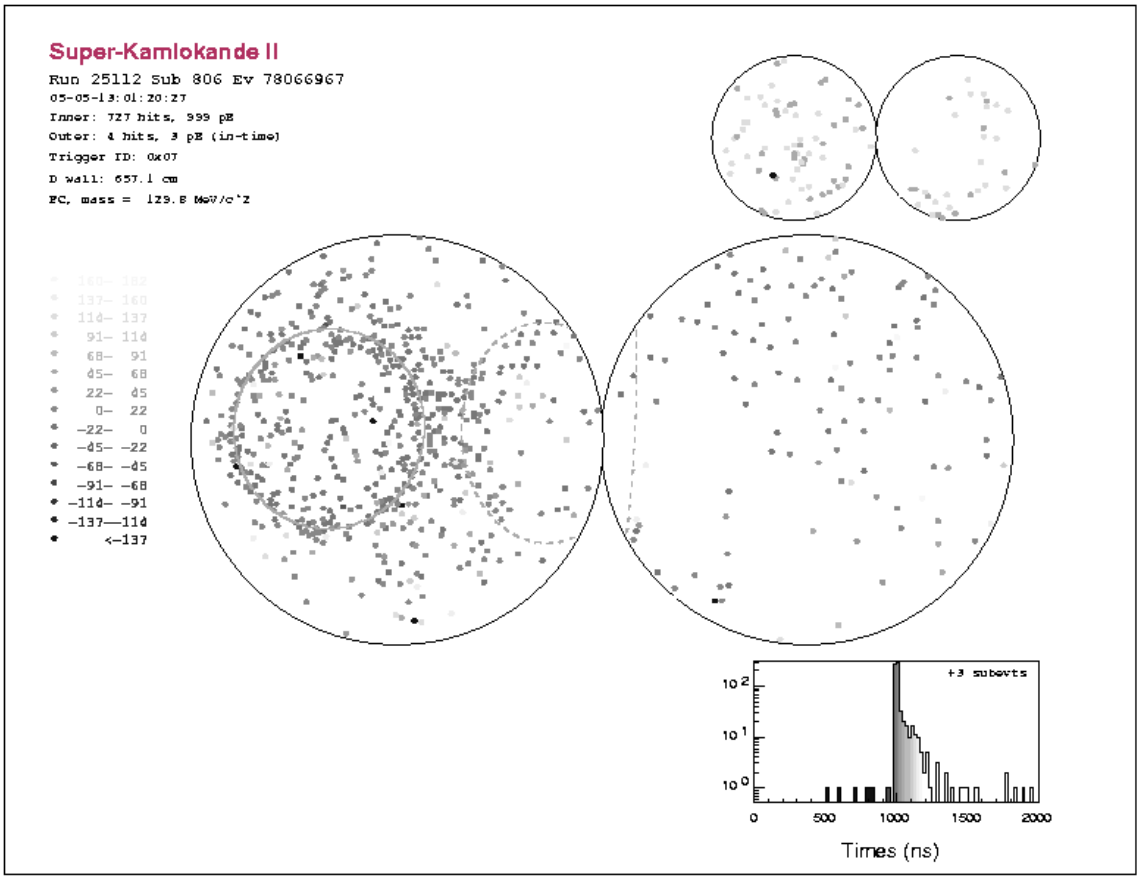

Figure 7.37: The first $p \to \bar{\nu} K^+$, $K^+ \to \pi^+ \pi^0$ candidate event. It has quite low Q_{back}, at 21 PE.

Mode	SK-I NEUT	SK-I NUANCE	SK-II NEUT	SK-II NUANCE
CC single π	57%	35%	50%	29%
CC multi-π	29%	15%	25%	14%
NC single π	0%	25%	0%	0%
NC multi-π	7%	15%	19%	29%
Other	7%	10%	6%	14%
Total BG MC events (unnormalized)	14	20	16	12

Table 7.8: Modes contributing to background for $p \to \bar{\nu} K^+$, $K^+ \to \pi^+ \pi^0$.

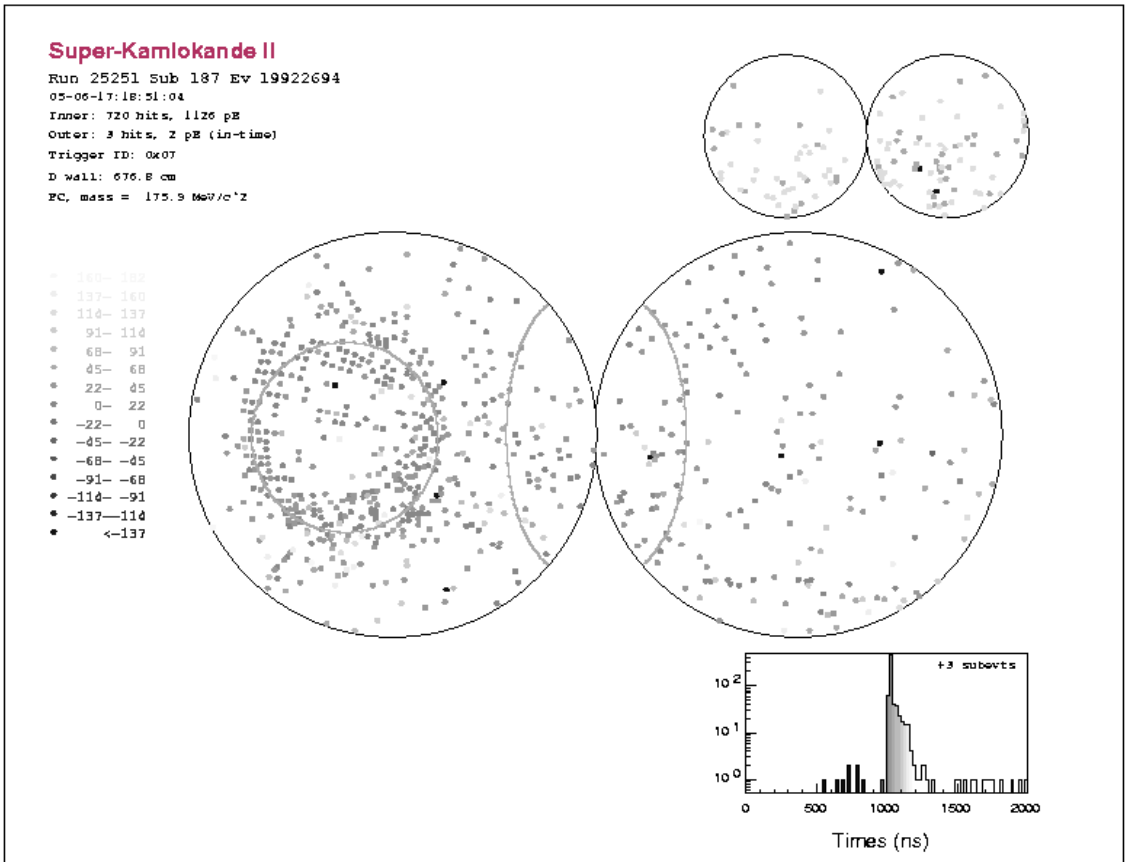

Figure 7.38: The second $p \to \bar{\nu} K^+$, $K^+ \to \pi^+ \pi^0$ candidate event. The π^0 mass is abnormally high at 180 MeV/c^2.

7.3.4 Systematics

For these searches, the systematic uncertainties have previously been studied in [21]. The dominant uncertainties for the $K^+ \to \mu^+ \nu$ with prompt γ search are the probability for prompt γ emission, at 19% uncertainty for both SK-I and SK-II, and the uncertainty due to light scattering. For $K^+ \to \mu^+ \nu$ without prompt γ, they are light scattering and a 2% energy scale uncertainty. The effect of this energy scale uncertainty is calculated in the same way as for $p \to e^+ \pi^0$, by multiplying all fitted momenta by 0.98 and 1.02 and calculating the change in efficiency. For $K^+ \to \pi^+ \pi^0$,

the dominant uncertainties are in the pion-^{16}O cross-section (previously calculated as 4.8% uncertain) and light scattering.

To calculate the systematic uncertainty due to light scattering, $p \to \bar{\nu}K^+$ Monte Carlo is simulated and reconstructed with a 20% increase, and a 20% decrease, in the light attenuation length. The efficiencies for this modified Monte Carlo sample are calculated, and compared to the results of the standard Monte Carlo. Any change in efficiency is taken to be the systematic uncertainty from this effect.

The systematic uncertainties in the background estimates are calculated in exactly the same manner as for the $p \to e^+\pi^0$ search. To determine the uncertainty in the background estimate, three different effects are considered. The first effect is the uncertainty in the Monte Carlo statistics, calculated as the square root of the number of background Monte Carlo events passing all cuts. The uncertainties in neutrino interaction cross-sections for various modes are also considered, with values previously estimated [14] as 10% for quasi-elastic and single meson production, 5% for multiple pion production and deep inelastic scattering, and 30% for coherent pion production. Finally, a 10% uncertainty in the total neutrino flux is assumed.

7.3.5 Limits

With the extended set of cuts, two candidates for $p \to \bar{\nu}K^+$, $K^+ \to \pi^+\pi^0$ proton decay exist in the final SK-II data sample, compared to an expected background of 0.46 ± 0.13 events. Applying the methods of Appendix C to the $K^+ \to \pi^+\pi^0$ and $K^+ \to \mu^+\nu$ with prompt γ tag searches, a combined limit on the partial lifetime into $p \to \bar{\nu}K^+$ is derived to be 1.5×10^{33} years. Due to the two candidates in SK-II and the separation of the monochromatic μ search (which was, in prior work, combined with the others), this limit is weaker than the limit from SK-I alone as published in

	Efficiency (%)	BG (# events)	Data (# events)	Limit ($\times 10^{32}$ yrs)
SK-I				
$\mu^+\nu$ w/ γ	8.4 (20%)	0.66 (28%)	0	10
$\pi^+\pi^0$	5.5 (8.2%)	0.54 (32%)	0	7.2
Combined	13.9 (13%)	1.12 (21%)	0	18
$\mu^+\nu$ w/o γ	-	-	-	5.3
SK-II, old cuts				
$\mu^+\nu$ w/ γ	4.7 (22%)	0.67 (30%)	2	0.15
$\pi^+\pi^0$	5.7 (6.8%)	0.51 (31%)	3	0.14
Combined	10.4 (9.3%)	1.21 (28%)	5	1.0
SK-II, new cuts				
$\mu^+\nu$ w/ γ	3.2 (22%)	0.04 (96%)	0	2.2
$\pi^+\pi^0$	5.4 (6.7%)	0.46 (28%)	2	0.18
Combined	8.6 (9.2%)	0.50 (27%)	2	2.9
$\mu^+\nu$ w/o γ	-	-	-	2.1
SK-I+II				
Combined, old cuts	12.7 (11%)	2.3 (19%)	5	0.20
Combined, new cuts	12.0 (10%)	1.7 (17%)	2	15
$\mu^+\nu$ w/o γ	-	-	-	5.9

Table 7.9: Summary of results for $p \to \bar{\nu}K^+$. Systematic uncertainties are in parentheses.

[21]. The results from all searches are summarized in Tbl. 7.9.

If the new cuts (C7-9 and D6) are not made, the SK-I combined limit does not change appreciably, and remains 1.8×10^{33} years. Since SK-II then has three candidates for the $K^+ \to \pi^+\pi^0$ search and two for the prompt γ search, the SK-II combined limit is 0.20×10^{33} years, with the limits from the individual searches being 0.14×10^{33} years for $K^+ \to \pi^+\pi^0$ and 0.15×10^{33} years for $K^+ \to \mu^+\nu$ with prompt γ. The combined SK-I+II limit in this case then becomes 1.0×10^{33} years, weaker than the original SK-I limit.

If the five events in the SK-I+II $K^+ \to \pi^+\pi^0$ and prompt γ searches using the old cuts, minus the total 2.3 expected background events, is supposed to be a proton

decay signal of 2.7 events, then this may be calculated as a lifetime τ_p using the relation:

$$\tau_p = \frac{n_p}{n_{obs}} \sum_i \epsilon_i \lambda_i \tag{7.7}$$

where n_p is the number of protons, n_{obs} the number of observed events, ϵ_i the efficiency of each search, and λ_i the live time for that search. This yields a proton lifetime of 1.2×10^{33} years, which is not ruled out by the monochromatic μ search. It is, however, inconsistent with the prior SK-I result.

Performing the same calculation with the new cuts, τ_p is determined to be 2.8×10^{33} years. Again, this is consistent with the monochromatic μ search. It is also consistent with the prior SK-I result.

It is also interesting to consider the probability that no candidates will appear in the SK-I data if the proton lifetime is assumed to be as suggested by the above analysis. With the lifetime of 1.2×10^{33} years as in the analysis without the new cuts, then the expected number of events in the SK-I prompt γ search would be 5.8. The probability of observing 0 events from this expected rate is 0.3%. Similarly, the expected number of events in the SK-I $K^+ \to \pi^+\pi^0$ search would be 3.8. The probability of observing 0 events in this case is 2.1%. So the rate of events seen in SK-I+II using this unbiased extension of the previous analysis is not supported by the SK-I dataset alone. The rate is perhaps due to an underestimate of the background in SK-II where the detector and analysis performance for small numbers of hits is weaker than SK-I.

As previously discussed, the probability that the expected background of 0.46 events in the SK-II $K^+ \to \pi^+\pi^0$ search will result in at least 3 candidates is 1.5%, while the probability of getting at least 2 candidates from the expected background

of 0.67 events in the prompt γ search is 15%. So, the chance that the observed rate is due to the estimated background is small but non-negligible in the analysis without new cuts. One of the prompt γ candidates appears weak by a visual scan, and all three $K^+ \to \pi^+\pi^0$ candidates are close to the edge of an acceptance region. So overall, the quality of the candidates and the statistical case do not support a discovery of proton decay via $p \to \bar{\nu}K^+$.

Considering the new cuts developed here, the efficiency and background are both reduced. But, the total SK-II $S/\sqrt{BG}$ is improved by 29%. With these cuts, there are no candidates in the prompt γ search, and two in the $K^+ \to \pi^+\pi^0$ search, both of which are, again, near the edge of an acceptance region. The probability of observing at least two candidates from the predicted background of 0.46 events is 8%.

If the proton lifetime were 2.8×10^{33} years as calculated above, then the expected number of events in the SK-II prompt γ search would be 0.91. The probability of observing 0 events from this rate is 40%. For the SK-I prompt γ search, the expected number of events would be 4.4, which has a 1.2% chance of resulting in 0 candidates. For the SK-I $K^+ \to \pi^+\pi^0$ search, the expectation would be 3.0 events, with a corresponding probability of 4.9% for getting no candidates. So the chance that these rates would be due to proton decay is small but non-negligible. However, the probability of observing these events from background is sizable, at 8%. Therefore, this tighter analysis also does not support a statistically significant signal for proton decay via $p \to \bar{\nu}K^+$.

7.4 $p \to \bar{\nu}K^*(892)^+$

The decay $p \to \bar{\nu}K^*(892)^+$ is very closely related to $p \to \bar{\nu}K^+$. The rate for these decays is expected to differ only by a phase space factor due to the greater mass of

the $K^*(892)^+$ relative to the K^+. Due to this factor, the rate for $p \to \bar{\nu}K^*(892)^+$ should be about an eighth the rate for $p \to \bar{\nu}K^+$. This difference is not so great that an efficient, low-background search for $p \to \bar{\nu}K^*(892)^+$ could not potentially provide a significant indirect improvement of the limit on $p \to \bar{\nu}K^+$.

The $K^*(892)^+$ in the decay $p \to \bar{\nu}K^*(892)^+$ is exceedingly short-lived, and decays almost immediately to a kaon and a pion with a branching ratio of nearly 100%. These decay particles can be $K^0_S\pi^+$, $K^0_L\pi^+$, or $K^+\pi^0$ with equal probability. The last possibility is expected to provide the cleanest signal of the three. This is because a π^0 produces a much clearer signal than a 290 MeV/c π^+. Additionally, K^0_L generally interacts in the water before decaying, presenting an additional difficulty. So, this search will concentrate on the $K^+\pi^0$ channel.

$p \to \bar{\nu}K^*(892)^+$, $K^*(892)^+ \to K^+\pi^0$ is much like the mode $p \to \bar{\nu}K^+$. The only difference is the presence of the π^0, which appears on the order of $\tau_{K^+} = 12$ ns before the decay of the K^+. It is therefore conceptually similar to the prompt γ discussed in Sec. 7.3, only very much brighter. Given the power of the prompt γ signal to eliminate background, the prompt π^0 may also work to make this search very powerful.

As in the $p \to \bar{\nu}K^+$ case, the two K^+ decay modes $K^+ \to \mu^+\nu$ and $K^+ \to \pi^+\pi^0$ are studied independently. 6000 $p \to \bar{\nu}K^*(892)^+$ Monte Carlo events are generated for each of SK-I and SK-II, with 4604 fiducial events in SK-I and 4623 in SK-II.

7.4.1 $K^+ \to \mu^+\nu$

In this mode, the search is for a π^0 of momentum 309 MeV/c and a μ^+ of momentum 236 MeV/c. Such an event is shown in Fig. 7.39. The initial selection criteria are:

E1. Two or three rings

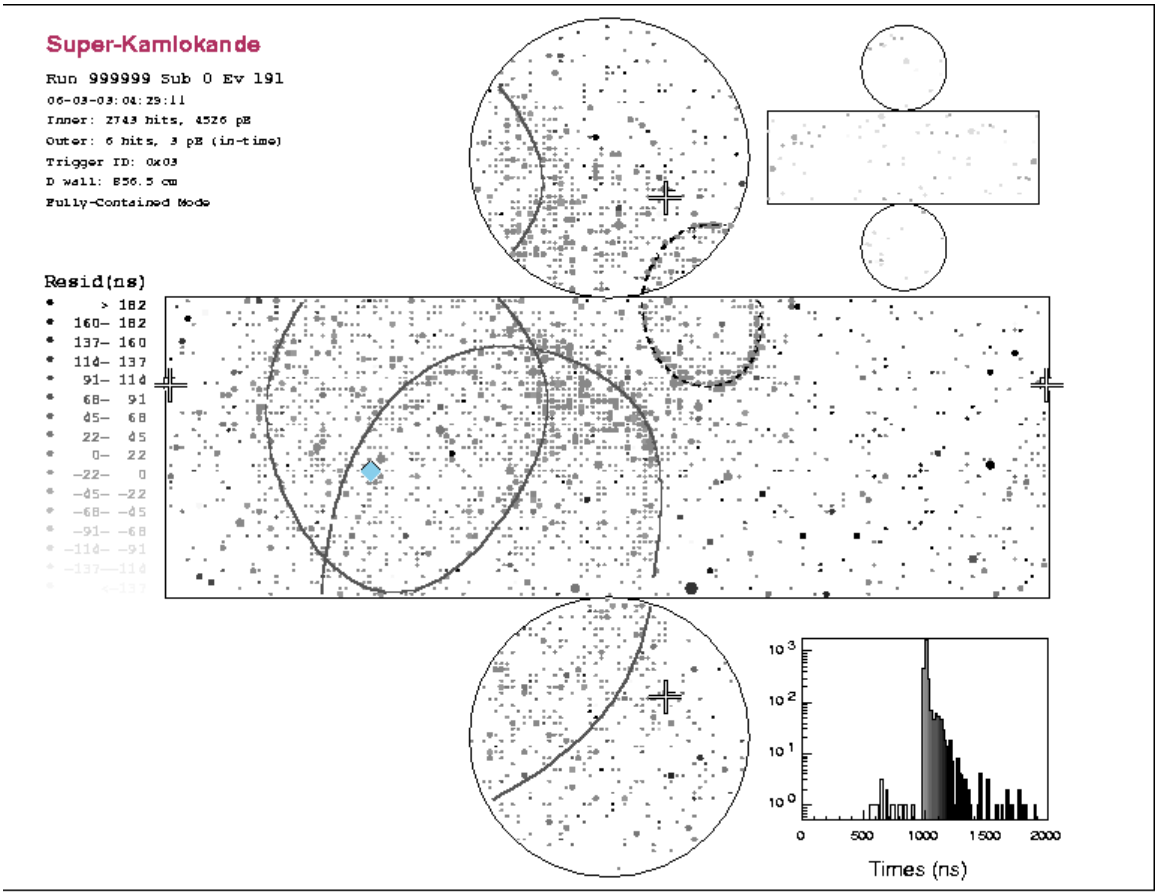

Figure 7.39: An example of a simulated $p \to \bar{\nu} K^*(892)^+$, $K^+ \to \mu^+ \nu$ event. Two e-like rings from the π^0 are visible to the left, and the single μ-like ring from the μ^+ is to the right.

E2. Exactly one μ-like ring

E3. One decay electron

E4. 85 MeV/$c^2 < m_\pi <$ 185 MeV/c^2 (3 ring events only).

Criterion E4 is applied only to three-ring events, where m_π is the total invariant mass of the two e-like rings. These criteria select events containing only a μ^+ and a π^0.

Since the μ^+ should be delayed relative to the π^0 by the K^+ lifetime of 12 ns, the next step in the analysis is an attempt to detect this delay. Since the π^0 is so much brighter than the prompt γ from $p \to \bar{\nu}K^+$, different methods are necessary to find it. Here, this is done by calculating a "time signature likelihood" L_{ts}.

This likelihood is based on two variables. The first is the goodness of the vertex fit from "afit," as described in Sec. 5.2.1. This goodness effectively measures how well the PMT hit times fit the hypothesis that all the light was emitted at one time from a single point. Due to the K^+ lifetime, this hypothesis is false for $p \to \bar{\nu}K^*(892)^+$ events. This leads to a generally lower goodness, as illustrated in Fig. 7.40.

The second variable considered for L_{ts} is the "cone time difference" ΔT_{cone}. To calculate this difference, two sets of PMT hits are chosen. One set consists of all hits within 45 degrees of the μ-like ring that are also more than 45 degrees away from either e-like ring – effectively, the hits that can confidently be attributed to the μ^+. The second set, conversely, consists of all hits within 45 degrees of either e-like ring that are also more than 45 degrees away from the μ-like ring, and is interpreted as the hits due to the π^0.

Then, the leading edge of the time distribution for each set of hits is determined, using the same procedure as the $p \to \bar{\nu}K^+$ prompt γ search uses to define t_μ. ΔT_{cone} is defined as

$$\Delta T_{cone} = T_\mu - T_e, \tag{7.8}$$

where $T_{\mu(e)}$ are the times for the hits associated with the μ-like (e-like) ring or rings.

The distribution of ΔT_{cone} is shown in Fig. 7.41. While it is generally larger for the $p \to \bar{\nu}K^*(892)^+$ sample, it is certainly not a 12 ns exponential decay. This is due to the limitations of the vertex fit algorithms, which are not designed to deal with

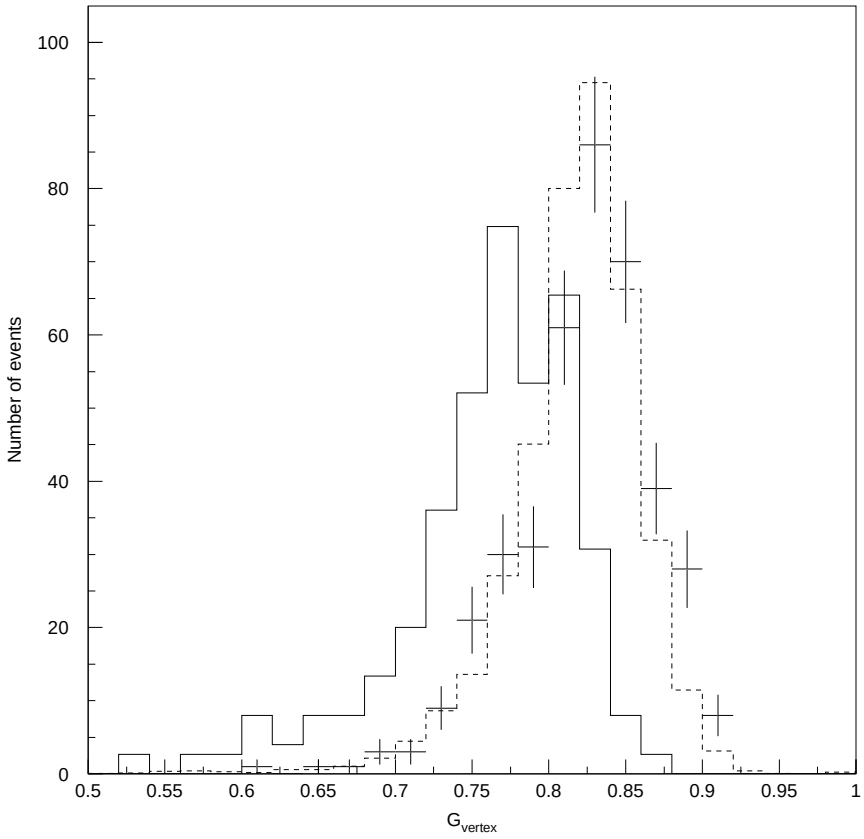

Figure 7.40: The "afit" goodness for events passing E1-E4 for $p \to \bar{\nu}K^*(892)^+$ (solid) and atmospheric neutrino (dashed) Monte Carlo, plus data, in SK-I.

the possibility that the light in the event was actually emitted at two distinct times. So, these algorithms naturally search for a vertex that minimizes ΔT_{cone}. Despite this shortcoming, there remains enough difference to be useful.

Based on these two variables, L_{ts} is calculated. First, samples of $p \to \bar{\nu}K^*(892)^+$ and atmospheric neutrino Monte Carlo which pass E1-E4, but are independent of the samples used for the actual analysis, are analyzed to determine the probability density function (PDF) of each variable for the signal and background. This is done

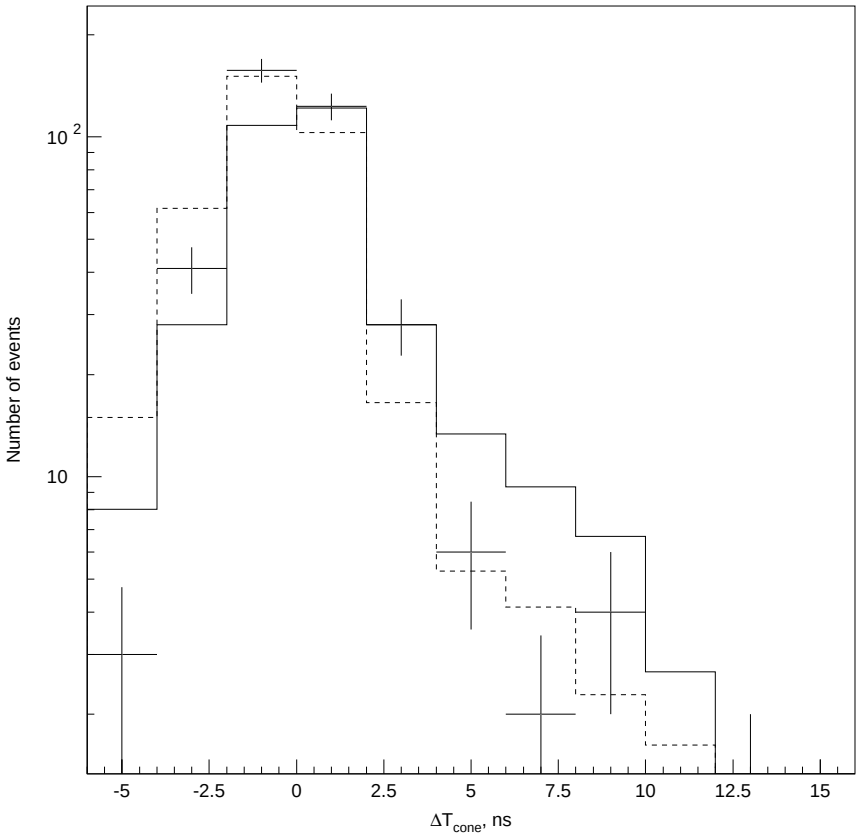

Figure 7.41: ΔT_{cone} for events passing E1-E4 for $p \to \bar{\nu} K^*(892)^+$ (solid) and atmospheric neutrino (dashed) Monte Carlo, plus data, in SK-I.

independently for SK-I and SK-II. L_{ts} is then defined as:

$$\begin{aligned} L_{ts} &= \log[P_{good}^{signal}(G_{vertex})] - \log[P_{good}^{BG}(G_{vertex})] + \\ &\quad \log[P_{\Delta T}^{signal}(\Delta T_{cone}] - \log[P_{\Delta T}^{BG}(\Delta T_{cone})], \end{aligned} \tag{7.9}$$

where $P(x)$ is the probability of observing a value x for the particular variable and sample. The distribution of L_{ts} is shown in Fig. 7.42.

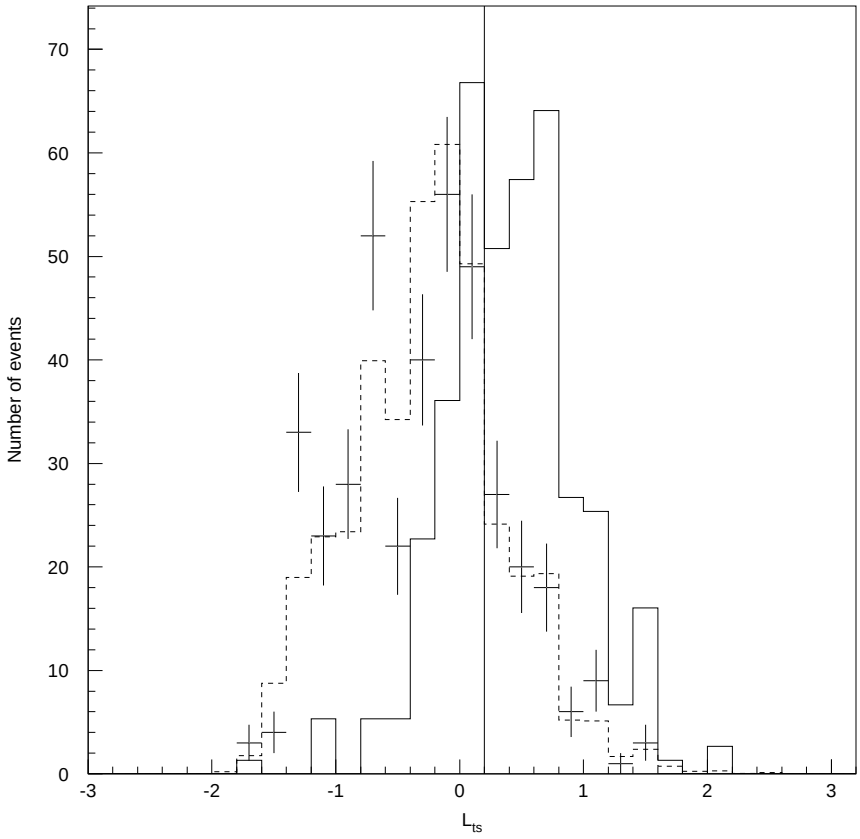

Figure 7.42: L_{ts} for events passing E1-E4 for $p \to \bar{\nu} K^*(892)^+$ (solid) and atmospheric neutrino (dashed) Monte Carlo, plus data (crosses), in SK-I. The vertical line represents criterion E5.

The next selection criteria are defined, by selecting values to maximize the signal-background separation, as

E5. $L_{ts} > 0.2$

E6. 100 MeV/c $< p_\mu <$ 250 MeV/c

E7. 250 MeV/c $< p_\pi <$ 370 MeV/c,

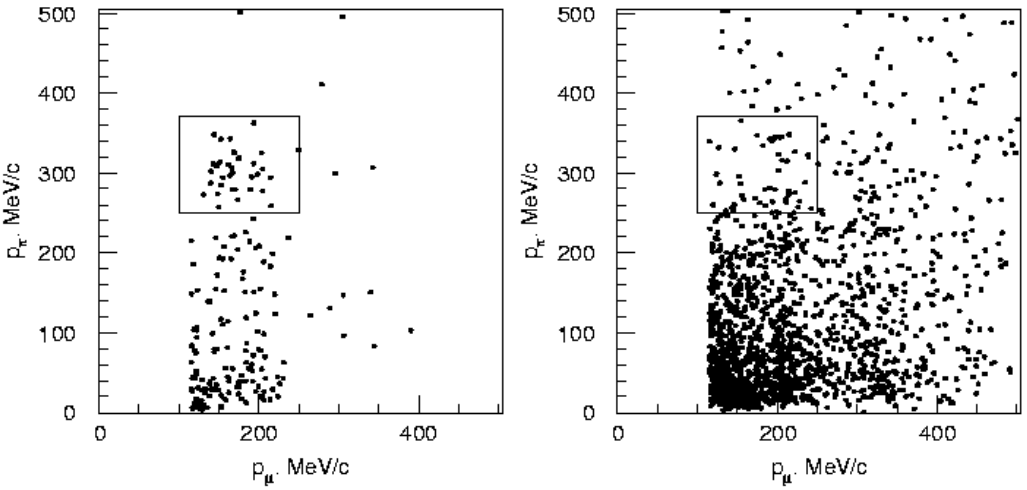

Figure 7.43: p_π vs. p_μ for events passing E1-E5 for $p \to \bar{\nu} K^*(892)^+$ (left) and atmospheric neutrino (right) Monte Carlo, in SK-I. The boxed region is kept by criteria E6-E7.

where p_μ is the momentum of the μ-like ring and p_π is the total momentum of the e-like rings. The distributions of these momenta are shown in Fig. 7.43.

It should be noted that E6 is not centered on the true value of the μ^+ momentum, 236 MeV/c. As Fig. 7.43 shows, the μ^+ is almost always reconstructed lower than its true value. This is believed to be due to a systematic effect of the momentum fitting, where it wrongly assigns some of the charge from the relatively faint μ^+ to the much brighter π^0. However, criterion E6 is adjusted to compensate for this effect.

By passing the SK-I $p \to \bar{\nu} K^*(892)^+$ and atmospheric neutrino Monte Carlo samples through criteria E1-E7, it is found that 35 proton decay events, and 40 (normalized) NEUT atmospheric neutrino events, pass the cuts, so the detection efficiency and background for this mode in SK-I are estimated to be 0.76% and 1.6 events (1.8 events/100 kiloton-years), respectively. The NUANCE Monte Carlo predicts a

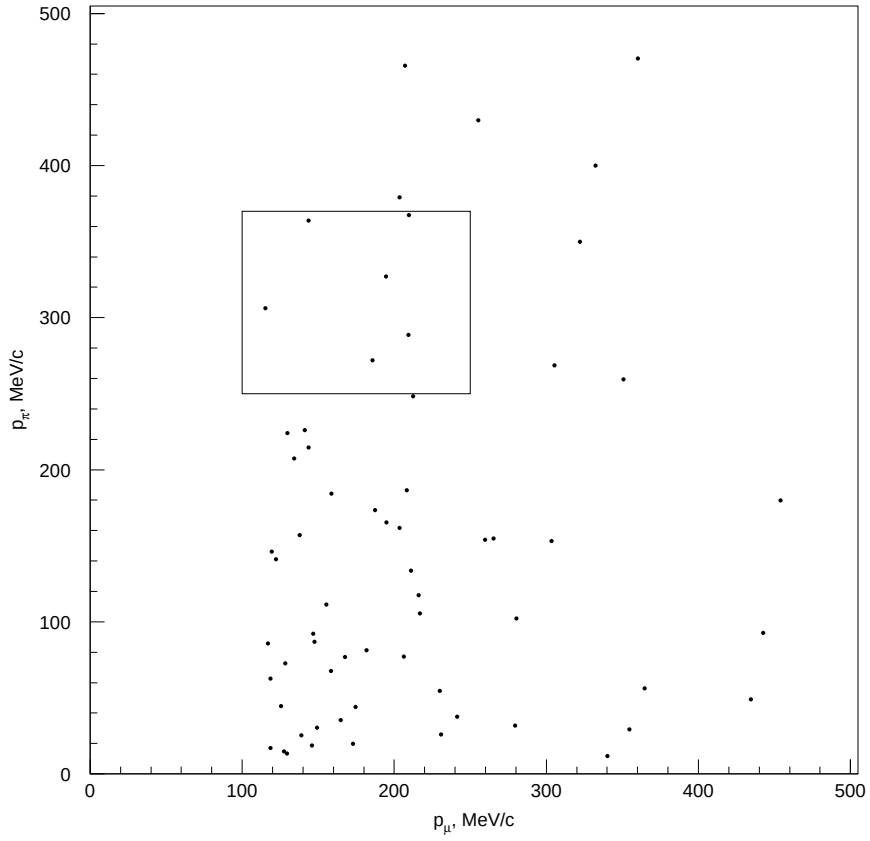

Figure 7.44: p_π vs. p_μ for events passing E1-E5 for SK-I 1489 days data. The boxed region is kept by criteria E6-E7.

similar background of 1.6 events, with 39 (normalized) events passing all cuts. Six events are found in the 1489 days data sample from SK-I (Fig. 7.44). The probability of a statistical fluctuation from 1.6 events up to 6 events is 0.6%.

Applying the same criteria to SK-II (Figs. 7.45 and 7.46), the detection efficiency and background are estimated to be 1.0% and 2.0 events (4.1 events/100 kiloton-years), from 48 $p \to \bar{\nu} K^*(892)^+$ and 56 (normalized) NEUT atmospheric neutrino events which pass all cuts. 54 (normalized) events in the NUANCE sample pass,

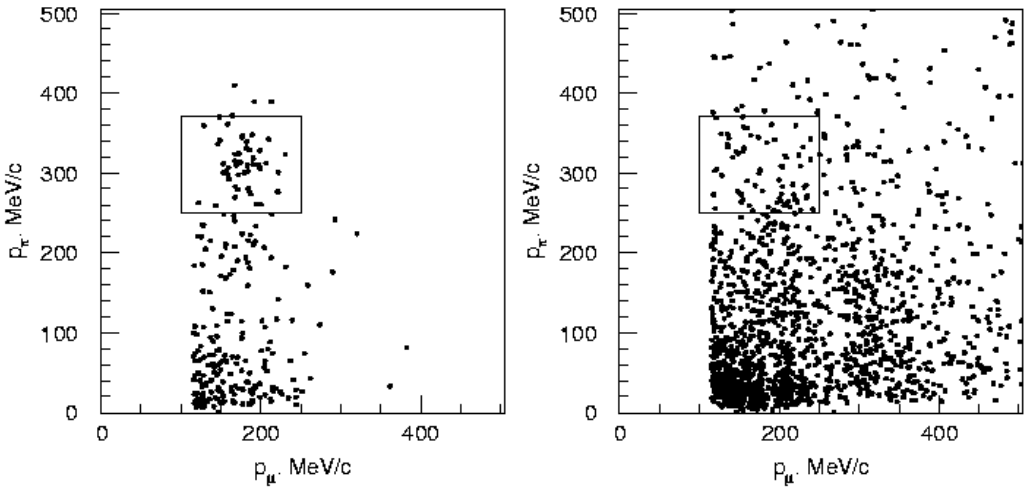

Figure 7.45: p_π vs. p_μ for events passing E1-E5 for $p \to \bar{\nu} K^*(892)^+$ (left) and atmospheric neutrino (right) Monte Carlo in SK-II. The boxed region is kept by criteria E6-E7.

	Efficiency (%)	NEUT BG (# events)	NUANCE BG (# events)	Data (# events)
SK-I	0.76	1.6 (20%)	1.6	6
SK-II	1.0	2.0 (18%)	2.0	2

Table 7.10: Summary of results for $p \to \bar{\nu} K^*(892)^+$, $K^+ \to \mu^+ \nu$ with time signature. Background uncertainties for NEUT are in parentheses.

which also predicts 2.0 events. Two events are found in the 804 days data sample.

The SK-I and SK-II results are tabulated in Tbl. 7.10.

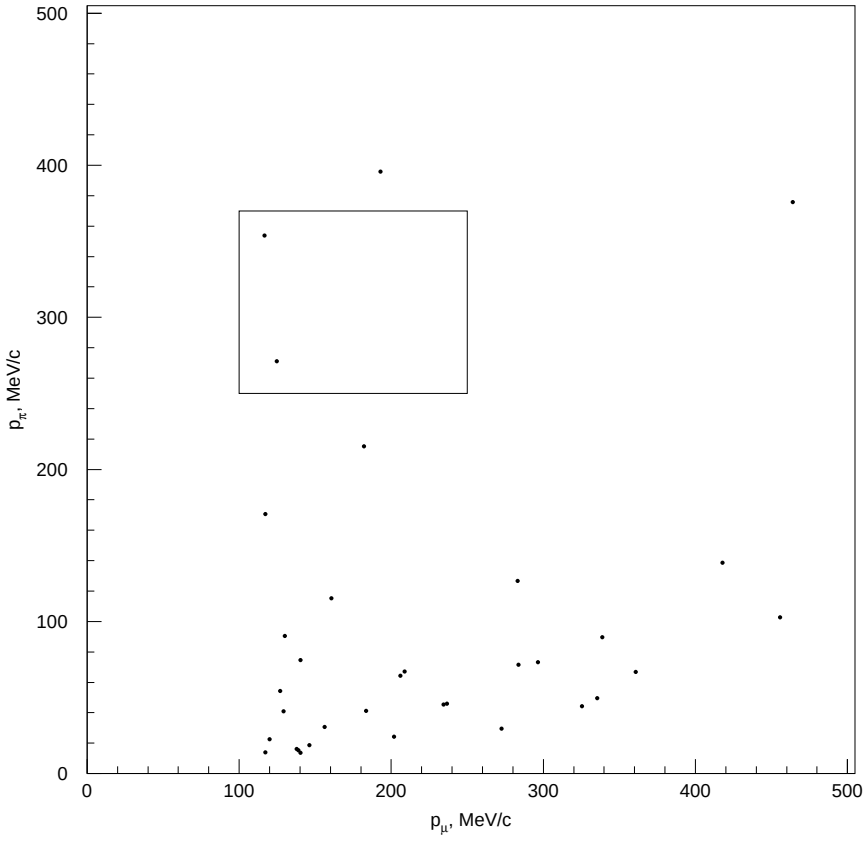

Figure 7.46: p_π vs. p_μ for events passing E1-E5 for SK-II 804 days data. The boxed region is kept by criteria E6-E7.

Mode	SK-I NEUT	SK-I NUANCE	SK-II NEUT	SK-II NUANCE
CC single π	46%	68%	59%	70%
CC multi-π	14%	7%	14%	3%
NC single π	16%	2%	4%	2%
NC multi-π	8%	9%	9%	17%
Other	16%	14%	12%	8%
Total BG MC events (unnormalized)	50	44	69	60

Table 7.11: Modes contributing to background for $p \to \bar{\nu} K^*(892)^+$, $K^+ \to \mu^+ \nu$ with time signature.

	Efficiency (%)	NEUT BG (# events)	NUANCE BG (# events)	Data (# events)
SK-I	1.9	18 (12%)	16	10
SK-II	1.7	7.0 (13%)	7.4	8

Table 7.12: Summary of results for $p \to \bar{\nu} K^*(892)^+$, $K^+ \to \mu^+ \nu$ without time signature. The uncertainty on the NEUT background is in parentheses.

The neutrino interaction modes contributing to the background in this search are shown in Tbl. 7.11. A substantial majority of the background is from charged-current single pion production. Since this search seeks a μ^+ plus a π^0, this is expected.

Due to the low efficiency of criterion E5, those events passing E1-E4, but failing E5, are also used. The requirement that E5 be failed ensures that the samples are statisically independent. Similarly to criteria E6-E7, additional kinematic criteria are defined:

E8. 100 MeV/$c < p_\mu <$ 225 MeV/c

E9. 0 MeV/$c < p_\pi <$ 350 MeV/c.

Figs. 7.47 and 7.48 show p_μ and p_π for SK-I, and 7.49 and 7.50 for SK-II. The results are tabulated in Tbl. 7.12.

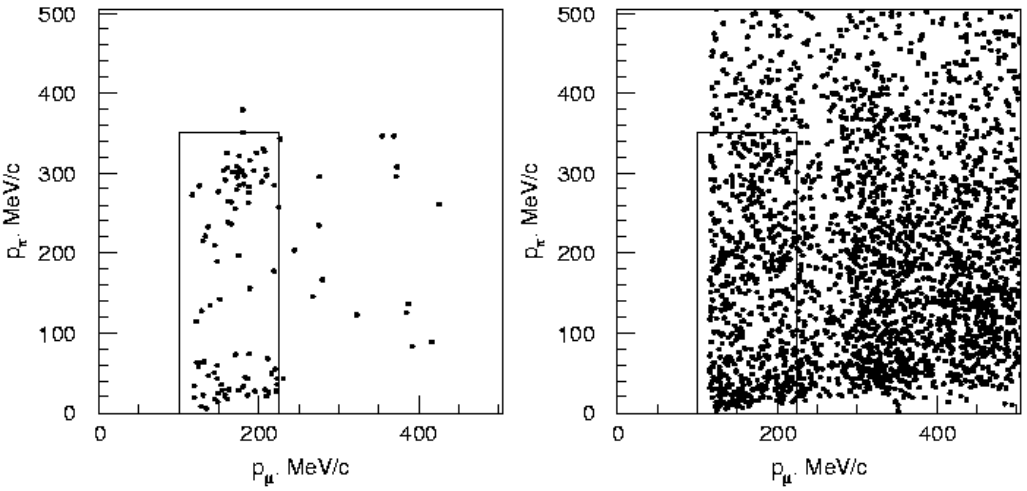

Figure 7.47: p_π vs. p_μ for events passing E1-E4, but failing E5, for $p \to \bar{\nu} K^*(892)^+$ (left) and atmospheric neutrino (right) Monte Carlo in SK-I. The boxed region is kept by criteria E8-E9.

The neutrino interaction modes contributing to the background in this search are shown in Tbl. 7.13. As in the search with time signature, the background is dominated by CC single pion production.

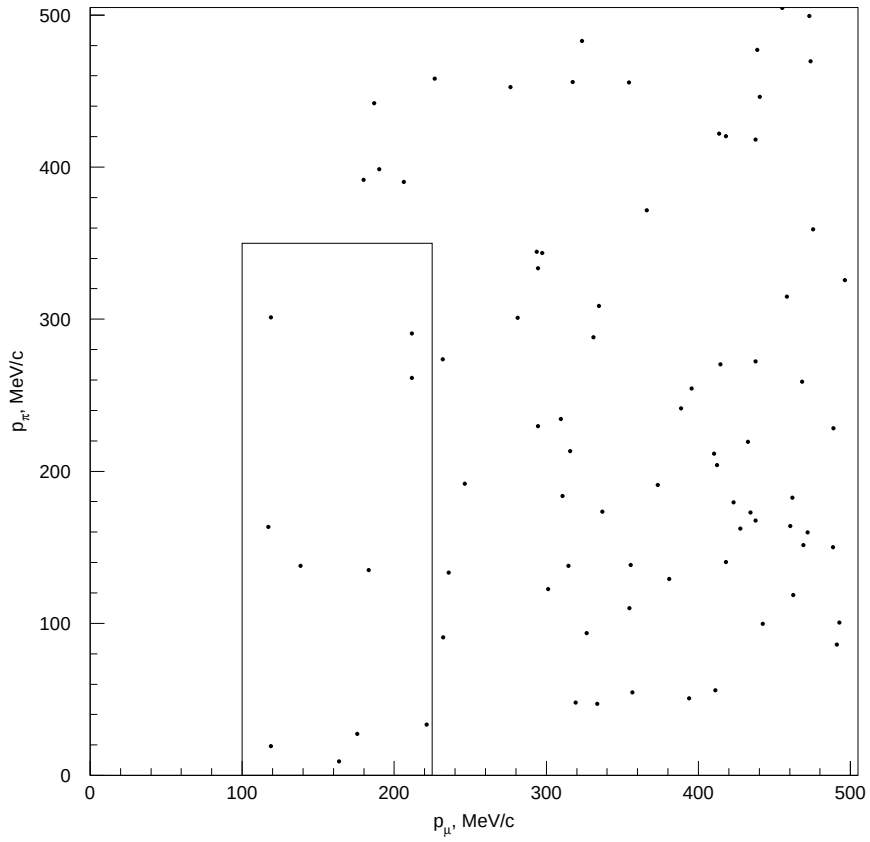

Figure 7.48: p_π vs. p_μ for events passing E1-E4, but failing E5, for SK-I 1489 days data. The boxed region is kept by criteria E8-E9.

Mode	SK-I NEUT	SK-I NUANCE	SK-II NEUT	SK-II NUANCE
Quasi-elastic	14%	14%	22%	12%
CC single π	49%	59%	46%	62%
CC multi-π	14%	4%	11%	4%
NC multi-π	11%	9%	12%	11%
Other	12%	15%	9%	11%
Total BG MC events (unnormalized)	584	482	245	253

Table 7.13: Modes contributing to background for $p \to \bar{\nu} K^*(892)^+$, $K^+ \to \mu^+ \nu$ without time signature.

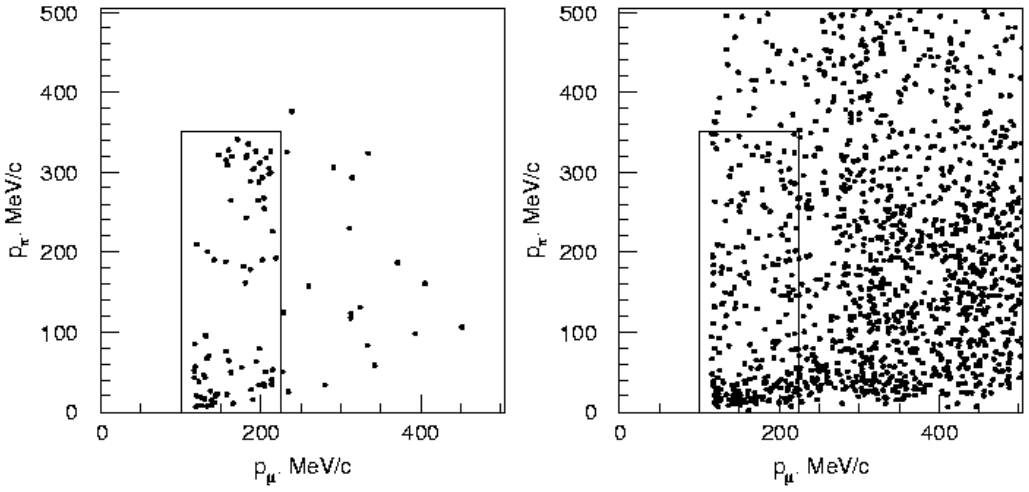

Figure 7.49: p_π vs. p_μ for events passing E1-E4, but failing E5 for $p \to \bar{\nu} K^*(892)^+$ (left) and atmospheric neutrino (right) Monte Carlo in SK-II. The boxed region is kept by criteria E8-E9.

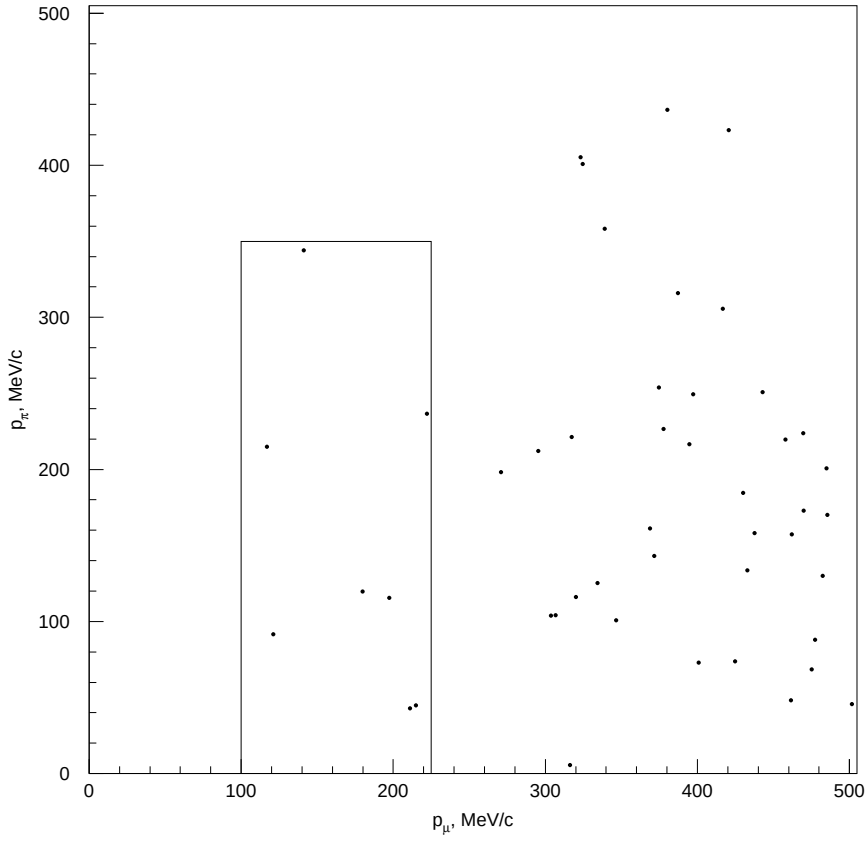

Figure 7.50: p_π vs. p_μ for events passing E1-E4, but failing E5 for SK-II 804 days data. The boxed region is kept by criteria E8-E9.

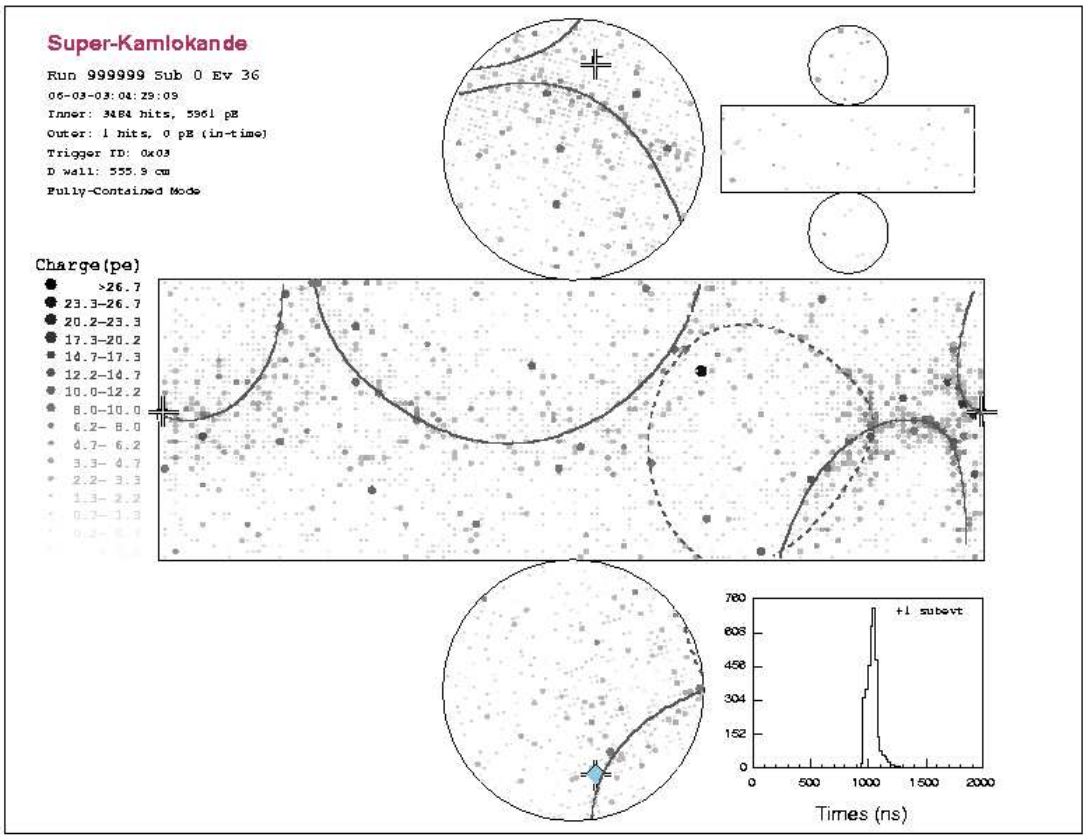

Figure 7.51: An example of a simulated $p \to \bar{\nu}K^*(892)^+$, $K^+ \to \pi^+\pi^0$ event. Four e-like rings are visible.

7.4.2 $K^+ \to \pi^+\pi^0$

If the K^+ decays via $K^+ \to \pi^+\pi^0$ (see Fig. 7.51 for an example), the π^+ is, as in the $p \to \bar{\nu}K^+$ case, barely above Cherenkov threshold. It is difficult to find the π^+ even against a single π^0. With a second π^0 in the event, it is effectively impossible. However, it still contributes a decay electron to the event, which can be detected. So, this is a search for the combination of a 309 MeV/c π^0, a 205 MeV/c π^0, and a decay electron from an invisible progenitor. Accordingly, preliminary cuts for this search are set as

F1. Two to four rings

F2. All rings e-like

F3. One decay electron.

For events passing criteria F1-F3, it is necessary to determine which ring or rings should be associated with each π^0. This is done using a χ^2 analysis.

In the two-ring case, there are only two possible ways to allocate the rings. The first ring may be associated with the $K^*(892)^+$ decay and the second with the K^+ decay, or vice versa. In either case, the momentum of each π^0 (denoted p_π^{K*} and p_π^{K+}) is assumed to be the momentum of the corresponding ring.

In each of the three- and four-ring cases, there are six possible allocations of rings. For each possibility, both π^0 momenta are reconstructed. If there are three rings, one π^0 will have two rings associated with it, and so the invariant mass of those rings is calculated. But if there are four rings, each π^0 will have two rings, and so an invariant mass is calculated for each. These masses are denoted m_π^{K*} and m_π^{K+}.

Having calculated the momenta and as many masses as possible for each hypothesis i, a χ^2 is defined for each hypothesis:

$$\chi_i^2 = \sum_j \frac{X_{i,j}^{calc} - X_{i,j}^{pred\,2}}{\sigma_j} \ , \tag{7.10}$$

where the sum runs over the calculated variables j, $X_{i,j}^{calc}$ and $X_{i,j}^{pred}$ are the calculated and predicted values for the j-th variable under the i-th hypothesis, and σ_j is the width of the distribution of that variable, as determined by a Gaussian fit. The values of $X_{i,j}^{pred}$ and σ_j are tabulated in Tbl. 7.14. Once the χ^2 has been calculated for each hypothesis, the hypothesis with the smallest χ^2 is accepted. Using this

	p_π^{K*} (MeV/c)	p_π^{K+} (MeV/c)	m_π (MeV/c^2)
X^{pred}	309	205	135
σ, 2 rings	50	50	N/A
σ, 3 rings	50	50	30
σ, 4 rings	50	50	40

Table 7.14: Parameters used for $p \to \bar{\nu} K^*(892)^+$, $K^+ \to \pi^+\pi^0$ χ^2 analysis.

allocation of rings, the next criterion is defined as

F4. π^0 mass cuts.

The form of criterion F4 depends on the number of rings. For the two-ring case, neither hypothetical π^0 is fully reconstructed, and so their invariant mass cannot be determined. However, the total invariant mass m_π of the two rings can be determined, and should not form a π^0. So, in this case, F4 becomes

$$m_\pi < 85 \text{ MeV}/c^2 \text{ or } m_\pi > 185 \text{ MeV}/c^2. \tag{7.11}$$

In the three-ring case, one π^0 is fully reconstructed, and in the four-ring case, both are. So, F4 requires that the reconstructed π^0 masses be consistent with a π^0:

$$85 \text{ MeV}/c^2 < m_\pi < 185 \text{ MeV}/c^2, \tag{7.12}$$

for each fully reconstructed π^0.

For those events passing F1-F4, a time signature likelihood L_{ts} is calculated very similarly to the $K^+ \to \mu^+\nu$ search. The principal difference is that the hits to calculate ΔT_{cone} are selected differently – it is a difference between the rings allocated to the K^+ decay π^0 and the $K^*(892)^+$ decay π^0, rather than between the μ-like and e-like rings. The PDFs are also calculated independently. The resulting likelihoods

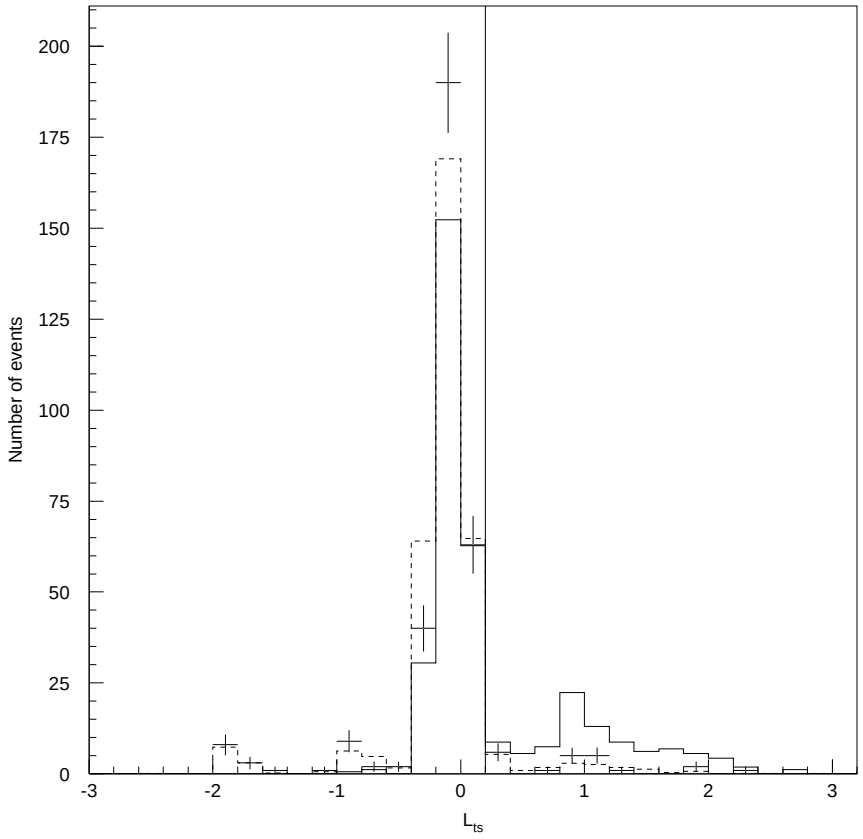

Figure 7.52: L_{ts} for events passing F1-F4 for $p \to \bar{\nu} K^*(892)^+$ (solid) and atmospheric neutrino (dashed) Monte Carlo, plus data (crosses), in SK-I. Events to the right of the vertical line pass cut F5, while those to the left are rejected.

are shown in Fig. 7.52.

Accordingly, criteria F5-F7 are defined similarly to E5-E7:

F5. $L_{ts} > 0.2$

F6. 210 MeV/c $< p_\pi^{K*} <$ 410 MeV/c

F7. 0 MeV/c $< p_\pi^{K+} <$ 300 MeV/c.

The distributions of p_π^{K*} and p_π^{K+} are shown in Figs. 7.53, 7.54, 7.55, and 7.56.

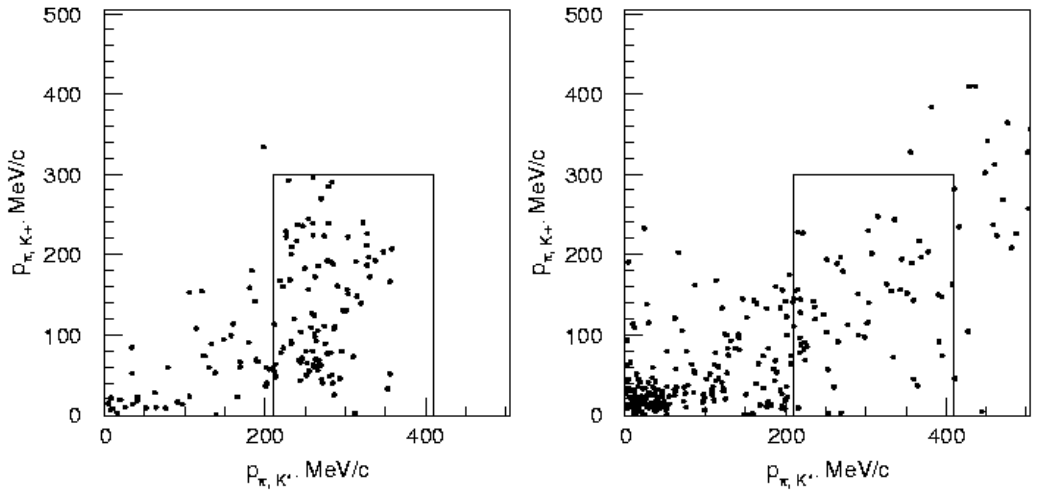

Figure 7.53: p_π^{K+} vs. p_π^{K*} for events passing F1-F5 for $p \to \bar{\nu} K^*(892)^+$ (left) and atmospheric neutrino (right) Monte Carlo in SK-I. The boxed region is kept by criteria F6-F7.

By passing the SK-I $p \to \bar{\nu} K^*(892)^+$ and atmospheric neutrino Monte Carlo through criteria F1-F7, 101 $p \to \bar{\nu} K^*(892)^+$ and 44 (normalized) NEUT atmospheric neutrino events are found to pass all of them. Accordingly, the detection efficiency and background for this mode in SK-I are estimated to be 2.2% and 1.8 events (2.0 events/100 kiloton-years), respectively. The NUANCE Monte Carlo, from which 31 (normalized) events pass, predicts a similar background of 1.3 events (1.3 events/100 kiloton-years). Five events are found in the 1489 days data sample from SK-I. The probability of a statistical fluctuation from 1.8 events up to 5 events is 3.6%.

Applying the same criteria to SK-II, the detection efficiency and background are estimated to be 2.4% and 2.6 events (5.3 events/100 kiloton-years), from 109 proton decay events and 72 (normalized) NEUT atmospheric events that pass the cuts. NUANCE, in which 59 (normalized) events pass, similarly predicts 2.2 events (4.4

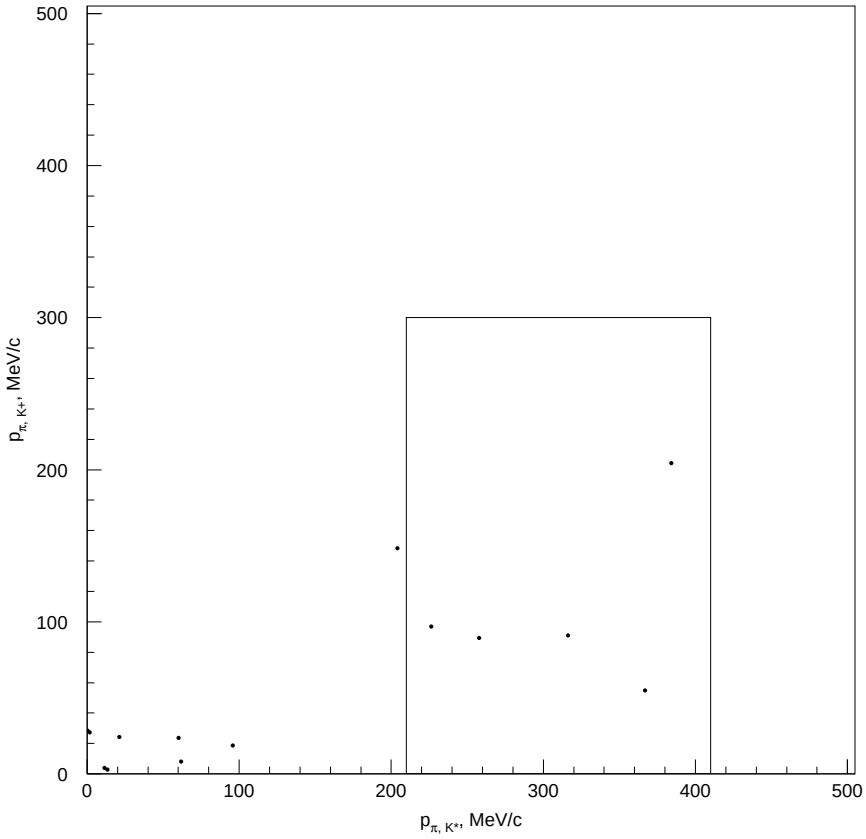

Figure 7.54: p_π^{K+} vs. p_π^{K*} for events passing F1-F5 for SK-I 1489 days data. The boxed region is kept by criteria F6-F7.

events/100 kiloton-years). 2 events are found in the 804 days data sample. The SK-I and SK-II results are tabulated in Tbl. 7.15.

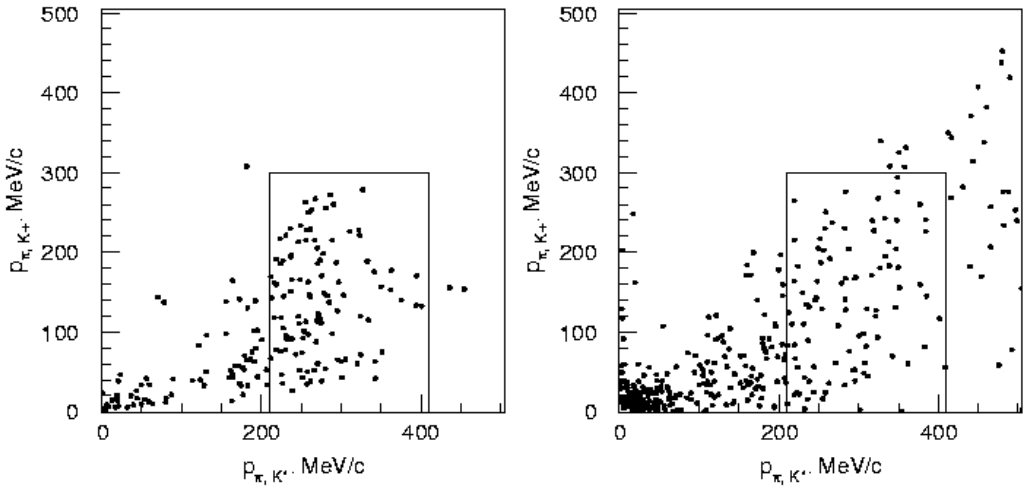

Figure 7.55: p_π^{K+} vs. p_π^{K*} for events passing F1-F5 for $p \to \bar{\nu} K^*(892)^+$ (left) and atmospheric neutrino (right) Monte Carlo in SK-II. The boxed region is kept by criteria F6-F7.

	Efficiency (%)	NEUT BG (# events)	NUANCE BG (# events)	Data (# events)
SK-I	2.2	1.8 (19%)	1.3	5
SK-II	2.4	2.6 (16%)	2.2	2

Table 7.15: Summary of results for $p \to \bar{\nu} K^*(892)^+$, $K^+ \to \pi^+ \pi^0$ with time signature. The uncertainty on the NEUT background is in parentheses.

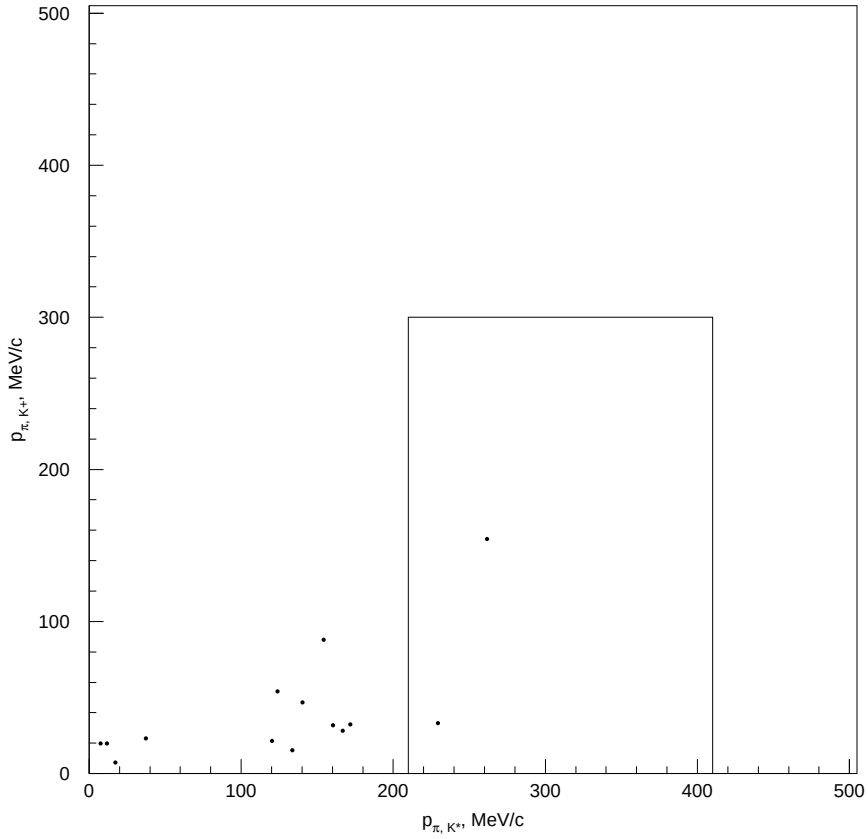

Figure 7.56: p_π^{K+} vs. p_π^{K*} for events passing F1-F5 for SK-II 804 days data. The boxed region is kept by criteria F6-F7.

Mode	SK-I NEUT	SK-I NUANCE	SK-II NEUT	SK-II NUANCE
CC single π	22%	28%	42%	30%
CC multi-π	16%	13%	13%	16%
NC single π	24%	9%	5%	6%
NC multi-π	17%	32%	15%	36%
λK	5%	11%	2%	3%
DIS	7%	0%	13%	0%
Other	9%	8%	10%	9%
Total BG MC events (unnormalized)	58	47	93	77

Table 7.16: Modes contributing to background for $p \to \bar{\nu}K^*(892)^+$, $K^+ \to \pi^+\pi^0$ with time signature.

The neutrino interaction modes contributing to the background in this search are shown in Tbl. 7.16. The background is almost entirely dominated by various types of pion production, with CC single pion and NC multiple pion being most prominent. When looking for a multiple-pion signature, this is to be expected.

Again, due to the low efficiency of criterion F5, those events passing F1-F4, but failing F5, are also used in a seperate search. Similarly to criteria F6-F7, additional kinematic criteria are defined:

F8. $0 \text{ MeV}/c < p_\pi^{K*} < 350 \text{ MeV}/c$

F9. $0 \text{ MeV}/c < p_\pi^{K+} < 300 \text{ MeV}/c$.

p_π^{K*} and p_π^{K+} for this case are shown in Figs. 7.57 and 7.58 for SK-I and 7.59 and 7.60 for SK-II. The results are tabulated in Tbl. 7.17.

The neutrino interaction modes contributing to the background in this search are shown in Tbl. 7.18.

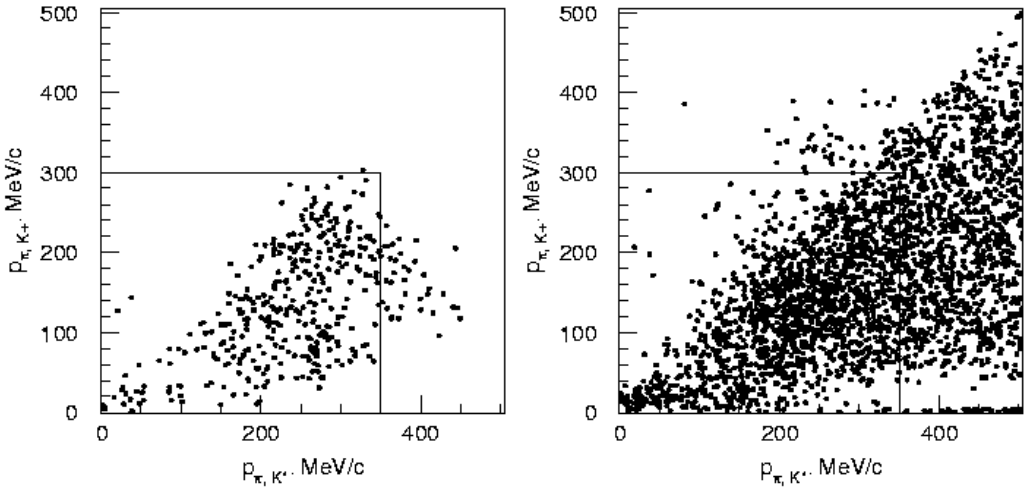

Figure 7.57: $p_\pi^{K^+}$ vs. $p_\pi^{K^*}$ for events passing F1-F4, but failing F5, for $p \to \bar{\nu} K^*(892)^+$ (left) and atmospheric neutrino (right) Monte Carlo in SK-I. The boxed region is kept by criteria F8-F9.

	Efficiency (%)	NEUT BG (# events)	NUANCE BG (# events)	Data (# events)
SK-I	7.8	46 (11%)	43	59
SK-II	7.3	25 (11%)	24	30

Table 7.17: Summary of results for $p \to \bar{\nu} K^*(892)^+$, $K^+ \to \pi^+ \pi^0$ without time signature. The uncertainty on the NEUT background estimate is in parentheses.

Mode	SK-I NEUT	SK-I NUANCE	SK-II NEUT	SK-II NUANCE
CC single π	35%	51%	36%	41%
CC multi-π	28%	11%	25%	13%
NC multi-π	15%	18%	13%	25%
Other	21%	19%	25%	20%
Total BG MC events (unnormalized)	1639	1343	987	813

Table 7.18: Modes contributing to background for $p \to \bar{\nu} K^*(892)^+$, $K^+ \to \pi^+ \pi^0$ without time signature.

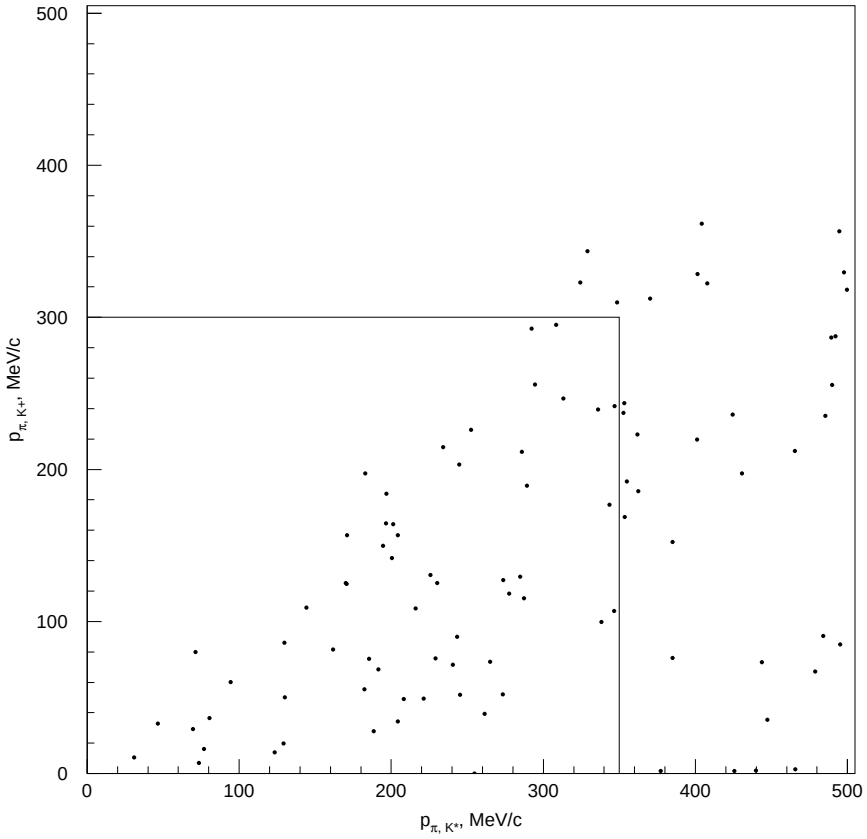

Figure 7.58: p_π^{K+} vs. p_π^{K*} for events passing F1-F4, but failing F5, for SK-I 1489 days data. The boxed region is kept by criteria F8-F9.

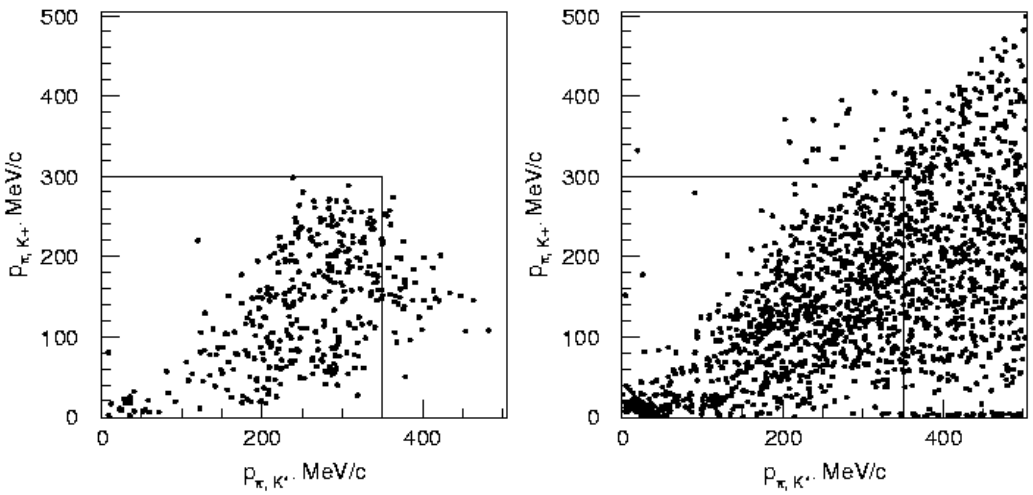

Figure 7.59: p_π^{K+} vs. p_π^{K*} for events passing F1-F4, but failing F5, for $p \to \bar{\nu} K^*(892)^+$ (left) and atmospheric neutrino (right) Monte Carlo in SK-II. The boxed region is kept by criteria F8-F9.

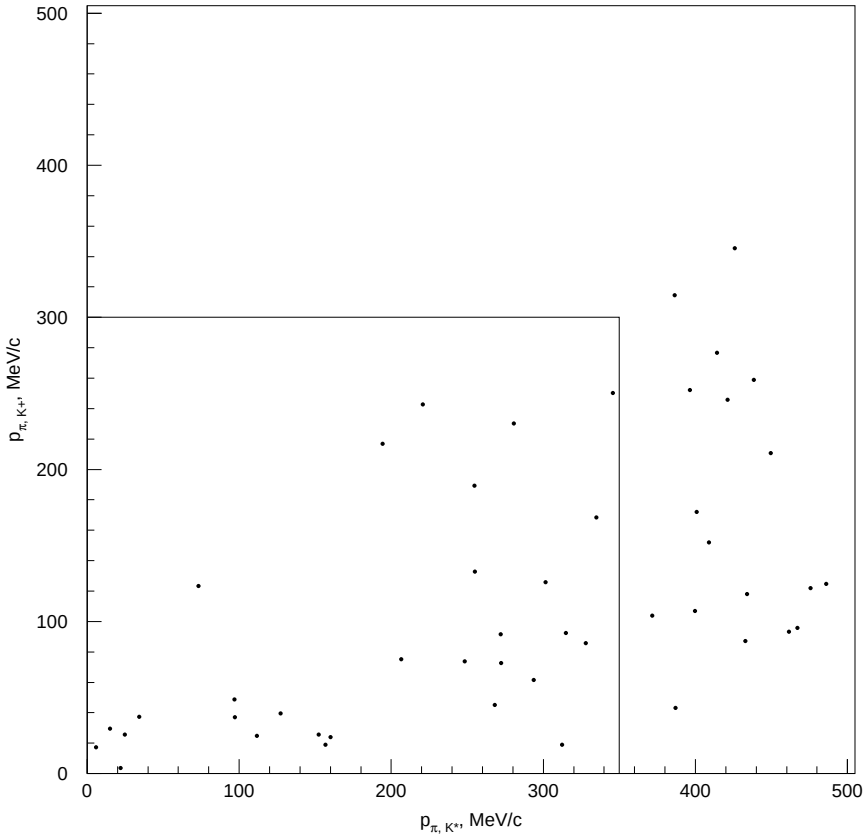

Figure 7.60: p_π^{K+} vs. p_π^{K*} for events passing F1-F4, but failing F5, for SK-II 804 days data. The boxed region is kept by criteria F8-F9.

7.4.3 Systematics

For these searches, background uncertainties are considered in the same manner as for $p \to e^+\pi^0$. Three different effects are considered. The first effect is the uncertainty in the Monte Carlo statistics, calculated as the square root of the number of background Monte Carlo events passing all cuts. The uncertainties in neutrino interaction cross-sections for various modes are also considered, with values previously estimated [14] as 10% for quasi-elastic and single meson production, 5% for multiple pion production and deep inelastic scattering, and 30% for coherent pion production. Finally, a 10% uncertainty in the total neutrino flux is assumed.

Since the study of this mode is, at this time, exploratory, intended to determine whether this mode may be used to improve the limit on $p \to \bar{\nu}K^+$, systematic uncertainties on the efficiency are not currently included in the analysis.

7.4.4 Limits

Out of eight independent searches performed for $p \to \bar{\nu}K^*(892)^+$ decays, three found a number of candidates with less than a 10% probability of that number arising from the estimated background. However, the remaining five found no significant excess of candidates. Accordingly, when considered as a whole, there is no convincing evidence for proton decay into this mode. Therefore, a 90% confidence lower limit is calculated, combining the eight searches using the method in Appendix C.

This combined lower limit on the partial lifetime into $p \to \bar{\nu}K^*(892)^+$ is 15×10^{31} years at 90% confidence. This is a factor of 3 better than the previous best world limit of 5.1×10^{31} years set by IMB [10]. However, this does not compare favorably to the substantially greater improvements relative to IMB obtained in other modes. That difference is due to the excess of candidates in three of the searches. These

	Efficiency	BG	Data	Limit ($\times 10^{31}$ yrs)
SK-I				
$\mu^+\nu$, TS	0.76%	1.6 (20%)	6	0.26
$\mu^+\nu$, no TS	1.9%	18 (12%)	10	12
$\pi^+\pi^0$, TS	2.2%	1.8 (19%)	5	0.89
$\pi^+\pi^0$, no TS	7.8%	46 (11%)	59	0.89
Combined				11
SK-II				
$\mu^+\nu$, TS	1.0%	2.0 (18%)	2	4.4
$\mu^+\nu$, no TS	1.7%	7.0 (13%)	8	4.1
$\pi^+\pi^0$, TS	2.4%	2.6 (16%)	2	11
$\pi^+\pi^0$, no TS	7.3%	25 (11%)	30	8.2
Combined				15
SK-I+II				13

Table 7.19: Summary of results for $p \to \bar{\nu}K^*(892)^+$. The background uncertainties are in parentheses. "TS" stands for Time Signature.

results are summarized in Tbl. 7.19.

It should also be noted that this limit is much weaker than that set on $p \to \bar{\nu}K^+$. Due to this and the phase space factor, the limit on $p \to \bar{\nu}K^*(892)^+$ cannot significantly strengthen the limit on $p \to \bar{\nu}K^+$. So, while improvements to this search could be made (most notably a specialized vertex fitter optimized to deal with the time delay between the $K^*(892)^+$ and K^+ decays), it seems unlikely that such improvements would strengthen the limit enough for it to be a powerful constraint.

Finally, it is observed that there is no large difference between the performance of SK-I and SK-II for this mode. This is consistent with the prior observations that $p \to e^+\pi^0$ and $p \to \mu^+\pi^0$ are largely unaffected, as this search also does not deal with small numbers of hits or small numbers of photoelectrons.

Chapter 8

Discussion

As of the completion of the SK-I and SK-II running periods, a total of 2293 days of data has been taken, corresponding to a total exposure of 141.3 kiloton-years over nine and a half years of operation. This data sample is searched for events corresponding to proton decay via the modes $p \to e^+\pi^0$, $p \to \mu^+\pi^0$, $p \to \bar{\nu}K^+$, and $p \to \bar{\nu}K^*(892)^+$. No evidence for proton decay into any of these modes is found, and therefore 90% confidence lower limits are set on the partial lifetime of the proton into these modes.

For $p \to e^+\pi^0$ and $p \to \mu^+\pi^0$, these limits represent an extension of the prior Super-K result by inclusion of the full SK-I and SK-II datasets, and the limits are improved according to the increased live time. These limits further constrain theories such as $SO(10)$ that predict proton decay into $p \to e^+\pi^0$ or $p \to \mu^+\pi^0$.

The $p \to \bar{\nu}K^+$ result is also an extension of the prior Super-K result, but here the observation of candidates in the SK-II data leads to a weaker limit than the prior result. This weakens the constraints on theories such as SUSY $SO(10)$ where $p \to \bar{\nu}K^+$ is the dominant mode.

$p \to \bar{\nu}K^*(892)^+$ had not previously been studied in Super-K, and the best world

Limit summary (10^{33} years, 90% confidence)

Mode	New limit	Prior best limit
$p \to e^+\pi^0$	8.0	2.6 (SK)
$p \to \mu^+\pi^0$	6.3	2.1 (SK)
$p \to \bar{\nu}K^+$	1.5/0.59	2.3 (SK)
$p \to \bar{\nu}K^*(892)^+$	0.13	0.051 (IMB)

Table 8.1: Summary of limits for modes studied in this dissertation.

limit was set by IMB [10]. This limit has been improved by a factor of 3. This does not add significantly to the $p \to \bar{\nu}K^+$ constraint.

These results are summarized in Tbl. 8.1.

While unfortunate in many ways, the necessity of running SK-II with 20% photocathode coverage instead of SK-I's 40% provided a unique opportunity to explore the impact of PMT density on proton decay searches. These observations are of obvious relevance to the design of future large water Cherenkov detectors for which proton decay is a major physics goal.

In modes such as $p \to e^+\pi^0$, $p \to \mu^+\pi^0$, and $p \to \bar{\nu}K^*(892)^+$, the search can be effectively carried out using only particles with energies in the hundreds of MeV. In such a case, the difference between 20% and 40% photocathode coverage is small.

However, modes such as $p \to \bar{\nu}K^+$ require searching for particles with much lower light deposition, such as few-MeV photons or charged pions just above the Cherenkov threshold. The impact of PMT density in this case is large, as shown by the fact that the performance of the $p \to \bar{\nu}K^+$ search is very much worse in SK-II.

It can therefore be concluded that, if modes such as $p \to \bar{\nu}K^+$ are a major physics goal, future large water Cherenkov detectors will be well served to use a photocathode coverage greater than 20%, and significant benefits could likely be obtained with even higher coverage. Conversely, for modes such as $p \to e^+\pi^0$, it is not as important to

have such a high PMT density, and the cost savings of 20% coverage are likely to be quite substantial.

It should be noted that, with the lone exception of the $p \to \bar{\nu}K^+$ with prompt γ search, all of these modes have expected backgrounds that are either fast approaching 1 event for the total Super-K running period or have already passed that point. Due to this, these modes are currently background-limited, and further exposure will only strengthen the limits as the square root of the exposure. Running Super–Kamiokande for 10 times as long, for example, would increase the limits only by a factor of 3.2 (assuming the detection efficiency and background rejection remained the same).

Further extensions of these studies, whether using a longer exposure or a larger detector, will therefore be well served to improve the signal/background separation from its current level. This could be done, for example, by improved and more accurate reconstruction algorithms, or with better cuts. For $p \to e^+\pi^0$ and $p \to \mu^+\pi^0$, in particular, it may be useful to reduce the limit on p_{tot} to restrict the search to free protons, as this should reduce the background significantly.

Appendix A

Ring Counting Algorithm

After the event vertex and the location of one Cherenkov ring (usually the brightest) are determined by "afit," as described in Sec. 5.2.1, the task of determining the number and location of additional Cherenkov rings is performed by the ring counting algorithm. This algorithm consists of two basic steps.

First, the charge distribution in the detector is analyzed using a technique called the Hough transform [80]. This produces a list of possible ring locations, or "candidates." These candidates are then checked using a likelihood analysis. If at least one candidate passes a likelihood threshold cut, then the candidate with the greatest likelihood is accepted and added to the list of "found" rings. This process then repeats from the Hough transform either until no candidate passes the likelihood threshold or until a total of five rings have been found.

It should also be noted that, in order to reduce computation time, the ring counting assumes that all rings are e-like.

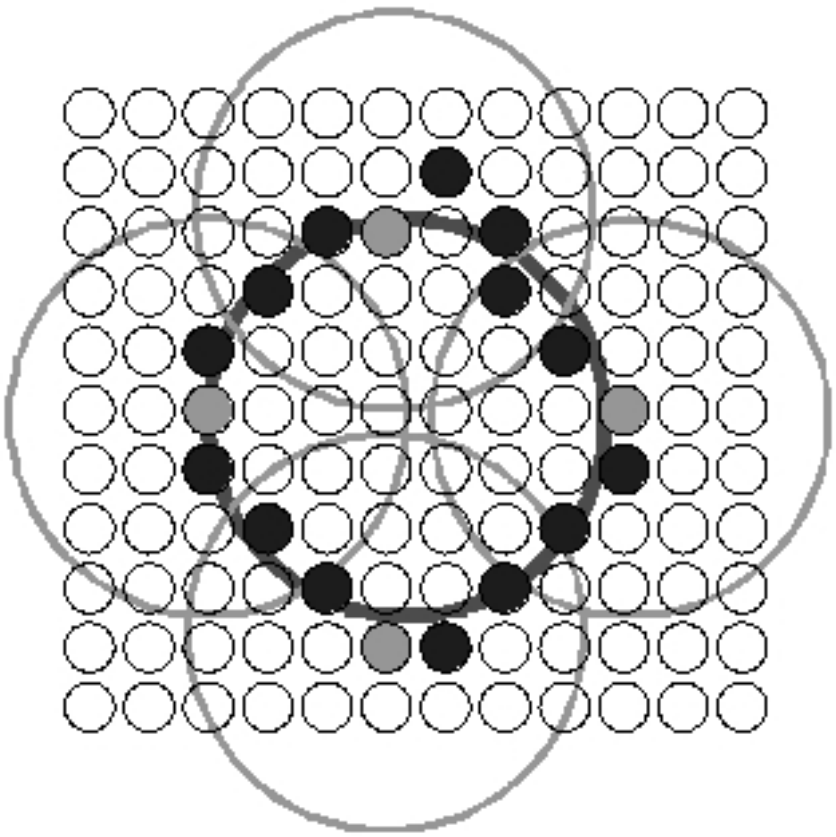

Figure A.1: An illustration of the Hough transform. The small circles are PMTs, with hit PMTs shaded. Circles are drawn around the gray PMTs.

A.1 The Hough Transform

The Hough transform is a standard image processing technique which is often used to find circles or circle segments. The general concept of the Hough transform is based on a specific observation. Consider a circle, and imagine drawing another circle, of the same radius, around each point on the first circle. All of these circles will intersect at the center of the original circle. This process is illustrated in Fig. A.1.

So, given a 2-D histogram representing light intensity, a transformation of that histogram is performed by distributing the light in each bin into a circle centered on

that bin. In this transformed histogram, there will be a peak at the center of any circular features in the image, in analogy to the intersection of all the test circles. In this way, the Hough transform turns a circle finding problem into a peak finding problem. As peak finding is a well understood problem with many readily available and effective algorithms, the difficulty of the problem has been greatly decreased.

One drawback of the Hough transform is that one must search for circles of a particular radius, since the radius of the test circles must be fixed. This problem is dealt with by performing independent Hough transforms for a range of possible radii. This results in a 3-D histogram (two spatial coordinates, plus radius) which are then searched for peaks.

The more limiting drawback is computational. The process of distributing charge into a circle, while straightforward, is computationally intensive, and must be done for each PMT and each possible radius. In fact, it is done multiple times for each PMT and each possible radius. This makes the ring counting the most time-consuming part of the reconstruction algorithms.

A.2 Using the Hough Transform in Super-K

The initial step in using the Hough transform in Super-K is to make four different charge distributions, on which Hough transforms will later be performed. This is done to enhance the algorithm's sensitivity - a ring that might not appear in one distribution could be visible if looked at in a different way.

- The first distribution is the observed charge in the detector minus the charge expected to be generated by the rings which have already been found.

- The second distribution is similar to the first, but the charge in any PMTs

where the expected charge from the found rings Q_{exp} is greater than 0.2 photoelectrons is scaled down by a factor of $0.2/Q_{exp}$. This reduces the contribution from PMTs in regions overlapping the found rings.

- The third distribution uses only the charge in PMTs more than 50 degrees away from any found ring. This eliminates any contribution from PMTs in overlap regions.

- The final "clean" distribution uses all charge, but is treated differently when performing the Hough transform. The details of this are discussed below.

To use the Hough transform in this way, the features being searched for must be circular. However, since the Super-K detector is cylindrical, the intersection of a Cherenkov ring with the detector wall and PMTs will in general be distorted. Therefore, the next step in applying the Hough transform is to transform each charge distribution from (x, y, z) space into (θ, ϕ) space, centered on the event vertex. This ensures that the Cherenkov rings will form circles detectable by the Hough transform.

Then, the Hough transform is applied to each of the four distributions, for trial ring radii ranging from 24 degrees to 46 degrees in steps of two degrees. For each of these radii, the charge in each PMT is distributed around that PMT. This produces four three-dimensional (θ, ϕ, radius) histograms.

After the normal Hough transform is applied, the fourth "clean" distribution is processed further. For each bin in the (θ,ϕ) histogram, the circle around it is examined to find the point in the Hough transform with the greatest charge. Then, that bin's charge is put into a second Hough transform, but only at that greatest-charge point. The charge that would normally be distributed along the rest of the circle is ignored. This makes the peaks in Hough space sharper.

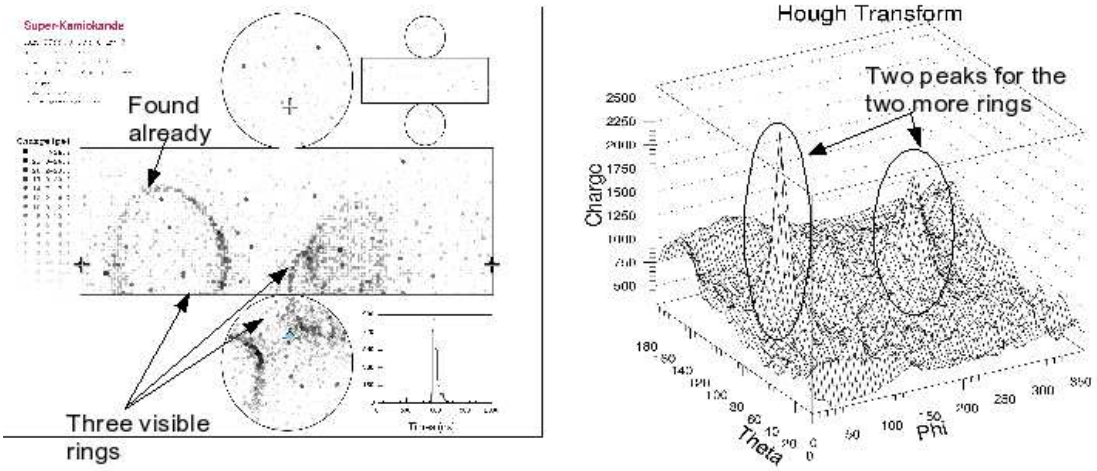

Figure A.2: An example of the Hough transform as used in Super-K. The contour plot is generated from the event on the left when searching for a second ring.

Once the four Hough transforms are complete, they are searched for peaks. Up to three of the highest peaks from each transform are added to a list of ring candidates which are analyzed in the next step of the process.

An illustration of this process is shown in Fig. A.2. The contour plot on the right is the first Hough transform, for an opening angle of 42 degrees, when looking for the second ring. The event (a simulated $p \rightarrow e^{+}\pi^{0}$ decay) is shown on the left. The prominent ring on the left has already been found, and its charge has been subtracted from the Hough transform. Two other overlapping rings are present, and contribute two peaks to the Hough transform.

A.3 Likelihood Analysis of Candidates

The list of candidates is evaluated based on several different variables. Four of these were used in SK-I and predate this dissertation. Two additional variables were developed for SK-II, one as a part of the research for this dissertation and

one by other research. Additionally, modifications had to be made to several of the calculations to reflect SK-II's reduced PMT density.

These calculations are the result of a long evolution of the code, starting from the original Kamiokande experiment. They have been modified by many different people, and contain many different, seemingly arbitrary, parameters. The original meaning and rationale for many of these parameters is no longer understood.

It is useful to define some parameters for these calculations. First, X and Y, which are related to the logarithm of the total charge in the inner detector Q_{tot} and the charge assigned to the candidate ring Q_{cand}:

$$X = \log[A \times (Q_{tot} - Q_{cand})] \quad \text{(A.1)}$$

$$Y = \log(A \times Q_{tot}), \quad \text{(A.2)}$$

where A is a correction factor equal to 1.0 in SK-I and 2.405 in SK-II. Also define

$$Z_i = \arccos(\theta_i/2), \quad \text{(A.3)}$$

where θ_i is the angle between the candidate ring and the i-th brightest ring already found, as well as

$$C_1 = \frac{(Z_1 + 0.03)^3}{0.0164} \quad \text{(A.4)}$$

$$C_2 = 0.6e^{(18-\theta_C)/5}, \quad \text{(A.5)}$$

where θ_C is the opening angle of the candidate ring.

The first variable, L_{prob}, reflects the relative probability that the observed charge

distribution would occur with and without the candidate. It is calculated based on P_{tot}, which is a sum over PMTs i:

$$P_{tot} = \sum_i \log[P(Q_i^{obs}, Q_i^{exp,with})] - \log[P(Q_i^{obs}, Q_i^{exp,without})], \tag{A.6}$$

where Q_i^{obs} is the observed charge in the i-th PMT, $Q_i^{exp,with(out)}$ is the expected charge in that PMT assuming the candidate ring is (not) present, and $P(Q_1, Q_2)$ is the probability of observing a charge of Q_1 if the expected charge is Q_2.

A value of $P_{tot} > 0$ therefore implies that the observed charge distribution would be more likely if the candidate were a real track, and $P_{tot} < 0$ indicates that it is more likely if the candidate is not real. Because of this, any candidate with $P_{tot} < 0$ is immediately vetoed and will not be accepted, regardless of the values taken by the other five variables. In SK-I, this vetoing only occurs when searching for a second ring – if a second ring has already been found, no veto is allowed. As part of the work for this dissertation, this has been changed, and in SK-II the veto can take place for any number of found rings.

L_{prob} is then calculated:

$$L_{prob} = \log[B \times P_{tot}] - 0.8Y - 2.6, \tag{A.7}$$

where B is a correction factor equal to 1 in SK-I and 2 in SK-II.

The second, third, and fourth variables are closely related to each other. They all are comparisons of the charge density in different annular regions. To characterize this, $\theta_{peak,i}$ is defined for the ith found ring as the opening angle at which the charge density for the ring is greatest. Also, Θ is defined similarly, but for the candidate ring.

Q_a^b is defined as a sum over those PMTs j which are more than a degrees and less

than b degrees from the candidate ring direction and are also more than $1.2\theta_{peak,i}$ away from the other rings i:

$$Q_a^b = \frac{\sum_j Q_j \times w_j}{\sum_j w_j}, \tag{A.8}$$

where Q_i is the charge in the PMT and w_i is a weighting factor for that PMT based on the fraction of charge in the PMT expected to be from the candidate ring.

The second through fourth variables as are defined by

$$\begin{aligned}
L_{peak} &= [\ln(Q_{\Theta-2}^{\Theta+2}) - X - C_1 + 4.5](C_1 + 550) - C_2, N = 1 \\
&= \ln(Q_{\Theta-2}^{\Theta+2}) - X - C_2 + \sum_j \frac{Z_j - 0.6}{j} + 4.5, N > 1 \qquad \text{(A.9)} \\
L_{diff} &= [\ln(Q_{\Theta-2}^{\Theta+2} - Q_{\Theta+13}^{\Theta+22}) - 0.8X - C_1 + 4.2](C_1 + 550) \\
&\quad -C_2, N = 1 \\
&= \ln(Q_{\Theta-2}^{\Theta+2} - Q_{\Theta+13}^{\Theta+22} - 0.8X + 0.86Z_1 - C_2 + 3.45, N > 1 \qquad \text{(A.10)} \\
L_{diff,2} &= [\ln(Q_{\Theta-2}^{\Theta+2} - \frac{1}{2}(Q_0^{\Theta-10} + Q_{\Theta+13}^{\Theta+22})) - 0.8X - C_1 + 4.4](C_1 + 550) \\
&\quad -C_2, N = 1 \\
&= \ln\left[Q_{\Theta-2}^{\Theta+2} - \frac{1}{2}(Q_0^{\Theta-10} + Q_{\Theta+13}^{\Theta+22})\right] - 0.8X + 0.86Z_1 - C_2 + 3.65 \qquad \text{(A.11)}
\end{aligned}$$

where N is the number of rings already found and the sum over j is over rings already found. L_{peak} is therefore related to the charge density at the peak of the candidate ring, L_{diff} to the difference in charge density at the peak compared to outside of that peak, and $L_{diff,2}$ to the difference in charge density at the peak compared to the average of inside and outside.

The fifth variable, L_{vec}, is based on a vector sum, $\vec{Q}$, over PMTs i, of the charge not yet accounted for:

$$\vec{Q} = \sum_i (Q_i^{obs} - Q_i^{exp})\vec{d}_i, \tag{A.12}$$

where Q_i^{obs} is the charge in the PMT, Q_i^{exp} is the expected charge in the PMT based on the rings already found, and $\vec{d}_i$ is a unit vector pointing from the vertex to the PMT. Then, L_{vec} is calculated:

$$L_{vec} = \log|\vec{Q}| - \frac{4X}{3} - 0.6. \tag{A.13}$$

The final variable, L_{asym} is based on an old analysis tool, no longer a core part of the reconstruction, called "ringer." This tool is predicated on an interesting observation – a single-ring event should be azimuthally symmetric about the direction to that ring, while a multi-ring event will generally be asymmetric about the direction to any ring. A high degree of symmetry is therefore associated with single-ring events, while a low degree of symmetry indicates a multi-ring event.

Ringer works by calculating the "imbalance," I, a measure of asymmetry, for the charge in different annular regions around the direction to the first ring. These regions are 80 degrees wide, and run from 80 degrees to 180 degrees away from the ring in 10 degree steps. There is also an additional narrow region, 120 degrees to 140 degrees from the first ring direction, which is checked. The greatest value of the imbalance for any region is then taken as I_{max}.

To calculate I within an annulus, the charge within that annulus is histogrammed in 20 degree bins in ϕ, measured relative to the direction to the first ring. I is then defined as a χ^2 relative to the average charge $\bar{Q}$ over those bins:

$$I = \sum_{i=1}^{18} \frac{Q_i - \bar{Q}}{\sigma_i}, \tag{A.14}$$

where Q_i is the charge in the bin, and σ_i is the uncertainty in that charge based on shadowing and the vertex fit uncertainty's effects on distance and angle of incidence.

Given I_{max}, A is calculated:

$$A = \frac{1}{2}\left(I_{max} - 2 + \frac{Q_{tot}}{2500}\right), \tag{A.15}$$

where Q_{tot} is the total charge in the inner detector. This is then bounded between 0 and 10 to produce L_{asym}, as

$$L_{asym} = \begin{cases} 0 & A < 0 \\ A & 0 \leq A < 10 \\ 10 & 10 \leq A \end{cases} . \tag{A.16}$$

These variables are then combined in one of two ways. For SK-I, and initially for SK-II, a linear combination is used. However, after the work on ring counting for this dissertation was complete, other collaborators modified the ring counting to combine the six variables into a likelihood for the SK-II analysis. As a matter of convention, the older linear combination of the variables is also referred to as a "likelihood," despite the fact that it cannot be interpreted as a product of probabilities.

For SK-I, the calculation is a linear combination, which varies depending on how many rings have already been found. For the case where N rings have been found, the final likelihood L is given by

$$L = \begin{cases} L_{prob} + L_{peak} + 6L_{diff} + 1.5L_{vec} & N = 1 \\ 1.5L_{peak} + 7L_{diff} + 3L_{vec} - 3.0 & N > 1 \end{cases} . \tag{A.17}$$

The -3.0 at the end of the $N > 1$ case is a tuning constant. Since only rings with $L > 0$ will be accepted, adjusting this tuning constant allows for the acceptance of

more or fewer rings.

SK-II used the same approach for some time, with adjusted tuning constants needed to reproduce the response of SK-I while using half the PMTs. This is still used for the case of $N > 1$, where

$$L = 1.5L_{peak} + 7.0L_{diff} + L_{diff,2} + 3L_{vec} - 4.0. \tag{A.18}$$

For the case of $N = 1$, SK-II now uses a true likelihood. By examining two samples of Monte Carlo, one known to be true single-ring events and one known to be true multi-ring events, probability density functions (PDFs) for these six variables have been determined for the single-ring and multi-ring cases. These PDFs are then combined into a final likelihood:

$$L = \sum_i \log[P(L_i)_{multi}] - \log[P(L_i)_{single}], \tag{A.19}$$

where $P(L_i)_{multi}$ is the probability to get a value L_i for the i-th variable in a multi-ring event and similarly for $P(L_i)_{single}$. Hence, $L > 0$ if the observed values are more likely to happen in a multi-ring event, and $L < 0$ if they are more likely to happen in a single-ring event. So, there is a clear and meaningful zero point in this approach, and hence there is no need for a tuning constant.

After combining the variables to make a final likelihood for each candidate, the combined likelihoods are compared. If at least one candidate has $L > 0$, then the candidate with the highest L is accepted and added to the list of found rings.

If a candidate ring was accepted and there are still fewer than five rings found, the process repeats from the Hough transform. If no candidate passes the likelihood cut, or if a total of five rings have now been found, the reconstruction proceeds to the particle identification as described in Ch. 5.

A.4 Ring Correction

After all reconstruction algorithms described in Sec. 5.2 are completed, a final step is applied to determine the final number of rings. This is called the ring correction. The concept of ring correction is that rings which kinematically appear to be unlikely to be real are removed. This is done by a pair of cuts.

1. If a ring is less than 30 degrees away from another ring, and also has less than 60 MeV/c of momentum perpendicular to that ring's direction, it is removed.

2. If a ring's momentum is both less than 40 MeV/c and less than 5% of the total momentum in the event, it is removed.

Originally, these cuts were made based only on the momentum determined without using PID information. However, as part of this work, a second ring correction step was added. This second ring correction performs the same cuts, but based on the momentum determined using PID information.

A.5 Performance

The distribution of L for the best second-ring candidate is shown in Figs. A.3 for sub-GeV events and A.4 for multi-GeV events. An $L < 0$ represents single-ring events, while $L > 0$ is multi-ring. While the range of L is compressed for SK-II, it should be noted that the single-ring and multi-ring peaks are more clearly separated, which suggests superior performance. Also shown are the quasi-elastic interactions (hatched). These should in general be single-ring.

The performance of the ring counting is more precisely evaluated by considering the efficiency for single-ring and multi-ring events to be correctly identified. For

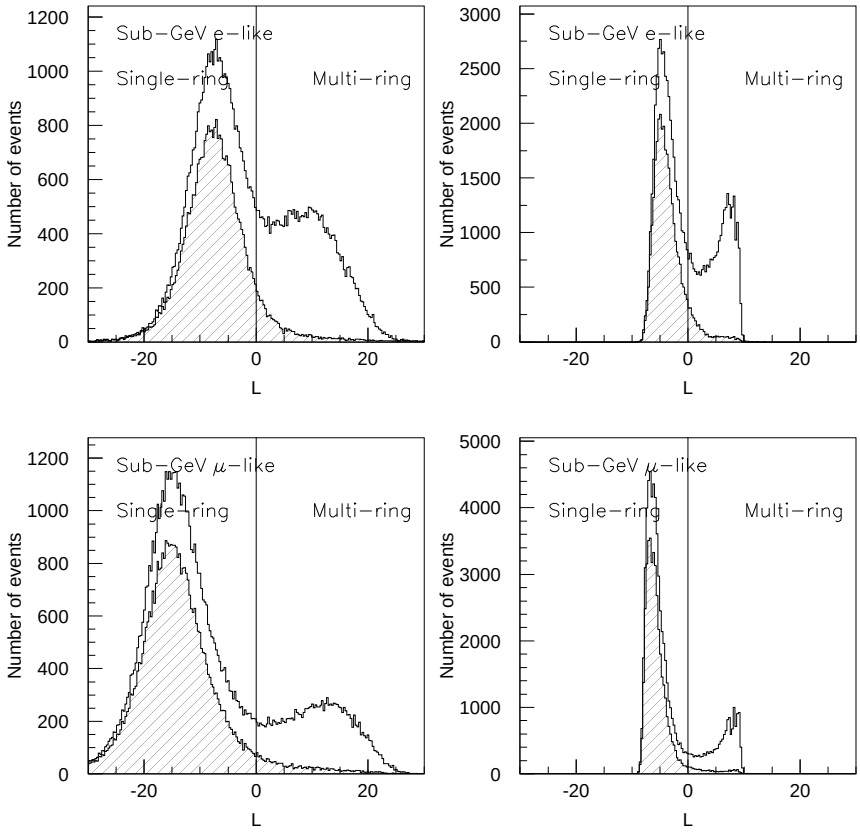

Figure A.3: The ring counting likelihood of the second ring for sub-GeV subsamples, SK-I (left) and SK-II (right). Quasi-elastic interactions are hatched.

single-ring efficieny, the events used are all quasi-elastic interactions, and the efficiency listed is the fraction of these events fit with exactly one ring. Multi-ring efficiency is determined by considering two samples. The first is charged-current events with at least one π^0 in the final state, with a momentum of at least 500 MeV/c and a direction more than 30 degrees away from the lepton. Also considered are neutral-current single π^0 production events where the pion has less than 500 MeV/c of momentum and the lower-energy decay photon still has at least 30% of

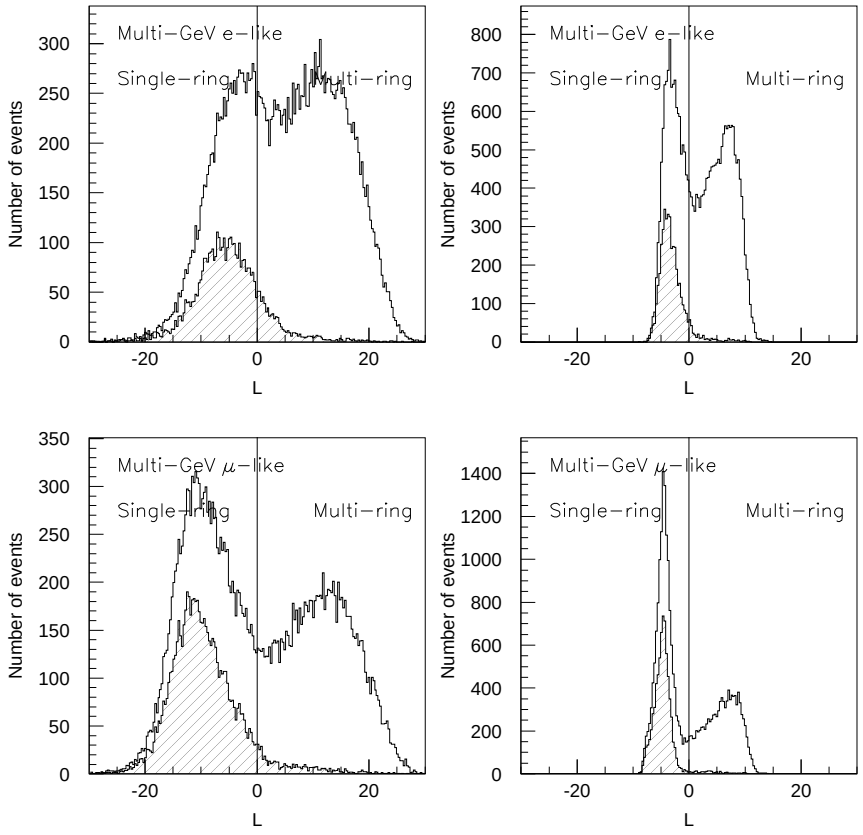

Figure A.4: The ring counting likelihood of the second ring for multi-GeV subsamples, SK-I (left) and SK-II (right). Quasi-elastic interactions are hatched.

the total energy. Again, the efficieny is defined as the fraction of events in these groups that are fit with multiple rings. These results are tabulated in Tbl. A.1.

For the sub-GeV events, there is relatively little difference between SK-I and SK-II. Efficiencies are generally decreased by up to 1%, but there are no large changes.

Multi-GeV events show substantially greater change. Single-ring efficiencies are higher in SK-II, but multi-ring efficiencies are lower. These both reflect an overall higher acceptance threshold in the SK-II PDF analysis.

Sample	SK-I efficiency	SK-II efficiency
Sub-GeV e-like single-ring	93.4%	92.4%
Sub-GeV e-like multi-ring	92.1%	91.8%
Sub-GeV μ-like single-ring	96.0%	95.9%
Sub-GeV μ-like multi-ring	89.9%	89.4%
Multi-GeV e-like single-ring	85.5%	93.3%
Multi-GeV e-like multi-ring	85.4%	83.3%
Multi-GeV μ-like single-ring	93.8%	96.6%
Multi-GeV μ-like multi-ring	86.2%	82.5%

Table A.1: Ring counting efficiencies.

Appendix B

Comparison of NEUT and NUANCE MC

For this analysis, the NUANCE Monte Carlo sample is used as a cross-check on the background estimate provided by the NEUT Monte Carlo. The actual background estimates yielded by the two models are generally similar, but it is useful to compare them in more detail to further check the reliability of NEUT. The differences between the two models are discussed in Sec. 6.2.2.

The first interesting question is how the interaction modes compare for the sub-GeV events that provide the background to proton decay. After converting the modes as represented by NUANCE into the NEUT representation, this comparison is shown in Tbl. B.1 (without any normalization or correction for oscillations). There are some inconsistencies due to the internal representation of modes. For example, NUANCE modes do not exactly map to what NEUT calls deep inelastic scattering, except in energies characteristic of multi-GeV events. There are also certain interactions that do not have an exact NEUT analog, which are listed under Other.

Another comparison of interest is in the distributions of p_{tot} versus m_{tot}, and the

Mode	SK-I NEUT	SK-I NUANCE	SK-II NEUT	SK-II NUANCE
Total	276075	251673	160569	148870
Quasi-elastic	150692	144195	88060	83598
Elastic	3842	2690	1713	1011
CC single π	53066	50748	30849	30374
CC multiple π	17946	7799	10773	5600
NC single π	20494	22661	11306	12172
NC multiple π	11014	9250	6419	7156
Coherent π	9856	11286	5751	7343
η	2604	1326	1642	866
λ, K	287	369	174	84
Deep inelastic	6274	0	3882	0

Table B.1: Breakdown of modes for sub-GeV events in SK-I and SK-II NEUT versus NUANCE atmospheric Monte Carlo.

attendant L distribution (see Fig. 7.6), for the $p \to e^+\pi^0$ search. These comparisons are shown in Figs. B.1 and B.2, respectively. The agreement between NEUT and NUANCE is quite reasonable.

Variables of interest from the various sub-searches for $p \to \bar{\nu}K^+$ include $N_{hit\gamma}$ (Fig. B.3), p_μ (Fig. B.4), and Q_{back} versus p_π (Fig. B.5). Again, the agreement between NEUT and NUANCE in all cases is good.

It is also interesting to check the agreement for the newly introduced variables H (Fig. B.6), N_{early} and N_{late} (Fig. B.7), and F_1 (Fig. B.8). The agreement in all these is good.

In the $p \to \bar{\nu}K^*(892)^+$ search, interesting comparisons include L_{ts} (Figs. B.9 and B.11) and the final momentum comparisons (Figs. B.10 and B.12). As before, NEUT and NUANCE show no great differences.

Based on these general comparisons, and on the overall agreement in the final background estimates, it may be concluded that those background estimates do not depend strongly on the choice of neutrino interaction model.

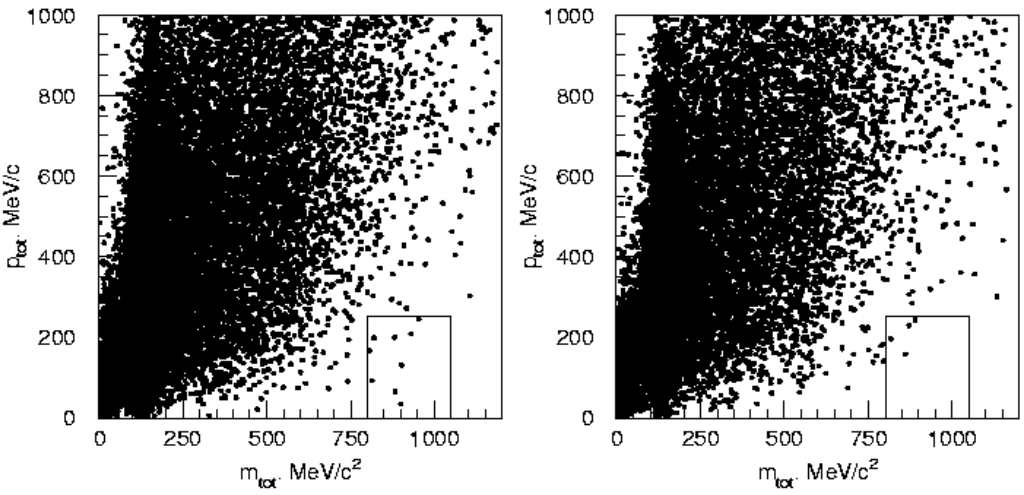

Figure B.1: Comparison of p_{tot} vs. m_{tot} for events passing A1-A4 in the $p \to e^+\pi^0$ search, SK-I NEUT (left) and NUANCE (right). The boxed region is kept by criteria A5-A6.

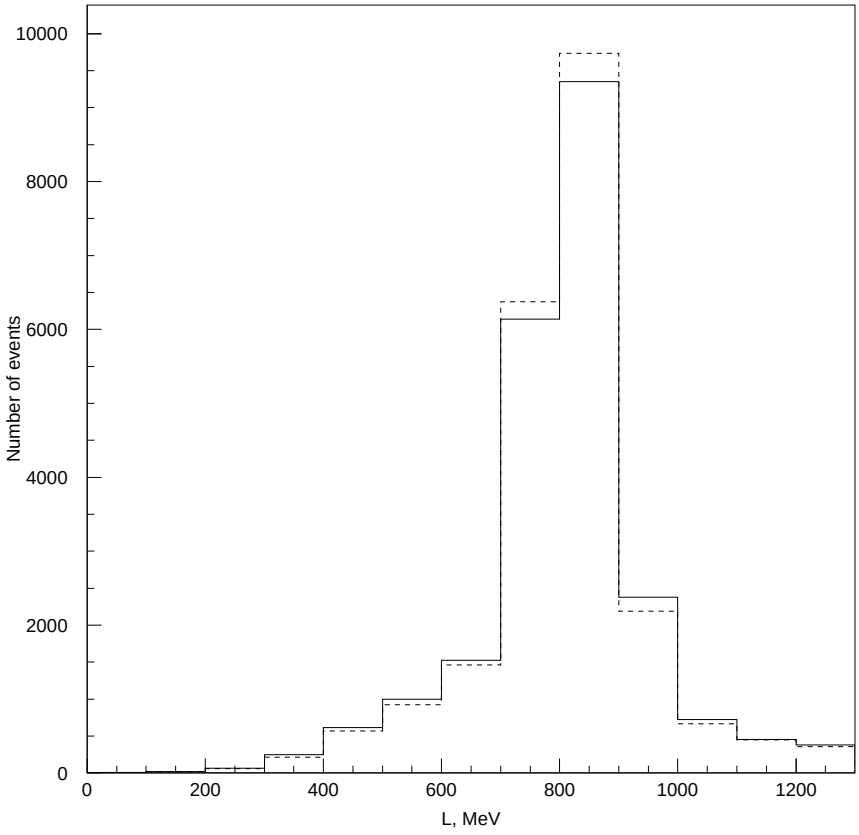

Figure B.2: Comparison of L for events passing A1-A4 in the $p \to e^+\pi^0$ search, SK-I NEUT (solid) and NUANCE (dashed).

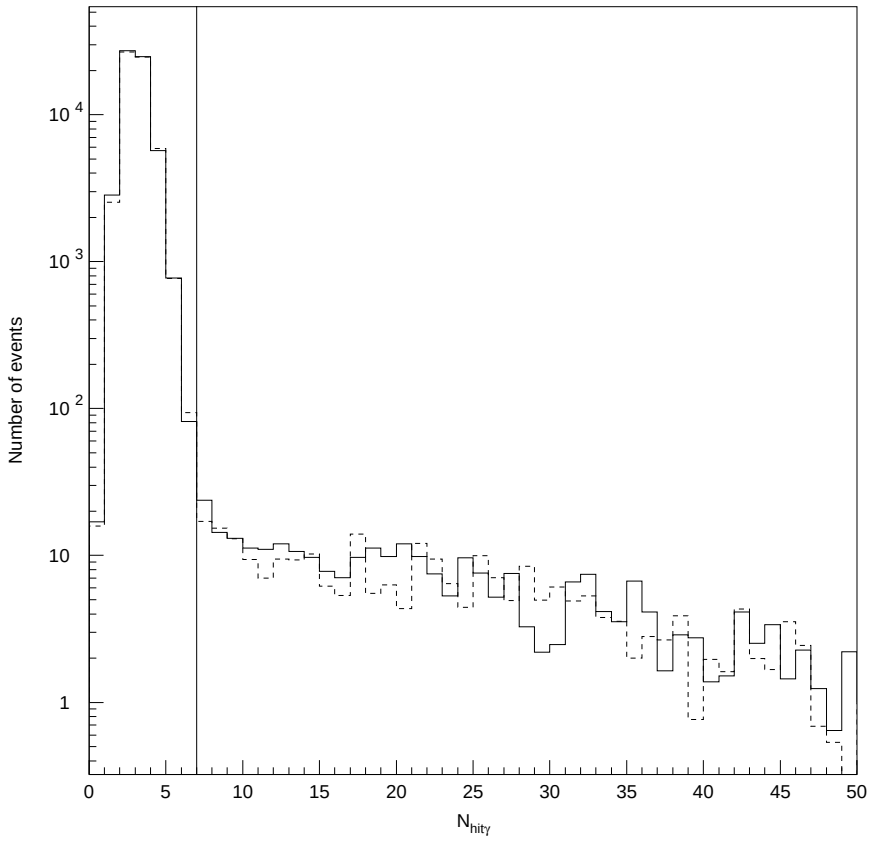

Figure B.3: Comparison of $N_{hit\gamma}$ for events passing C1-C4 in the $p \to \bar{\nu} K^+$, $K^+ \to \mu^+ \nu$ search, SK-I NEUT (solid) and NUANCE (dashed). The vertical line indicates cut C5.

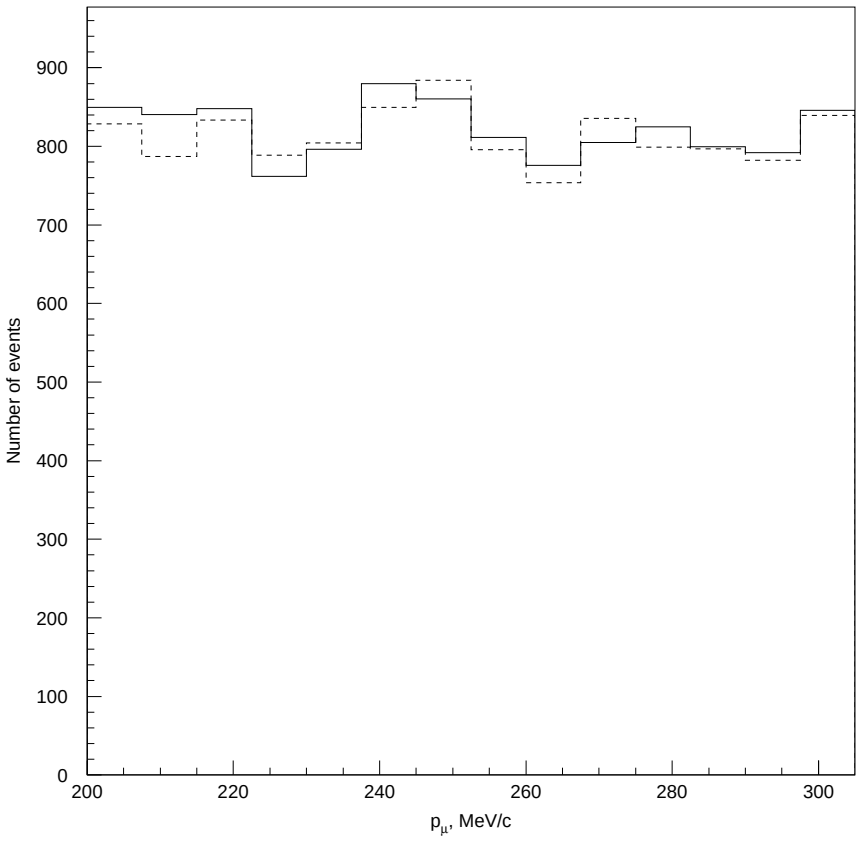

Figure B.4: Comparison of p_μ for events passing C1-C4, but failing C5, in the $p \to \bar{\nu} K^+$ monochromatic μ search, SK-I NEUT (solid) and NUANCE (dashed).

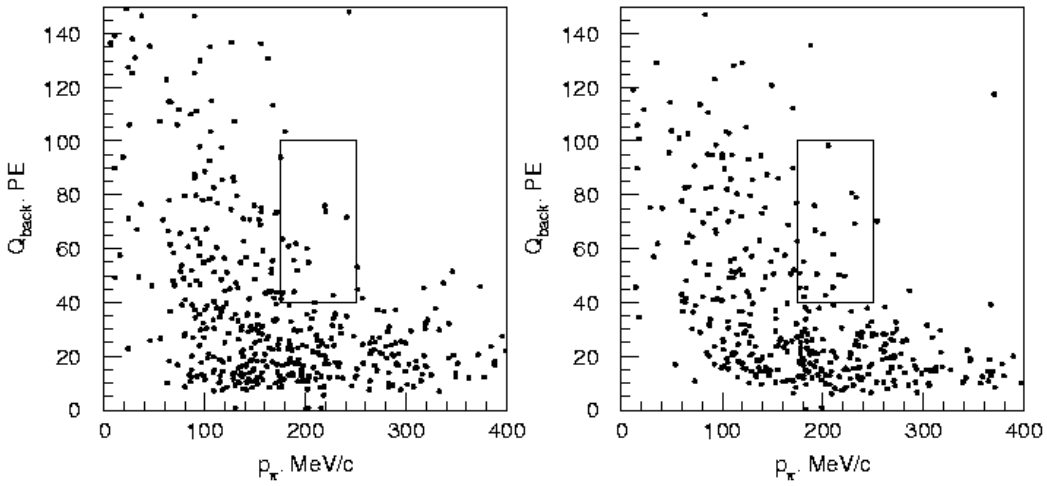

Figure B.5: Comparison of Q_{back} vs. p_π for events passing D1-D6 in the $p \to \bar{\nu} K^+$, $K^+ \to \pi^+ \pi^0$ search, SK-I NEUT (left) and NUANCE (right). The boxed region is kept by criteria D7-D8.

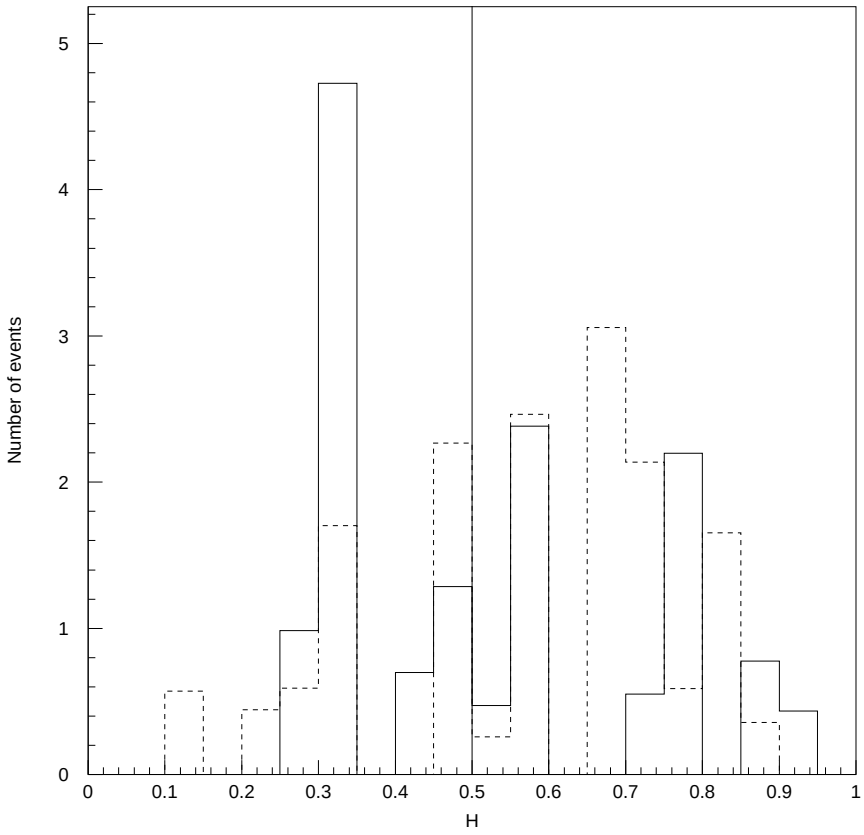

Figure B.6: Comparison of H for events passing C1-C6 in the $p \to \bar{\nu}K^+$, $K^+ \to \mu^+\nu$ search, SK-II NEUT (solid) and NUANCE (dashed). The vertical line indicates cut C7.

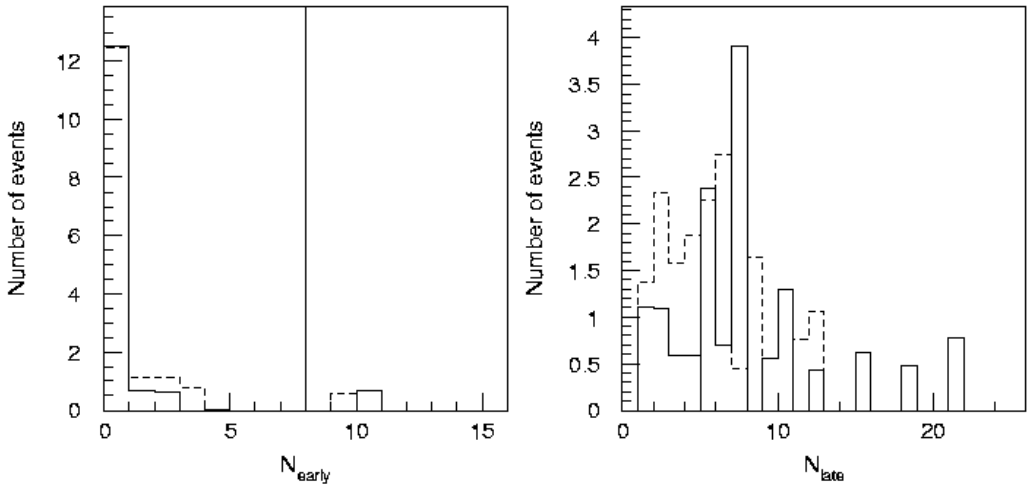

Figure B.7: Comparison of N_{early} and N_{late} for events passing C1-C6 in the $p \to \bar{\nu} K^+$, $K^+ \to \mu^+ \nu$ search, SK-II NEUT (solid) and NUANCE (dashed). Vertical lines indicate cuts C8 and C9.

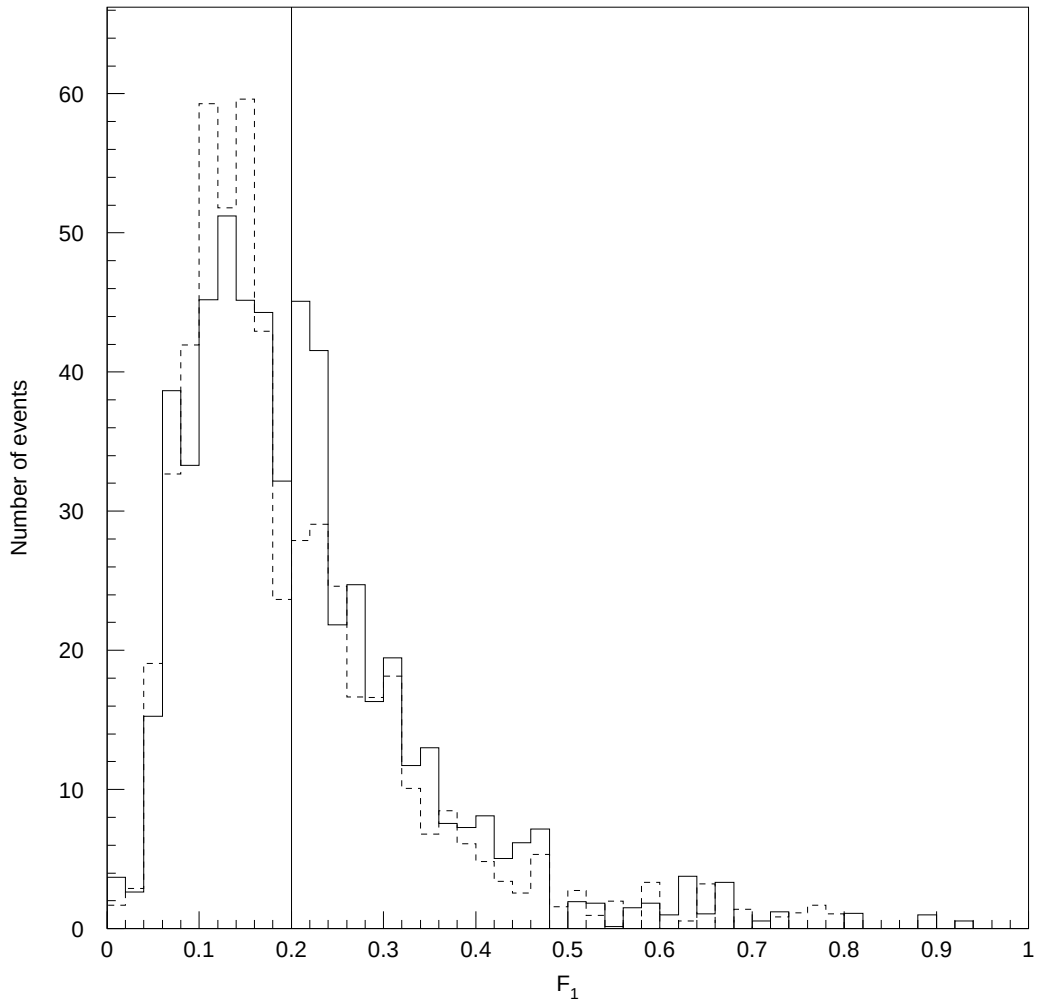

Figure B.8: Comparison of F_1 for events passing D1-D5 in the $p \to \bar{\nu}K^+$, $K^+ \to \pi^+\pi^0$ search, SK-I NEUT (solid) and NUANCE (dashed). The vertical line indicates cut D6.

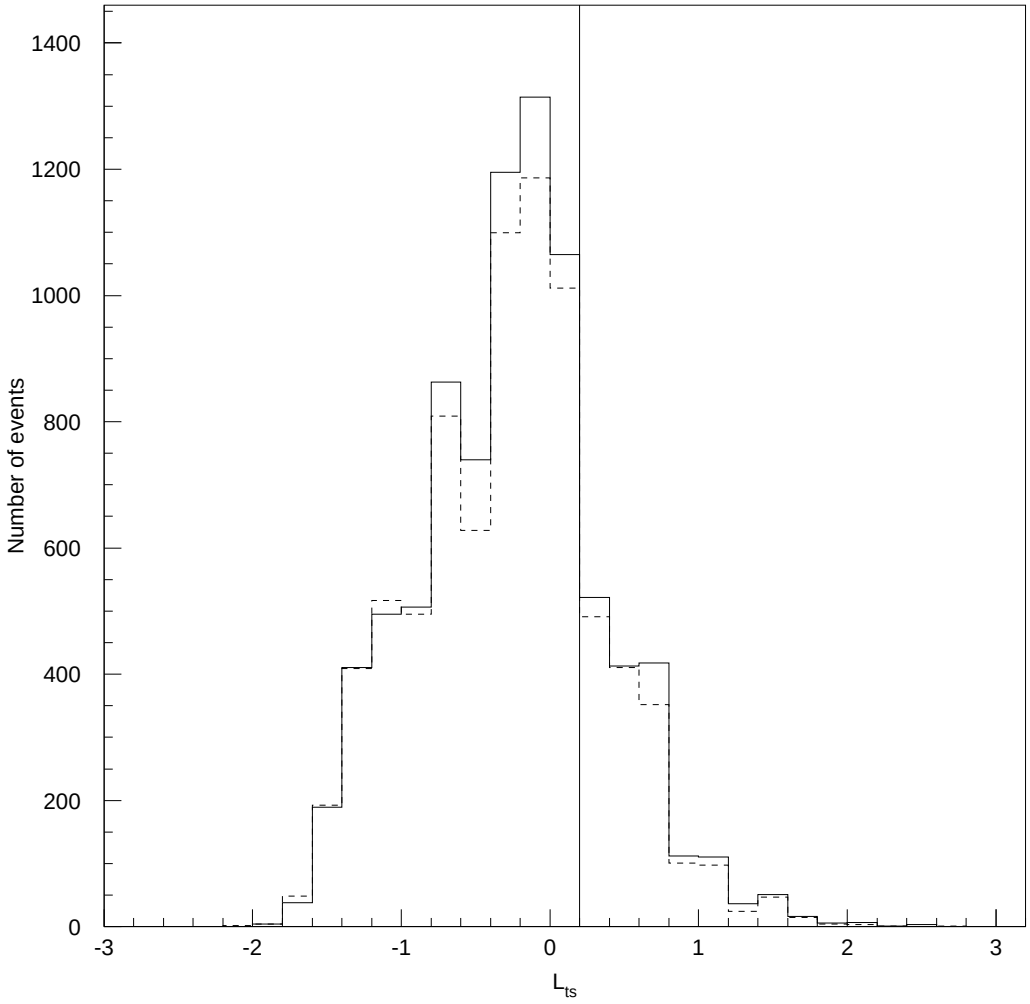

Figure B.9: Comparison of L_{ts} for events passing E1-E4 in the $p \to \bar{\nu}K^*(892)^+$, $K^+ \to \mu^+\nu$ search, SK-I NEUT (solid) and NUANCE (dashed). The vertical line indicates cut E5.

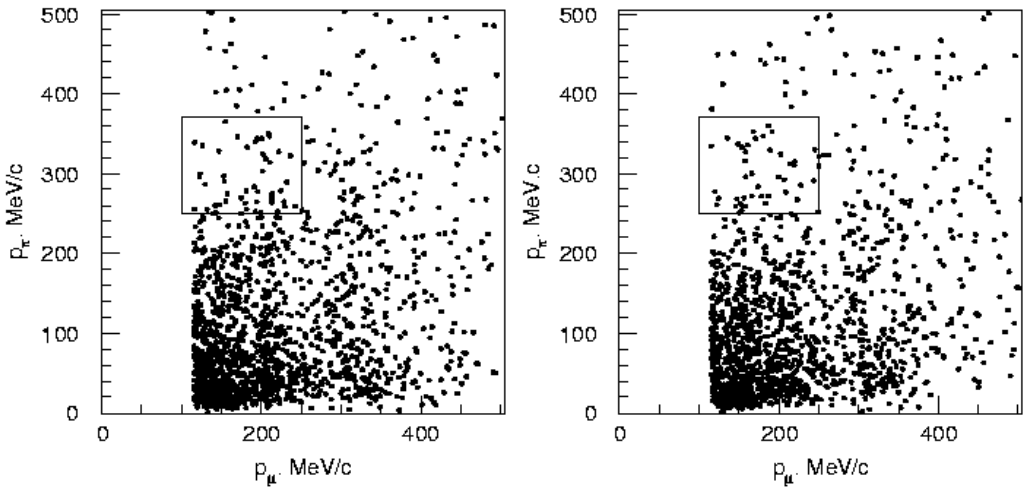

Figure B.10: Comparison of p_π vs p_μ for events passing E1-E5 in the $p \to \bar{\nu} K^*(892)^+$, $K^+ \to \mu^+ \nu$ search, SK-I NEUT (left) and NUANCE (right). The boxed region is kept by criteria E6-E7.

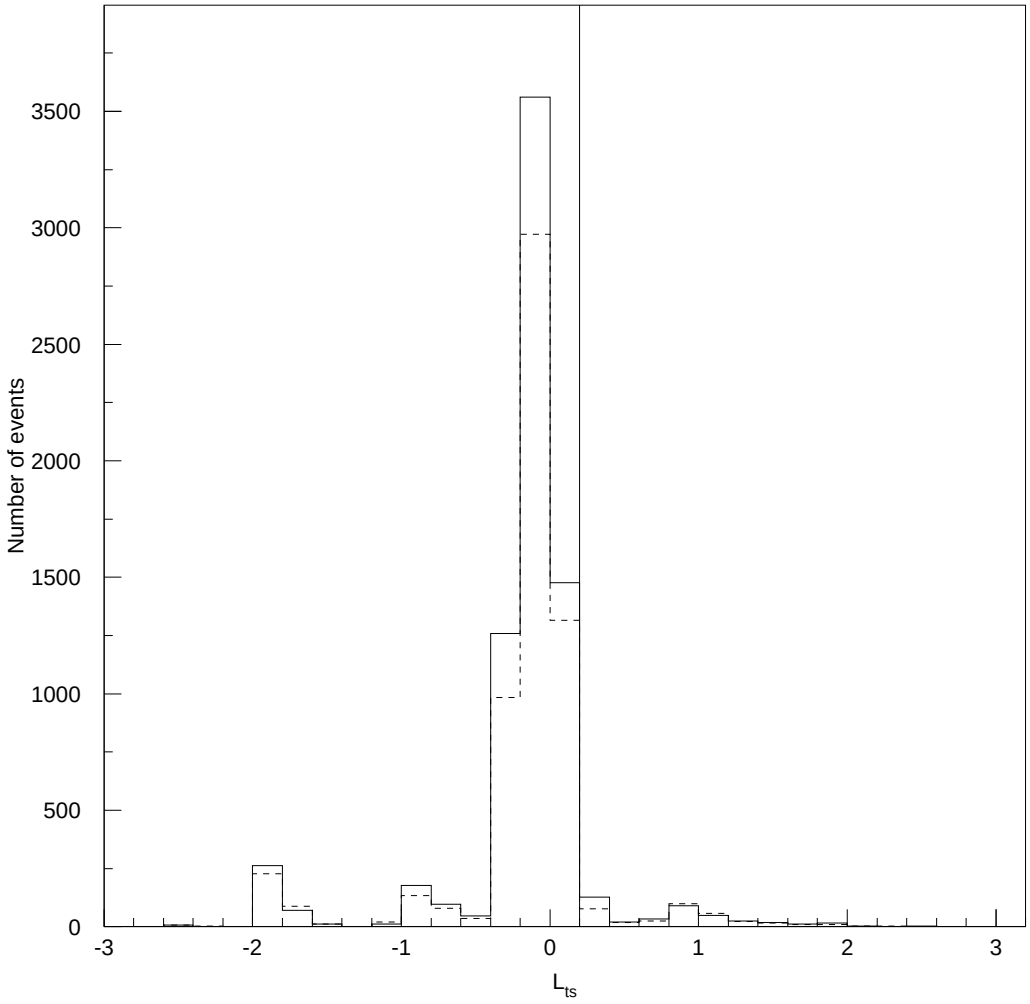

Figure B.11: Comparison of L_{ts} for events passing F1-F4 in the $p \to \bar{\nu}K^*(892)^+$, $K^+ \to \pi^+\pi^0$ search, SK-I NEUT (solid) and NUANCE (dashed). The vertical line indicates cut F5.

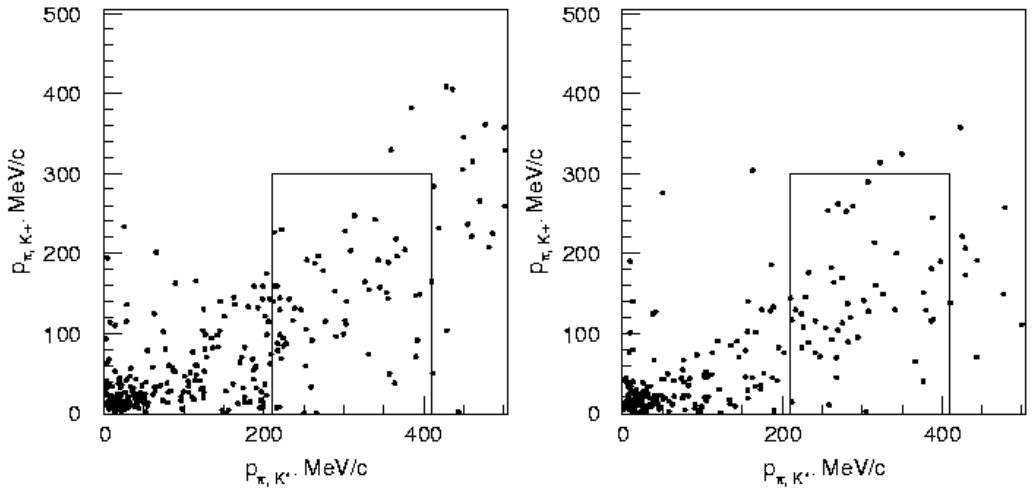

Figure B.12: Comparison of $p_{\pi,K+}$ vs $p_{\mu,K*}$ for events passing F1-F5 in the $p \to \bar{\nu}K^*(892)^+$, $K^+ \to \pi^+\pi^0$ search, SK-I NEUT (left) and NUANCE (right). The boxed region is kept by criteria F6-F7.

Appendix C

Setting Lifetime Limits

C.1 Bayesian approach

In this dissertation, most limits on proton lifetimes are set using the Bayesian method described in [13], using an equivalent implementation to that in [21]. In all cases, the probability $\mathcal{P}$ of a given number of decays n given an expected number of events N is assumed to be Poisson:

$$\mathcal{P}(n|N) = \frac{e^{-N}N^n}{n!}. \tag{C.1}$$

For studies of proton decay, N generally includes both signal and background:

$$N = \Gamma\lambda\epsilon + b, \tag{C.2}$$

where Γ is the rate of proton decay, λ the detector exposure (3.05×10^{34} proton-years for SK-I and 1.65×10^{34} proton-years for SK-II), ϵ the proton decay detection efficiency, and b the expected background.

The probability of proton decay at a rate Γ is then, by Bayes' theorem, given by

$$P(\Gamma|n_i) = A \int \int \mathcal{P}(n_i|\Gamma\lambda\epsilon_i + b_i) P(\Gamma) P(\epsilon_i) P(b_i) d\epsilon_i db_i, \tag{C.3}$$

where ϵ_i and b_i are the (uncertain) efficiency and background for the particular search, n_i is the observed number of events, and A is a normalization factor to ensure the probability integrates to unity.

$P(\Gamma)$ is taken to be 0 for $\Gamma < 0$ and 1 otherwise, while $P(\epsilon_i)$ is assumed to be a Gaussian, centered at the estimated efficiency $\epsilon_{0,i}$ with uncertainty $\sigma_{\epsilon,i}$, with ϵ_i bounded between 0 and 1. b_i is bounded below by 0, and $P(b_i)$ takes the form

$$P(b_i) = \frac{1}{b_i} \int_0^\infty \mathcal{P}(b'|n_{b,i}) e^{-\frac{-(b_i - b')^2}{2\sigma_{b,i}^2}} db', \tag{C.4}$$

where $n_{b,i}$ and $\sigma_{b,i}$ are the expected number of background events and the estimated uncertainty in that background.

Given $P(\Gamma|n_i)$ for a total of n independent searches, a 90% confidence level (CL) limit Γ_{lim} is calculated according to

$$0.9 = \frac{\int_0^{\Gamma_{lim}} \prod_{i=1}^n P(\Gamma|n_i) d\Gamma}{\int_0^\infty \prod_{i=1}^n P(\Gamma|n_i) d\Gamma}, \tag{C.5}$$

and a lower limit on the proton partial lifetime τ/B, with τ the proton lifetime and B the branching ratio into the mode being studied, is given by

$$\frac{\tau}{B} = \frac{1}{\Gamma_{lim}} \sum_{i=1}^n \epsilon_{0,i} \lambda_{0,i}. \tag{C.6}$$

The calculations of these integrals and limits is carried out, using Monte Carlo integration techniques, by a program named corlim.f, graciously provided by John Conway of the University of California at Davis [81]. This code also takes correlations between systematic uncertainties into account.

C.2 The pull method

For the $p \to \bar{\nu}K^+$, $K^+ \to \mu^+\nu$ without prompt γ tag search, described in Sec. 7.3.2, the "pull method" used in [14] is applied. A χ^2 statistic is defined:

$$\chi^2 = \sum_i \frac{\left[N_i^{obs} - N_i^{exp}\right]^2}{\sigma_i^2} + \sum_j (\delta_j)^2 \quad \text{(C.7)}$$

$$N_i^{exp} = aN_i^{bg} + \Gamma\lambda_i\epsilon_i(1 + \sum_j f_j^i\delta_j) \quad \text{(C.8)}$$

$$\simeq (1 + \sum_j f_j^i{\prime}\delta_j{\prime})(aN_i^{bg} + \Gamma\lambda_i\epsilon_i). \quad \text{(C.9)}$$

Here N_i^{obs} is the number of observed events in a bin, N_i^{exp} is the number of expected events in the bin, and σ_i is the combined statistical uncertainty in these.

N_i^{exp} is a function of the predicted number of background events N_i^{bg}, the normalization of that background a, the proton decay rate Γ, the exposure for the bin λ_i (depending on whether the bin is from SK-I or SK-II), and the predicted efficiency ϵ_i. Uncertainties in that efficiency are accounted for by the f_j^i, which characterize how much the efficiency in a bin will change due to a one-sigma change in the systematic uncertainty j. The δ_j reflect how far off from the central value that systematic uncertainty lies.

In order to apply the pull method as used in [14], however, the form C.9 must be used, so that the $f_j^i{\prime}$ terms multiply the entire prediction for a bin, rather than just that part due to proton decay. This is accomplished by defining

$$(1 + \sum_j f_j^i{\prime}\delta{\prime}_j)(aN_i^{bg} + \Gamma\lambda_i\epsilon_i) = aN_i^{bg} + \Gamma\lambda_i\epsilon_i(1 + \sum_j f_j^i\delta_j), \quad \text{(C.10)}$$

evaluated at $a = 1$, $b = 12.5$, which corresponds to the predicted atmospheric ν

background and the 90% CL limit for the monochromatic μ search set in [21].

This χ^2 is then minimized, as a function of Γ, a, and the δ_j. For SK-I or SK-II only, there are 14 bins i and two systematic uncertainties j, while for the combined fit there are 28 bins and four uncertainties.

Bibliography

[1] LEP, M. W. Gruenewald, (2004), hep-ex/0412015.

[2] Muon G-2, G. Bennet *et al.*, Physical Review **D73**, 072003 (2006), hep-ex/0602035.

[3] S. L. Glashow, Nuclear Physics **22**, 579 (1961).

[4] S. Weinberg, Physical Review Letters **19**, 1264 (1967).

[5] A. Salam and J. C. Ward, Physics Letters **13**, 168 (1964).

[6] P. W. Higgs, Physics Letters **12**, 132 (1964).

[7] P. Nath and P. F. Perez, (2006), hep-ph/0601023.

[8] H. Georgi and S. L. Glashow, Physical Review Letters **32**, 438 (1974).

[9] P. Langacker, Physics Reports **72**, 185 (1981).

[10] C. McGrew *et al.*, Physical Review **D59**, 052004 (1999).

[11] B. Viren, *A Search for the Decay of Protons to* $e^+\pi^0$ *and* $\mu^+\pi^0$, PhD thesis, State University of New York at Stony Brook, 2000.

[12] P. Langacker and M.-x. Luo, Physical Review **D44**, 817 (1991).

[13] Particle Data Group, S. Eidelman *et al.*, Physics Letters **B592**, 1 (2004).

[14] Super-Kamiokande, Y. Ashie *et al.*, Physical Review **D71**, 112005 (2005), hep-ex/0501064.

[15] Y. Tosa, G. C. Branco, and R. E. Marshak, Physical Review **D28**, 1731 (1983).

[16] D.-G. Lee, R. N. Mohapatra, M. K. Parida, and M. Rani, Physical Review **D51**, 229 (1995), hep-ph/9404238.

[17] J. C. Pati and A. Salam, Physical Review **D10**, 275 (1974).

[18] J. Wess and B. Zumino, Nuclear Physics **B70**, 39 (1974).

[19] U. Amaldi, W. de Boer, and H. Furstenau, Physics Letters **B260**, 447 (1991).

[20] H. Murayama and A. Pierce, Physical Review **D65**, 055009 (2002), hep-ph/0108104.

[21] Super-Kamiokande, K. Kobayashi *et al.*, Physical Review **D72**, 052007 (2005), hep-ex/0502026.

[22] B. Bajc, P. Fileviez Perez, and G. Senjanovic, Physical Review **D66**, 075005 (2002), hep-ph/0204311.

[23] A. H. Chamseddine, R. Arnowitt, and P. Nath, Physical Review Letters **49**, 970 (1982).

[24] T. Goto and T. Nihei, Physical Review **D59**, 115009 (1999), hep-ph/9808255.

[25] R. Arnowitt and P. Nath, Prepared for 6th International Symposium on Particles, Strings and Cosmology (PASCOS 98), Boston, Massachusetts, 22-27 Mar 1998.

[26] V. Lucas and S. Raby, Physical Review **D55**, 6986 (1997), hep-ph/9610293.

[27] Q. Shafi and Z. Tavartkiladze, Physical Review **D67**, 075007 (2003), hep-ph/0210181.

[28] J. L. Lopez and D. V. Nanopoulos, (1991), hep-th/9110036.

[29] M. Goldhaber, P. Langacker, and R. Slansky, Science **210**, 851 (1980).

[30] G. Flerov *et al.*, Soviet Physics Doklady **3**, 79 (1958).

[31] R. I. Steinberg and J. Evans, J. C., Invited paper presented at the International Conference on Neutrino Physics and Astrophysics, Elbrus, USSR, Jun 18-24, 1977.

[32] F. Reines, C. L. Cowan, and M. Goldhaber, Physical Review **96**, 1157 (1954).

[33] J. Learned, F. Reines, and A. Soni, Physical Review Letters **43**, 907 (1979).

[34] M. R. Krishnaswamy *et al.*, Physics Letters **B106**, 339 (1981).

[35] J. Bartelt *et al.*, Physical Review **D36**, 1990 (1987).

[36] G. Battistoni *et al.*, Nuclear Instruments and Methods in Physics Research **A245**, 277 (1986).

[37] FREJUS, C. Berger *et al.*, Nuclear Instruments and Methods in Physics Research **A262**, 463 (1987).

[38] W. W. M. Allison *et al.*, Physics Letters **B391**, 491 (1997), hep-ex/9611007.

[39] HPW, T. J. Phillips *et al.*, Physics Letters **B224**, 348 (1989).

[40] R. Becker-Szendy *et al.*, Nuclear Instruments and Methods in Physics Research **A324**, 363 (1993).

[41] KAMIOKANDE-II, K. S. Hirata *et al.*, Physics Letters **B220**, 308 (1989).

[42] SNO, S. N. Ahmed *et al.*, Physical Review Letters **92**, 102004 (2004), hep-ex/0310030.

[43] KamLAND, T. Araki *et al.*, Physical Review Letters **96**, 101802 (2006), hep-ex/0512059.

[44] Borexino, H. Back *et al.*, Physics Letters **B563**, 23 (2004), hep-ex/0302002.

[45] Y. Fukuda *et al.*, Nuclear Instruments and Methods in Physics Research **A501**, 418 (2003).

[46] A. Suzuki *et al.*, Nuclear Instruments and Methods in Physics Research **A329**, 299 (1993).

[47] S. Desai, *High Energy Neutrino Astrophysics with Super-Kamiokande*, PhD thesis, Boston University, 2004.

[48] M. Messier, *Evidence for Neutrino Mass from Observations of Atmospheric Neutrinos using Super-Kamiokande*, PhD thesis, Boston University, 1999.

[49] K. Nakamura *et al.*, Nuclear Physics **A268**, 381 (1976).

[50] H. Ejiri, Physical Review **C48**, 1442 (1993).

[51] M. Honda, T. Kajita, K. Kasahara, and S. Midorikawa, (2004), astro-ph/0404457.

[52] G. D. Barr, T. K. Gaisser, P. Lipari, S. Robbins, and T. Stanev, (2004), astro-ph/0403630, (Also, private communication with the authors. A slightly different flux is used in the present analysis.).

[53] G. Battistoni, A. Ferrari, T. Montaruli, and P. R. Sala, (2003), hep-ph/0305208.

[54] Y. Shikaze *et al.*, (2003), Proceedings of the 28th International Cosmic Ray Conferences (ICRC 2003), Tsukuba, Japan, 31 Jul - 7 Aug 2003, Vol.7, p.4027.

[55] http://ulysses.sr.unh.edu/NeutronMonitor/.

[56] Y. Hayato, Nuclear Physics Proceedings Supplements **112**, 171 (2002).

[57] D. Casper, Nuclear Physics Proceedings Supplements **112**, 161 (2002), hep-ph/0208030.

[58] C. H. Llewellyn Smith, Physics Reports **3**, 261 (1972).

[59] D. Rein and L. M. Sehgal, Annals of Physics **133**, 79 (1981).

[60] D. Rein and L. M. Sehgal, Nuclear Physics **B223**, 29 (1983).

[61] BEBC WA59, P. Marage *et al.*, Zeitschrift fur Physik **C31**, 191 (1986).

[62] KAMIOKANDE, M. Nakahata *et al.*, Journal of the Physical Society of Japan **55**, 3786 (1986).

[63] T. Sjostrand, Computer Physics Communications **82**, 74 (1994).

[64] M. Gluck, E. Reya, and A. Vogt, Zeitschrift fur Physik **C67**, 433 (1995).

[65] M. Derrick *et al.*, Physical Review **D17**, 1 (1978).

[66] Amsterdam-Bologna-Padua-Pisa-Saclay-Turin, S. Barlag *et al.*, Zeitschrift fur Physik **C11**, 283 (1982).

[67] P. Musset and J. P. Vialle, Physics Reports **39**, 1 (1978).

[68] J. E. Kim, P. Langacker, M. Levine, and H. H. Williams, Reviews of Modern Physics **53**, 211 (1981).

[69] L. L. Salcedo, E. Oset, M. J. Vicente-Vacas, and C. Garcia-Recio, Nuclear Physics **A484**, 557 (1988).

[70] R. G. Glasser *et al.*, Physical Review **D15**, 1200 (1977).

[71] Particle Data Group, C. Caso *et al.*, The European Physical Journal **C3**, 1 (1998).

[72] G. Rowe, M. Salomon, and R. H. Landau, Physical Review **C18**, 584 (1978).

[73] GEANT4, S. Agostinelli *et al.*, Nuclear Instruments and Methods in Physics Research **A506**, 250 (2003).

[74] T. A. Gabriel, J. E. Brau, and B. L. Bishop, IEEE Transactions on Nuclear Science **36**, 14 (1989).

[75] M. Shiozawa, *Search for Proton Decay via $p \to e^+\pi^0$ in a Large Water Cherenkov Detector*, PhD thesis, University of Tokyo, 1999.

[76] Super-Kamiokande, M. Shiozawa *et al.*, Physical Review Letters **81**, 3319 (1998), hep-ex/9806014.

[77] Super-Kamiokande, Y. Hayato *et al.*, Physical Review Letters **83**, 1529 (1999), hep-ex/9904020.

[78] M. Earl, *A Search for Nucleon Decay Into Modes Favored by Supersymmetry Using Super-Kamiokande*, PhD thesis, Boston University, 2000.

[79] K. Kobayashi *et al.*, (2006), nucl-ex/0604006.

[80] E. Davies, *Machine Vision: theory, algorithms, practicalities* (Elsevier, 2005).

[81] J. Conway, Calculation of cross section upper limit combining channels incorporating correlated and uncorrelated systematic uncertainties, Collider Detector at Fermilab collaboration note 6428.